

RICE UNIVERSITY

**Molecular Modeling the Microstructure and Phase Behavior of
Bulk and Inhomogeneous Complex Fluids**

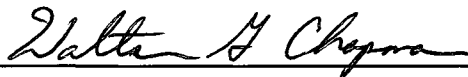
By

ADAM BYMASTER

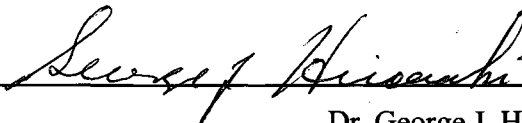
A THESIS SUBMITTED
IN PARTIAL FULFILLMENT OF THE
REQUIREMENTS FOR THE DEGREE

DOCTOR OF PHILOSOPHY

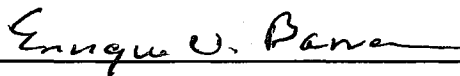
APPROVED, THESIS COMMITTEE



Dr. Walter G. Chapman, Chair
William W. Akers Professor
Chemical and Biomolecular Engineering



Dr. George J. Hirasaki
A. J. Hartsook Professor
Chemical and Biomolecular Engineering



Dr. Enrique V. Barrera
Professor
Mechanical Engineering and Materials Science

HOUSTON, TEXAS

APRIL 2009

UMI Number: 3362135

Copyright 2009 by
Bymaster, Adam

INFORMATION TO USERS

The quality of this reproduction is dependent upon the quality of the copy submitted. Broken or indistinct print, colored or poor quality illustrations and photographs, print bleed-through, substandard margins, and improper alignment can adversely affect reproduction.

In the unlikely event that the author did not send a complete manuscript and there are missing pages, these will be noted. Also, if unauthorized copyright material had to be removed, a note will indicate the deletion.

UMI[®]

UMI Microform 3362135
Copyright 2009 by ProQuest LLC
All rights reserved. This microform edition is protected against
unauthorized copying under Title 17, United States Code.

ProQuest LLC
789 East Eisenhower Parkway
P.O. Box 1346
Ann Arbor, MI 48106-1346

Copyright

Adam Bymaster

2009

To Kristen

Abstract

Molecular Modeling the Microstructure and Phase Behavior of Bulk and Inhomogeneous Complex Fluids

**By
Adam Bymaster**

Accurate prediction of the thermodynamics and microstructure of complex fluids is contingent upon a model's ability to capture the molecular architecture and the specific intermolecular and intramolecular interactions that govern fluid behavior. This dissertation makes key contributions to improving the understanding and molecular modeling of complex bulk and inhomogeneous fluids, with an emphasis on associating and macromolecular molecules (water, hydrocarbons, polymers, surfactants, and colloids). Such developments apply broadly to fields ranging from biology and medicine, to high performance soft materials and energy.

In the bulk, the perturbed-chain statistical associating fluid theory (PC-SAFT), an equation of state based on Wertheim's thermodynamic perturbation theory (TPT1), is extended to include a crossover correction that significantly improves the predicted phase behavior in the critical region. In addition, PC-SAFT is used to investigate the vapor-liquid equilibrium of sour gas mixtures, to improve the understanding of mercaptan/sulfide removal via gas treating.

For inhomogeneous fluids, a density functional theory (DFT) based on TPT1 is extended to problems that exhibit radially symmetric inhomogeneities. First, the influence of model solutes on the structure and interfacial properties of water are investigated. The DFT successfully describes the hydrophobic phenomena on

microscopic and macroscopic length scales, capturing structural changes as a function of solute size and temperature.

The DFT is used to investigate the structure and effective forces in nonadsorbing polymer-colloid mixtures. A comprehensive study is conducted characterizing the role of polymer concentration and particle/polymer size ratio on the structure, polymer induced depletion forces, and tendency towards colloidal aggregation.

The inhomogeneous form of the association functional is used, for the first time, to extend the DFT to associating polymer systems, applicable to any association scheme. Theoretical results elucidate how reversible bonding governs the structure of a fluid near a surface and in confined environments, the molecular connectivity (formation of supramolecules, star polymers, etc.) and the phase behavior of the system.

Finally, the DFT is extended to predict the inter-and intramolecular correlation functions of polymeric fluids. A theory capable of providing such local structure is important to understanding how local chemistry, branching, and bond flexibility affect the thermodynamic properties of polymers.

Acknowledgements

This dissertation was made possible through the support and contributions of many. First and foremost, I thank God, for it is under His grace that we live, learn, and flourish. He has blessed my life in more ways than I deserve.

I am grateful to Professor Walter Chapman, who, as my thesis advisor and mentor, introduced me to the world of complex fluid behavior and statistical mechanics. I thank him for his support and contributions to this work, as well as his direction throughout this thesis, which exposed me to a wide variety of topics and sciences.

I thank Professor George Hirasaki and Professor Enrique Barrera for serving on my thesis committee and for providing critical evaluation and input to this dissertation.

I thank Professor Ken Cox for sharing his valuable ideas, insight, and advice during group discussions and presentations.

I wish to thank Scott Northrop and Tim Cullinane for their fruitful discussions and guidance of the sour gas modeling. I would also like to thank ExxonMobil for granting permission to publish my internship work in this thesis.

A number of professional contacts also provided helpful discussions. I gratefully acknowledge Fèlix Llovel and Professor Lourdes Vega, as well as Professor Dong Fu for their helpful discussions about modeling phase behavior in the critical region. I also wish to thank Professor Hank Ashbaugh for his stimulating discussions about hydrophobic hydration and Juan Carlos Araque for his insight into the behavior of polymer-particle mixtures.

To my research group, I am grateful for our friendship and for the experiences we shared. I acknowledge Aleksandra Dominik and thank her for her patience in answering all my questions about the theory early in my research. I am indebted to Shekhar Jain, whose own work and ideas had great influence on this research. To Clint Aichele, who turned out to be an alright cowboy, and an even better friend; I thank him for his friendship and our discussions on research and life. In addition, I thank Francisco Vargas, Chris Emborsky, and Zhengzheng Feng for their comments during our group discussions.

Last, but not least, I would like to thank my family for their love and support over the years. I especially wish to thank my parents, Mark and Telesa Bymaster, who have been tremendous influences on my life and work ethic. To my wife Kristen, I dedicate this thesis. I owe you much, not only for your love, encouragement, and sacrifices, but also for making me a better person.

The financial support for this work was provided by the Robert A. Welch Foundation (Grant No. C1241) and by the National Science Foundation (CBET-0756166). This work was supported in part by the Shared University Grid at Rice funded by the NSF under Grant EIA-0216467, and a partnership between Rice University, Sun Microsystems, and Sigma Solutions, Inc.

Table of Contents

CHAPTER 1: Introduction	1
1.1 Motivation and challenges	1
1.1.1 Bulk fluids	3
1.1.2 Inhomogeneous fluids	5
1.2 Laying the ground work: Wertheim's TPT1 for associating fluids	8
1.3 Scope of the thesis	12
CHAPTER 2: Renormalization-group corrections to a perturbed chain statistical associating fluid theory for pure fluids near to and far from the critical region.....	15
2.1 Introduction.....	15
2.2 Background on renormalization-group methods	17
2.3 PC-SAFT outside the critical region.....	19
2.4 Recursive relations.....	23
2.5 Results and discussion	27
2.5.1 Applying RG theory to PC-SAFT.....	27
2.5.2 Reproducing Llovell et al.'s Soft-SAFT results.....	31
2.5.3 Reproducing Fu et al.'s PC-SAFT results	32
2.5.4 Improving PC-SAFT+RG	33
2.6 Conclusions.....	42
CHAPTER 3: A thermodynamic model for sour gas treating	44
3.1 Introduction and motivation.....	44
3.2 Theoretical model	48
3.2.1 Model selection	48
3.2.2 PC-SAFT for associating mixtures	50
3.3 Results and discussion	54
3.3.1 Parameter fitting for the mercaptans and sulfides	54
3.3.2 Hydrocarbon/H ₂ S binary mixtures	58
3.3.3 Hydrocarbon/sulfide binary mixtures	60
3.3.4 H ₂ S/sulfide binary mixtures	63
3.3.5 Solvent/sulfide binary mixtures.....	64
3.3.6 Multicomponent mixtures.....	67

3.3.7 <i>Mercaptan physical solubility versus mercaptan chemical solubility</i>	69
3.4 Conclusions.....	71
3.5 Future work and recommendations.....	72
CHAPTER 4: Density functional theory	76
4.1 Introduction and background	76
4.2 A general density functional formalism.....	78
4.3 Approximations for the free energy functional.....	82
4.3.1 <i>Atomic fluids</i>	83
4.3.2 <i>Polyatomic fluids</i>	85
4.4 Notable density functional theories	86
4.4.1 <i>Chandler, McCoy and Singer</i>	86
4.4.2 <i>Density functionals based on TPT1</i>	87
4.4.2.1 <i>Kierlik and Rosinberg</i>	88
4.4.2.2 <i>Segura, Chapman and Shukla</i>	89
4.4.2.3 <i>Yu and Wu</i>	92
4.4.2.4 <i>Chapman and coworkers</i>	95
CHAPTER 5: Hydration structure and interfacial properties of water near a hydrophobic solute from a fundamental measure density functional theory	101
5.1 Introduction.....	101
5.2 Theory	106
5.2.1 <i>Model</i>	106
5.2.2 <i>Density functional theory</i>	109
5.3 Results and discussion	115
5.4 Conclusions.....	125
CHAPTER 6: Microstructure and depletion forces in polymer-colloid mixtures from an <i>i</i> SAFT DFT	128
6.1 Introduction.....	128
6.2 <i>i</i> SAFT model.....	135
6.2.1 <i>Free energy functionals</i>	136
6.2.2 <i>Free energy functional derivatives</i>	140
6.2.3 <i>Equilibrium density profile and grand free energy</i>	141
6.3 Results and discussion	142

6.3.1 Local structure	143
6.3.2 Polymer mediated forces.....	150
6.3.3 Second virial coefficient.....	156
6.3.4 A preliminary study: Effect of attractive interactions.....	159
6.4 Conclusions.....	164
CHAPTER 7: An <i>i</i> SAFT density functional theory for associating polyatomic molecules	168
7.1 Introduction.....	168
7.2 Theory	174
7.2.1 Model	174
7.2.2 <i>i</i> SAFT density functional theory.....	177
7.2.2.1 Free energy functionals	178
7.2.2.2 Free energy functional derivatives	181
7.3 Results and discussion	182
7.3.1 Associating polymers near a wall	184
7.3.2 Self-assembly of associating polymers into inhomogeneous phases	188
7.4 Conclusions.....	195
CHAPTER 8: An <i>i</i> SAFT density functional theory for the intermolecular and intramolecular correlation functions of polymeric fluids	196
8.1 Introduction.....	196
8.2 <i>i</i> SAFT model.....	199
8.2.1 Inter- and intramolecular correlation functions.....	199
8.2.2 Free energies	202
8.2.3 Free energy derivatives.....	202
8.2.4 Equilibrium density profiles.....	203
8.3 Results and discussion	207
8.4 Conclusions.....	212
CHAPTER 9: Concluding remarks.....	213
APPENDIX A: Derivation of $\frac{\delta\beta A^{ex,assoc}}{\delta\rho_j(\mathbf{r})}$ (For Chapter 7)	220

APPENDIX B: Solving for $\chi_A^i(\mathbf{r}_1)$ (For Chapter 7)	227
References.....	229

List of Figures

Figure 1.1: Qualitative features of the microstructure of a fluid adsorbed at a surface at high density (blue) and low density (green).	5
Figure 1.2: Schematic of the association interaction potential model, in the framework of TPT1.	8
Figure 1.3: Bonding constraints between two associating molecules in TPT1.	9
Figure 2.1: (a) Temperature-density diagram for <i>n</i> -octane before modification of the perturbing potential function ($L=2\sigma$ and $\phi=18.75$). (b) Pressure-temperature diagram for <i>n</i> -octane before modification of the perturbing potential function ($L=2\sigma$ and $\phi=18.75$). Circles are experimental data, ⁸⁵ the solid line represents PC-SAFT+RG, and the dotted line is PC-SAFT.....	30
Figure 2.2: PC-SAFT crossover (RG) parameter dependence on molecular weight.....	36
Figure 2.3: (a) Temperature-density diagram for <i>n</i> -octane using the modified perturbing potential function. (b) Pressure-temperature diagram for <i>n</i> -octane using the modified perturbing potential function. Symbols and lines defined as in Figure 2.1.	38
Figure 2.4: (a) Temperature-density diagram and (b) pressure-temperature diagram for select light <i>n</i> -alkanes (C_3 , C_5 , and C_7).	39
Figure 2.5: Phase equilibria predictions for heavy <i>n</i> -alkanes (C_{20} , C_{24} , C_{36}). The circles represent simulation data, ⁹³ and critical points from experiments. ⁸⁶	40
Figure 2.6: (a) Critical temperatures and (b) critical pressures for <i>n</i> -alkanes, from C_2 to C_{36} as predicted by PC-SAFT +RG (solid lines) and PC-SAFT (dashed lines). Symbols represent experimental critical points. ^{86,88,91,92}	40
Figure 2.7: In (a), calculation of β critical exponent. The circles are calculated results and the solid line is a power fit used to determine β . In (b), calculation of δ critical exponent. The filled circles are calculated results below the critical density and the open circles are calculated results above the critical density. The solid line is a power fit used to determine δ	41
Figure 3.1: Simplified schematic of the absorption/stripping process for removal of sour gas impurities.	46
Figure 3.2: Temperature-density diagram for methane and the sulfide series. The pure component parameters were regressed to the saturated liquid densities of each component.....	55

Figure 3.3: Pressure-temperature diagram for methane and the sulfide series. The pure component parameters were regressed to the vapor pressures of each component. 56

Figure 3.4: Pure component parameter trends for the sulfide series. Other compound families demonstrate similar trends with molecular weight. 58

Figure 3.5: P-x diagram for alkane+H₂S mixtures. Symbols are experimental data, lines represent predictions from the PC-SAFT model: (a) CH₄+H₂S mixture, where symbols are experimental data, ¹²⁶ $k_{ij}=0.055$, (b) C₂H₆+H₂S mixture, where symbols are experimental data, ¹²⁷ $k_{ij}=0.07$, and (c) C₃H₈+H₂S mixture, where symbols are experimental data, ¹²⁸ $k_{ij}=0.08$ 59

Figure 3.6: P-x diagram for (a) CH₄+MSH (methyl mercaptan) mixture, where symbols are experimental data, ¹³¹⁻¹³³ lines represent predictions from the PC-SAFT model ($k_{ij}=0.04$), and (b) CH₄+EtSH (ethyl mercaptan) mixture, where symbols are experimental data, ¹³¹⁻¹³³ lines represent predictions from the PC-SAFT model ($k_{ij}=0.037$). 61

Figure 3.7: P-x diagram for (a) CH₄+DMS (dimethyl sulfide) mixture, where lines represent predictions from the PC-SAFT model ($k_{ij}=0.03$), and (b) CH₄+EMS (methylethyl sulfide) mixture where lines represent predictions from the PC-SAFT model ($k_{ij}=0.035$). Symbols represent experimental data. ¹³¹⁻¹³³ 62

Figure 3.8: P-x diagram for (a) C₆H₁₄+MSH (methyl mercaptan) mixture, where lines represent predictions from the PC-SAFT model ($k_{ij}=0.035$), and (b) C₄H₁₀+PrSH (propyl mercaptan) mixture, where lines represent predictions from the PC-SAFT model ($k_{ij}=0.025$). Symbols represent experimental data. ¹³¹⁻¹³³ 62

Figure 3.9: P-x diagram for (a) H₂S+COS (carbonyl sulfide) mixture, where symbols are experimental data, ^{131,132} lines represent predictions from the PC-SAFT model ($k_{ij}=0.045$), (b) H₂S+DMS mixture, where symbols are experimental data, ^{131,132} lines represent predictions from the PC-SAFT model ($k_{ij}=-0.015$), and (c) H₂S+EMS mixture, where symbols are experimental data, ^{131,132} lines represent predictions from the PC-SAFT model ($k_{ij}=0.00$). The T-x-y diagram for the H₂S+MSH mixture is shown in (d), where symbols are experimental data, ¹³⁴ and lines represent predictions from the PC-SAFT model ($k_{ij}=0.06$). 63

Figure 3.10: P-x diagram for (a) H₂O+MSH mixture, where symbols represent experimental data, ¹³⁷ and lines represent predictions from the PC-SAFT model ($k_{ij}=-9.01157E-5*T(K) + 5.46720E-2$), (b) H₂O+EtSH mixture, where symbols are experimental data, ¹³⁷ and lines represent predictions from the PC-SAFT model ($k_{ij}=-6.66667E-5*T(K) - 6.54333E-3$), (c) H₂O+ H₂S mixture, where symbols are experimental data, ¹³⁸ and lines represent predictions from the PC-SAFT model ($k_{ij}=0.025$), and (d) H₂O+ MDEA mixture, where symbols are experimental data ¹³⁵ (correlated using Raoult's law), and lines represent predictions from the PC-SAFT model ($k_{ij}=-0.055$). 65

- Figure 3.11: Effect of temperature and molecular weight of mercaptan on the Henry's constant. As H_{RSH} increases, the solubility or pickup of mercaptan in the liquid solvent decreases. Symbols are experimental data¹³⁷ taken over a range of pressures. For comparison, lines represent predictions from the PC-SAFT model at a total pressure of $P=2.5$ bar. 66
- Figure 3.12: In (a), P-x diagram for MSH + H₂O+ MDEA mixture. The aqueous amine solution is 50 wt% MDEA. Symbols are experimental data,¹⁰⁸⁻¹¹⁰ lines represent predictions from the PC-SAFT model. The binary interaction parameters for MSH/H₂O and MDEA/H₂O were the same as before for the binary systems. The binary interaction parameter for MSH/MDEA was determined to be $k_{ij}=0.085$. From (b), P-x diagram for MSH + H₂O+ MDEA mixture. The mass percent of MDEA in the aqueous amine solution is varied from 0%, 35 wt%, 50wt%, 75wt%, respectively..... 67
- Figure 3.13: Effect of temperature and molecular weight of mercaptan on the Henry's constant in the ternary mixture RSH-MDEA-H₂O (no acid gas loading). The aqueous amine solution is 50 wt% MDEA. As H_{RSH} increases, the solubility or pickup of mercaptan in the liquid solvent decreases. Symbols are experimental data,¹⁰⁸⁻¹¹⁰ lines represent predictions from the PC-SAFT model. The PC-SAFT predictions shown are at $P=1.0$ bar. 68
- Figure 3.14: Effect of temperature and molecular weight of mercaptan on the Henry's constant in the mixture RSH-toluene. Opposite to the aqueous amine solutions, the solubility increases as the size of the mercaptans increase. The k_{ij} for MSH/toluene and EtSH/toluene were fit to experimental VLE data,¹³⁷ and were determined to be $k_{ij}=0.01$ and 0.0025, respectively. 70
- Figure 3.15: Effect of temperature and solvent choice on the solubility of the mercaptan. The physical solvents (hexane and toluene) show considerably more RSH pickup when compared to pure water or the aqueous amine solution (50wt% MDEA). The k_{ij} value for MSH/hexane was determined by experimental VLE data,¹³⁷ and determined to be $k_{ij}=0.035$ 71
- Figure 3.16: Effect of temperature and acid gas loading on the solubility of the mercaptan. Symbols are experimental data.¹⁰⁸⁻¹¹⁰ 74
- Figure 4.1: Schematic of chain formation from a mixture of associating spheres. 96
- Figure 5.1: Water represented using the four site model (4[2,2]) accounts for the two electron lone pairs (e^-) and the two hydrogen sites (H^+) of the water molecule..... 107
- Figure 5.2: The association interaction potential model. From the theory, if molecule 1 is oriented within the constraints given in eq. (5.6) with respect to molecule 2, then a

bond will form between the two molecules, given that their bonding sites are compatible.
 108

Figure 5.3: Geometry of a water molecule, with radius r_w , in contact with a hard solute, with radius r_s . R is the distance of closest approach between the solute and water molecule..... 109

Figure 5.4: Density profiles for water around a hard sphere solute at conditions away from coexistence: (a) Low density condition at $T=400\text{K}$ ($\epsilon^{HB}/k_bT=6.250$, $\epsilon^{LJ}/k_bT=0.634$) and $\rho_b\sigma^3=0.20$ and (b) liquid-like condition $T=298\text{K}$ ($\epsilon^{HB}/k_bT=8.385$, $\epsilon^{LJ}/k_bT=0.850$) and $\rho_b\sigma^3=0.90$. The sizes of the solute particles in (a) are $R=\sigma$, 2.5σ , and ∞ (corresponding to planar wall), and in (b) $R=1.5\sigma$, 5.0σ , and ∞ , respectively. 117

Figure 5.5: Density distribution of water around hard solutes of various sizes at coexistence conditions: $T=298\text{K}$ ($\epsilon^{HB}/k_bT=8.385$, $\epsilon^{LJ}/k_bT=0.850$) and $\rho_b\sigma^3=0.830$. The inset compares contact densities from this work (dashed line) with simulation and other theory (symbols). The diamonds represent data from simulations performed by Floris²⁰⁵ and squares represent predictions from revised SPT by Ashbaugh and Pratt.²⁰⁴ 119

Figure 5.6: Surface tension of water near a solute of size R . The arrows at 72 mN/m and 66 mN/m represent the vapor-liquid interfacial tension of water obtained from experiment²³³ and SPC/E simulation.²⁴⁴ The solid line represents this work and the squares represent predictions from revised SPT by Ashbaugh and Pratt.²⁰⁴ 121

Figure 5.7: (a) Fraction of molecules in the monomer state (X_0) through the fraction of molecules with the maximum allowable bonds (X_4) for different size solutes at $T=298\text{K}$. (b) Average number of hydrogen bonds per molecule $\langle N_{HB} \rangle$ at $T=298\text{K}$ for different size solutes as a function of the position in the fluid. The arrow and symbols refer to $\langle N_{HB} \rangle$ obtained from experiments by Luck²³⁴ and Soper et al.,²³⁵ and from TIP4P simulations for water by Jorgensen and Madura.²²² 122

Figure 5.8: Contact density curves at $T=300\text{K}$, 340K , 380K and 420K , respectively, for water around solutes of different size. Contact densities are along the liquid saturation curve for each respective temperature..... 124

Figure 5.9: (a) Fraction of molecules in the monomer state (X_0) through the fraction of molecules with the maximum allowable bonds (X_4) for different size solutes at $T=380\text{K}$. (b) Average number of hydrogen bonds per molecule $\langle N_{HB} \rangle$ at $T=380\text{K}$ for different size solutes as a function of the position in the fluid. 125

Figure 6.1: The density distribution of polymer segments near a LJ repulsive particle with diameter $\sigma_s/\sigma=4.9$ at concentrations $\rho_b\sigma_s^3=0.025$, 0.2 , and 0.6 for the chain lengths (a) $m=16$ and (b) $m=120$. The symbols are simulation data²⁶⁶ and the solid lines are from *i*SAFT. In (b), the dashed lines represent results from PRISM-PY-LJ.²⁶⁶ 145

Figure 6.2: The fraction of end segment density to middle segment density ($f_e(r)$) normalized to the bulk value ($f_{e,bulk}$) as a function of distance from the surface of a LJ repulsive colloidal particle ($\sigma_c/\sigma_s=4.9$). Results are presented for the case of $m=16$ at densities $\rho_b\sigma_s^3=0.025$ and 0.6 . In the inset, the normalized contact fraction is plotted as a function of chain length ($m=16$ and $m=120$) and density. The symbols are simulation results²⁶⁶ and the solid lines are from *iSAFT*..... 147

Figure 6.3: The density distribution of polymer segments near isolated hard particles of size $\sigma_c/\sigma_s=5, 15,$ and ∞ are shown and represented by solid, dashed, and dotted lines, respectively. In all panels the chain length of $m=1000$ is used. The concentrations are (a) $\rho_b\sigma_s^3=0.001$, (b) $\rho_b\sigma_s^3=0.1$, and (c) $\rho_b\sigma_s^3=0.5$, respectively..... 149

Figure 6.4: Depletion forces between two interacting particles of size ($\sigma_c/\sigma_s=5$) as a function of colloidal separation. Solid lines denote *iSAFT* results and symbols denote simulation data.²⁶⁹ Results are presented for $\rho_b\sigma_s^3=0.1$ and $m=30$ (\square), $\rho_b\sigma_s^3=0.225$ and $m=20$ (\circ), and $\rho_b\sigma_s^3=0.3$ and $m=10$ (\diamond). The inset shows the corresponding potential of mean force (PMF)..... 152

Figure 6.5: Effect of concentration on (a) the potential of mean force (PMF) between two interacting particles ($\sigma_c/\sigma_s=4.9$; $m=16$), and (b) the depletion force between two interacting particles ($\sigma_c/\sigma_s=5$; $m=20$). In (a), solid lines represent the *iSAFT* predictions and symbols denote MC simulations.²⁶⁵ The particle-polymer interaction is modeled via a LJ repulsive potential, consistent with the simulation data. The concentration is varied $\rho_b\sigma_s^3=0.1$ (\square), 0.2 (\diamond), and 0.3 (\circ). In (b), solid lines represent the *iSAFT* predictions and symbols denote MC simulations.²⁶⁹ All nonbonded interactions are of hard-sphere type, consistent with the simulation data. The concentration is varied: $\rho_b\sigma_s^3=0.225$ (\square), 0.3 (\circ), and 0.45 (\diamond). The inset shows the corresponding PMF..... 153

Figure 6.6: Effect of (a) chain length and (b) colloid/segment size ratio (σ_c/σ_s) on the depletion forces between two interacting particles. In (a), interacting particles are of size ($\sigma_c/\sigma_s=5$). The bulk segment density is $\rho_b\sigma_s^3=0.3$ and the chain length of the polymer chain is varied: $m=1, 4, 10,$ and 100 , respectively, from bottom to top at contact. In (b), the bulk segment density is $\rho_b\sigma_s^3=0.3$ and the chain length of the polymer chain is $m=50$. The size ratio is varied: $\sigma_c/\sigma_s=2.5, 5,$ and 10 , respectively. The corresponding PMFs are shown in each inset. 155

Figure 6.7: Second-virial coefficient as a function of bulk density ($\rho_b\sigma_s^3$) for different chain lengths. *iSAFT* predictions are represented by the solid lines; the thin red solid line represents the case $\sigma_c/\sigma_s=5, m=20$ while the thick solid lines represent cases $\sigma_c/\sigma_s=4.9, m=16$ (red) and $m=120$ (blue), respectively. Symbols represent simulation data from Doxastakis et al.,²⁶⁵ $\sigma_c/\sigma_s=4.9, m=16$ (\circ) and $m=120$ (\square), and from Striolo et al.,²⁶⁹ $\sigma_c/\sigma_s=5, m=20$ (\blacktriangle). PRISM-PY predictions (dashed lines) for $\sigma_c/\sigma_s=5, m=20$ (red, Patel et al.¹⁸⁰) and $\sigma_c/\sigma_s=4.9, m=120$ (blue, Doxastakis et al.²⁶⁵) are included for comparison.. 157

Figure 6.8: Second-virial coefficient for varying size ratios ($\sigma_c/\sigma_s=2.5, 5, 7.5, 10$) as a function of (a) chain length and (b) bulk polymer density. In (a) the bulk density is constant at $\rho_b\sigma_s^3=0.3$, while in (b) the chain length is constant at $m=20$ 159

Figure 6.9: The density distribution of polymer segments near an attractive particle with diameter $\sigma_c/\sigma_s=5$, at a concentration $\rho_b\sigma_s^3=0.7$, with polymer chain length $m=20$. The temperature was chosen to be $T^*=1.33$. All non-bonded interactions are modeled using a truncated and shifted LJ potential. The symbols represent MD simulation results,²⁹⁹ whereas the solid lines represent *i*SAFT predictions for $\epsilon_{cs}/\epsilon_{ss}=1$ (blue, Δ) and $\epsilon_{cs}/\epsilon_{ss}=2$ (red, \square). 162

Figure 6.10: The density distribution of polymer segments near an attractive particle with diameter $\sigma_c/\sigma_s=5$, at a concentration $\rho_b\sigma_s^3=0.7$, with polymer chain length $m=20$. The temperature is varied ($T^*=1.0, T^*=1.33$, and $T^*=3.33$) for (a) a weakly attractive polymer-colloid system, and (b) a strongly attractive polymer-colloid system..... 163

Figure 7.1: Illustration of associating schemes used in this work: (a) end associating functional groups (terminal associating segment with one site) and (b) schemes capable of forming a star polymer architecture (3 arms, $N=16$) at high association strengths. 183

Figure 7.2: Effect of varying bonding strength (ϵ^{assoc}) on the structure of an associating fluid (associating scheme from Figure 7.1 (a)) near a smooth hard surface. Here dispersion interactions are neglected, $\epsilon^{LJ}=0$. Lines represent theoretical results using the inhomogeneous association free energy functional (solid lines) and the weighted bulk form association free energy functional (dashed lines, provided for comparison at highest association energies). In (a), a dimerizing hard sphere fluid is presented at $\rho_b\sigma^3=0.1999$ and $\beta\epsilon^{assoc}=14$ (right vertical axis), and at $\rho_b\sigma^3=0.4868$ and $\beta\epsilon^{assoc}=11$ (left vertical axis). Symbols represent simulation data.³⁰ In (b), the structure of an associating polymer fluid ($m=4$) is presented at $\rho_b\sigma^3=0.2$ (right vertical axis) and $\rho_b\sigma^3=0.5$ (left vertical axis). Here, symbols represent results for a nonassociating 4mer (\diamond) and 8mer (\square). 185

Figure 7.3: The density distribution of a star polymer (3 arms, $N=16$) between two hard walls separated at a distance $H=16\sigma$ (profile only given near one wall) at $\eta_{avg}=0.3, 0.2$, and 0.1 . A high population of star polymers is formed in the melt at high bonding strengths (e.g., $\beta\epsilon^{assoc}=30$) using any of the association schemes given in Figure 7.1 (b). Symbols represent simulation data from Yethiraj and Hall³⁴¹ and lines represent results from *i*SAFT. The density profiles are normalized to the bulk value. 187

Figure 7.4: Phase diagram for an associating polymer mixture. The binary mixture is at a total segment density of $\rho_b\sigma^3=0.85$ and is symmetric ($m_{C1}=8$ and $m_{C2}=8$, equal concentrations, association scheme from Figure 7.1 (a)). Three distinct phases are present in the phase diagram: a homogeneous disordered phase, a 2 phase macrophase, and a lamellar microphase. 189

Figure 7.5: (a) Example of a typical density profile for a liquid-liquid macrophase separation. (b) Example of a typical density profile for a lamellar microphase separation. A lamellar phase can form at higher association strengths where a higher concentration of copolymer exists in the mixture. The lamellar period for this example structure is $L=8\sigma$. The equilibrium lamellar period (L_e) for the microphase is determined via the grand free energy (See Figure 7.6; changing the bonding energy or the dispersion energy affects the equilibrium spacing of the lamellar structure). 190

Figure 7.6: Grand free energy per volume as a function of the computational domain at given association and dispersion energies ($m_{C1}=8$, $m_{C2}=8$, $N=16$). The equilibrium spacing is determined as the width at which a minimum in the free energy occurs. Similar results and trends are predicted under other sets of conditions and chain lengths. 191

Figure 7.7: Phase diagram for associating polymer mixtures ($N=16$ and $N=100$) highlighting the effect of chain length and temperature on the phase behavior. Three distinct phases are present in the phase diagram: a homogeneous disordered phase (DIS), a macrophase (2 phase), and a lamellar microphase (LAM). Reentrant behavior is observed (DIS-2 phase-DIS and LAM-DIS-LAM) upon raising/lowering the temperature. 192

Figure 8.1: Schematic of the test particle model used in this work. Here a middle segment from a hard-sphere chain of 8 segments is fixed at the origin. The inter- and intramolecular segment-segment correlation functions are calculated from the density distributions of the tethered segments (T_1 and T_2) and of the free molecules (F) around the fixed segment at the origin. 199

Figure 8.2: In (a-c), the intermolecular site-site distribution functions of freely jointed hard-sphere 4mers are given at the overall packing fractions of $\eta=0.1$, 0.2, and 0.34: (a) $g_{11}(r)$, $g_{12}(r)$, and (c) $g_{22}(r)$. The corresponding average pair correlation function $g(r)$ is given in (d). Symbols represent simulation data from Yethiraj et al.³⁶¹ 208

Figure 8.3: In (a-c), the intermolecular site-site distribution functions of freely jointed hard-sphere 8mers are given at the overall packing fractions of $\eta=0.05$, 0.25, and 0.35: (a) $g_{11}(r)$, $g_{14}(r)$, and (c) $g_{44}(r)$. The corresponding average pair correlation function $g(r)$ is given in (d). Symbols represent simulation data from Yethiraj et al.³⁶¹ 209

Figure 8.4: The average correlation functions of freely-jointed 4mers at $\eta=0.0524$, 0.2618, and 0.4189. The average intermolecular correlation function is presented in (a), and the average nonbonded intramolecular correlation function is presented in (b). Symbols represent simulation data from Chang and Sandler.³⁵⁸ 210

Figure 8.5: The average correlation functions of freely-jointed 8mers at $\eta=0.0524$, 0.2618, and 0.4189. The average intermolecular correlation function is presented in (a), and the average nonbonded intramolecular correlation function is presented in (b). Symbols represent simulation data from Chang and Sandler.³⁵⁸ 211

List of Tables

Table 2.1: Molecular parameters and crossover (RG) parameters ϕ , L , and ξ	35
Table 2.2: Critical constants for light n -alkanes, compared with experimental data ^{88,91,92}	37
Table 2.3: Critical constants for heavy n -alkanes, compared with experimental data ^{86,91}	39
Table 3.1: Pure component parameters for the components considered in this study. All components are main constituents typically found in natural gas mixtures or in the solvents used in treating	57
Table 5.1: Molecular parameters for water.....	116

CHAPTER 1

Introduction

This dissertation makes key contributions to improving the understanding and molecular modeling of complex bulk and inhomogeneous fluids, with an emphasis on associating and macromolecular molecules (e.g., water, hydrocarbons, polymers, surfactants, and colloids). Such developments apply broadly to fields ranging from biology and medicine, to high performance soft materials and energy. In this chapter, the motivation, objectives, and outline of this research will be identified and introduced.

1.1 Motivation and challenges

Understanding the microscopic structure and macroscopic properties of complex fluids from a molecular perspective is central to chemical process and material design. Over the past several decades, accurate methods have been developed for describing the thermodynamic behavior of fluids composed of simple molecules. Simple fluids are characterized by their near spherical molecular shape and weak attractive forces, where the structure of the liquid is dominated by geometric packing constraints. The attractive forces contribute little to fluid structure and thus the fluid is a function of a single length scale, in this case, the size of the molecules. Nevertheless, a great number of fluids do not fall within this simple class. In contrast to simple fluids, much is left to be

investigated and understood for complex fluid behavior. The molecular thermodynamics of complex fluids is dependent on multiple length scales. In addition to molecular size and shape, the behavior of the fluid can also be dependent on molecular flexibility, polar interactions, and other specific molecular interactions such as hydrogen bonding.

Associating fluids, polymers, surfactants, colloids, liquid crystals, gels, and biomolecules all belong to this class of fluids.

Physical experiments are essential to advancing our knowledge and understanding of complex fluid behavior, but unfortunately can be difficult to perform under certain conditions (e.g., critical property measurements for heavier components), and can be hampered by the large parameter space involved in such systems (e.g., material design). Molecular theories can be applied in tandem with experiments to accelerate the understanding of complex fluid behavior and material design. Still, modeling these systems is not an easy task, due to the multiple length scales involved in such problems. Accurate prediction of the thermodynamics and microstructure of a complex fluid is contingent upon a model's ability to capture the molecular architecture and the specific intermolecular and intramolecular interactions that govern fluid behavior, all while satisfying thermodynamic consistency and remaining computationally tractable. Unfortunately, even the more sophisticated existing theories fail in meeting such challenges. This research is motivated by the need to fill this void. The primary focus of this work is accurate prediction of the equilibrium phase behavior, thermodynamics, and microstructure of complex fluids. The research has two components: bulk fluids and inhomogeneous fluids.

1.1.1 Bulk fluids

The van der Waals equation of state (EOS), proposed in 1873, was the first equation to predict vapor-liquid coexistence of a bulk fluid. Even today, many conventional engineering equations of state are variants on the van der Waals equation. Such equations of state represent repulsive interactions via a hard-sphere reference term, and long-range attractions via a mean-field term. The commonly used EOSs (e.g., Redlich-Kwong,¹ Peng-Robinson²) improve the accuracy of the van der Waals equation by introducing improvements to the hard-sphere and/or the mean field terms. The advantages of using these equations include their easy implementation and their ability to represent the relation between temperature, pressure, and phase compositions in binary and multicomponent mixtures. However, such models are only suitable for simple molecules (e.g., low molecular weight hydrocarbons, simple inorganics). In addition, it is well known that such equations are restricted to the prediction of vapor pressure and suffer invariably in estimating saturated liquid densities.³

For polyatomic molecules, a more appropriate reference fluid must be chosen to account for the molecular size and shape. Advances in statistical mechanics have led to the development of more fundamental, molecular based equations of state. In the mid 1980s, Wertheim⁴⁻⁷ proposed a thermodynamic perturbation theory of first order (TPT1) to describe the phase behavior and thermodynamic properties of a fluid of hard spheres with multiple association sites. Such work formed the basis for a number of equations of state for chain fluids, most notably the statistical associating fluid theory (SAFT) developed by Chapman et al.⁸⁻¹² Chapman et al. extended TPT1 to mixtures of associating atomic fluids and derived an EOS for hard chain fluids by taking the limit of

complete association between the spheres. Additional contributions such as dispersion attractions, polarity and permanent dipole moments, to name a few, can be included as additional perturbations to the reference fluid to mimic real fluid behavior. For example, polarity is an important consideration for ketones, alcohols, esters, and water, where permanent dipole moments are induced by imbalances in the electron density around a molecule. Several SAFT versions are available today, as the SAFT approach has become a standard equation for engineering purposes, especially for larger macromolecular fluids with complex inter- and intramolecular interactions. One of the more prominent versions of SAFT, perturbed-chain SAFT (PC-SAFT), is presented in chapters 2 and 3, along with a brief review of other versions of SAFT and alternative bulk theories.

Despite years of work and development, even the more sophisticated and more versatile equations of state still suffer from shortcomings. Some of the problematic issues of bulk equations of state include the inability to accurately predict thermodynamic properties in the critical region for fluids, as well as capture anomalous behavior in aqueous systems. Some of these problems are not trivial and have been under investigation for some time. Improving the predicted thermodynamic properties in the critical region is a specific objective in this research and is addressed in chapter 2. In addition, the SAFT equation of state is still finding wide use and application in the study of new systems and more complex mixtures. Chapter 3 presents new results using PC-SAFT to predict the phase behavior of mixtures containing constituents found in sour gas treating services.

1.1.2 Inhomogeneous fluids

An inhomogeneous fluid is characterized by its non-uniformity in density with respect to spatial coordinates. Figure 1.1 illustrates a simple example of the microstructure of a fluid near a surface. In this example, the inhomogeneity in the density profile occurs in one dimension, normal to the surface. The normal distance (r) is scaled by the segment diameter (σ) and the total segment density is scaled by the bulk value (ρ_b). As shown in the figure, fluids at interfaces or confined in pores have properties qualitatively different from their bulk counterparts. At higher densities, density enhancement and oscillations can occur near the surface, while at lower densities depletion from the surface can occur. Far from the surface, the density reaches its bulk limit, where the effects of the surface are no longer felt. Inhomogeneous structure is a

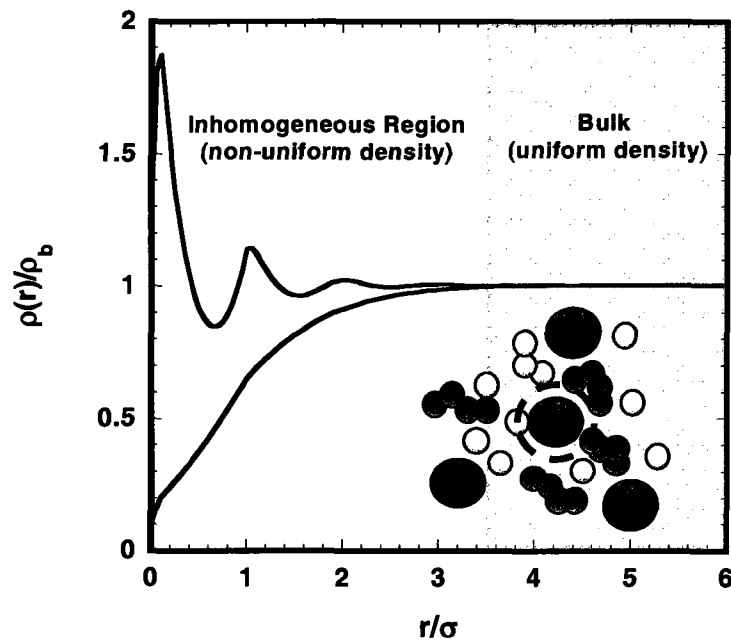


Figure 1.1: Qualitative features of the microstructure of a fluid adsorbed at a surface at high density (blue) and low density (green).

consequence of the interactions of the fluid molecules with a solid surface and/or the interactions between the fluid itself. An understanding of such behavior is important as fluid-wall and fluid-fluid interactions can compete against each other, thus leading to surface driven phase behavior (e.g., layering, wetting) that is not present in bulk systems.¹³ Such non-uniformity occurs in many natural systems such as at interfaces, in confined spaces, and in self-assembling systems, thereby providing a great interest to the chemical, oil and gas, pharmaceutical, and biological industries. Specific technological processes where such work is important include processes involving oil recovery, paints and coatings, detergents and shampoos, food production, pharmaceutical suspensions, self-healing materials, affinity based separations, chemically modified surfaces for sensors, drug delivery and medical diagnostics, and performance/smart materials.

Understanding the physics (surface forces, varying dimensionality, and interplay of multiple length scales) behind such systems is a very challenging problem. Experimental studies continue to provide many insights into inhomogeneous systems, yet can become hampered by the inability to understand behavior on a molecular scale and, as previously mentioned, by the inefficiency of studying the broad parameter space involved.

Theoretical models therefore play an important role in understanding and aiding the experimental design of these complex systems. Still, these models have limitations and must be chosen carefully. Early scaling and mean field theories do not provide detailed microstructure information accurately and are often limited to specific systems.

Examples include the scaling theory of deGennes¹⁴ for polymer brushes and the Asakura-Oosawa (AO) theory^{15,16} for athermal polymer-colloid suspensions. More sophisticated approaches have been used extensively and have found wide success, most

notably self-consistent field theory (SCFT)^{17,18} and integral equation theory (IET).^{19,20} Still even these more sophisticated approaches suffer from limitations, as will be discussed in more detail in later chapters. For example, SCFT is not suitable for studying denser polymer fluids near surfaces or in confined nanoslits,^{21,22} where local density fluctuations and liquid-like ordering become important, and IET can be very sensitive to the particular closures employed within the theory, often giving unreliable results.²³⁻²⁶ Molecular simulations have played an important role; however, due to the overwhelming amount of information that is retained in these computations, simulations can become computationally expensive, especially when considering supramacromolecules composed of long polymeric chains.

Density functional theory (DFT) has emerged as a valuable tool that can be used to better understand the microstructure, thermodynamics, and phase behavior of inhomogeneous fluids. Rather than the coarse-grained representation of polymers used in mean field theories and SCFT, density functional theory retains the microscopic details of a macroscopic system, at a computational expense significantly lower than simulation. In addition, the theory provides a single framework for predicting both bulk and interfacial properties. A thorough review of classical DFT is given by Evans,¹³ while many applications of DFT are discussed by Wu.^{27,28} A basic formalism and literature review of density functional theory is given in chapter 4. The focus of this review, as well as the developments in this dissertation, are density functional theories based on TPT1. Because Wertheim's TPT1 serves as an important precursor for all the work in this thesis, both for bulk and inhomogeneous fluid modeling, the key features of Wertheim's theory of association is presented in the section below.

1.2 Laying the ground work: Wertheim's TPT1 for associating fluids

As mentioned, Wertheim derived a first order perturbation theory (TPT1) to describe the short-ranged, highly anisotropic attractions that govern the structure and phase behavior of associating fluids.⁴⁻⁷ The theory has been successfully utilized to study both homogeneous and inhomogeneous systems, serving as an important basis and framework for the development of equations of state and density functional theory. Wertheim initially developed the theory for molecules with one associating site, and later generalized the theory to account for any number of associating sites on the surface of the molecules. In later work, Chapman¹² extended Wertheim's TPT1 to mixtures of associating fluids. The key features of the theory are discussed here using Chapman's notation.

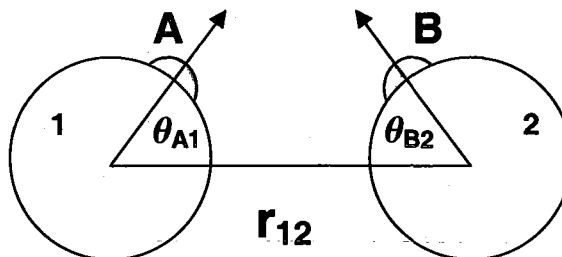


Figure 1.2: Schematic of the association interaction potential model, in the framework of TPT1.

Two associating molecules (represented as hard spheres with off-centered, short-ranged, and highly directional associating sites on the surface, as illustrated in Figure 1.2) can interact through the potential of interaction, given as the sum of the hard core contribution, the anisotropic attractive contribution, and the association contribution.

$$u(\mathbf{r}_{12}, \omega_1, \omega_2) = u^{ref}(\mathbf{r}_{12}) + \sum_A \sum_B u_{AB}^{assoc}(\mathbf{r}_{12}, \omega_1, \omega_2) \quad (1.1)$$

where u^{ref} represents the reference fluid (hard core+ attractive) contribution, u^{assoc} is the directional contribution, r_{12} is the distance between segment 1 and segment 2, ω_1 and ω_2 are the orientations of the two segments, and the summations are over all association sites in the system. The association contribution is modeled via off centered sites that interact through a square-well potential of short range r_c . The interaction between site A on one segment and site B on another segment are modeled using the following association potential,

$$u_{AB}^{assoc}(\mathbf{r}_{12}, \omega_1, \omega_2) = \begin{cases} -\epsilon_{AB}^{assoc}, & r_{12} < r_c; \theta_{A1} < \theta_c; \theta_{B2} < \theta_c \\ 0, & \text{otherwise} \end{cases} \quad (1.2)$$

where θ_{A1} is the angle between the vector from the center of segment 1 to site A and the vector \mathbf{r}_{12} , and θ_{B2} is the angle between the vector from center of segment 2 to site B and the vector \mathbf{r}_{12} , as previously illustrated in Figure 1.2.

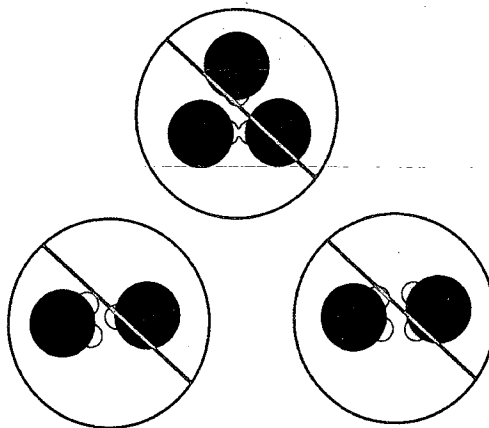


Figure 1.3: Bonding constraints between two associating molecules in TPT1.

Within the theory, only bonding between compatible sites is permitted (two incompatible sites A and B have a bonding energy of zero, $\epsilon_{AB}^{assoc} = 0$). Additional

constraints between two associating molecules are illustrated in Figure 1.3. These constraints include: (1) Once two associating molecules are bonded at their respective sites A and B , sites A and B are no longer eligible to bond with any other molecules in the fluid; (2) any given site on a molecule cannot simultaneously associate with more than one site on another molecule; and (3) two sites on a molecule cannot associate with two sites on another molecule simultaneously.

Using perturbation theory, the free energy functional of m associating spheres can be written as

$$A = A^{ref} + A^{assoc} \quad (1.3)$$

where A^{ref} is the free energy functional of the reference fluid, and A^{assoc} represents the free energy contribution due to association, given as

$$\beta A^{assoc} = \frac{\int d\mathbf{r} d\boldsymbol{\omega} \sum_{i=1}^m \rho_i(\mathbf{r}) \sum_{A \in \Gamma^{(i)}} \left(\ln \chi_A^i(\mathbf{r}, \boldsymbol{\omega}) - \frac{\chi_A^i(\mathbf{r}, \boldsymbol{\omega})}{2} + \frac{1}{2} \right)}{\int d\boldsymbol{\omega}} \quad (1.4)$$

where $\rho_i(\mathbf{r})$ is the density of species i at position \mathbf{r} , $\beta = 1/k_b T$, k_b is the Boltzmann constant, and T is the temperature. The summations, from left to right, are over all the segments and over all the association sites on segment i , respectively, where $\Gamma^{(i)}$ is the set of all the associating sites on segment i . The fraction of molecules of type i that are not bonded at site A is given by

$$\chi_A^i(\mathbf{r}, \boldsymbol{\omega}) = \frac{1}{1 + \sum_{J=1}^m \sum_{B \in \Gamma^{(J)}} \frac{\int d\mathbf{r}' d\boldsymbol{\omega}' \chi_B^j(\mathbf{r}', \boldsymbol{\omega}') g^{ref}(|\mathbf{r} - \mathbf{r}'|) f_{AB}(|\mathbf{r} - \mathbf{r}'|, \boldsymbol{\omega}, \boldsymbol{\omega}')}{\int d\boldsymbol{\omega}'}} \quad (1.5)$$

In the above expression, g^{ref} is the radial distribution function of the reference hard sphere fluid, and f_{AB} is the Mayer f -function for the association potential given as

$$f_{AB} = [\exp(-\beta u_{AB}^{assoc}) - 1].$$

One challenge in the area of molecular thermodynamics is the development of a model capable of predicting both interfacial and bulk properties within a single framework. As one can see from the above expressions, and as noted by Chapman,¹² Wertheim's theory is formulated for inhomogeneous fluids and serves as the basis for developing theories for both bulk and inhomogeneous associating fluids. In addition, the theory can be extended to chain-like molecules by imposing the limit of complete association between the different associating species in the mixture. To arrive at the free energy expressions for a homogeneous bulk fluid (e.g., SAFT), the position dependence of the density is ignored. As will be illustrated in chapters 2 and 3, such an equation of state can be used to describe the phase behavior and thermophysical properties of real fluids (after including additional perturbations such as dispersion attractions). By preserving the position dependence of all variables in the system, the free energy is suitable for use in an inhomogeneous environment. Eqs. (1.4) and (1.5) can be simplified by relaxing and averaging over all orientations, therefore reducing the free energy expressions as a functional of position \mathbf{r} only. Segura et al.²⁹⁻³¹ used this approach in the development of a density functional theory based on TPT1 for associating spheres at a hydrophobic wall. In addition, a density functional theory for chain fluids known as inhomogeneous SAFT (*i*SAFT) was later developed on this basis.³²⁻³⁴ These works are presented in chapter 4 and serve as important precursors to the research presented in this dissertation (chapters 5-8).

1.3 Scope of the thesis

As mentioned, this research is devoted to the development of molecular theories based on statistical mechanics to investigate the structural and thermodynamic properties of bulk and inhomogeneous complex fluids. The foundation of this research comes from Wertheim's first order thermodynamic perturbation theory (TPT1). A number of equations of state based on TPT1 have been developed in an effort to meet the challenges of modeling the fluid-phase-equilibria of larger molecules with more complex molecular interactions. Despite such advancements, much work still remains, including addressing theoretical shortcomings and meeting the challenges of predicting the phase behavior of complex mixtures and polymer solutions. Chapter 2 extends the perturbed-chain statistical associating fluid theory (PC-SAFT) to include a crossover correction using renormalization-group theory. The crossover PC-SAFT equation of state significantly improves the predicted phase behavior of the *n*-alkane family in the critical region in comparison with available vapor-liquid equilibrium (VLE) experimental data. Chapter 3 presents new work using PC-SAFT as a predictive tool for investigating the phase behavior of natural gas mixtures, aimed specifically at improving the understanding of mercaptan/sulfide removal via gas treating. The model is validated against available VLE mixture data.

The heart of the dissertation is the development and application of density functional theory. Chapter 4 provides the background, a basic formalism of the theory, and a literature review of important work that is relevant to this research. Chapters 5-8 provide new theoretical developments which are validated with available simulation and/or experimental data. In these chapters, the new developments of the theory are used to

investigate some of the more challenging problems of today involving interfacial and inhomogeneous fluids.

In chapter 5, an atomic density functional theory is used to investigate the influence of model solutes on the structure and interfacial properties of water. Results indicate that hydrogen bonding is depleted near the surface of larger solute particles, thus leading to a drying effect of the solvent at the surface of the non-polar solute and to long-ranged hydrophobic attraction. The fundamental aspects of hydrophobic phenomena for such a model system is important in understanding the role of hydrophobic interactions in more complex systems, including surfactant self-assembly, protein folding, and the formation of biological membranes.

In chapter 6, the inhomogeneous statistical associating fluid theory (*i*SAFT), a polyatomic density functional theory, is used to investigate nonadsorbing polymer-colloid mixtures. Such systems are of interest to a wide range of fields, from biology and medicine to the design of property specific materials. However, many challenges still remain for both experimentalists and theoreticians. The broad parameter space and multiple length scales involved make the behavior of such a system difficult to understand and model. Here, *i*SAFT is used to characterize the role of polymer concentration and particle/polymer size ratio on the structure, polymer induced depletion forces, and colloidal interactions.

While chapter 5 extends the previous work of Segura et al.²⁹⁻³¹ for associating spheres to investigate the radially symmetric (in inhomogeneities) water/solute problem, the extension of molecular association to polyatomic systems is more challenging as it can involve complex associating schemes (multiple associating sites located on different

polymer segments). Chapter 7 extends the inhomogeneous form of the association functional to associating polymer systems. Results elucidate the importance of this development, highlighting how reversible bonding governs the structure of a fluid near a surface and in confined environments, the molecular connectivity (formation of supramolecules, star polymers, etc.) and the phase behavior of the system (including reentrant order-disorder phase transitions).

The *i*SAFT DFT is extended to predict the inter- and intramolecular correlation functions of polymeric fluids in chapter 8. Correlation functions play a central role in conventional liquid state theories. Knowledge of the inter- and intramolecular structure can be used to enhance our understanding of the effect of local chemistry, bond flexibility, and chain branching on the thermodynamic properties of polymers.

Finally, chapter 9 summarizes the key achievements of this dissertation. Attention is also given to future applications and development of the density functional theory.

CHAPTER **2****Renormalization-group corrections to a perturbed chain statistical associating fluid theory for pure fluids near to and far from the critical region**

2.1 Introduction

The development of an equation of state that is accurate in describing thermodynamic properties of fluids both near to and far from the critical region is of much interest in the chemical industry. Accurate prediction of the phase envelope, particularly in the near critical region, is essential in modeling processes encountered in natural gas and gas-condensates production and processing, supercritical extraction, and fractionation of petroleum. A multitude of equations of state have been developed that describe very well the fluid properties away from the critical region, some of which include the cubic equations of state, such as Peng-Robinson (PR) and Redlich-Kwong-Soave (SRK), as well as molecular theory-based equations of state such as the statistical associating fluid theory (SAFT). Unfortunately, no classical equation of state can describe properties near to and far from the critical point with a single set of parameters. When fit to properties away from the critical region, these equations of state provide very poor descriptions of fluid behavior in the critical region. Alternatively, when fit to the critical point, a classical equation of state gives poor results away from the critical region. Classical equations of state assume that a Taylor series in density and temperature can be used to

expand the free energy about the critical point. Since the critical point is a non-analytic point for the free energy, no such expansion is possible. By ignoring this effect, classical equations of state produce a liquid-vapor coexistence curve that is quadratic near the critical point. This quadratic behavior disagrees with experiment.

The true thermodynamic behavior in the critical region is a consequence of long-range density/concentration fluctuations.^{35,36} Classical equations of state perform well in the region where the correlation length is small (far from the critical region), where only correlations between a few molecules make significant contributions to the free energy. However, as the critical point is approached, the correlation length increases and larger numbers of molecules make significant contributions to the free energy. Here, the large correlation lengths imply that the system is not homogenous near the critical point and the long-wavelength density fluctuations become important. Mean-field theories are not capable of accurately describing correlations between large numbers of molecules. As a result, long-wavelength density fluctuations are neglected, providing the reason why these classical equations fail near the critical point.

To predict thermodynamic properties over the entire fluid region, a method that incorporates the accuracy of these classical equations of state away from the critical region, but is augmented with a correction to correctly describe behavior near the critical region must be implemented. The crossover treatment discussed in this chapter provides the needed corrections due to density fluctuations as the critical point is approached, and reduces to the original classical equation of state (in the case studied here PC-SAFT, described later) far from the critical region. This crossover treatment is based on renormalization-group (RG) arguments.

2.2 Background on renormalization-group methods

Renormalization-group (RG) theory has proven to successfully describe the fluid properties near the critical region. There are many approaches that apply the method to account for the long-wavelength density fluctuations, some of which include work by Chen, Albright, and Senger^{37,38} as well as White, Zhang, and Salvino.³⁹⁻⁴³ Chen et al. describes the free energy of a fluid near its critical point through an Ising-like singularity, written as a Landau expansion that contains an analytic contribution as well as a contribution from the singularity due to long-range molecular correlations. The singular contribution is represented by a scaling function of the rescaled temperature (temperature modified by a crossover function) and density, and is incorporated in the critical region. Away from the critical region, the Helmholtz free energy reduces to the classical expansion. Kiselev and Ely^{44,45} also apply a method based on the renormalized Landau expression to a classical equation of state, and actually use Chen et al.'s³⁷ scaling function near the critical point. Adidharma and Radosz⁴⁶ and McCabe and Kiselev⁴⁷ have applied Kiselev's method to SAFT and have shown improved results in the critical region. The equation of state developed by Kiselev has the advantage that it is in a closed form (does not require to be solved numerically). Unfortunately, these theories based on the renormalized Landau expansion have the disadvantage of requiring many adjustable parameters to fit experimental data.

White et al.'s work is an extension of the theory developed by Wilson^{48,49}, who incorporated density fluctuations in the critical region using the phase-space cell approximation. Here, White employs a recursive procedure that modifies the free energy for a non-uniform fluid, thereby accounting for fluctuations in density. The subsequent

recursive steps account for longer and longer wavelength fluctuations. White and co-workers extended the range beyond the critical region, but was only accurate within 20% of the critical temperature. Lue and Prausnitz^{50,51} and Tang⁵² independently improved this region of accuracy and extended White's RG theory to general mean field theories. Lue and Prausnitz incorporated a first-order mean spherical approximation with White's RG method to provide an equation of state for simple square-well fluids and fluid mixtures. Jiang and Prausnitz^{53,54} further applied Lue's work to an equation of state for chain fluids (EOSCF) to describe the pure *n*-alkane family and chain mixtures. Tang, on the other hand, combined White's RG transformation with a density functional theory and the superposition approximation for a Lennard-Jones (LJ) fluid. The work of Prausnitz and co-workers and Tang demonstrate that White's RG mechanisms can be applied to achieve accurate equations of state that grasp the global behavior of different fluids. The advantage of White's method is the addition of only two parameters, thereby making the theory more predictive than the model devised by Chen et al. and Kiselev et al. The main disadvantage is that the crossover method used can only be solved numerically and does not lead to explicit expressions for the equation of state.

This work applies White's crossover treatment, while incorporating the improved approximations developed by Lue and Prausnitz,^{50,51} to the perturbed-chain SAFT (PC-SAFT) equation of state. Llovell et al.^{55,56} have also applied an approach based on Lue and Prausnitz's work with success to a Soft-SAFT equation of state. Recently, Fu et al.⁵⁷ presented results using the same renormalization procedure with the PC-SAFT equation of state. In the following sections, a brief overview of the PC-SAFT equation of state is given, followed by a description of the recursive relations from White's work. Previous

results from Llovell et al.⁵⁵ and Fu et al.⁵⁷ are discussed, with special emphasis on the approximations and methods (not previously documented) used to obtain their results. Differences between results from Fu et al. and the results reported in this chapter are discussed in terms of the approximations made. Results from this work are then presented. From this work, it is found that when using this RG method, coupled with PC-SAFT, the proposed crossover equation of state does not accurately predict properties in the critical region for longer chain molecules. However, excellent results near to and far from the critical region are obtained by modifying the renormalization scheme with an additional parameter.

As previously noted, the work of Lue and Prausnitz extended the region of accuracy (White's work) beyond the critical region. However, when applying the work of Lue and Prausnitz to other equations of state, other authors have demonstrated that it is sometimes necessary to alter the equation of state parameters to improve results obtained in the critical region.^{53,55} When these changes are made, the equation of state cannot accurately describe the coexistence curve far away from the critical point. In this work, the original molecular parameters from PC-SAFT⁵⁸ are used so that an accurate description of the fluid can be predicted over the entire range of conditions, from the triple point to the critical point. This is advantageous as one can use the original PC-SAFT molecular parameters over the entire range of conditions without concern as to what parameters to use for the given region of interest.

2.3 PC-SAFT outside the critical region

SAFT is one of the most widely used equations of state for calculating phase equilibria for a wide variety of complex polymer systems. The theory's success comes

from its strong statistical mechanics foundation, which allows for physical interpretation of the system. It was first derived by Chapman et al.,⁸⁻¹⁰ and is based on Wertheim's first-order thermodynamic perturbation theory.⁴⁻⁷ There are several SAFT versions in common use today, including LJ-SAFT,^{11,59-64} in which Lennard-Jones spheres serve as a reference for chain formation, CK-SAFT which was suggested by Huang and Radosz^{65,66} who applied a dispersion term developed by Chen and Kregleqski,⁶⁷ SAFT-VR which uses a square-well of variable range developed by Gil-Villegas et al.,⁶⁸ and PC-SAFT which uses a perturbed-chain dispersion term developed by Gross and Sadowski.⁵⁸ In this work, the crossover treatment will be applied to PC-SAFT, as described below. Just recently, Dominik, Jain, and Chapman developed SAFT-D, an improved version of PC-SAFT based on a dimer reference fluid.⁶⁹

PC-SAFT applies Barker and Henderson's^{70,71} second-order perturbation theory to a hard-chain reference fluid, resulting in a dispersion term that is dependent on the chain length of a molecule. Here the main features of PC-SAFT relevant to this work are described. For details, the reader is referred to the work of Gross and Sadowski.⁵⁸ For simplicity, the reduced Helmholtz free energy $a(=A/Nk_bT)$ is used throughout this work, where N is the total number of molecules, k_b is the Boltzmann constant, and T is the temperature. For non-associating chain systems, the total residual Helmholtz free energy is written as

$$a^{res} = a^{hc} + a^{disp}, \quad (2.1)$$

where the superscripts *hc* and *disp* refer to the respective hard-chain and dispersion contributions. The hard-chain contribution to the free energy is written in terms of the

hard-sphere (*hs*) free energy, the chain length (*m*), and the radial distribution function of a fluid of hard spheres (g^{hs}),⁸

$$a^{hc} = a^{hs} + (1 - m) \ln g^{hs}. \quad (2.2)$$

The hard-sphere interaction, given below, was developed by Carnahan and Starling⁷²

$$a^{hs} = m \frac{4\eta - 3\eta^2}{(1 - \eta)^2}, \quad (2.3)$$

where η represents the packing fraction defined by

$$\eta = \left(\frac{\pi}{6}\right) \rho m d^3. \quad (2.4)$$

Here, ρ represents the number density of molecules, and d is the temperature-dependent segment diameter, defined as⁶⁷

$$d = \sigma \left[1 - 0.12 \exp\left(\frac{-3\epsilon}{k_b T}\right) \right]. \quad (2.5)$$

The dispersion term developed by Gross and Sadowski is a sum of contributions of the first and second-order, given by

$$a^{disp} = -2\pi\rho I_1 m^2 \epsilon \sigma^3 - \pi\rho m C_1 I_2 m^2 \epsilon \sigma^3, \quad (2.6)$$

where the parameters ϵ and σ are the well-depth of the potential and temperature-independent segment diameter, respectively, and C_1 is from the local compressibility approximation of Barker and Henderson, written in terms of the hard-chain contribution to the compressibility factor.

$$C_1 = \left(1 + Z^{hc} + \rho \frac{\partial Z^{hc}}{\partial \rho} \right)^{-1}. \quad (2.7)$$

The integrals I_1 and I_2 in eq. (2.6) are given as

$$I_1 = \int_1^{\infty} \tilde{u}(x) g^{hc} \left(m; x \frac{\sigma}{d} \right) x^2 dx \quad (2.8)$$

$$I_2 = \frac{\partial}{\partial \rho} \left[\rho \int_1^{\infty} \tilde{u}(x)^2 g^{hc} \left(m; \frac{\sigma}{d} \right) x^2 dx \right], \quad (2.9)$$

where \tilde{u} is the pair potential, and x is the reduced radial distance between two segments.

The above integrals are fit by simple power series in density η

$$I_1(\eta, m) = \sum_{i=0}^6 a_i(m) \eta^i \quad (2.10)$$

$$I_2(\eta, m) = \sum_{i=0}^6 b_i(m) \eta^i, \quad (2.11)$$

where the coefficients a_i and b_i are dependent on chain length according to

$$a_i(m) = a_{0i} + \frac{m-1}{m} a_{1i} + \frac{m-1}{m} \frac{m-2}{m} a_{2i} \quad (2.12)$$

$$b_i(m) = b_{0i} + \frac{m-1}{m} b_{1i} + \frac{m-1}{m} \frac{m-2}{m} b_{2i}. \quad (2.13)$$

The model constants a_{ji} and b_{ji} are fit to experimental data of n -alkanes, and are reported by Gross and Sadowski.⁵⁸

The PC-SAFT equation of state has been applied with great success to a wide variety of systems including associating and non-associating molecules,^{58,73,74} polar systems,^{73,75,76} polymer systems,⁷⁶⁻⁷⁹ as well as other complex systems.^{80,81} The EOS

requires few parameters that scale well within a homologous series, making it a powerful tool for systems where little experimental data is available. Despite its improved accuracy in the critical region (compared to other equations of state), PC-SAFT still experiences inaccuracies of thermodynamic properties as the critical point is approached, and would benefit from a crossover correction.

2.4 Recursive relations

Using the renormalization method of White,³⁹⁻⁴³ the long-wavelength fluctuations to the free energy density are included. The theory consists of recursive relations that account for the fluctuations as the critical region is approached, and exhibits a crossover between the classical equation of state (in this case PC-SAFT) and the universal scaling behavior in the near-critical region.

This work follows Lue and Prausnitz's^{50,51} implementation of White's RG method, who transformed the grand canonical partition function for simple fluids into a functional integral. The interaction potential consists of a reference contribution and a perturbative contribution, [$u(r) = u_{ref}(r) + u'(r)$]. The reference contribution is due mainly to the repulsive interactions, while the perturbative contribution is due mainly to the attractive part of the potential. Since the reference term contributes mainly with density fluctuations of very short-wavelengths, renormalization is only applied to the attractive part of the potential. The attractive part of the potential consists of short and long-wavelength contributions. It is assumed that the mean-field theory can accurately evaluate contributions from fluctuations of wavelengths less than a certain cutoff length L (one of the added parameters). It is also assumed that the approach can be applied to molecules made of chains of spherical segments.

The functional F^s below accounts for the contribution from short-wavelength fluctuations, estimated using a local-density approximation

$$F^s(\rho) = \int f^s(\rho) d\mathbf{r}, \quad (2.14)$$

where f^s is the Helmholtz energy density for a homogenous system with molecular (number) density ρ ; f^s can be calculated using the PC-SAFT equation of state, or any other mean-field theory. It is important to note that f^s should only include short-wavelength fluctuations. Therefore, the long-wavelength fluctuations from the PC-SAFT equation must be subtracted using the van der Waals approximation $-\alpha(m\rho)^2$. The factor of m^2 appears since there are m^2 segment-segment interactions between a pair of molecules. As a result, f^s is described as

$$f^s = f^{tot} + \alpha(m\rho)^2, \quad (2.15)$$

where α , the interaction volume (units of energy volume), is given by

$$\alpha = -\frac{1}{2} \int u'(r) dr. \quad (2.16)$$

The total free energy, f^{tot} , can be described as follows

$$f^{tot} = f^{id} + f^{res}, \quad (2.17)$$

where the ideal⁸² and residual contributions are defined

$$f^{id} = \rho k_b T [\ln(\rho) - 1] \quad (2.18)$$

$$f^{res} = \rho k_b T a^{res}. \quad (2.19)$$

The zero-order solution, f_0 , is evaluated using the saddle point approximation.⁸³ The saddle point approximation neglects all density fluctuations of all wavelengths that are not already accounted for by the reference fluid.

$$f_0 = f^s - \alpha(m\rho)^2 \quad (2.20)$$

Combining with eq. (2.15), the following is obtained

$$f_0 = f^{tot}. \quad (2.21)$$

The contributions of the long-wavelength density fluctuations are accounted for using the following recursive relations for the Helmholtz free energy density of a system at density ρ .

$$f_n(\rho) = f_{n-1}(\rho) + \delta f_n(\rho). \quad (2.22)$$

In the above equation, f_n represents the Helmholtz free energy density and δf_n the term that corrects for long-wavelength fluctuations, given by

$$\delta f_n(\rho) = -K_n \ln \frac{\Omega_n^s(\rho)}{\Omega_n^l(\rho)}, \quad 0 \leq \rho \leq \rho_{max}/2 \quad (2.23)$$

$$\delta f_n(\rho) = 0, \quad \rho_{max}/2 \leq \rho \leq \rho_{max} \quad (2.24)$$

where Ω_n^s and Ω_n^l refer to the density fluctuations for the short-range attraction and the long-range attraction. The coefficient K_n is defined by

$$K_n = \frac{k_b T}{2^{3n} L^3} \quad (2.25)$$

at temperature T and cutoff length L . The procedure for calculating the density fluctuations uses the following integral,

$$\Omega_n^\beta(\rho) = \int_0^\rho \exp\left[\frac{-G_n^\beta(\rho, x)}{K_n}\right] dx \quad (2.26)$$

where,

$$G_n^\beta(\rho, x) = \frac{\bar{f}_n^\beta(\rho+x) - 2\bar{f}_n^\beta(\rho) + \bar{f}_n^\beta(\rho-x)}{2}. \quad (2.27)$$

Above, β refers to both the short (s) and long (l) range attraction, respectively, and G^β depends on the function \bar{f} , calculated below,

$$\bar{f}_n^l(\rho) = f_{n-1}(\rho) + \alpha(m\rho)^2 \quad (2.28)$$

$$\bar{f}_n^s(\rho) = f_{n-1}(\rho) + \alpha(m\rho)^2 \frac{\phi w^2}{2^{2n+1} L^2}. \quad (2.29)$$

Above, ϕ is an adjustable parameter (the other added critical scaling parameter, representative of the average gradient of the wavelet⁸⁴) and w represents the range of the attractive potential, defined

$$w^2 = -\frac{1}{3\alpha} \int r^2 u'(r) dr. \quad (2.30)$$

In the above procedure, Ω_n^l refers to density fluctuations for the long-range attractive potential, while Ω_n^s refers to the density fluctuations for the short-range attractive potential. Referring to eq. (2.29), note that less of the initial attractive contribution is subtracted out as the longer and longer fluctuation wavelengths are included (at successive recursive steps). The procedure above can therefore be interpreted as the calculation of the ratio of non-mean-field contributions to mean-field contributions as the wavelength increases. From eqs. (2.23) and (2.24), it can be seen that the long-wavelength fluctuations are only relevant when the density is less than half the maximum

density. Mentioned above, ρ_{max} is the maximum molecular density allowed in the system. To obtain this value, recall the basic relation for the packing fraction given by eq. (2.4). Values of $\eta > 0.7405$ $\left[= \pi/(3\sqrt{2})\right]$ have no physical relevance since they represent packing fractions greater than the closest packing of segments.⁵⁸ If the maximum value of the packing fraction allowed is $(\pi/3\sqrt{2})$, then the maximum molecular density can be described in the following way,

$$\rho_{max} = \frac{6}{\pi m d^3} \cdot \frac{\pi}{3\sqrt{2}} = \frac{2}{m d^3 \sqrt{2}}. \quad (2.31)$$

In theory, the above recursive procedure should be carried out until n approaches infinity, therefore obtaining the final full free energy density in the infinite order limit

$$f = \lim_{n \rightarrow \infty} f_n. \quad (2.32)$$

However, as other authors have observed,^{50,51,53-56} the thermodynamic properties become stable after just a few iterations ($n=5$). The integral in eq. (2.26) is evaluated numerically using the simple trapezoid rule. It was found that a density step of $\left(\frac{\rho_{max}}{400}\right)$ was sufficient in terms of accuracy. The resulting free energy was fit using a cubic spline function and derivatives of this spline fit were then used to compute the chemical potential and pressure.

2.5 Results and discussion

2.5.1 Applying RG theory to PC-SAFT

As mentioned earlier, in the framework of PC-SAFT, the dispersion interaction is a result from a fitting to experimental data for the n -alkanes. Before obtaining the pure

component parameters for the n -alkane components, Gross and Sadowski⁵⁸ took an intermediate step where they assumed a Lennard-Jones perturbing potential. If we assume that the perturbation potential for this system is that of a Lennard-Jones-like fluid, the constants α and w^2 can be obtained. The reference potential is approximated using a hard-sphere potential, given by,

$$u_{ref}(r) = \begin{cases} \infty & r < \sigma \\ 0 & r > \sigma \end{cases} \quad (2.33)$$

and the perturbation potential is approximated by

$$u'(r) = \begin{cases} 0 & r < \sigma \\ 4\epsilon \left[\left(\frac{\sigma}{r} \right)^{12} - \left(\frac{\sigma}{r} \right)^6 \right] & r \geq \sigma \end{cases} \quad (2.34)$$

The constants α and w^2 for the fluid are therefore given as

$$\alpha = -\frac{1}{2} \int_{\sigma}^{\infty} 4\pi r^2 u'(r) dr = \frac{16\pi\epsilon\sigma^3}{9} \quad (2.35)$$

$$w^2 = \frac{1}{3!\alpha} \int_{\sigma}^{\infty} 4\pi r^2 u'(r) r^2 dr = \frac{9\sigma^2}{7}. \quad (2.36)$$

The added parameters ϕ and L are adjusted to fit the critical properties. When fitting the parameters, the critical point is evaluated from the standard critical criteria:

$$\begin{cases} \left(\frac{\partial P}{\partial V} \right)_T = 0 \\ \left(\frac{\partial^2 P}{\partial V^2} \right)_T = 0 \end{cases} \quad (2.37)$$

In previous work, Lue and Prausnitz⁵¹ fixed ϕ to a particular value ($\phi=10$) and used L as an adjustable parameter to fit the critical temperature of square-well fluids. However, for simple mixtures,⁵⁰ they changed this criteria, fixing L ($L=2\sigma$) and using ϕ as the adjustable parameter to fit the critical temperature. Jiang and Prausnitz⁵³ also fixed L and used ϕ as the adjustable parameter to fit the critical temperature for real chain fluids. However, they fixed L to a constant value ($L=11.5\text{\AA}$). Llovell, Pàmies, and Vega^{55,56} were the first to make both ϕ and L adjustable to better systematize the fitting procedure and optimize results.

When coupling RG theory with the PC-SAFT equation of state, all the above approaches were considered. While the method proved successful in improving the temperatures in the critical region, a major drawback of the method was realized as the pressures in the critical region were overestimated by a large margin of error. Figure 2.1 illustrates the influence of the crossover treatment in the phase envelope for *n*-octane, first in the temperature-density diagram and then in the pressure-temperature diagram. The circles are experimental data,⁸⁵ the dotted lines represent results from the PC-SAFT equation, and the solid line comes from the PC-SAFT + RG. From Figure 2.1 (b), it is seen that the pressures in the critical region are overestimated. Alternative solutions were investigated and it was found that reasonable results could be obtained by going to high values of L . However, these values of L may not represent physical values and therefore were not considered further. The other alternative is to alter the molecular parameters so that the pressures agree with the experimental values in the critical region. However, this approach cannot describe the behavior of the fluid globally. We have developed an alternative approach to provide global descriptions of the phase behavior. This approach

is presented below. While studying why poor results were initially obtained, we found that several applications of White's theory are not as they appear in the literature.

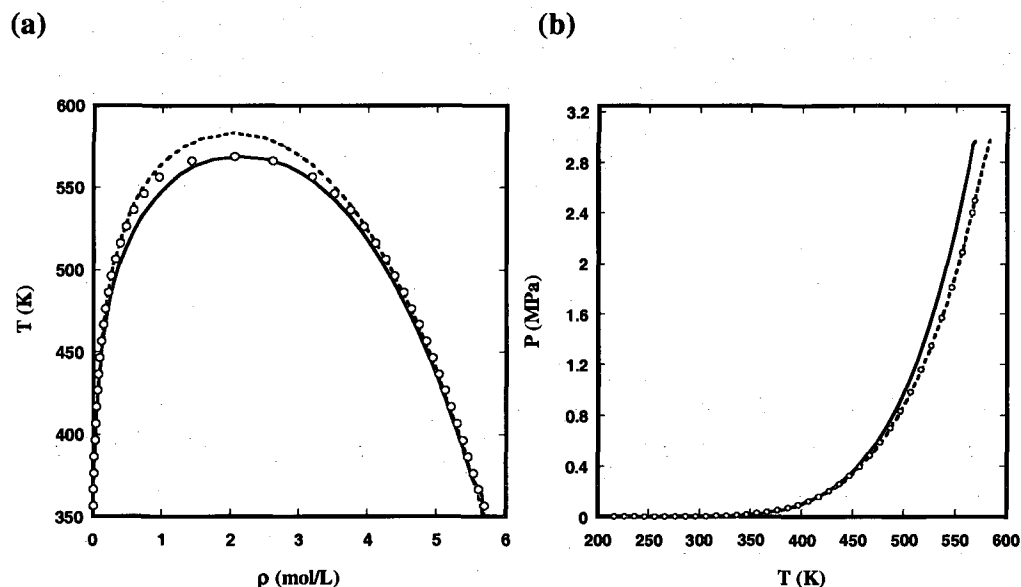


Figure 2.1: (a) Temperature-density diagram for *n*-octane before modification of the perturbing potential function ($L=2\sigma$ and $\phi=18.75$). (b) Pressure-temperature diagram for *n*-octane before modification of the perturbing potential function ($L=2\sigma$ and $\phi=18.75$). Circles are experimental data,⁸⁵ the solid line represents PC-SAFT+RG, and the dotted line is PC-SAFT.

As mentioned earlier, previous published results using this renormalization technique coupled with other equations of state apparently do not suffer from inaccurate predictions of the pressure in the critical region. To verify that the renormalization schemes used in this work were correct and consistent with the schemes implemented previously by other groups, we attempted to reproduce the published work by several groups including Llovel et al.⁵⁵ and later Fu et al.⁵⁷ Although we have not successfully reproduced the results of all groups, we have reproduced the results of Llovel et al. and Fu et al. after considerable input from the authors. It is now clear that several groups using White's approach have introduced additional numerical and, in some cases, empirical approximations. Both groups use the same renormalization-group approach discussed in

section 2.4 and apply it to versions of the SAFT equation of state. Specifically, Llovell et al.⁵⁵ use a Soft-SAFT equation of state, while Fu et al.⁵⁷ use PC-SAFT, as in this work.

In the next two subsections, the approximations used from both of these groups are identified and discussed. Section 2.5.4 proposes modifications needed to overcome the shortcomings mentioned in this section and presents the improved results.

2.5.2 Reproducing Llovell et al.'s Soft-SAFT results

As discussed previously, Llovell et al.⁵⁵ applied White's RG method to the Soft-SAFT equation of state with impressive results. To verify that the problems we were experiencing (as outlined in the previous section) were specific to PC-SAFT, and that the schemes implemented were correct and consistent, we attempted to reproduce the results from Llovell et al.⁵⁵ When applying this method to the Soft-SAFT equation of state, we found that very good results could be obtained using the expressions and schemes presented previously in section 2.4, thereby suggesting that our recursive schemes were correct and consistent with previous work. However, to reproduce the results by Llovell et al. exactly, it was realized after a discussion with Llovell and Vega that additional approximations were introduced in their approach. For the values of the free energy density at previous recursive steps needed in eqs. (2.28-29), Llovell et al. use the value of \bar{f}_{n-1}^l and \bar{f}_{n-1}^s instead of f_{n-1} for all steps greater than one, thus introducing the approximation,

$$\begin{cases}
\bar{f}_n^l(\rho) = f_{n-1}(\rho) + \alpha(m\rho)^2 \\
\bar{f}_n^s(\rho) = f_{n-1}(\rho) + \alpha(m\rho)^2 \frac{\phi w^2}{2^{2n+1} L^2} & \text{for } n=1 \\
\bar{f}_n^l(\rho) = \bar{f}_{n-1}^l(\rho) + \alpha(m\rho)^2 \\
\bar{f}_n^s(\rho) = \bar{f}_{n-1}^s(\rho) + \alpha(m\rho)^2 \frac{\phi w^2}{2^{2n+1} L^2} & \text{for } n>1
\end{cases} \quad (2.38)$$

Using this approximation, along with the published molecular and RG parameters used by Llovel et al.,⁵⁵ we were able to successfully reproduce their results. It should be noted that we did find that good results could be obtained without using this approximation (using expressions from section 2.4) and without altering the original molecular parameters. This occurs because Soft-SAFT with the original parameters underestimates the vapor pressure at the critical temperature. The critical scaling tends to increase the pressure to produce good agreement with the experimental critical pressure.

2.5.3 Reproducing Fu et al.'s PC-SAFT results

Similar to this work, Fu et al.⁵⁷ recently published results demonstrating White's RG method coupled with the PC-SAFT equation of state. From their paper, Fu et al.⁵⁷ use a square-well perturbation potential to calculate the interaction volume, α , and the range of the attractive potential, w ; however, the expressions are not documented. It might be assumed that the perturbation potential is the same as in earlier works.^{51,53} Regarding the RG parameters, Fu et al. declare both to be constant, using $L=2.0\sigma$ and $\phi = 13.5$.

Unfortunately, we were unable to reproduce Fu et al.'s results using the above parameter values with potential expressions from earlier work.^{51,53} It was soon realized after a discussion with Fu that there existed some significant differences between the recursive

expressions published and those implemented to obtain their results. The following identifies these differences.

First, Fu et al. use a slightly modified form of the interaction volume from the form used by Lue and Prausnitz⁵¹ and Jiang and Prausnitz.⁵³ Here α takes the form

$$\alpha = -\frac{1}{2} \int_{\sigma}^{\lambda\sigma} 4\pi r^2 (-\varepsilon) dr = \frac{2\pi\varepsilon}{3} [(\lambda\sigma)^3 - \sigma^3]. \quad (2.39)$$

To be consistent, the range of the attractive potential should also be modified over a similar range of the square-well potential. However, in Fu et al.'s calculations, they used the following

$$w^2 = \frac{32}{45} (\lambda\sigma)^2. \quad (2.40)$$

Further, Fu et al. multiply the free energy density to be renormalized by a factor of m ($f_0 = m\rho k_b Ta^{tot}$); however, they express the long-wavelength fluctuations using the same mean-field approximation used by other groups ($-\alpha m^2 \rho^2$) that is not scaled by an additional factor of m . Justification for the inconsistent scaling of the free energy and the long wavelength contribution was not stated. Still, using these inconsistent expressions, Fu et al. obtain excellent correlations of the phase behavior. In section 2.5.4, we present a modified scaling approach to improve the behavior of the PC-SAFT+RG equation of state.

2.5.4 Improving PC-SAFT+RG

We applied scaling relations to improve the behavior of the PC-SAFT equation of state simultaneously and independently of Fu et al. As discussed previously, in the PC-SAFT equation of state the dispersion interaction is a result from a fitting procedure to

real substances. The perturbation part of the potential is therefore not well defined.

Thus, a slightly different approach is taken. A third adjustable parameter ξ is introduced to modify the Lennard-Jones potential used above in section 2.5.1 in the calculation of α and w^2 . Therefore the new perturbing potential takes on the form

$$u^*(r) = \xi u'(r) \quad (2.41)$$

and α and w^2 are now defined as

$$\alpha = -\frac{1}{2} \int_0^\infty 4\pi r^2 \xi u'(r) dr = \frac{16\pi\epsilon\sigma^3 \xi}{9} \quad (2.42)$$

$$w^2 = \frac{1}{3!\alpha} \int_0^\infty 4\pi r^2 \xi u'(r) r^2 dr = \frac{9\sigma^2}{7}. \quad (2.43)$$

Using these relations, the parameters ϕ , L , and ξ can be adjusted to optimize the predicted properties in the critical region. For a given alkane, the parameter ϕ is used to fit the critical temperature at designated values of L and ξ . The parameters L and ξ can be adjusted accordingly to match the critical pressure and critical density.

For low molecular weight n -alkanes (up to C_9H_{20}) the critical properties are well known from experiment. However, for heavier n -alkanes, critical property measurements are impeded since the critical temperatures exceed the temperature of the onset of thermal decomposition.⁸⁶ Teja and coworkers^{87,88} and Nikitin et al.^{89,90} represent the few to successfully make critical property measurements for heavier alkanes, but the experimental error of these critical values can be quite large. For these reasons, in this work the crossover parameters were fit, using the procedure described above, for C_2 - C_8 and for C_{12} and C_{16} .

Table 2.1: Molecular parameters and crossover (RG) parameters ϕ , L , and ξ .

<i>n</i> -alkane	m	σ (Å)	ϵ/kb (K)	ϕ	L/σ	ξ
C ₂ H ₆	1.6069	3.5206	191.42	15.38	1.40	0.520
C ₃ H ₈	2.0020	3.6184	208.11	20.37	1.63	0.397
C ₄ H ₁₀	2.3316	3.7086	222.88	23.43	1.75	0.304
C ₅ H ₁₂	2.6896	3.7729	231.20	25.30	1.83	0.261
C ₆ H ₁₄	3.0576	3.7983	236.77	33.25	2.24	0.205
C ₇ H ₁₆	3.4831	3.8049	238.40	38.10	2.35	0.173
C ₈ H ₁₈	3.8176	3.8373	242.78	42.06	2.63	0.155
C ₁₂ H ₂₆	5.3060	3.8959	249.21	49.21	2.77	0.142
C ₁₆ H ₃₄	6.6485	3.9552	254.70	56.56	2.95	0.136

The critical parameters were found to correlate well with molecular weight. The values of the optimized parameters are presented in Table 2.1, and Figure 2.2 illustrates the optimized parameter trends with molecular weight for C₂-C₁₆. As observed in previous work,^{53,55} $m\phi$ and mL/σ show linear behavior with respect to molecular weight. The parameter ξ also follows a well-defined trend with molecular weight. When extrapolating to heavier *n*-alkanes, the proposed correlations (correlated from Table 2.1) for the new parameters are

$$m\phi = 1.8316M_w - 47.947 \quad (2.44)$$

$$mL/\sigma = 0.091M_w - 0.9085 \quad (2.45)$$

$$\xi/m^2 = 318.42M_w^{-2.1477} \quad (2.46)$$

The original PC-SAFT equation needs three molecular parameters: m the chain length, σ the temperature independent segment diameter, and ϵ the interaction energy. Gross and Sadowski⁵⁸ have already regressed these three parameters without

renormalization for several chain-like molecules, including the n -alkane family (C_1 - C_{20}). It is important to emphasize that the original molecular parameters m , σ , and ϵ proposed by Gross and Sadowski⁵⁸ were used and remained unaltered in all calculations. By using these original parameters, the crossover equation can reduce to and maintain the good behavior of the original PC-SAFT equation outside the critical region. It is known that these three molecular parameters can be correlated as functions of molecular weight,⁵⁸ providing extrapolative abilities for the heavier n -alkanes. Altogether, the three molecular parameters, coupled with the new crossover parameters, are enough to describe all thermodynamic properties.

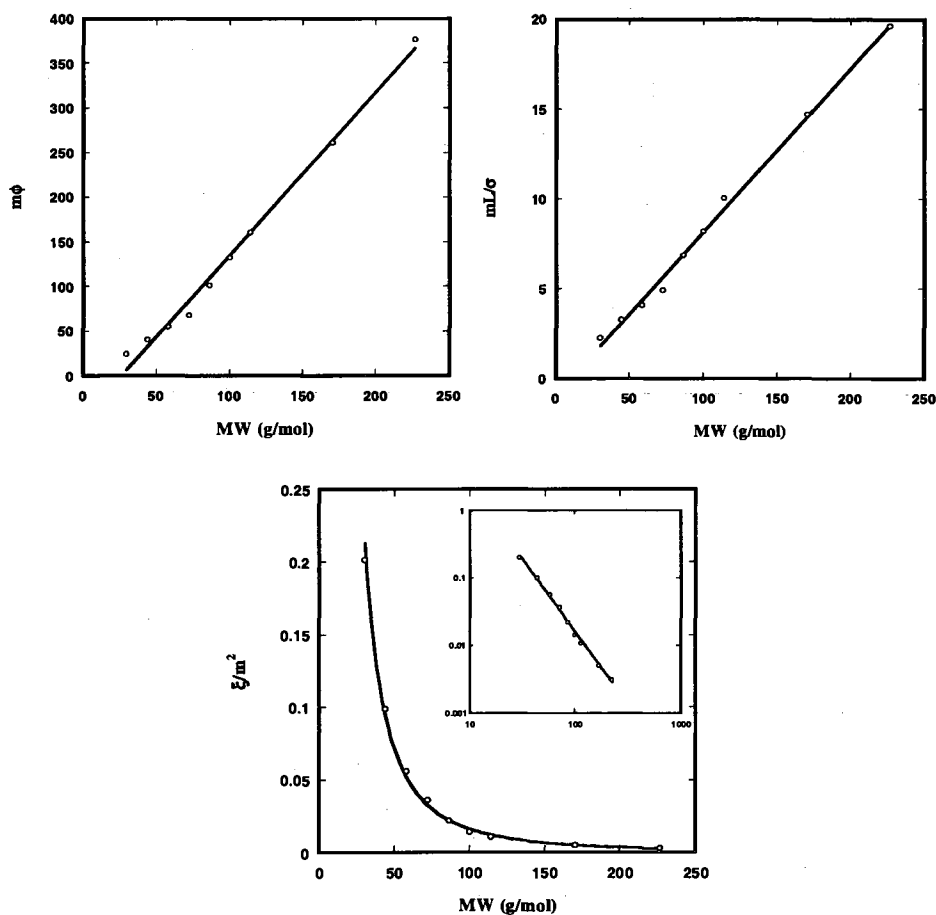


Figure 2.2: PC-SAFT crossover (RG) parameter dependence on molecular weight.

Table 2.2: Critical constants for light n-alkanes, compared with experimental data^{88,91,92}

<i>n</i> -alkane	T_c (K)			P_c (MPa)			ρ_c (mol/L)		
	Exp.	PC-SAFT+RG	PC-SAFT	Exp.	PC-SAFT+RG	PC-SAFT	Exp.	PC-SAFT+RG	PC-SAFT
C ₂ H ₆	305.3	305.3	309.0	4.87	4.88	5.10	6.75	6.75	6.39
C ₃ H ₈	369.8	369.8	375.1	4.25	4.25	4.55	4.92	4.92	4.73
C ₄ H ₁₀	425.1	425.1	432.5	3.80	3.80	4.16	3.92	3.92	3.77
C ₅ H ₁₂	469.7	469.7	479.3	3.37	3.37	3.77	3.22	3.22	3.10
C ₆ H ₁₄	507.3	507.3	519.3	3.03	3.03	3.50	2.72	2.72	2.65
C ₇ H ₁₆	540.2	540.2	552.6	2.74	2.78	3.24	2.34	2.36	2.32
C ₈ H ₁₈	568.7	568.7	583.1	2.49	2.52	2.98	2.03	2.07	2.03
C ₁₂ H ₂₆	658.0	658.0	673.3	1.83	1.88	2.24	1.33	1.37	1.34
C ₁₆ H ₃₄	722.4	722.4	737.6	1.40	1.49	1.77	1.00	1.00	0.98

Table 2.2 gives the experimental, PC-SAFT, and PC-SAFT + crossover (RG) critical constants T_c , P_c , and ρ_c for *n*-ethane to *n*-hexadecane. As already noted, PC-SAFT overestimates T_c and P_c , while giving a very good estimate for the critical density ρ_c . The predictions of the critical constants made by the crossover PC-SAFT equation are much improved. By fitting the three critical parameters, all three critical constants T_c , P_c , and ρ_c are matched with their respective experimental values. In cases where the critical pressures and densities deviate slightly, the values given are still within experimental error. In regard to the critical densities predicted by the crossover PC-SAFT equation, other authors were unable to predict the critical densities as closely. Jiang and Prausnitz,⁵³ as well as Llovell et al.,⁵⁵ observed over-predictions of the critical density in their work, most likely due to changing the original molecular parameters.

Figure 2.3 illustrates the influence of the crossover treatment in the phase envelope for *n*-octane, first in the temperature-density diagram and then in the pressure-temperature diagram. The circles are experimental data,⁸⁵ the dotted lines represent results from the PC-SAFT equation, and the solid line comes from the PC-SAFT + RG. These diagrams support the data in Table 2.2, illustrating an overestimation in critical

temperature and critical pressure from the PC-SAFT equation, but excellent results from the PC-SAFT + RG equation. Note the improved results in the critical region of Figure 2.3 versus Figure 2.1.

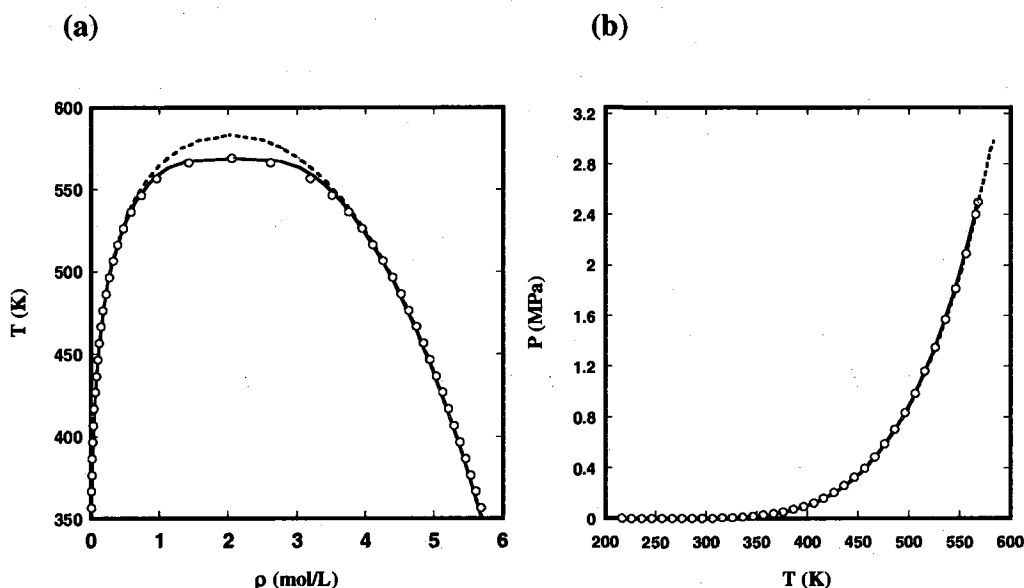


Figure 2.3: (a) Temperature-density diagram for *n*-octane using the modified perturbing potential function. (b) Pressure-temperature diagram for *n*-octane using the modified perturbing potential function. Symbols and lines defined as in Figure 2.1.

Figure 2.4 (a) shows vapor-liquid coexistence curves for some select light *n*-alkanes (C_3 , C_5 , C_7) and Figure 2.4 (b) shows vapor pressures for the same group considered. The results are in excellent agreement with experimental data and are representative of all *n*-alkanes considered in this work. This is due to the PC-SAFT + RG equation's ability to correct the inadequacies of the PC-SAFT equation by accounting for the density fluctuations in the critical region. Outside the critical region, the PC-SAFT + RG reduces to PC-SAFT, where PC-SAFT is accurate and reliable.

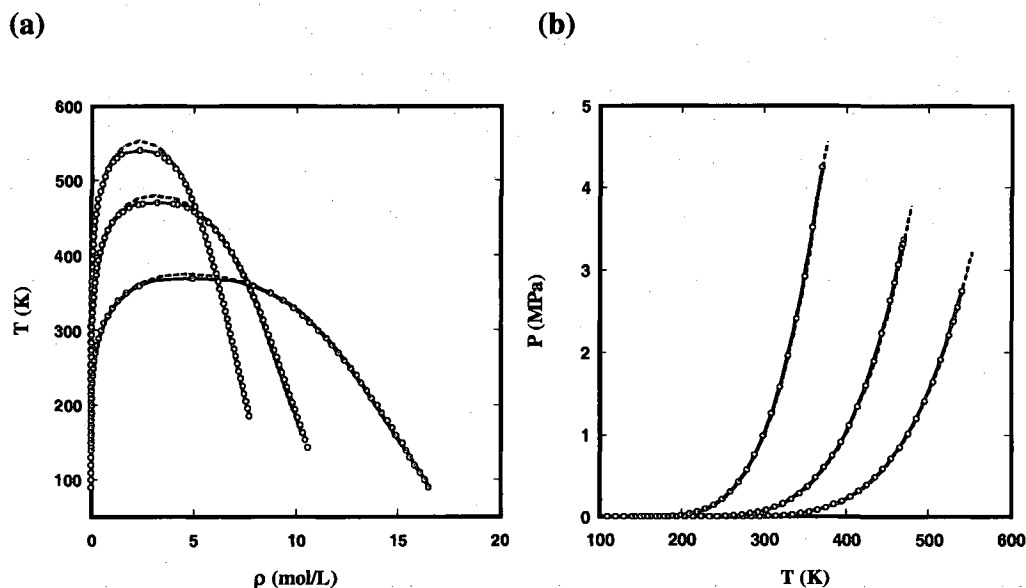


Figure 2.4: (a) Temperature-density diagram and (b) pressure-temperature diagram for select light n -alkanes (C_3 , C_5 , and C_7).

The previously given correlations (eqs. 2.44-46) for ϕ , L , and ζ , coupled with the correlations given by Gross and Sadowski⁵⁸ for m , σ , and ε , are tested for select heavy n -alkanes (C_{20} , C_{24} , C_{30} , and C_{36}). Table 2.3 and Figure 2.5 elucidate the remarkable ability to predict the critical behavior for the heavy members using these correlations, when compared with simulation data⁹³ and available experimental data.^{86,87,91} Figure 2.6 shows the critical temperature T_c , and critical pressure P_c as a function of carbon number before and after renormalization corrections.

Table 2.3: Critical constants for heavy n -alkanes, compared with experimental data^{86,91}

n -alkane	T_c (K)			P_c (MPa)			ρ_c (mol/L)		
	Exp.	PC-SAFT+RG	PC-SAFT	Exp.	PC-SAFT+RG	PC-SAFT	Exp.	PC-SAFT+RG	PC-SAFT
$C_{20}H_{42}$	767.5	765.6	785.0	1.10	1.16	1.45	--	0.79	0.77
$C_{24}H_{50}$	803.2	803.6	824.8	0.90	0.96	1.23	--	0.62	0.63
$C_{30}H_{62}$	843.5	845.2	868.6	--	0.72	0.97	--	0.50	0.49
$C_{36}H_{74}$	873.6	877.8	902.8	--	0.56	0.78	--	0.42	0.39

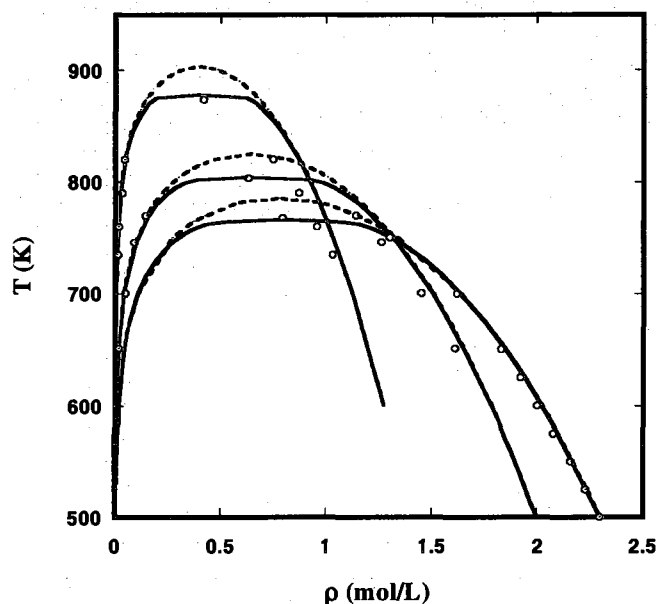


Figure 2.5: Phase equilibria predictions for heavy n -alkanes (C_{20} , C_{24} , C_{36}). The circles represent simulation data,⁹³ and critical points from experiments.⁸⁶

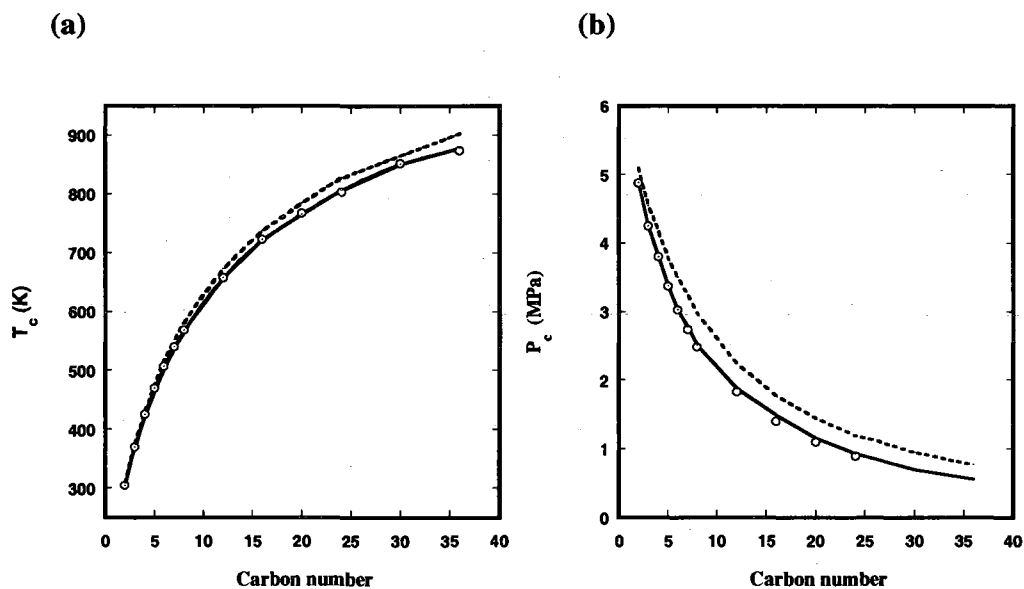


Figure 2.6: (a) Critical temperatures and (b) critical pressures for n -alkanes, from C_2 to C_{36} as predicted by PC-SAFT +RG (solid lines) and PC-SAFT (dashed lines). Symbols represent experimental critical points.^{86,88,91,92}

A final test of the theory is to calculate the critical exponents. The critical exponents are important parameters to represent fluid critical behavior. Here we present results from *n*-butane; similar results can be obtained for other *n*-alkanes. First the critical exponent β is determined from Figure 2.7 (a), which is comprised of values from the density coexistence curve. The plot covers temperatures in the range 0.1% to 5% below T_c . From the figure, $\beta=0.327$, which compares very well with the value found in literature $\beta_{lit}=0.326$.³⁶ Another critical exponent δ is calculated from Figure 2.7 (b). The δ exponent is determined by plotting $\Delta\mu/\mu_c$ versus $\Delta\rho/\rho_c$ on a log-log scale. From the figure, it is determined that $\delta=4.786$ which agrees with the literature value of $\delta_{lit}=4.80$.³⁶ Using the scaling relation $\gamma = \beta(\delta - 1)$, it is determined from the two exponents calculated above that $\gamma=1.238$, which agrees with the literature value $\gamma=1.239$.³⁶ In all calculations of the critical exponents, $n=5$ recursive steps were sufficient.

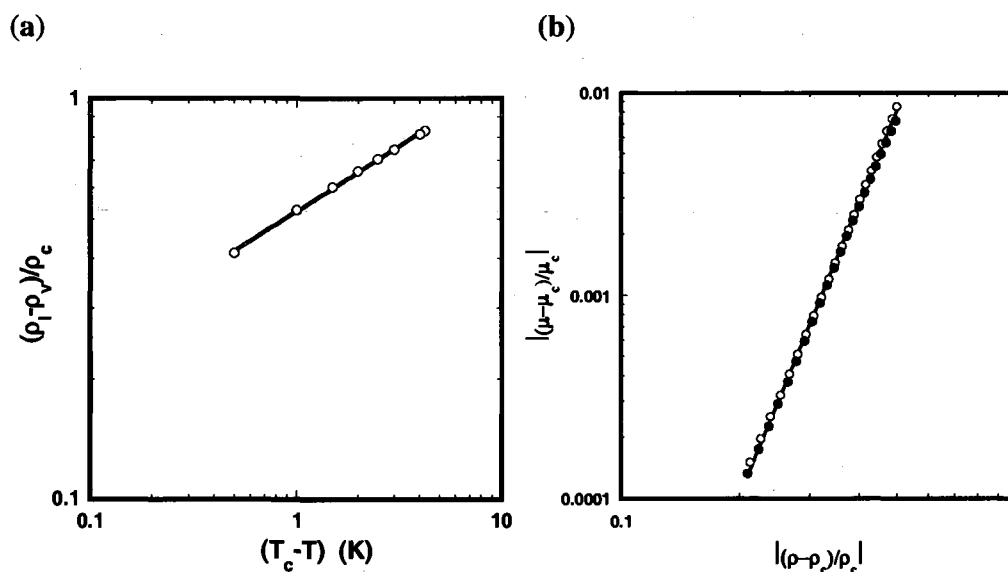


Figure 2.7: In (a), calculation of β critical exponent. The circles are calculated results and the solid line is a power fit used to determine β . In (b), calculation of δ critical exponent. The filled circles are calculated results below the critical density and the open circles are calculated results above the critical density. The solid line is a power fit used to determine δ .

2.6 Conclusions

As demonstrated, PC-SAFT, when coupled with renormalization-group theory, is capable of accurately describing fluid properties both near to and far from the critical region. Outside the critical region, where the correlation length is small, the PC-SAFT + crossover (RG) equation reduces to the original PC-SAFT equation, where the latter is already accurate and reliable. Inside the critical region, the crossover PC-SAFT equation accounts for long-wavelength density fluctuations and reduces the inaccuracies of PC-SAFT in this region (that are due to its mean-field nature).

The theory presented requires a parameter ζ to account for the non-ideal perturbing potential since the PC-SAFT dispersion term is fit to real *n*-alkane data, and also two renormalization-group parameters ϕ and L . All crossover parameters are adjusted to fit the experimental critical temperature, critical pressure, and critical density. As with the original molecular parameters from PC-SAFT (m , σ , and ε), the critical parameters also exhibit relationships with molecular weight, thus providing the ability to correlate parameters for heavier alkanes where little experimental data is available. The only limitation to the theory is that it must be implemented numerically. Future applications include applying the theory to simple fluid mixtures^{50,54,56,94} and within a density functional construct.^{52,95,96}

Although it is assumed that there are m^2 segment-segment interactions between a pair of molecules (used in the van der Waals approximation $-\alpha m^2 \rho^2$), both the scaling procedure presented in this work, particularly the added parameter ζ , and the additional m factor in the approximation implemented by Fu et al. suggest the possibility that the intermolecular dispersion energy may go as m^x where $x < 2$. Such an effect may occur due

to screening effects, where a given segment on a chain could be surrounded by other segments on the same chain, and therefore prevent the segment from interacting with other segments in the fluid. This would have a larger effect on longer molecules than shorter molecules. Such ideas are not trivial and thus require further consideration.

CHAPTER 3

A thermodynamic model for sour gas treating

3.1 Introduction and motivation

Hydrogen sulfide (H_2S), carbon dioxide (CO_2) and mercaptan (methyl-mercaptan, ethyl-mercaptan, etc.) gases are common components encountered in natural gas, synthesis gas and various refinery process streams. Typical concentrations of the above components in the host gas stream can range anywhere from several parts per million to 50 percent by volume. The removal of acid gas impurities is a significant operation in gas processing due to the highly corrosive and toxic nature of such components. In addition, the removal of CO_2 is highly desirable to avoid pumping any extra volume of gas (which leads to high transportation costs) and because CO_2 reduces the heating value of the gas. For natural gas production, typical pipeline specifications require less than 4ppm by volume H_2S ;^{97,98} sales gas specification for natural gas typically requires the CO_2 to be less than 1-2% and feed quality for liquefaction into LNG require less than 50ppm by volume CO_2 .^{97,98} Total concentration of all sulfur species in the purified gas stream typically must be less than 20-50ppm by volume.⁹⁸

Research interests have therefore focused on developing highly economical and selective gas treating methods to meet the increasing strict environmental regulations, and

to exploit poorer quality crude and natural gas. One example is the Controlled Freeze Zone (CFZ™) technology invented at ExxonMobil Upstream Research Company⁹⁹ which achieves the removal of CO₂ and H₂S from natural gas in a single step via cryogenic distillation. Such a process is particularly advantageous for handling natural gas mixtures of high CO₂ and H₂S content. An alternative to the CFZ™ technology and a more conventional method used for removal of CO₂, H₂S, and other sulfur species is via absorption and regeneration. Such processes are solvent-based, which generally capture the acid gas and other sulfur impurities via a chemical, physical, or hybrid solvent.

Figure 3.1 shows a simplified schematic of a typical absorption/regeneration process.

The main constituents of a sour gas mixture typically involve hydrocarbons (C₁-C_n), nitrogen (N₂), hydrogen sulfide (H₂S), carbon dioxide (CO₂), and components of the other sulfides (carbonyl sulfide, carbon disulfide, dimethyl sulfide, methyl-ethyl sulfide, methyl mercaptan, ethyl mercaptan, etc.). The sour gas mixture enters the absorber and is contacted countercurrently with the lean solvent, which absorbs the acid gases and other sulfur impurities to produce a sweetened gas stream as a product and a rich solvent (rich in impurities). The rich solvent is then sent through a heat recovery exchanger and then into the regenerator (a stripper with a reboiler). The heated reboiler (steam) provides the high temperature needed to reverse the absorption process and regenerate the solvent, which is then recycled for reuse in the absorber. The desorbed gases are then either sent to a sulfur recovery unit (SRU) which involves a Claus process to generate elemental sulfur, or to an acid gas injection (AGI) site for geosequestration or enhanced oil recovery. Typical operating ranges are 35-50 °C and 5-200 bar for the absorber, and 115-125 °C at reduced pressure (~1.5 bar) for the stripping unit.¹⁰⁰

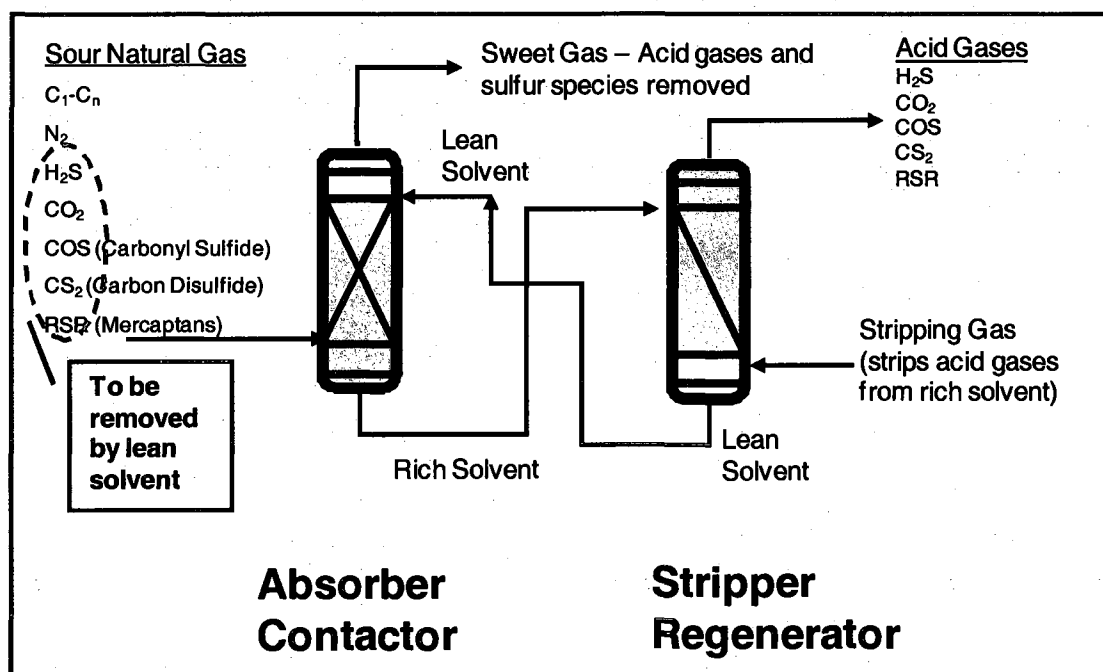


Figure 3.1: Simplified schematic of the absorption/stripping process for removal of sour gas impurities.

This research is specifically aimed at improving the understanding of mercaptan/sulfide removal from sour gas mixtures. Knowledge of the vapor-liquid equilibria (VLE) behavior of sour gas mixtures with different solvents is required for the design of gas treating systems. For example, the equilibrium solubility of acid gases and sulfur impurities in different solvents (maximum capacity of the solvent for the acid gases and sulfur impurities) can be used to determine what solvent works best given the inlet feed gas quality and final specifications, and to determine optimal operating conditions (e.g., operating temperature, pressure, and the required circulation rate of the solution to treat the supplied sour gas stream and meet product gas specifications).

The objective of this work was to build a simple model to estimate the pickup of mercaptans by different amines in gas treating services. The model would then be validated against available data. Experimental data for the vapor-liquid equilibria (VLE)

of mixtures containing the primary acid gases (H_2S and CO_2) in aqueous amines is readily available in the literature¹⁰¹⁻¹⁰⁶ and covers a wide range of concentrations and temperatures. However, fewer experiments have been done to quantify the VLE behavior containing the mercaptan and other sulfide components. The available data¹⁰⁷⁻¹¹⁰ encompasses only a few mercaptans (methyl-, ethyl-, and propyl-mercaptans), at one concentration for the lean solvent (50 wt% MDEA, 35 wt% DEA), over a very small temperature range. Therefore the development of a model capable of accurately capturing the solubility of mercaptans in aqueous amine solutions over a wide range of conditions is a very challenging problem. Popular models used in industry include semi-empirical methods, quasi-chemical and group-contribution methods, and the classical cubic equations of state. While all these models have been used successfully to model simple fluids such as hydrocarbon mixtures, none of these models are suited ideally for the system of interest in this study. As mentioned previously, there is little data available for the mercaptan solubilities in amine solutions, and such systems involve molecules with large degrees of asymmetry in molecular size and complex molecular interactions (hydrogen bonding species). For these reasons, a more sophisticated approach must be used. In this work, a molecular based equation of state (EOS) was chosen, the perturbed-chain statistical associating fluid theory (PC-SAFT) equation of state. The PC-SAFT equation of state is designed to account for the effects of molecular association (hydrogen bonding), the molecular size and shape, and the repulsive and dispersion interactions. It is therefore well suited for nonideal phase behavior, typical of the mixtures encountered in sour gas treating.

This chapter is organized as follows. The model selection and the theory of the PC-SAFT EOS are discussed in detail in section 3.2. The results and discussion are found in section 3.3. PC-SAFT has not been used to model many of the components and mixtures of the sulfides and mercaptans. To validate the model, the theory was tested against available VLE data for binary mixtures of constituents typically found in sour gas treating services (hydrocarbons/H₂S, hydrocarbons/sulfides*, H₂S/sulfides*, solvent[†]/sulfides*). The aforementioned systems provide a tough test of the theory, involving a wide range of conditions and a wide variety of phase behavior. Finally, sections 3.4 and 3.5 highlight the conclusions from the project, and discuss ideas and recommendations for future work.

3.2 Theoretical model

3.2.1 Model selection

As previously discussed, building a model to predict the phase behavior for sour gas treating applications is a challenging task and a difficult test for many models. Because of the lack of data for mercaptans, the use of semi-empirical methods, quasi-chemical and group-contribution methods (NRTL[‡], UNIQUAC[£], and UNIFAC[£])¹¹¹⁻¹¹⁴ would most likely not be reliable, especially over a wide range of concentrations and temperatures. Use of such activity coefficient models are typically coupled with equations of state (which model the vapor phase), can be complex and involve many parameters that must be fitted to match experimental data, and are often accurate over a very limited range of

* Includes mercaptans

† Includes water and alkanolamines (e.g., MDEA, MEA, DEA)

‡ Nonrandom Two Liquid Model

£ Universal Quasi Chemical Approach

£ Universal Functional Activity Coefficient Model

conditions, especially for cases where experimental data is scarce as considered here. The classical cubic equations of state (EOS) such as Peng-Robinson (PR)² and Soave-Redlich-Kwong (SRK)¹¹⁵ face many challenges in modeling such mixtures as well. The PR and SRK EOS have been used with much success to model simple molecules (e.g., hydrocarbons). The advantages of using these equations include their easy implementation and their ability to represent the relation between temperature, pressure, and phase compositions in binary and multicomponent mixtures. Unfortunately, they do not represent well systems with large degrees of asymmetry in molecular size and/or molecular interactions. Therefore, they are not best suited for mixtures involving large molecules with complex interactions (e.g., hydrogen bonding, polarity, etc.); the chemical and physical solvents typically used in gas treating involve large molecules (amines, glycols, etc.) and molecules with hydrogen bonding capabilities (water, amines, glycols, alcohols, etc.). In addition, it is well known that PR and SRK are restricted to the prediction of vapor pressure and suffer invariably in estimating saturated liquid densities.³ One alternative for modeling such systems is to use a molecular based equation of state. Examples include the equation of state for chain fluids (EOSCF)¹¹⁶ and the perturbed-chain statistical associating fluid theory (PC-SAFT) equation of state.⁵⁸ In this work, the PC-SAFT EOS is chosen because it is well developed and has been applied successfully to a wide range of systems. As discussed in chapter 2, the PC-SAFT equation of state is derived from statistical mechanics and is designed to account for the effects of molecular association (hydrogen bonding), the molecular size and shape, and the repulsive and dispersion interactions. It is a predictive model with a strong theoretical basis, requires few parameters (that are fit to pure component data, discussed

later), and requires no input mixture data. It is well suited for nonideal phase behavior, typical of the mixtures encountered in sour gas treating. Detailed reviews on the above mentioned models are available in the literature.^{3,117-119}

3.2.2 PC-SAFT for associating mixtures

In chapter 2 (section 2.3), the background and theoretical formulation for the PC-SAFT equation of state was given for a nonassociating, pure component fluid. In this section, the extension of PC-SAFT to mixtures is described, and an additional association contribution to the free energy is included. Again, for simplicity, the reduced Helmholtz free energy $a(=A/Nk_bT)$ is used, where N is the total number of molecules, k_b is the Boltzmann constant, and T is the temperature. For associating chain systems, the total residual Helmholtz free energy is written as

$$a^{res} = a^{hc} + a^{disp} + a^{assoc}, \quad (3.1)$$

where the superscripts *hc*, *disp*, and *assoc* refer to the respective hard-chain, dispersion, and association contributions. Additional contributions can be added as perturbations (when applicable), including free energy contributions due to polarity and ionic interactions. In this work, these contributions can be neglected for simplicity. The hard-chain contribution to the free energy is written in terms of the hard-sphere (*hs*) free energy, the chain length (m), and the radial distribution function of a fluid of hard spheres (g^{hs}),

$$a^{hc} = \bar{m}a^{hs} + \sum_i x_i(1 - m_i) \ln g_{ii}^{hs}(\sigma_{ii}). \quad (3.2)$$

where i is the i^{th} component of the mixture, x_i is the mole fraction of component i , and

$\bar{m} = \sum_i x_i m_i$. The free energy for the hard-sphere fluid and the pair correlation function of hard spheres was extended to mixtures by Boublik¹²⁰ and Mansoori et al.,¹²¹ given by

$$a^{hs} = \frac{1}{\xi_0} \left[\frac{3\xi_1\xi_2}{(1-\xi_3)} + \frac{\xi_2^3}{\xi_3(1-\xi_3)^2} + \left(\frac{\xi_2^3}{\xi_3^2} - \xi_0 \right) \ln(1-\xi_3) \right], \quad (3.3)$$

where ξ_n is defined as

$$\xi_n = \frac{\pi}{6} \rho \sum_i x_i m_i d_i^n \quad n \in \{0, 1, 2, 3\}. \quad (3.4)$$

Here, ρ represents the number density of molecules, and d is the temperature-dependent segment diameter, defined as⁶⁷

$$d_i = \sigma_i \left[1 - 0.12 \exp\left(\frac{-3\epsilon_i}{k_b T}\right) \right]. \quad (3.5)$$

The dispersion term developed by Gross and Sadowski⁵⁸ is a sum of contributions of the first and second-order, given by

$$a^{disp} = -2\pi\rho \overline{I_1 m^2 \epsilon \sigma^3} - \pi\rho \overline{m C_1 I_2 m^2 \epsilon \sigma^3}, \quad (3.6)$$

where the parameters ϵ and σ are the well-depth of the potential and temperature-independent segment diameter, respectively, and

$$\overline{m^2 \epsilon \sigma^3} = \sum_i \sum_j x_i x_j m_i m_j \left(\frac{\epsilon_{ij}}{k_b T} \right) \sigma_{ij}^3 \quad (3.7)$$

$$\overline{m^2 \epsilon^2 \sigma^3} = \sum_i \sum_j x_i x_j m_i m_j \left(\frac{\epsilon_{ij}}{k_b T} \right)^2 \sigma_{ij}^3 \quad (3.8)$$

C_1 is from the local compressibility approximation of Barker and Henderson, written in terms of the hard-chain contribution to the compressibility factor.

$$C_1 = \left(1 + Z^{hc} + \rho \frac{\partial Z^{hc}}{\partial \rho} \right)^{-1}. \quad (3.9)$$

The integrals I_1 and I_2 in eq. (3.6) are given as

$$I_1 = \int_1^{\infty} \tilde{u}(x) g^{hc} \left(\bar{m}; x \frac{\sigma}{d} \right) x^2 dx \quad (3.10)$$

$$I_2 = \frac{\partial}{\partial \rho} \left[\rho \int_1^{\infty} \tilde{u}(x)^2 g^{hc} \left(\bar{m}; \frac{\sigma}{d} \right) x^2 dx \right], \quad (3.11)$$

where \tilde{u} is the pair potential, and x is the reduced radial distance between two segments.

The above integrals are fit by simple power series in density η

$$I_1(\eta, \bar{m}) = \sum_{i=0}^6 a_i(\bar{m}) \eta^i \quad (3.12)$$

$$I_2(\eta, \bar{m}) = \sum_{i=0}^6 b_i(\bar{m}) \eta^i, \quad (3.13)$$

where the coefficients a_i and b_i are dependent on chain length according to

$$a_i(\bar{m}) = a_{0i} + \frac{\bar{m}-1}{m} a_{1i} + \frac{\bar{m}-1}{m} \frac{\bar{m}-2}{m} a_{2i} \quad (3.14)$$

$$b_i(\bar{m}) = b_{0i} + \frac{\bar{m}-1}{m} b_{1i} + \frac{\bar{m}-1}{m} \frac{\bar{m}-2}{m} b_{2i}. \quad (3.15)$$

The model constants a_{ji} and b_{ji} are fit to experimental data of n -alkanes, and are reported by Gross and Sadowski.⁵⁸

The association term, derived by Chapman et al.⁸⁻¹⁰ is based on the first order thermodynamic perturbation theory (TPT1) of Wertheim.⁴⁻⁷ Chapman et al. showed that by using Wertheim's theory, there is a relationship between the fraction of molecules not bonded at a particular association site and the Helmholtz energy contribution due to association. This relationship is given by^{9,10,65,66}

$$a^{assoc} = \sum_i x_i \left[\sum_{A_i} \left[\ln X_i^A - \frac{X_i^A}{2} \right] + \frac{1}{2} M_i \right] \quad (3.16)$$

where M_i is the number of association sites on species i . The fraction of molecules of component i not bonded at site A is calculated as

$$X_i^A = \left[1 + \rho \sum_j \sum_{B_j} x_j X_j^B \Delta^{AB_j} \right]^{-1} \quad (3.17)$$

The association strength can be approximated as⁹

$$\Delta^{AB_j} = g^{hs}(d_{ij}) \left[\exp\left(\frac{\epsilon^{AB_j}}{k_b T}\right) - 1 \right] \left(\sigma_{ij}^3 \kappa^{AB_j} \right) \quad (3.18)$$

Although each association site can have its own value for ϵ^{AB}/k_b and κ^{AB} , a common simplification is to assume that all sites on a segment have the same volume κ^{AB} and interaction energy ϵ^{AB}/k_b , thus leading to closed form solutions for X_i^A .^{65,66}

For mixtures, common mixing rules are applied. The Lorentz-Berthelot combining rules for mixing are employed

$$\epsilon_{ij} = \sqrt{\epsilon_i \epsilon_j} (1 - k_{ij}) \quad (3.19)$$

$$\sigma_{ij} = \frac{1}{2}(\sigma_i + \sigma_j) \quad (3.20)$$

where k_{ij} is the binary interaction parameter obtained from fitting binary vapor-liquid equilibrium data. For cross-associating systems (e.g., water + alkanolamine, water + methanol, water + glycol, etc.) the following combining rules were used, as suggested by Wolbach and Sandler¹²²

$$\varepsilon^{A_i B_j} = \frac{1}{2}(\varepsilon^{A_i B_i} + \varepsilon^{A_j B_j}) \quad (3.21)$$

$$K^{A_i B_j} = \sqrt{K^{A_i B_i} K^{A_j B_j}} \left(\frac{2\sqrt{\sigma_{ii}\sigma_{jj}}}{(\sigma_{ii} + \sigma_{jj})} \right)^3 \quad (3.22)$$

PC-SAFT, similar to the other forms of the SAFT family, is not strongly dependent on the values of the binary interaction parameters. Molecular interactions responsible for inducing non-ideality in the system are explicitly included in the equation of state per the TPT1 framework. As mentioned previously, the PC-SAFT equation of state has been applied with great success to a wide variety of systems including associating and non-associating molecules,^{58,73,74} polar systems,^{73,75,76} polymer systems,⁷⁶⁻⁷⁹ the phase behavior of asphaltenes⁸⁰ and the thermodynamic inhibition of gas hydrates.¹²³ The EOS requires few parameters that scale well within a homologous series, making it a powerful tool for systems where little experimental data is available.

3.3 Results and discussion

3.3.1 Parameter fitting for the mercaptans and sulfides

While there is a large database of PC-SAFT parameters for pure components available in the literature, the parameters for the mercaptans and sulfides considered in

this work have not been studied and are not available. Therefore, the pure component parameters for this series were regressed against available saturated liquid density and vapor pressure data for each component. The experimental data was taken from the DIPPR* database¹²⁴ (large database with data for over 2,000 components). Figures 3.2 and 3.3 illustrate the accuracy of the PC-SAFT equation of state in describing the phase behavior of some of the pure components considered in this study, namely the sulfides, first in the temperature-density diagram and then in the pressure-temperature diagram.

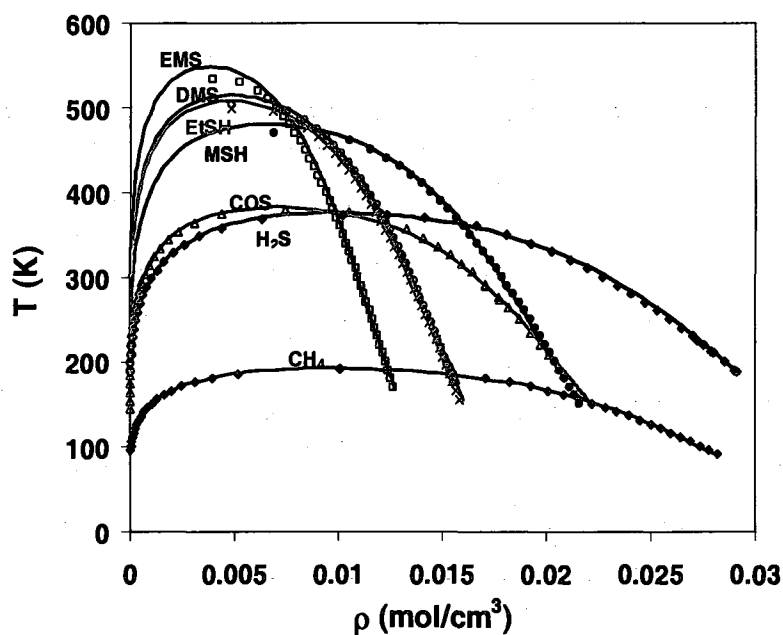


Figure 3.2: Temperature-density diagram for methane and the sulfide series. The pure component parameters were regressed to the saturated liquid densities of each component.

The circles are experimental data¹²⁴ and the lines represent results from the PC-SAFT equation of state. As can be seen, the equation of state does very well in describing the phase behavior, especially away from the critical point. Compared to other equations of state, PC-SAFT also does very well in describing the critical region. Any error in this

* Design Institute for Physical Properties, Sponsored by AIChE © 2005; 2008 Design Institute for Physical Property Data/AIChE

region can be corrected¹²⁵ (see chapter 2), however this is not necessary for the purposes of this study, as the predictions from the original equation of state are assumed to be sufficient in this region, and critical conditions are not expected to be encountered.

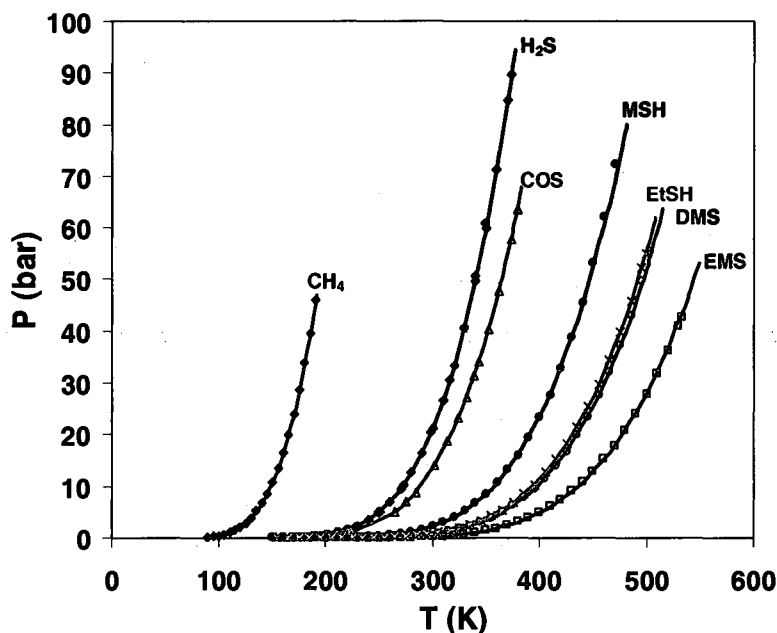


Figure 3.3: Pressure-temperature diagram for methane and the sulfide series. The pure component parameters were regressed to the vapor pressures of each component.

Table 3.1 lists the regressed parameters considered in this work. For the sulfide series, while there is a small degree of hydrogen bonding that is present (from the $-SH$ group), these energies are very low when compared to other hydrogen bonding fluids, such as water, alcohols, or alkanolamines. Therefore, for simplicity, the association contributions to the free energy for the sulfide series were neglected. These terms can be included, although the improvement would most likely be negligible. Figure 3.4 illustrates the predictability of the PC-SAFT equation of state. From the figure, one can see that the parameters for the sulfide series follow well-defined trends with molecular weight. Other series (e.g., alkanes, alcohols, etc.) follow similar trends with molecular

weight. As a result, correlations for each series can be used to extrapolate for any unknown/unfitted components and used with confidence in predicting the phase behavior accurately. The alkanolamine methyldiethanolamine (MDEA) was also fitted for this study. All other parameters (alkanes, water, etc.) can be found in the literature.^{58,74}

Table 3.1: Pure component parameters for the components considered in this study. All components are main constituents typically found in natural gas mixtures or in the solvents used in treating.

Species	Molecular Formula	m	$\sigma(\text{\AA})$	ϵ/k_b (K)	κ^{AB}	ϵ^{AB}/k_b (K)
Hydrogen sulfide	H ₂ S	1.6575	3.0404	229.51	--	--
Dimethyl sulfide	C ₂ H ₆ S	2.2330	3.4786	270.42	--	--
Methyl ethyl sulfide	C ₃ H ₈ S	2.4912	3.6243	274.09	--	--
Methyl mercaptan	CH ₄ S	1.8791	3.3345	275.17	--	--
Ethyl mercaptan	C ₂ H ₆ S	2.2687	3.4667	265.01	--	--
Propyl mercaptan	C ₃ H ₈ S	2.5355	3.6045	272.28	--	--
Carbonyl sulfide	COS	1.6426	3.4141	234.64	--	--
Methane	CH ₄	1.0000	3.7039	150.03	--	--
Ethane	C ₂ H ₆	1.6069	3.5206	191.42	--	--
Propane	C ₃ H ₈	2.0020	3.6184	208.11	--	--
Butane	C ₄ H ₁₀	2.3316	3.7086	222.88	--	--
Pentane	C ₅ H ₁₂	2.6896	3.7729	231.20	--	--
Hexane	C ₆ H ₁₄	3.0576	3.7983	236.77	--	--
Toluene	C ₇ H ₈	2.8149	3.7169	285.69	--	--
Water	H ₂ O	1.0656	3.0007	366.51	0.034868	2500.70
MDEA	C ₅ H ₁₃ NO ₂	3.9019	3.5502	281.50	0.068780	1501.95

In the following sections, the model's ability to predict the phase behavior of complex, multicomponent natural gas mixtures will be tested by comparing with available binary mixture data (consisting of main constituents of natural gas mixtures). This provides insight into the properties and structure of the multicomponent systems, and tests the theory's ability to model the intermolecular forces involved that are responsible for driving the thermodynamic behavior.

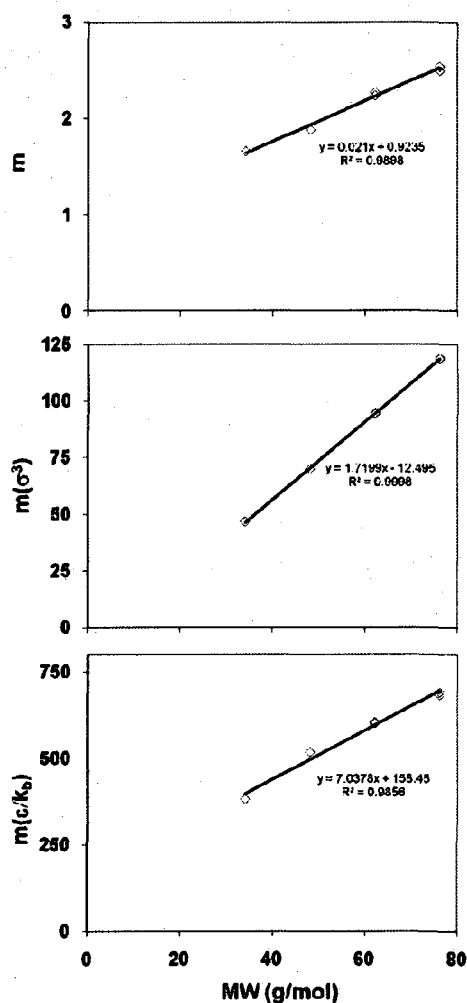


Figure 3.4: Pure component parameter trends for the sulfide series. Other compound families demonstrate similar trends with molecular weight.

3.3.2 Hydrocarbon/H₂S binary mixtures

As mentioned previously, hydrogen sulfide exists in many natural gas reservoirs. To sweeten the gas, this acid gas must be removed. Therefore accurate knowledge of the phase behavior of hydrogen sulfide with other components in a natural gas mixture is very important. Figure 3.5 illustrates PC-SAFT's ability to accurately reproduce available binary mixture data for CH₄+H₂S, C₂H₆+H₂S, and C₃H₈+H₂S, respectively.

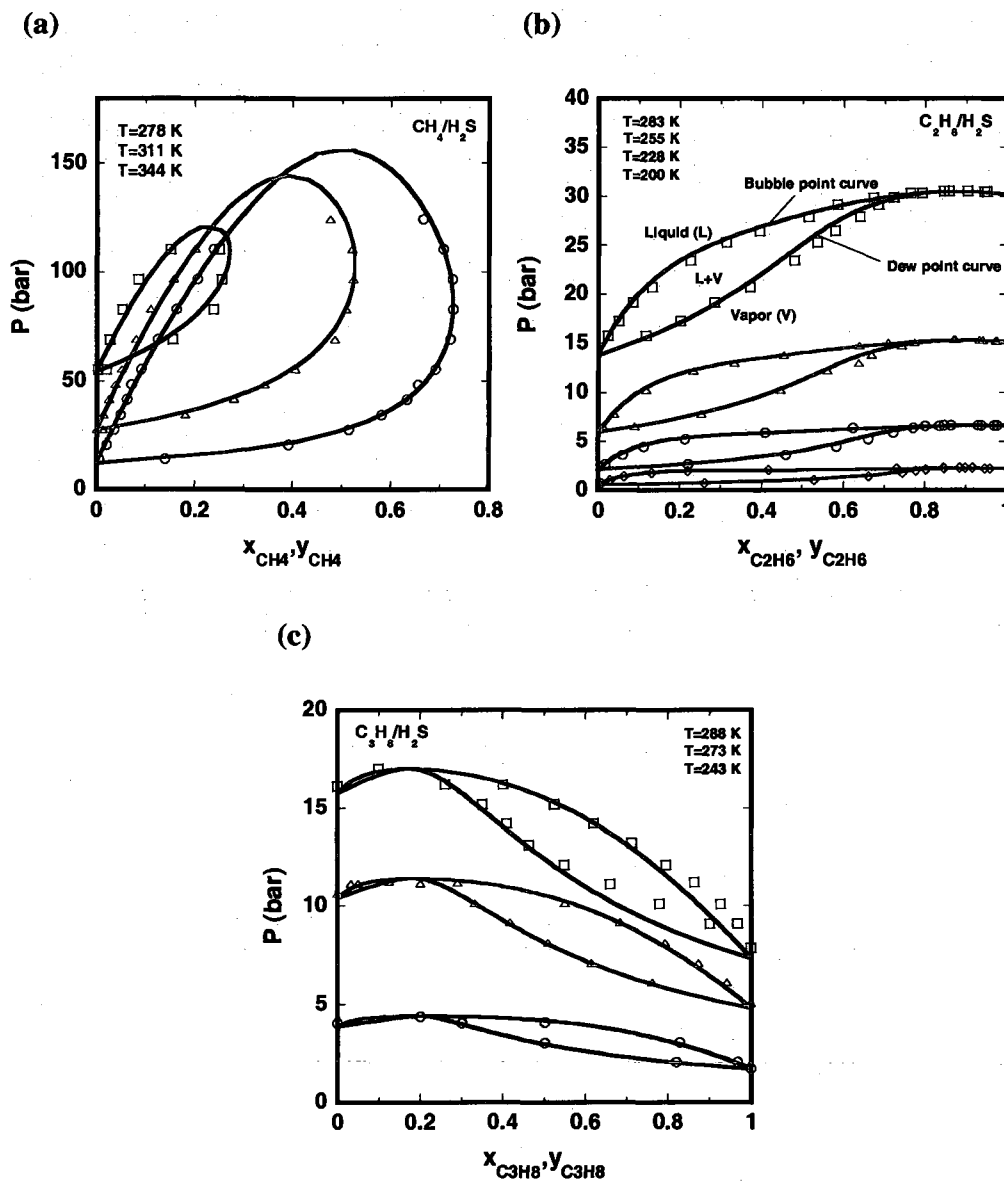


Figure 3.5: P-x diagram for alkane+H₂S mixtures. Symbols are experimental data, lines represent predictions from the PC-SAFT model: (a) CH₄+H₂S mixture, where symbols are experimental data,¹²⁶ $k_{ij}=0.055$, (b) C₂H₆+H₂S mixture, where symbols are experimental data,¹²⁷ $k_{ij}=0.07$, and (c) C₃H₈+H₂S mixture, where symbols are experimental data,¹²⁸ $k_{ij}=0.08$.

As can be seen from the figure, the different hydrocarbons behave differently in respect to their phase behavior with H₂S. For the CH₄+H₂S system, we see a “closed-looped” like behavior, which is a characteristic of type III phase behavior according to the

classification scheme of Scott and van Konynenburg,^{129,130} and is most likely dominated by large regions of liquid-liquid immiscibility. Referring back to Table 3.1, one sees that this behavior is associated with a large disparity in the intermolecular forces involved between the two components in the mixture (high disparity in the dispersion energy parameter (ϵ)). In contrast, for the mixtures involving ethane and propane, another interesting phenomena, azeotropic behavior, is observed. Again, the molecular size and interactions of the constituents in the system are responsible for such behavior. For these components, the chain length (m) and dispersion energy (ϵ) are close enough (when compared to the parameters of H₂S) so that the volatility of these components are similar to the volatility of the hydrogen sulfide, thus leading to the observed azeotrope. PC-SAFT predicts well this complex behavior with the available experimental data, over a wide range of temperatures. Longer hydrocarbons do not demonstrate azeotropic behavior.

3.3.3 Hydrocarbon/sulfide binary mixtures

Figures 3.6-3.8 illustrate the predictions of PC-SAFT against available experimental data of isothermal dew and bubble curves for several hydrocarbon/sulfide (including mercaptan) systems. Note how the phase behavior of mercaptans in methane (Figures 3.6 and 3.7) are qualitatively different than those observed for the heavier hydrocarbons (Figure 3.8). Again such behavior is due to the compatibility of the two components in the mixture for each other, which is driven by the differences in the size of the molecules and intermolecular dispersion energies.

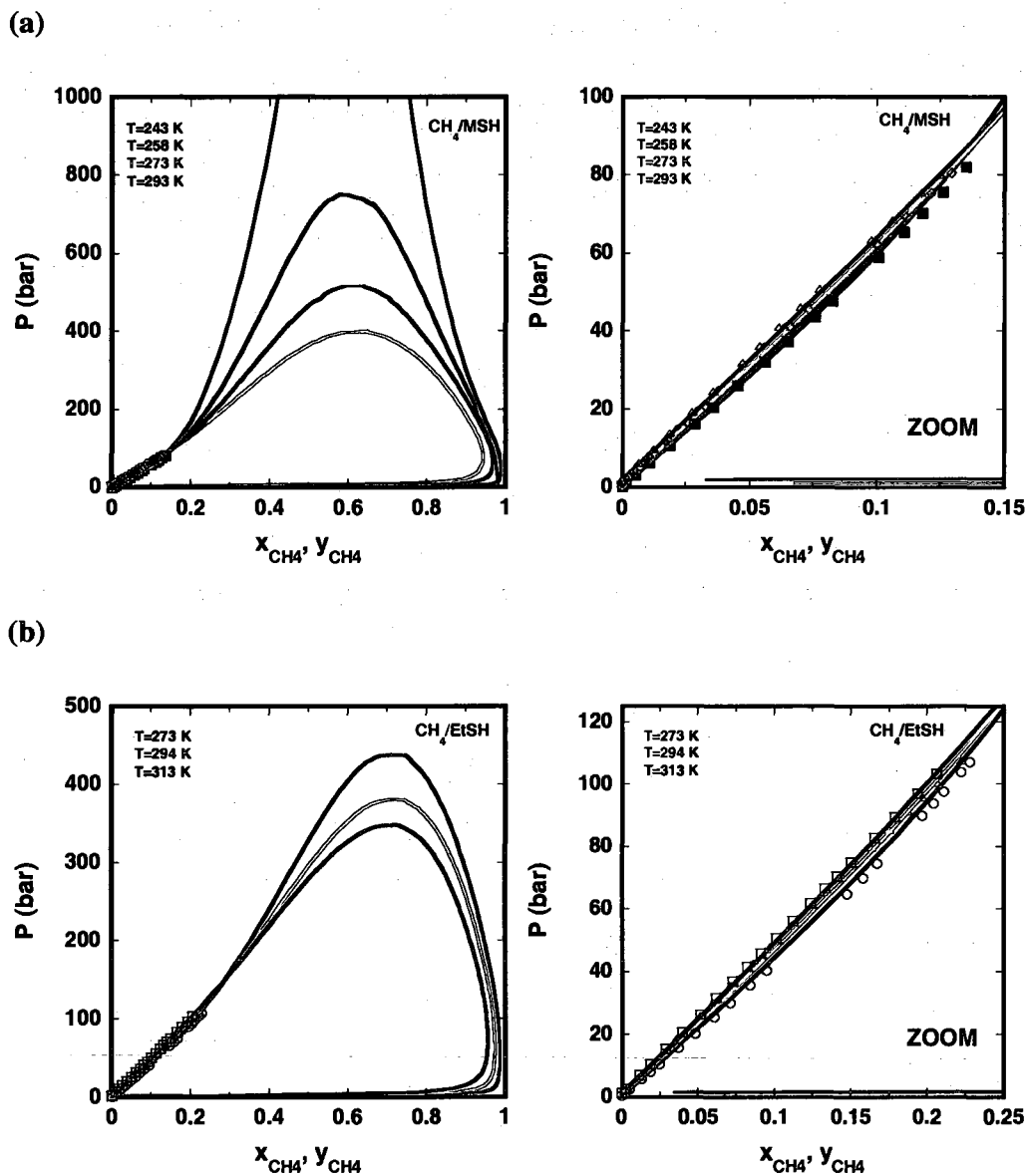


Figure 3.6: P-x diagram for (a) CH_4 +MSH (methyl mercaptan) mixture, where symbols are experimental data,¹³¹⁻¹³³ lines represent predictions from the PC-SAFT model ($k_{ij}=0.04$), and (b) CH_4 +EtSH (ethyl mercaptan) mixture, where symbols are experimental data,¹³¹⁻¹³³ lines represent predictions from the PC-SAFT model ($k_{ij}=0.037$).

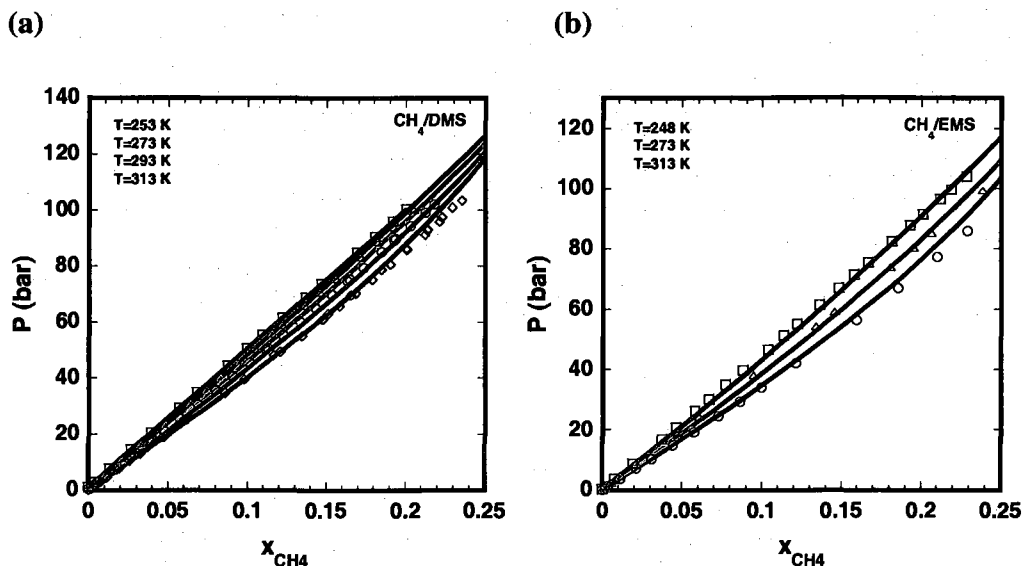


Figure 3.7: P-x diagram for (a) CH_4+DMS (dimethyl sulfide) mixture, where lines represent predictions from the PC-SAFT model ($k_{ij}=0.03$), and (b) CH_4+EMS (methylethyl sulfide) mixture where lines represent predictions from the PC-SAFT model ($k_{ij}=0.035$). Symbols represent experimental data.¹³¹⁻¹³³

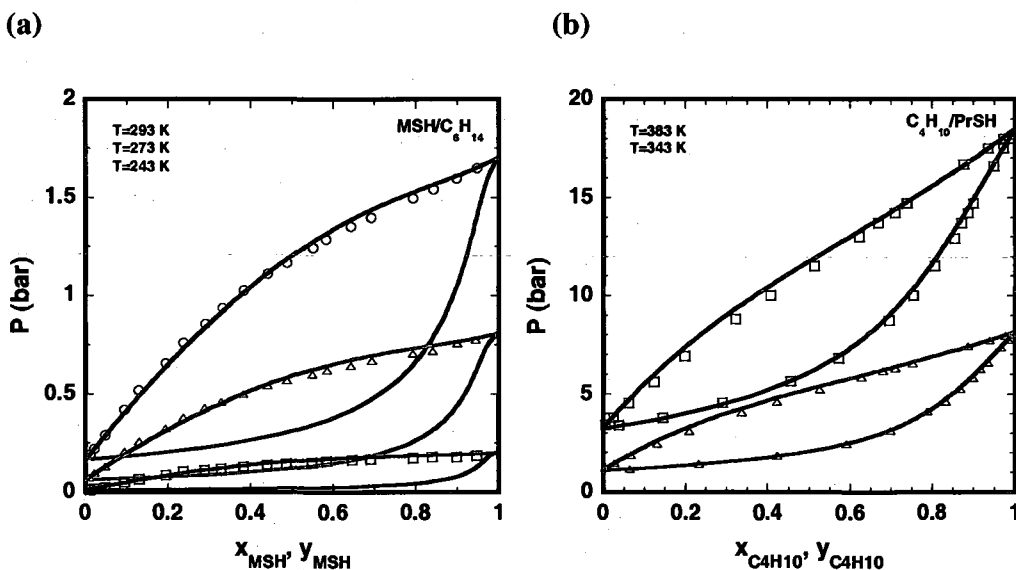


Figure 3.8: P-x diagram for (a) $C_6H_{14}+MSH$ (methyl mercaptan) mixture, where lines represent predictions from the PC-SAFT model ($k_{ij}=0.035$), and (b) $C_4H_{10}+PrSH$ (propyl mercaptan) mixture, where lines represent predictions from the PC-SAFT model ($k_{ij}=0.025$). Symbols represent experimental data.¹³¹⁻¹³³

3.3.4 H₂S/sulfide binary mixtures

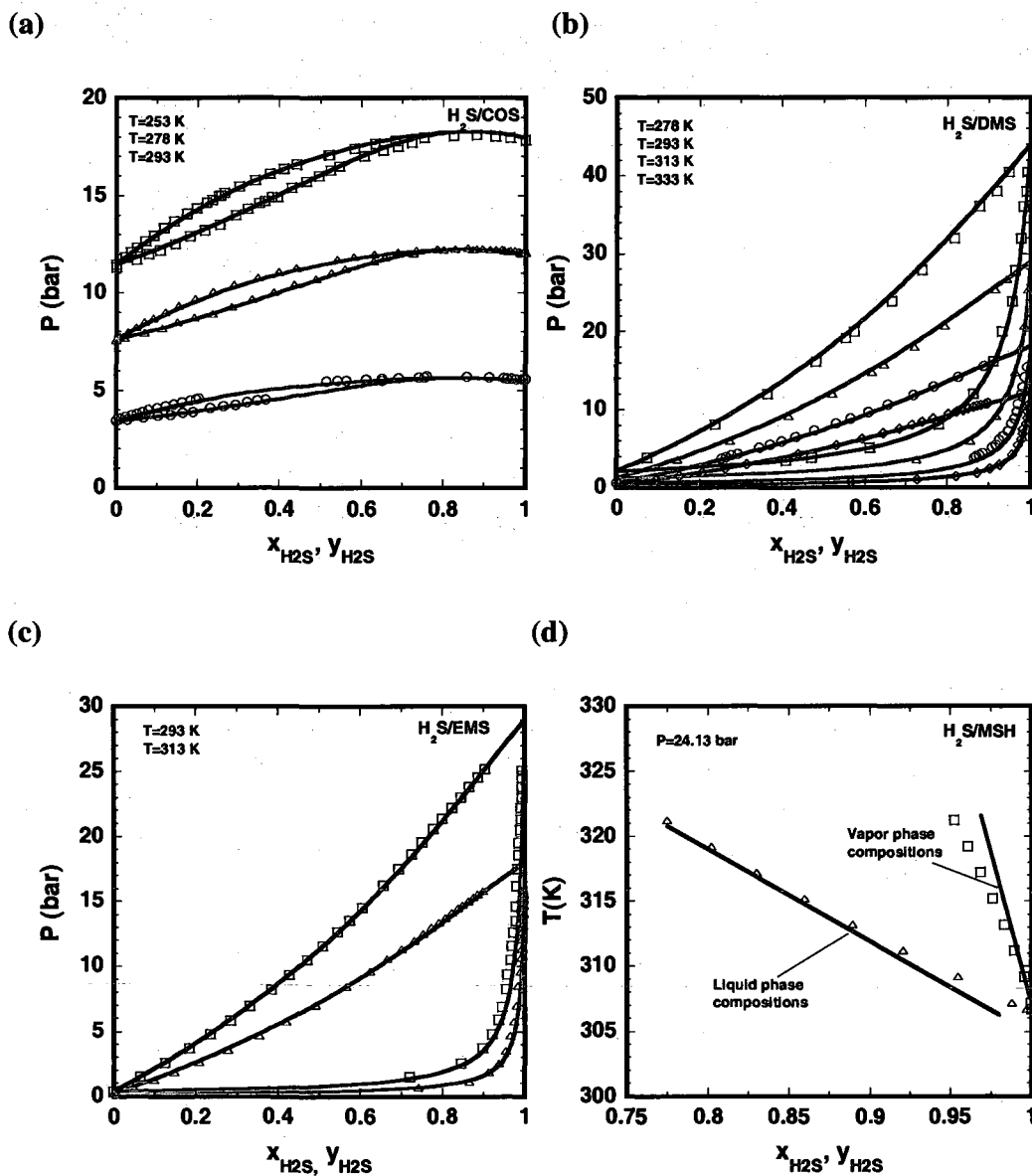


Figure 3.9: P-x diagram for (a) H₂S+COS (carbonyl sulfide) mixture, where symbols are experimental data,^{131,132} lines represent predictions from the PC-SAFT model ($k_{ij}=0.045$), (b) H₂S+DMS mixture, where symbols are experimental data,^{131,132} lines represent predictions from the PC-SAFT model ($k_{ij}=-0.015$), and (c) H₂S+EMS mixture, where symbols are experimental data,^{131,132} lines represent predictions from the PC-SAFT model ($k_{ij}=0.00$). The T-x-y diagram for the H₂S+MSH mixture is shown in (d), where symbols are experimental data,¹³⁴ and lines represent predictions from the PC-SAFT model ($k_{ij}=0.06$).

Figure 3.9 illustrates the predictions of PC-SAFT against available experimental data for several hydrogen sulfide/sulfide (including mercaptan) systems. In Figure 3.9

(a), azeotropic behavior occurs for the H₂S+CO₂ system. Referring back to Table 3.1, one sees that the size of the molecules (m) and dispersion energies (ϵ) between the two species are very similar, which, as discussed previously, drives such behavior.

3.3.5 Solvent/sulfide binary mixtures

Of course, to fully test the theory, one must also validate the model against available binary data for the constituents of the natural gas with solvents (e.g., water and MDEA). Figure 3.10 demonstrates the accuracy of the model in predicting the behavior with water and methyldiethanolamine (MDEA). Capturing the correct behavior is very challenging for the other conventional equations of state (PR, SRK, etc.), largely due to complex intermolecular forces involved. As one can see, PC-SAFT is capable of correctly describing such behavior, accounting for the hydrogen bonding capabilities and the larger molecular sizes typically involved in absorption solvents. In Figure 3.10 (d), experimental data by Xu et al.¹³⁵ showed that Raoult's law does a very good job in correlating the vapor pressures. Therefore to fit optimal k_{ij} values, instead of using the scatter data by Xu et al., we used Raoult's law to provide isothermal predictions of the vapor pressure

$$x_i P_i^0 = y_i P \quad (3.23)$$

where i = water or MDEA, P_i^0 is the vapor pressure of pure component i , and P is the total pressure or in this case the vapor pressure of the solution. The vapor pressure of water was calculated using the correlation of Saul and Wagner,¹³⁶ while the MDEA vapor pressures were correlated using the Clausius-Clapeyron equation¹³⁵

$$\ln P_{MDEA}^0 = 26.29418 - \frac{7657.862}{T} \quad (3.24)$$

where P is in Pascals (Pa) and T is in Kelvin (K).

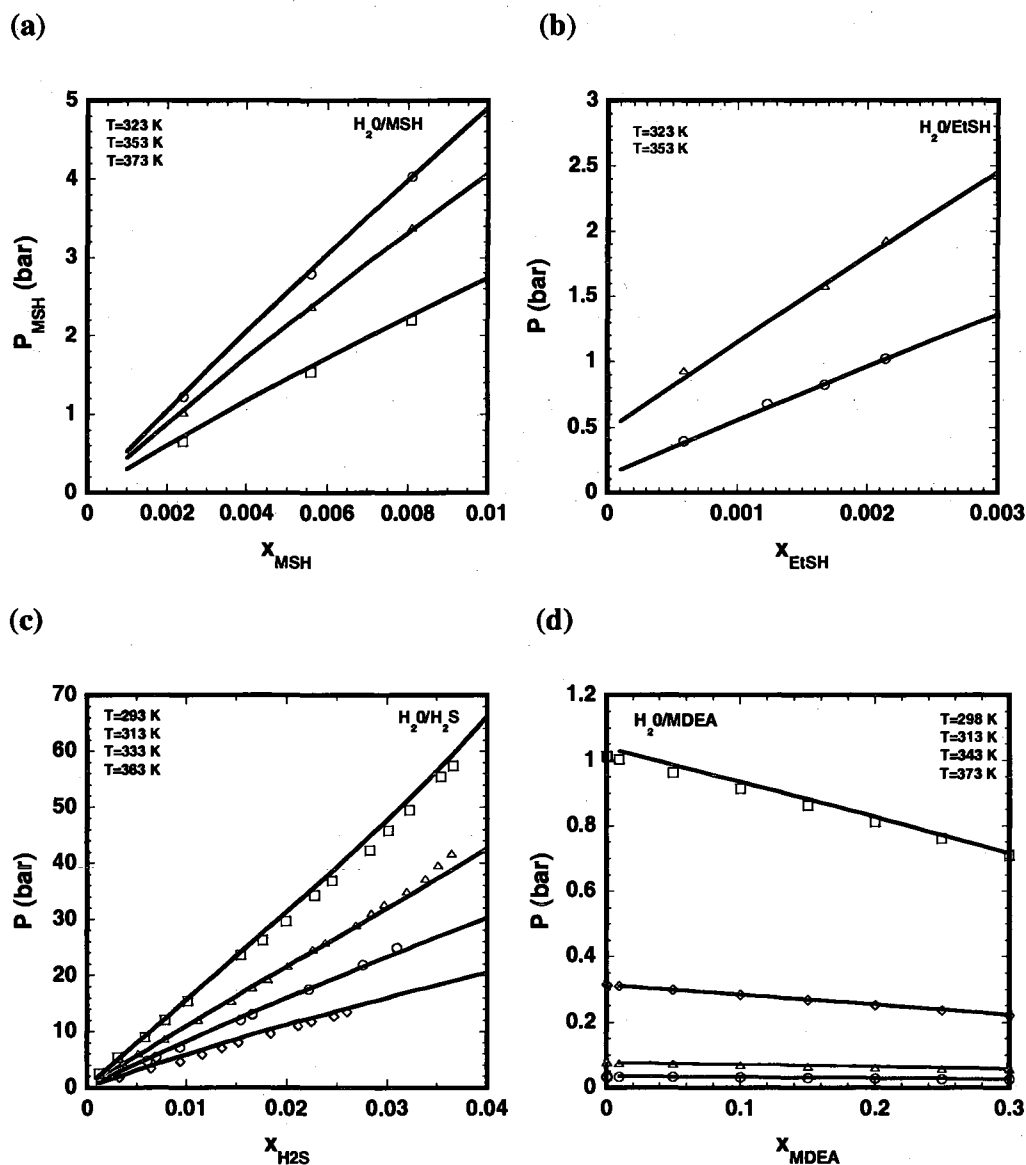


Figure 3.10: P-x diagram for (a) H_2O+MSH mixture, where symbols represent experimental data,¹³⁷ and lines represent predictions from the PC-SAFT model ($k_{ij}=-9.01157E-5*T(K) + 5.46720E-2$), (b) $H_2O+EtSH$ mixture, where symbols are experimental data,¹³⁷ and lines represent predictions from the PC-SAFT model ($k_{ij}=-6.66667E-5*T(K) - 6.54333E-3$), (c) H_2O+H_2S mixture, where symbols are experimental data,¹³⁸ and lines represent predictions from the PC-SAFT model ($k_{ij}=0.025$), and (d) $H_2O+MDEA$ mixture, where symbols are experimental data¹³⁵ (correlated using Raoult's law), and lines represent predictions from the PC-SAFT model ($k_{ij}=-0.055$).

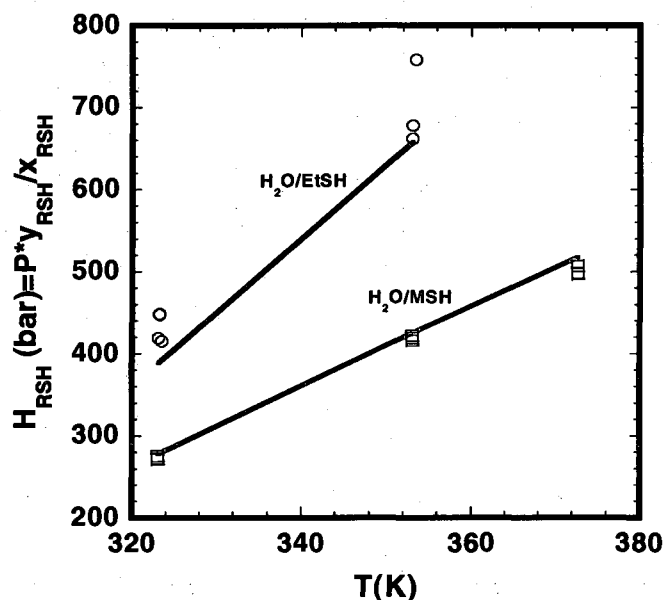


Figure 3.11: Effect of temperature and molecular weight of mercaptan on the Henry's constant. As H_{RS_H} increases, the solubility or pickup of mercaptan in the liquid solvent decreases. Symbols are experimental data¹³⁷ taken over a range of pressures. For comparison, lines represent predictions from the PC-SAFT model at a total pressure of $P=2.5$ bar.

Above in Figure 3.11, one can see that the Henry's constant for the mercaptans in water are calculated from the model. As the temperature increases, the solubility of the gases decrease, as demonstrated by the increasing value of the Henry's constant. The explanation for such behavior is similar to the reason why the vapor pressure increases with temperature. As the temperature increases, higher temperatures increase the kinetic energy of the molecules, causing them to break intermolecular bonds and to escape to the vapor phase, away from the liquid solution. Another interesting observation from Figure 3.11 is the decrease in solubility for the longer chain mercaptans, therefore indicating a relationship between the molecular size and the solubility. However, as will be discussed later in section 3.3.7, more important is the compatibility between the solute and the solvent.

3.3.6 Multicomponent mixtures

Finally, after validating the model versus available binary mixture data (consisting of the many constituents found in natural gas mixtures and the typical solvents that treat the sour gas), it is desirable to apply the model to some multicomponent mixtures. Of course, such calculations are much more challenging. Previous experimental work¹⁰⁸⁻¹¹⁰ indicated that the effect of system pressure on MSH solubility is within the experimental uncertainty. For this reason, and to simplify the problem, the methane that was used in the experiments to maintain the system pressure was not included here in the model. It was therefore assumed that the system pressure and methane solubility had a negligible effect on the solubility of the mercaptan species. Any such effect can, for now, be accounted for through the k_{ij} interaction parameter. It is suggested that this effect be included in the future for more exact calculations.

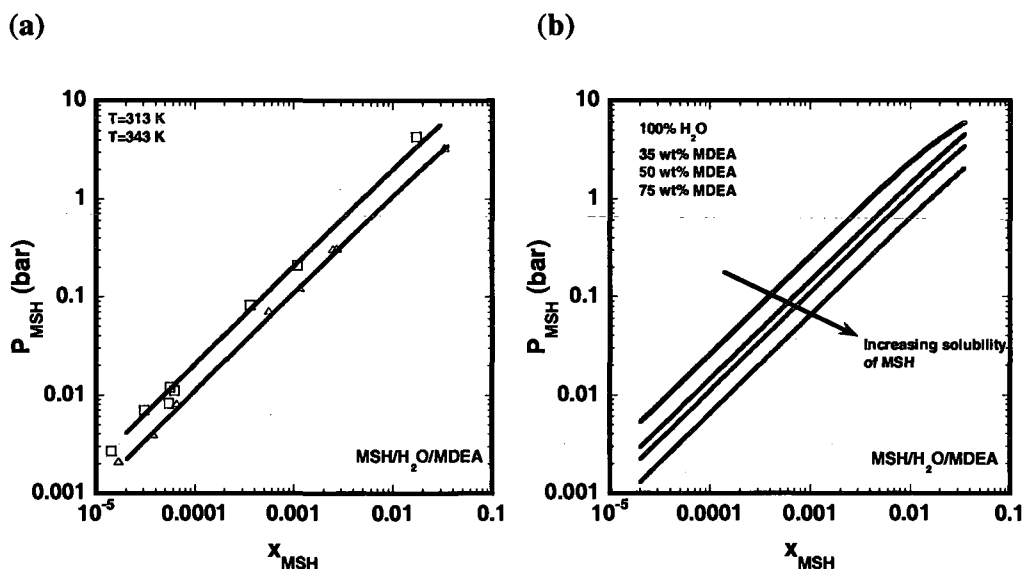


Figure 3.12: In (a), P-x diagram for MSH + H₂O+ MDEA mixture. The aqueous amine solution is 50 wt% MDEA. Symbols are experimental data,¹⁰⁸⁻¹¹⁰ lines represent predictions from the PC-SAFT model. The binary interaction parameters for MSH/H₂O and MDEA/H₂O were the same as before for the binary systems. The binary interaction parameter for MSH/MDEA was determined to be $k_{ij}=0.085$. From (b), P-x diagram for MSH + H₂O+ MDEA mixture. The mass percent of MDEA in the aqueous amine solution is varied from 0%, 35 wt%, 50wt%, 75wt%, respectively.

In Figure 3.12 (a), PC-SAFT accurately predicts the partial pressure of methyl mercaptan as a function of the amount absorbed in the solvent. Figure 3.12 (b) demonstrates the effect of changing the concentration of the MDEA in the aqueous amine solution. Clearly, as illustrated by the figure and predicted from the model, the solubility or amount of mercaptan picked up by the solution increases for higher wt% MDEA solutions. Other studies¹³⁹ have indicated the pickup of mercaptan in aqueous amines to be pH dependent, suggesting that more basic solutions will better dissolve the mercaptans. The results here are consistent with that work, although a more comprehensive study could be conducted to include other amine solutions. Such chemical absorption is discussed further in the next section. Finally, in Figure 3.13, similar to the solubility trends presented in Figure 3.11 for the mercaptan-water system,

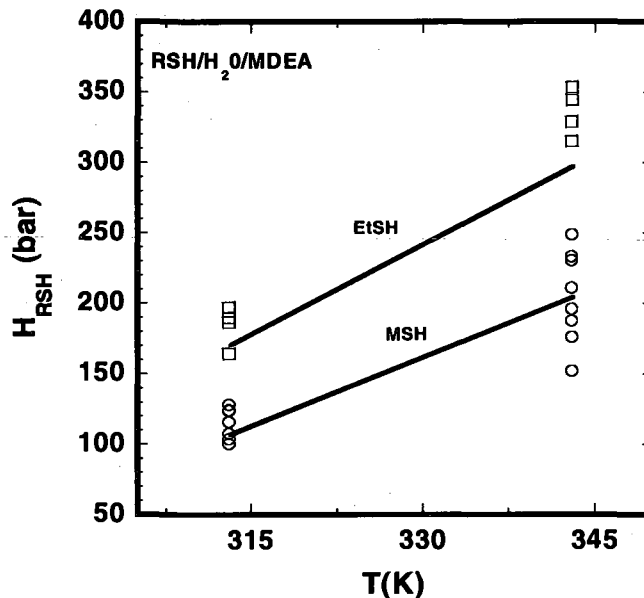


Figure 3.13: Effect of temperature and molecular weight of mercaptan on the Henry's constant in the ternary mixture RSH-MDEA-H₂O (no acid gas loading). The aqueous amine solution is 50 wt% MDEA. As H_{RSH} increases, the solubility or pickup of mercaptan in the liquid solvent decreases. Symbols are experimental data,¹⁰⁸⁻¹¹⁰ lines represent predictions from the PC-SAFT model. The PC-SAFT predictions shown are at $P=1.0$ bar.

the Henry's constant increases for increasing chain length of the mercaptan, and with increasing temperature (therefore indicating a decrease in solubility).

3.3.7 Mercaptan physical solubility versus mercaptan chemical solubility

In the previous sections, the mercaptan solubility in water and in aqueous solutions of amines was demonstrated. The experimental data and model confirmed an increased solubility of the mercaptans in the aqueous amine solutions. Also, as demonstrated by the model, a higher degree of mercaptan removal is achieved for the more basic MDEA solutions. Finally, lower molecular weight mercaptans with higher acidities will exhibit larger chemical solubilities than longer mercaptans in amine solutions.

While there is chemical solubility taking place between the amine and the mercaptan, there is also a degree of physical absorption taking place, as indicated by the case with the pure water solvent. In fact, it is the physical absorption that is dominating the behavior as demonstrated by the decrease in solubility for the higher molecular weight mercaptans. Water is a polar solvent. If one thinks about the molecular structure of a mercaptan component, it is the sulfide group (-SH) that encourages solubilization of the gas in the liquid solution. Here the affinity, or the hydrogen bonding, between the -OH part of the water and the -SH part of the mercaptan enable the two molecules to intermix. Much like nonpolar hydrocarbons (that do not mix with water), when the alkyl part of the mercaptan gets longer, the hydrogen bonding becomes less pronounced and less able to encourage the mercaptan to stay in the solution.

Future work entails conducting a detailed study on the physical solubility of commercial physical solvents typically used in gas treating services (e.g., Selexol, Rectisol, Purisol, and/or solfolane). Such solvents are typically used at high pressure

conditions for bulk removal of acid gases. To understand the effect that a physical organic (nonamine) solvent might have on the pickup of mercaptans, Figure 3.14 and Figure 3.15 show the solubility of mercaptan in *n*-hexane and toluene. It is evident that considerably more RSH dissolves in the organic solvent compared to water or the aqueous amine solutions (H_{RSH} decreases by an order of magnitude). In addition, the solubility increases as the size of the mercaptan increases (opposite trend to that of the aqueous solutions and pure water). Such results suggest that physical solvents or hybrid solvents (mixtures of amines with physical solvents) are perhaps better suited for mercaptan pickup. By replacing the water with a physical solvent in amine solutions, hybrid solvents should allow for the same lean amine reactions (with CO_2 , H_2S , and mercaptans) plus greater sustained physical solubility at higher loading of acid gas.

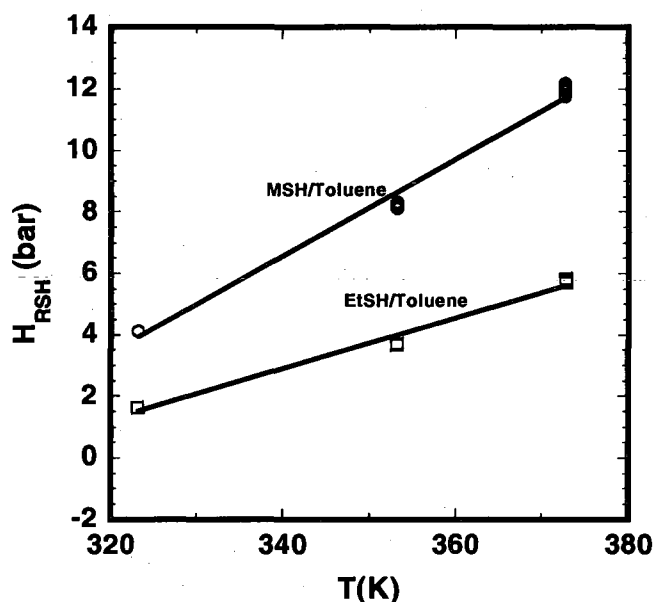


Figure 3.14: Effect of temperature and molecular weight of mercaptan on the Henry's constant in the mixture RSH-toluene. Opposite to the aqueous amine solutions, the solubility increases as the size of the mercaptans increase. The k_{ij} for MSH/toluene and EtSH/toluene were fit to experimental VLE data,¹³⁷ and were determined to be $k_{ij}=0.01$ and 0.0025 , respectively.

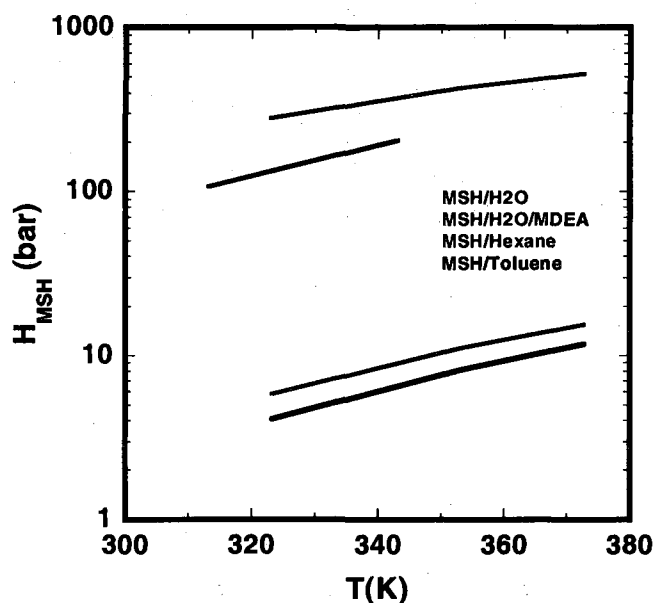


Figure 3.15: Effect of temperature and solvent choice on the solubility of the mercaptan. The physical solvents (hexane and toluene) show considerably more RSH pickup when compared to pure water or the aqueous amine solution (50wt% MDEA). The k_{ij} value for MSH/hexane was determined by experimental VLE data,¹³⁷ and determined to be $k_{ij}=0.035$.

3.4 Conclusions

The recovery of sulfur compounds is a very important and challenging problem for sour gas treating processes, as indicated by the dependence on many variables including temperature, pressure, gas composition, solvent choice, and final specifications. In the recovery of such compounds, it is important to understand the phase behavior for sour gas components (and solvents) for more efficient design and operation. Experimental data for the VLE of mixtures containing the primary acid gases (H_2S and CO_2) in aqueous amines is readily available in the literature and covers a wide range of concentrations and temperatures. However, fewer studies have been done to quantify the VLE behavior containing the mercaptan and other sulfide components. The aim of this work was to improve the understanding of mercaptan/sulfide removal from sour gas

mixtures. In this work, it was demonstrated how PC-SAFT can be used as a predictive tool for natural gas mixtures, to aid in the understanding of the complex phase behavior involved, and in the design and operation of more efficient removal processes. The theory was tested over a wide range of conditions, capturing the correct, diverse phase behavior that can occur, in agreement with available experimental VLE data.

From the results shown, the phase behavior of natural gas mixtures is very sensitive to the constituents involved (due to differences in molecular size and interactions). The solubility of the sulfides and mercaptan species increase as the temperature decreases (in all solvents). Results from the model suggest that mercaptan solubilities are pH dependent, as more basic amine solutions yield higher RSH solubilities. Further, as expected, solvent choice is crucial to mercaptan pickup in gas treating. Results from this work suggest an increased solubility in organic (nonamine, physical) solvents, compared to water and aqueous amine solutions. While aqueous chemical solvents demonstrate an increased solubility trend for smaller mercaptans, organic physical solvents show an increased solubility for larger mercaptans (and also hydrocarbons, although available experiments¹³⁹⁻¹⁴² demonstrate that the hydrocarbon solubilities are much lower than those of the mercaptan). A more detailed investigation should be carried out on the performance of commercial physical solvents in the future.

3.5 Future work and recommendations

This work demonstrated the capability of PC-SAFT to be used as a predictive tool for research on sour gas treating services. More detailed calculations can be continued for this study. First, in this study, the alkanolamine MDEA was investigated. Other alkanolamines typically used in gas treating include diethanolamine (DEA),

monoethanolamine (MEA), and diglycolamine (DGA). Calculations could be extended for these cases to quantify which amine performs best in mercaptan pickup. It is expected that similar Henry's constants (high compared to the physical solvents) will be obtained. Similarly, the work could also be extended to conduct a detailed analysis on the performance of commercial physical solvents (e.g., Selexol, Rectisol, Purisol, and/or solfolane) as well as select hybrid solvents at different temperatures and pressures. While it may not be possible to model these commercial solvents exactly, the main constituents found in these solvent mixtures could be included in the model. For studying the physical solvents, the following references are recommended.¹³⁹⁻¹⁴²

Next, the model could be further used for multicomponent mixtures. In this work, results were presented for binary and ternary mixtures. It would be interesting to study the solubility of mercaptans in different solvents, while quantifying the effect of acid gas (CO_2 and H_2S) loadings on the pickup of mercaptans. Limited experimental data¹⁰⁸⁻¹¹⁰ suggest that acid gas loadings will hinder the pickup of mercaptans, as illustrated in Figure 3.16. Further calculations could be done to quantify the degree of such an effect. The acid gases (H_2S and CO_2) are more acidic than the mercaptans, and therefore it is believed that the chemical solubility will be greatly reduced at high acid gas loadings since these components react much faster with the amine solvent.

Of course, the solubility of all compounds in the natural gas mixture should be investigated. In particular, how is the pickup of the acid gases (H_2S and CO_2) affected in relation to the pickup of mercaptan? Also, it is known that physical solvents suffer from the disadvantage of cosolubility of the hydrocarbons.¹³⁹⁻¹⁴² The mercaptans should be

much more soluble in the organic solvents than the hydrocarbons, however it would be useful to know how much hydrocarbon is being lost in the absorption process.

There are emerging technologies that can be investigated. Dow Chemical has been testing new mercaptan removal agents (MRAs) that provide another reactive means for increasing mercaptan removal.¹⁴³ The MRAs can be added in different quantities to the typical amine blends used in acid gas removal to achieve various degrees of mercaptan removal. Modeling such MRAs or using the model to determine MRAs would be an interesting investigation.

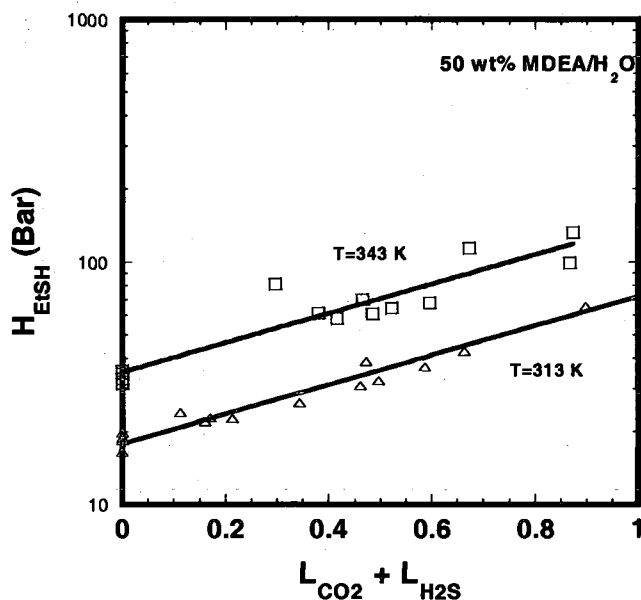


Figure 3.16: Effect of temperature and acid gas loading on the solubility of the mercaptan. Symbols are experimental data.¹⁰⁸⁻¹¹⁰

Finally, the program written for this work works well for binary and ternary mixtures, and can be applied further for multicomponent mixtures. However, such calculations can become difficult, especially in regard to solution convergence. Any additional modifications would require knowledge of the theory and experience in the FORTRAN language environment. There are available software tools that incorporate the PC-SAFT

equation of state into a user friendly environment. Such software include VLXE (<http://www.vlxe.com>) and InfoChem's Multiflash (<http://www.infochemuk.com>). Both of these are available as Microsoft Excel Add-In Software, and provide many benefits:

- Easy to use, handles multicomponent mixtures well
- Includes equation of state (cubics, PC-SAFT, etc.), activity coefficient, and transport property models
- Performs wide variety of calculations (thermodynamic and transport properties)
- Interoperability with Aspen+, Proll, gPROMS and HYSYS

Individual licenses for this software can be obtained on an individual basis, or as part of a network, with full support.

CHAPTER 4**Density functional theory**

4.1 Introduction and background

The past quarter century has experienced a sharp learning curve in the understanding of homogeneous (bulk) fluids. On the other hand, much of the understanding of inhomogeneous fluids has yet to be discovered. Some might attribute the shortcomings of the molecular modeling of bulk fluids also to our lack of understanding of inhomogeneous fluids – that our understanding of homogeneous fluids is incomplete without first an understanding of inhomogeneous fluids. This gives reason why much research has shifted focus to inhomogeneous liquids, where a great industrial and scientific interest exists in regard to technological processes involving interfaces and confined spaces (e.g., oil recovery and colloidal stability).

An important theoretical tool to the theory of inhomogeneous fluids is the density functional (DF) method. DF methods have advantages over alternative learning tools such as experimental methods and molecular simulation in the study of inhomogeneous fluids. Experimental methods are difficult to apply on a microscopic level, therefore making it near impossible to distinguish from what theoretical contributions a given system's behavior is driven (difficult to isolate competing effects). Molecular

simulations can work on this level, however they are very expensive computationally, and therefore are limited to systems of small-to-moderate molecules (too expensive to simulate long polymeric molecules). Like experimental results, results obtained from simulations often require analytic methods to explain the underlying physics of the problem. In contrast, density functional theory offers a much less computationally demanding method that can be applied to a wide variety of systems, including long molecules, under a wider range of conditions. The explanation for this is that molecular simulations focus on an overwhelming amount of data generated by all constituent particles in the simulation, whereas DF methods center on the direct connection between free energy and density profiles (molecular structure).

The last two decades have seen much growth in the use of density functional methods to predict microstructure and thermodynamics of both atomic (simple) and molecular (polymeric) bulk and inhomogeneous fluids. Density functional theory (DFT) has two approaches – the quantum approach developed by Hohenberg and Kohn¹⁴⁴ and Kohn and Sham,¹⁴⁵ and the classical approach first applied by Ebner, Saam, and Stroud.¹⁴⁶ The work of Kohn and co-workers is based on quantum chemistry, and their DF treatment was originally developed to describe the electronic structure for a ground state of an inhomogeneous electronic liquid. Their work has formed and still forms much of the basis of density functional techniques used today, and eventually evolved and led to the application to a classical system made by Ebner et al. to model the interfacial properties of a Lennard-Jones (LJ) fluid. The classical approach forms the basis for much of the work presented here, as it centers its attention on constructing theories for inhomogeneous fluids. Any subsequent references to the term density functional theory

therefore refer to the classical version. Evans¹³ offers a detailed background and mathematical description of the classical DFT for the interested reader.

Density functional theory has a statistical mechanics foundation, with the underlying motive to express the free energy of an inhomogeneous system in terms of its density field functional (with spatial variation) $\rho(\mathbf{r})$. Once this functional is obtained, it can be used to calculate the structure and thermodynamic functions such as phase behavior, interfacial properties, surface forces, and molecular structure. Because density functional can be used to model a wide variety of physical systems based on functionals, it should be emphasized that DFT is more a framework with which to work in rather than a theory as its name implies. The research in this thesis involves investigations to both atomic and polyatomic systems. This chapter consists of a description of the basic structure of the theory, followed by approximations for the free energy functional and recent developments important to this work for both atomic and polyatomic systems.

4.2 A general density functional formalism

In this section, the basic structure of density functional theory will be summarized for a one-component atomic (monatomic) fluid. In general, the molecules can, of course, be polyatomic chains, of like or different species. These more complex scenarios can be incorporated into the theory; however the basic formalism remains the same. It may be important to note that the discussion below assumes that the reader has a knowledge of elementary statistical mechanics (see standard texts by McQuarrie¹⁴⁷ and/or Huang¹⁴⁸).

Consider the above monatomic fluid of volume V , comprised of N molecules at a temperature T . The Hamiltonian for the fluid of N molecules, each of mass m , consists of

contributions due to kinetic energy (K), potential energy (U), and the external potential (E). In that order, the N -molecule Hamiltonian is defined as

$$H_N = \sum_{i=1}^N \frac{|\mathbf{p}_i|^2}{2m} + \frac{1}{2} \sum_{i=1}^N \sum_{j=1}^N u_{ij}(|\mathbf{r}_i - \mathbf{r}_j|) + \sum_{i=1}^N V_i^{ext}(\mathbf{r}_i), \quad (4.1)$$

$$= K + U + E$$

where \mathbf{p}_i is the momentum of molecule i , \mathbf{r}_i and \mathbf{r}_j are position coordinates for molecules i and j , u_{ij} is the intermolecular potential between molecules i and j , and V_i^{ext} is the external potential at position \mathbf{r}_i . The grand canonical ensemble has fixed V , T , and μ (chemical potential) and proves to be convenient to work in. The grand canonical partition function (Ξ) written in terms of the Hamiltonian H_N is

$$\Xi = \sum_{N=0}^{\infty} \frac{e^{\beta\mu N}}{N! h^{3N}} \int \prod_{i=1}^N d\mathbf{p}_i d\mathbf{r}_i e^{-\beta H_N}. \quad (4.2)$$

In the above function, β is defined as the inverse temperature $\left(\beta = \frac{1}{k_B T}\right)$, h is the Planck's constant (with units = momentum x distance) and k_b represents the Boltzmann's constant. It follows that the grand potential Ω is the natural logarithmic of this function, defined as

$$\Omega = -k_b T \ln \Xi. \quad (4.3)$$

In the grand canonical ensemble, different phases with different densities will coexist if their grand potentials are equal (equal grand potentials imply equality of pressures, which when coupled with equality of μ and T from the grand canonical ensemble, warrant phase coexistence).

In the above expressions, the Hamiltonian and thus the grand potential is a functional of $V_i^{ext}(\mathbf{r}_i)$ and therefore of the combination

$$\phi(\mathbf{r}) = [\mu - V^{ext}(\mathbf{r})]. \quad (4.4)$$

The thermal de Broglie wavelength is $\Lambda = (h^2 / 2\pi m k_b T)^{1/2}$. Combining this with eq. (4.4) and integrating over the momentum coordinates leads to the following simplification of eq. (4.2)

$$\Xi = \sum_{N=0}^{\infty} \frac{1}{N! \Lambda^{3N}} \int e^{\left(\beta \sum_{i=1}^N \phi(\mathbf{r}_i)\right)} e^{(-\beta U_N)} \prod_{i=1}^N d\mathbf{r}_i. \quad (4.5)$$

Here it is appropriate to introduce the microscopic density operator,

$$\hat{\rho}(\mathbf{r}) = \sum_{i=1}^N \delta(\mathbf{r} - \mathbf{r}_i), \quad (4.6)$$

where δ signifies the multi-dimensional Dirac-delta function. The average over the ensemble ($\langle \rangle$) below represents the equilibrium density of monomers

$$\rho(\mathbf{r}) = \langle \hat{\rho}(\mathbf{r}) \rangle. \quad (4.7)$$

The previous two equations can be used to develop the thermodynamic potentials in terms of $\rho(\mathbf{r})$. Using the operator given in eq. (4.6) leads to the simplification of eq. (4.5)

$$\Xi = \sum_{N=0}^{\infty} \frac{1}{N! \Lambda^{3N}} \int e^{\left(\beta \int \phi(\mathbf{r}) \hat{\rho}(\mathbf{r}) d\mathbf{r}\right)} e^{(-\beta U_N)} \prod_{i=1}^N d\mathbf{r}_i. \quad (4.8)$$

Functional differentiation leads to

$$\frac{\delta \Xi}{\delta \phi(\mathbf{r})} = \sum_{N=0}^{\infty} \frac{1}{N! \Lambda^{3N}} \int e^{\left(\beta \int \phi(\mathbf{r}) \hat{\rho}(\mathbf{r}) d\mathbf{r}\right)} e^{(-\beta U_N)} \prod_{i=1}^N d\mathbf{r}_i \frac{\delta}{\delta \phi(\mathbf{r})} \left(\beta \int \phi(\mathbf{r}) \hat{\rho}(\mathbf{r}) d\mathbf{r} \right). \quad (4.9)$$

Since

$$\left. \begin{aligned} \hat{\rho}(\mathbf{r}') &= \frac{\delta}{\delta\phi(\mathbf{r}')} \left(\int \phi(\mathbf{r}) \hat{\rho}(\mathbf{r}) d\mathbf{r} \right) \\ \rho(\mathbf{r}') &\equiv \langle \hat{\rho}(\mathbf{r}') \rangle \end{aligned} \right\} \quad (4.10)$$

then it follows after applying the definition of the ensemble average (given above) that

$$\begin{aligned} \rho(\mathbf{r}') = \langle \hat{\rho}(\mathbf{r}') \rangle &= k_b T \frac{1}{\Xi} \frac{\delta \Xi}{\delta \phi(\mathbf{r}')} = k_b T \frac{\delta \ln \Xi}{\delta \phi(\mathbf{r}')} \\ &= - \frac{\delta \Omega}{\delta \phi(\mathbf{r}')} \end{aligned} \quad (4.11)$$

This equation demonstrates the dependence of the field $\phi(\mathbf{r})$ on the grand potential Ω . In order to determine the fluid structure and thermodynamics, a function needs to be written in terms of the density field $\rho(\mathbf{r})$. This can be done using a Legendre transformation of Ω ¹⁴⁹

$$\begin{aligned} A[\rho(\mathbf{r})] &= -k_b T \ln \Xi + k_b T \int d\mathbf{r}' \frac{\delta \ln \Xi}{\delta \phi(\mathbf{r}')} \phi(\mathbf{r}') \\ &= \Omega[\rho(\mathbf{r})] + \int d\mathbf{r}' \rho(\mathbf{r}') \phi(\mathbf{r}') \end{aligned} \quad (4.12)$$

where the second equality comes from eq. (4.11) and A represents the Helmholtz free energy.

The functional $A[\rho(\mathbf{r})]$ above is defined as the equilibrium free energy of the system in an external field $V^{ext}(\mathbf{r})$, with an equilibrium density $\rho(\mathbf{r})$. The functional presented in eq. (4.13) is very similar, only here the functional is expressed in terms of an arbitrary non-equilibrium density field $\tilde{\rho}(\mathbf{r})$.

$$\tilde{\Omega}[\tilde{\rho}(\mathbf{r})] = A[\tilde{\rho}(\mathbf{r})] - \int d\mathbf{r}' \tilde{\rho}(\mathbf{r}') \phi(\mathbf{r}') \quad (4.13)$$

It can be shown that Ω is the minimum value of $\tilde{\Omega}$ (the functional $\tilde{\Omega}$ is minimized at constant $\phi(\mathbf{r})$ by the equilibrium density),¹⁵⁰ thereby giving rise to the following relations

$$\left. \begin{aligned} \frac{\delta \tilde{\Omega}[\tilde{\rho}(\mathbf{r})]}{\delta \tilde{\rho}(\mathbf{r})} \Big|_{\tilde{\rho}=\rho} &= 0 \\ \tilde{\Omega}[\rho(\mathbf{r})] &= \Omega \end{aligned} \right\} \quad (4.14)$$

Therefore, eq. (4.14) results in approximations to the equilibrium density and grand potential. This comes from first approximating the free energy functional $A[\tilde{\rho}(\mathbf{r})]$ and thus $\tilde{\Omega}$, and then following the above variational principle to minimize the $\tilde{\Omega}$ with respect to the equilibrium density field.

Since the exact form of $A[\tilde{\rho}(\mathbf{r})]$ is known only for an ideal monatomic fluid in two and three dimensions, how one approximates this quantity for all other systems is what distinguishes one DFT from another. Approximations vary and can be based on computer simulations or theoretical models, as discussed in the next section.

4.3 Approximations for the free energy functional

As touched on at the conclusion of the last section, any application of the density functional theory to a realistic physical problem requires an approximation to the free energy functional. The formulation of an effective free energy functional is guided by the specific intermolecular interactions in the considered system. Such interactions typically include contributions to the free energy from short range repulsions (due to molecular excluded volumes), long range van der Waals attractions, Coulomb interactions, and hydrogen bonding. Additionally, it is important to reflect the macromolecular architectures of the constituent molecules in the model. This includes

considerations such as the molecular shape, connectivity, and conformation. Once the free energy functional is obtained, the equilibrium density field and the grand potential of the system can be determined. Below is a summary of the approaches followed for atomic and polyatomic fluids.

4.3.1 Atomic fluids

Any fluid whose structure and thermodynamics can be described by considering the individual molecules as rigid entities with no internal degrees of freedom can be classified as an atomic fluid. Examples include small molecular systems such as water and carbon dioxide. The main objective in approximating the free energy functional for atomic fluids lies in the contribution to the free energy due to the excluded volume effects (the excess free energy functional). This is logical since the free energy of an ideal monatomic system is known explicitly,¹⁵¹ and a common strategy toward approximating $A[\tilde{\rho}(\mathbf{r})]$ is to write as a sum of ideal and excess contributions

$$A[\rho(\mathbf{r})] = A^{id}[\rho(\mathbf{r})] + A^{ex}[\rho(\mathbf{r})]. \quad (4.15)$$

Above, the excess contribution results from intermolecular interactions. For pure monatomic fluids, $A^{id}[\rho(\mathbf{r})]$ in its exact form is given by¹⁵¹

$$\beta A^{id}[\rho(\mathbf{r})] = \int d\mathbf{r} \rho(\mathbf{r}) [\ln \rho(\mathbf{r}) - 1]. \quad (4.16)$$

It is not uncommon for the ideal functional form to include λ^3 (λ representing the de Broglie wavelength) inside the logarithmic function. This term has been dropped here since it is not density dependent, and hence does not affect the fluid structure or the residual properties (i.e., it makes no direct contribution to the density profiles or the phase behavior).

Evans¹³ addresses several approaches for approximating the above excess free energy functional. One of the more popular methods chosen is based on weighted-density approximations (WDA) because of its highly accurate scheme and ability to adapt to most systems.¹³ WDA methods are capable of describing systems with strong density oscillations much better than other methods based on Taylor series expansions since it does not correspond to any finite order density expansion of the excess free energy functional $A^{ex}[\rho(\mathbf{r})]$. Because of its versatility and accuracy, the weighted-density approximation is the main approximation method described below.

The development of weighted-density approximations originates as a modification of the local density approximation (LDA). The LDA approximates the value of the free energy in the inhomogeneous system, $a^{inhom}(\mathbf{r})$, at a point \mathbf{r} in the inhomogeneous system with density field $\rho(\mathbf{r})$, by the free energy in the bulk $a^{bulk}[\rho(\mathbf{r})]$, evaluated at $\rho(\mathbf{r})$. Thus the excess free energy functional is given by

$$\begin{aligned} \beta A^{ex}[\rho(\mathbf{r})] &= \beta \int d\mathbf{r} \rho(\mathbf{r}) a^{inhom}(\mathbf{r}) \\ &\approx \beta \int d\mathbf{r} \rho(\mathbf{r}) a^{bulk}[\rho(\mathbf{r})] \end{aligned} \quad (4.17)$$

The disadvantage of this method is that for largely inhomogeneous fluids, the local density $\rho(\mathbf{r})$ may exceed that for close packing for pronounced peaks in the oscillatory profile. As a result, the bulk free energy, $a^{bulk}(\rho)$, at such densities gives unphysical values. The theory therefore cannot be used to describe pronounced oscillatory density profiles, which are significant in representing fluids in confined environments and at surfaces. Despite this drawback, the theory can still be used to provide good descriptions of the interfacial properties of systems, most notably vapor-liquid interfaces. Ultimately, however, since WDA based DFTs can provide the best description of inhomogeneous

fluids, especially strongly inhomogeneous fluids, the work in this thesis will utilize such a DFT over the alternative LDA based DFT.

WDA constructs a weighted (also referred to as smooth or course grained) density $\bar{\rho}(\mathbf{r})$ that prevents unphysical values of the free energy. Here the smoothed density is constructed as a weighted average of the density field $\rho(\mathbf{r})$ over a local volume, which is determined by the range of intermolecular forces. Therefore, the functional A^{Ex} using the WDA has the same form as for the LDA, but with the bulk free energy per particle $a^{bulk}(\rho)$ now evaluated at the weighted-density.

$$\beta A^{ex}[\rho(\mathbf{r})] = \beta \int d\mathbf{r} \rho(\mathbf{r}) a^{bulk}[\bar{\rho}(\mathbf{r})] \quad (4.18)$$

where,

$$\bar{\rho}(\mathbf{r}) = \int d\mathbf{r}' \rho(\mathbf{r}') \omega(|\mathbf{r} - \mathbf{r}'|; \bar{\rho}(\mathbf{r})). \quad (4.19)$$

In the above expression, the different versions of WDA correspond to different formulas for the weighting function ω . The weighting function is usually chosen such that the inhomogeneous fluid reduces to the form of the bulk system in the homogeneous limit. Evans¹³ discusses some of the more common approximations to hard-sphere systems, some of which include work by Tarazona,^{152,153} Curtin-Ashcroft,¹⁵⁴ Rosenfeld,^{155,156} and Meister-Kroll.¹⁵⁷

4.3.2 Polyatomic fluids

Unlike an atomic fluid, for a molecular system, intramolecular energetics (bonding constraints between the polymer segments constituting a chain) govern behavior, even for the ideal chain state. The existing DF methods for polyatomic systems differ in whether the intramolecular interactions are accounted for in the ideal functional contribution

($A^{id}[\rho(\mathbf{r})]$), the excess contribution ($A^{ex}[\rho(\mathbf{r})]$), or a combination of both. Further, a polyatomic DFT can be formulated in terms of *molecular density* or *segment density*, and can require additional input from other theories or simulations. Each therefore has its own advantages and disadvantages in regard to accuracy and computational expense. Some of the more popular and well established density functional theories, and how they differ in regard to their formulations and approximations, are discussed in section 4.4. As in the case for atomic fluids, weighted-density approximations are popular methods for estimating the free energy functionals in polyatomic fluids. The application of these approximations follows much the same procedure as in the case for atomic fluids.

4.4 Notable density functional theories

Today, most applications of DFT follow one of two routes:²⁷ (1) the theory developed by Chandler, McCoy, and Singer,¹⁵⁸⁻¹⁶⁰ or (2) Wertheim's first-order thermodynamic perturbation theory (TPT1).⁴⁻⁷ A brief review of these density functional theories are presented below. Most of the work discussed here focuses on polyatomic DFTs. The work by Segura et al. for associating atomic fluids is also included due to its important role in the development of recent polymer DFTs, as well as its role in the work of this dissertation (see chapter 5 and chapter 7).

4.4.1 Chandler, McCoy and Singer

Classical density functional theory was first applied to polymeric systems in 1986 by Chandler, McCoy, and Singer (CMS-DFT).¹⁵⁸⁻¹⁶⁰ Their theory is formulated on the basis of segment density functionals. In the CMS-DFT, all intramolecular interactions are accounted for in the ideal functional, while all intermolecular interactions are included in

the excess contributions. As a result, their ideal functional is very accurate and is exact for an ideal chain system. However, the intramolecular correlation functions come at the expense of a single-chain Monte Carlo simulation (a demanding iteration procedure that requires a single-chain simulation for each step). In addition, this approach requires input from the polymer integral equation theory (PRISM)¹⁶¹ for the direct correlation functions, leading to inconsistencies between the bulk and the interface (the CMS-DFT does not satisfy the wall contact theorem that relates the bulk pressure of a fluid to its contact density at a hard wall). Similar to integral equation theory, the CMS-DFT is also very sensitive to the particular closures employed, thus giving rise to potential complications and unreliable results under specific conditions (e.g., inability to describe phase transitions such as liquid-vapor coexistence).

4.4.2 Density functionals based on TPT1

A density functional theory based on thermodynamic perturbation theory holds a great value to this work. Wertheim's theory has been utilized for a wide range of applications and systems. Most notable is the development of the statistical associating fluid theory (SAFT) by Chapman et al.^{8,10} in 1988, which is very popular within industry in describing complex fluid properties in the bulk. Chapman⁸ was the first to recognize that Wertheim's TPT1 for association was written in general form for inhomogeneous fluids. Kierlik and Rosinberg¹⁶²⁻¹⁶⁴ then applied Chapman's idea and became the first to introduce a density functional theory based on Wertheim's theory. The main forms of DFT based on Wertheim's theory include work by Kierlik and Rosinberg,¹⁶²⁻¹⁶⁴ Chapman et al.,^{29-31,33,34,165-168} Wu et al.,^{95,169-172} Bryk, Sokolowski et al.,¹⁷³⁻¹⁷⁸ Patel and Egorov,^{179,180} and Jackson et al.^{181,182} These developments are discussed below.

4.4.2.1 Kierlik and Rosinberg

Kierlik and Rosinberg¹⁶²⁻¹⁶⁴ were the first to introduce a density functional theory for polyatomic fluids based on Wertheim's theory. Kierlik and Rosinberg's density functional is formed on the basis of molecular density functionals. The free energy functional, in the limit of complete association, is exact for ideal chains as it retains information about bond connectivity. Their excess functional accounts for all non-bonded intra- and inter-molecular forces, expressing chain connectivity in terms of a first-order perturbation theory, and the short-range correlations in terms of their own density-independent weighted free energy functional.^{155,183} An important attribute to the DFT developed by Kierlik and Rosinberg is that the intramolecular correlations in the inhomogeneous fluid agree with the bulk, and such correlations and density profiles are obtained in a self-consistent manner. As already discussed in section 4.4.1, this is not the case for the CMS-DFT, which relies on PRISM and suffers from inconsistencies between the bulk and the interface.

Kierlik and Rosinberg have applied their perturbation density functional theory to model rigid molecules,¹⁶² flexible molecules,¹⁶³ and freely-jointed chains in slit-like pores.¹⁶⁴ The theory performs well when compared with simulation,¹⁸⁴ although it overestimates chain enhancement near a wall at high densities, and underestimates the depletion of chain sites near a wall at low densities.¹⁶⁴ Although this polyatomic DFT is superior to other theories (e.g., the integral equation theory and polymer self-consistent field theory) in terms of describing the structure and thermodynamics of a system with complex (non-bonded) intermolecular interactions, it does have drawbacks. The free energy functional is written in terms of the molecular density, $\rho_M(\mathbf{R})$. Here the

multidimensional vector $\mathbf{R}=(\mathbf{r}_1, \mathbf{r}_2, \mathbf{r}_3, \dots, \mathbf{r}_m)$ denotes positions of all m monomers on a given polymer molecule. The multi-point-based molecular density formalism of the theory result in m^{th} order implicit integral equations for the density profile. Kierlik and Rosinberg¹⁶²⁻¹⁶⁴ employ numerical methods to solve the higher order implicit integral equations. However, these numerical techniques prove even more expensive than simulation techniques.¹⁸⁵

4.4.2.2 Segura, Chapman and Shukla

In 1997, Segura, Chapman, and Shukla²⁹ introduced a density functional theory for describing atomic associating fluids. The work of Segura et al. is based on Wertheim's perturbation theory, and is important to the discussion here as it introduced new ideas to the later development of polyatomic DFTs.

In the theory developed by Segura et al., the Tarazona^{152,153} weighted density approximation for hard-spheres is employed, and intermolecular association effects can be included through two perturbative approaches, both of which are discussed and demonstrated with success by Segura et al. Both of these approaches will be discussed here, as it is important to understand the basis for later developed theories, and will have application in this thesis work. The two approaches are (1) application of Wertheim's associating fluid functional as a perturbation to a reference fluid functional (in Segura's case, the Tarazona hard-sphere free energy functional), and (2) application of a weighted-density functional theory to the bulk equation of state for associating fluids.

In the first method outlined by Segura, the excess free energy functional can be written as⁸

$$A^{ex}[\rho(\mathbf{r})] = A^{ex,hs}[\rho(\mathbf{r})] + A^{ex,assoc}[\rho(\mathbf{r})] \quad (4.20)$$

where the hard-sphere and association contributions are denoted as *hs* and *assoc*, respectively. The Carnahan and Starling⁷² equation of state is used for the hard-sphere contribution, approximated at a weighted density using Tarazona weighting functions,^{152,153}

$$\beta A^{ex,hs}[\rho(\mathbf{r})] = \beta \int d\mathbf{r} \rho(\mathbf{r}) a^{hs}[\bar{\rho}(\mathbf{r})] \quad (4.21)$$

The association free energy functional for spherical molecules is given as^{4-8,10}

$$\beta A^{ex,assoc}[\rho(\mathbf{r})] = \sum_{A \in \Gamma} \int \rho(\mathbf{r}) \left(\ln \chi_A(\mathbf{r}) - \frac{\chi_A(\mathbf{r})}{2} + \frac{1}{2} \right) d\mathbf{r}, \quad (4.22)$$

where $\chi_A(\mathbf{r})$ is the fraction of molecules at position \mathbf{r} , not bonded at site A , defined as

$$\chi_A(\mathbf{r}_1) = \frac{1}{1 + \Delta \int \chi_A(\mathbf{r}_2) \rho(\mathbf{r}_2) d\mathbf{r}_2}. \quad (4.23)$$

The derivation of this expression is not included here, but can be found in Segura's work,^{29,186} as derived from Wertheim's theory.⁴⁻⁷ Above, it is assumed that the pair correlation function for the inhomogeneous fluid can be approximated by the hard-sphere pair correlation function at contact in the bulk ($y^{hs}(\sigma, \rho_{bulk})$), given in the expression below

$$\Delta \approx 4\pi\kappa y^{hs}(\sigma; \rho_{bulk}) f \quad (4.24)$$

where f is the Mayer f -function defined in terms of the site bonding energy (ϵ^{assoc})

$$f = \exp\left(\frac{\epsilon^{assoc}}{k_b T}\right) - 1. \quad (4.25)$$

In eq. (4.24), κ is a constant geometric factor²⁹ that accounts for the volume available for bonding between molecules 1 and 2.

In the second method proposed by Segura et al., it is assumed that the hard-sphere and association interactions are of similar range, so it is reasonable to apply a weighted DFT to the bulk equation of state. Therefore, a weighted-density can be used for both the hard-sphere and association free energy functionals. Again the hard-sphere terms are obtained by the Carnahan and Starling⁷² equation of state, while the bulk SAFT association relations are used for the association free energy functional²⁹

$$\beta A^{ex,assoc}[\rho(\mathbf{r})] = \beta \int d\mathbf{r} \rho(\mathbf{r}) a^{ex,assoc}[\bar{\rho}(\mathbf{r})] \quad (4.26)$$

where

$$\beta a^{ex,assoc}[\bar{\rho}(\mathbf{r})] = \sum_{A \in \Gamma} \left(\ln \bar{\chi}_A(\mathbf{r}) - \frac{\bar{\chi}_A(\mathbf{r})}{2} + \frac{1}{2} \right). \quad (4.27)$$

In eq. (4.27), the weighted-density and weighted fraction of molecules not bonded at site A are substituted by the bulk terms of Wertheim's theory.^{5-8,10} By using the bulk equations of this method, versus the inhomogeneous form of Wertheim's theory, the computational time can be greatly reduced.

Both methods above have been used with success in DFTs for atomic associating fluids. The first method introduced by Segura et al. demonstrates how Wertheim's associating fluid functional can be used as a perturbation to a reference fluid free energy functional. Although the second method is simpler and used by Segura and Chapman in later work (as well as others, discussed below), the importance of the first method shows up later in a polyatomic DFT developed by Tripathi and Chapman.^{33,34,187} This work is discussed in section 4.4.2.4. The second method has been applied with varying forms of weighting functions, but the basis of expressing this functional in terms of the bulk equation of state remains the same. This includes work studying the effects of various

confinements on the interfacial properties and phase behavior of associating fluids by Segura and Chapman,²⁹⁻³¹ Sokolowski et al.^{177,178} (who apply a modified Meister-Kroll^{157,188-190} weighting), Wu et al.^{95,172} (who apply Rosenfeld^{155,156} weighting), and Tripathi and Chapman¹⁶⁶⁻¹⁶⁸ (who also apply Tarazona^{152,153} weighting). In addition, Jackson and co-workers^{181,182} have demonstrated how such an approach can be applied within a local density approximation (LDA, discussed previously in section 4.3.1), to successfully describe the vapor-liquid interfacial properties, such as surface tension, of inhomogeneous associating fluids. Method 2 also forms the basis for the polyatomic DFT developed by Yu and Wu,¹⁷² which is briefly discussed in section 4.4.2.3. All tests of the theory (for both methods) are in good agreement with Monte Carlo molecular simulation.

It should be noted that the polyatomic DFTs mentioned that were later developed as extensions to Segura et al.'s work, consider the formation of chains in the limit of complete association, where all molecules are bonded. In contrast, the atomic DFT of Segura considers the full range of molecular association as a function of temperature, an important characteristic of hydrogen-bonding fluids. Work in this thesis incorporates such molecular interactions to study the effects of full range molecular association, first in a molecular model for water around a hydrophobic solute (chapter 5), and then to associating polymeric fluids (chapter 7).

4.4.2.3 Yu and Wu

As mentioned in the previous section, one of the density functional methods proposed by Segura et al.²⁹ for atomic associating fluids forms the basis for a polyatomic DFT developed by Yu and Wu.¹⁷² This DFT, similar to a DFT for associating atomic fluids

also developed by Yu and Wu,¹⁷¹ combines Wertheim's perturbation theory with the weighted-densities of Rosenfeld's fundamental measure theory (FMT).¹⁵⁵

The Helmholtz free energy functional for hard-sphere chains is expressed as the sum of an ideal gas term $A^{id}[\rho_M(\mathbf{R})]$ and an excess term $A^{ex}[\rho_M(\mathbf{R})]$ due to intra- and intermolecular interactions.

$$A[\rho_M(\mathbf{R})] = A^{id}[\rho_M(\mathbf{R})] + A^{ex}[\rho_M(\mathbf{R})] \quad (4.28)$$

Here the multidimensional vector $\mathbf{R}=(r_1, r_2, r_3, \dots, r_m)$ of the molecular density denotes positions of all m monomers on a given polymer molecule. Yu and Wu use the same exact ideal free energy functional as used by Woodward,¹⁹¹

$$\beta A^{id}[\rho_M(\mathbf{R})] = \int d\mathbf{R} \rho_M(\mathbf{R}) [\ln \rho_M(\mathbf{R}) - 1] + \beta \int d\mathbf{R} \rho_M(\mathbf{R}) V_b(\mathbf{R}) \quad (4.29)$$

where $d\mathbf{R} = dr_1 dr_2 \dots dr_m$ represents the set of differential volume, and $V_b(\mathbf{R})$ is the bonding potential which accounts for bonding connectivity, given by

$$\exp(-\beta V_b(\mathbf{R})) = \prod_{i=1}^{m-1} \frac{\delta(|r_{i+1} - r_i| - \sigma)}{4\pi\sigma^2} \quad (4.30)$$

Above, the ideal chain is composed of fully flexible, non-interacting monomers, held at a fixed bond length of σ (the diameter of any given monomer). The excess free energy is derived in terms of the segment densities

$$\beta A^{ex} = \int d\mathbf{r} (\Phi^{hs}(\{n_\alpha(\mathbf{r})\}) + \Phi^{chain}(\{n_\alpha(\mathbf{r})\})) \quad (4.31)$$

where $\Phi^{hs}(\{n_\alpha(\mathbf{r})\})$ and $\Phi^{chain}(\{n_\alpha(\mathbf{r})\})$ represent the excess free energy density due to hard-sphere repulsion and chain connectivity, respectively. The set of weighted densities is given by $n_\alpha(\mathbf{r})$, and both $n_\alpha(\mathbf{r})$ and $\Phi^{hs}(\{n_\alpha(\mathbf{r})\})$ are computed from FMT¹⁵⁵ (detailed

expressions can be found in given reference or in chapters 5-8). The above equation implies that the effect of chain connectivity on the intramolecular interactions can be accounted for using the segment densities. Yu and Wu assume (similar to the approach by Segura et al.) that the chain connectivity can be formulated on the basis of a bulk equation of state. From SAFT, the chain connectivity for a bulk fluid is given by

$$\Phi^{chain,bulk} = \frac{1-m}{m} \rho_b \ln y^{hs,bulk}(\sigma) \quad (4.32)$$

where ρ_b is the bulk density and $y^{hs,bulk}(\sigma)$ is the bulk cavity correlation function between segments, evaluated at contact. Yu and Wu extended this bulk form to the inhomogeneous region by using the weighted densities of FMT.

$$\Phi^{chain}(\{n_\alpha(\mathbf{r})\}) = \frac{1-m}{m} n_0 \zeta \ln y^{hs}(\sigma, \{n_\alpha(\mathbf{r})\}) \quad (4.33)$$

where

$$y^{hs}(\sigma, \{n_\alpha\}) = \frac{1}{1-n_3} + \frac{n_2 \sigma \zeta}{4(1-n_3)^2} + \frac{n_2^2 \sigma^2 \zeta}{72(1-n_3)^3} \quad (4.34)$$

and n_α are the same weighted densities as given by FMT, and $\zeta = 1 - \mathbf{n}_{v2} \cdot \mathbf{n}_{v2} / n_2^2$. One disadvantage of this formalism is its restriction that all chain segments must be of the same size. Like the model of Kierlik and Rosinberg, the DFT developed by Yu and Wu requires solving m^{th} order implicit integral equations due to the many-bonded nature of the ideal chain free energy functional (expressed in terms of molecular density).

This new polyatomic DFT has been tested with the same Monte Carlo simulations¹⁸⁴ as Kierlik and Rosinberg.¹⁶⁴ Like the predictions of Kierlik and Rosinberg, Yu and Wu's results underestimate chain depletion at the surface, though with better agreement than

Kierlik and Rosinberg. Kierlik and Rosinberg are able to give slightly better density distributions for the end and middle segments. Yu and Wu attribute this to Kierlik and Rosinberg's use of the inhomogeneous cavity correlation function for representing chain connectivity, whereas they rely on Wertheim's first-order perturbation theory for a bulk fluid to represent chain connectivity.

Wu and coworkers have applied their theory to mixtures of polymeric fluids,¹⁷² block co-polymers near selected surfaces,¹⁶⁹ and semi-flexible polymers.¹⁷⁰ Other work following the approach of Wu et al. includes work by Bryk, Sokolowski, and co-workers. They have studied adsorption,¹⁷⁵ surface phase transitions,¹⁷³ and capillary condensation¹⁷⁴ in polymer systems, and have also applied the theory to star polymer fluids.¹⁷⁶ In addition, Patel and Egorov,^{179,180} similar to Wu and coworkers, have employed a DFT based on a weighted free energy functional for chain fluids (using a bulk equation of state) to study polymer-colloid mixtures (using a different weighted formalism).

4.4.2.4 Chapman and coworkers

In 2005 Tripathi and Chapman^{33,34} developed a new density functional theory, interfacial statistical associating fluid theory (*i*SAFT), for inhomogeneous polyatomic fluids. This work extended the first method of Segura et al.²⁹ The chain contribution to the free energy functional was derived from Wertheim's TPT1 (similar to SAFT) by considering a mixture of associating atomic spheres that form a fluid of chains in the complete bonding limit (see Figure 4.1). This self-consistent DFT reduces to SAFT^{8,10,12} in the bulk and therefore offers all the features of SAFT, along with the ability to predict the microstructure of an inhomogeneous system. The theory uses a segment-based

formalism while offering an accuracy that compares well and exceeds that of the molecular density based and simulation dependent theories. The theory developed by Tripathi and Chapman^{33,34} served as an important precursor to the current version of *i*SAFT and to the work in this dissertation.

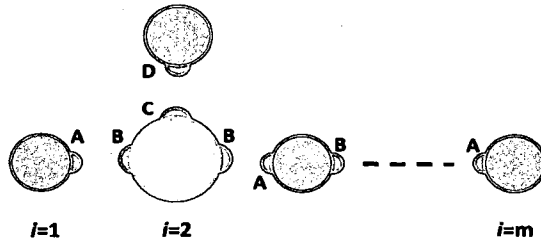


Figure 4.1: Schematic of chain formation from a mixture of associating spheres.

First, the total Helmholtz free energy of this associating mixture can be expressed as

$$A[\rho_i(\mathbf{r})] = A^{id}[\rho_i(\mathbf{r})] + \Delta A^{ex,hs}[\rho_i(\mathbf{r})] + \Delta A^{ex,assoc}[\rho_i(\mathbf{r})] + \Delta A^{ex,att}[\rho_i(\mathbf{r})] \quad (4.35)$$

where the superscripts above, in order of appearance, represent the contributions to the free energy due to the ideal gas free energy of the atomic mixture, excluded volume of the monomer segments, association between segments in the mixture, and long-range attraction. The subscript i represents the i^{th} molecule on a chain of m segments. The ideal functional is defined

$$\beta A^{id}[\rho_i(\mathbf{r})] = \int d\mathbf{r} \sum_{i=1}^m \rho_i(\mathbf{r}) [\ln \rho_i(\mathbf{r}) - 1] \quad (4.36)$$

$A^{ex,hs}$ is calculated using Rosenfeld's FMT,^{155,156} while $A^{ex,assoc}$ can be derived from TPT1. From Wertheim's theory for finite association, the association contribution to the free energy can be written as previously done by Segura et al.²⁹

$$\beta\Delta A^{ex,assoc} = \int d\mathbf{r}_1 \sum_{i=1}^m \rho_i(\mathbf{r}_1) \sum_A^{[A]} \left(\ln \chi_A^i(\mathbf{r}_1) - \frac{\chi_A^i(\mathbf{r}_1)}{2} + \frac{1}{2} \right) \quad (4.37)$$

where the summations, in order, are over all the segments on a given chain, and over all the association sites on segment i . $\chi_A^i(\mathbf{r})$ represents the fraction of segments i not bonded at association site A , defined as

$$\chi_A^i(\mathbf{r}_1) = \frac{1}{1 + \int d\mathbf{r}_2 \chi_B^j(\mathbf{r}_2) \Delta^{ij}(\mathbf{r}_1, \mathbf{r}_2) \rho_j(\mathbf{r}_2)}. \quad (4.38)$$

Note the above expression is defined as in eq. (4.23). In the limit of complete association, all the chains form and thus $\chi_A^i(\mathbf{r}) \rightarrow 0$. In regard to this condition, Tripathi and Chapman assumed that each association site on a given molecule reaches its complete bonding limit at the same rate, i.e., $\chi_B^j(\mathbf{r}_2) \approx \chi_A^i(\mathbf{r}_1)$. This simplifies eq. (4.38) to the following^{33,34}

$$\chi_A^i(\mathbf{r}_1)^2 = \frac{1 - \chi_A^i(\mathbf{r}_1)}{\int d\mathbf{r}_2 \Delta^{ij}(\mathbf{r}_1, \mathbf{r}_2) \rho_j(\mathbf{r}_2)}. \quad (4.39)$$

In the above expressions,

$$\Delta^{ij}(\mathbf{r}_1, \mathbf{r}_2) = y^{ij}(\mathbf{r}_1, \mathbf{r}_2) F^{ij}(\mathbf{r}_1, \mathbf{r}_2) K \quad (4.40)$$

where y^{ij} is the cavity correlation function between segment i and its neighbor j , and K is a constant geometric factor²⁹ that accounts for the volume available for bonding between two segments. The Mayer function is expressed as

$$F^{ij}(\mathbf{r}_1, \mathbf{r}_2) = \exp[\beta(\epsilon^{assoc} - V_b^{ij}(\mathbf{r}_1, \mathbf{r}_2))] - 1 \quad (4.41)$$

where ε^{assoc} represents the association energy of interaction between two segments, and $V_b^{ij}(\mathbf{r}_1, \mathbf{r}_2)$ is the energy of the bond (such as harmonic bonding potential for bond vibration). By taking the limit of complete association, (forcing $\chi_A^i(\mathbf{r}) \rightarrow 0$ as $\varepsilon^{assoc} \rightarrow \infty$) the chain functional is obtained upon dropping all constant contributions to the chemical potential, i.e., $\beta\varepsilon^{assoc}$ and $\ln K$ (these density independent contributions are the same in the bulk and in the inhomogeneous region and can be discarded for the same reason the thermal de Broglie wavelength was dropped from the ideal functional in section 4.3.1).^{33,34}

$$\beta\Delta A^{chain} = \int d\mathbf{r}_1 \sum_{i=1}^m \rho_i(\mathbf{r}_1) \sum_{j=1}^m \left[-\frac{1}{2} \ln \int d\mathbf{r}_2 \exp[-\beta V_b^{ij}(\mathbf{r}_1, \mathbf{r}_2)] y^{ij}(\mathbf{r}_1, \mathbf{r}_2) \rho_j(\mathbf{r}_2) + \frac{1}{2} \right] \quad (4.42)$$

Above, since the correlation function for an inhomogeneous system is not known, it is assumed that it can be approximated by the hard-sphere pair correlation function at contact in the bulk, evaluated at a coarse-grained (weighted) density. Finally, the long-range attraction is included using the mean field approximation

$$A^{ex,att}[\rho_i(\mathbf{r})] = \frac{1}{2} \sum_{i=1}^m \sum_{j=1}^m \int_{|\mathbf{r}_2 - \mathbf{r}_1| > \sigma_{ij}} d\mathbf{r}_1 d\mathbf{r}_2 u_{ij}^{att}(|\mathbf{r}_2 - \mathbf{r}_1|) \rho_i(\mathbf{r}_1) \rho_j(\mathbf{r}_2) \quad (4.43)$$

The DFT developed by Tripathi and Chapman performs very well in comparison to the DFTs developed by Kierlik and Rosinberg¹⁶⁴ and Yu and Wu.¹⁷² It accurately captures the density distributions for entire chains as well as end and middle segments in the chain, despite the fact that the other theories have an exact ideal chain free energy functional. This is due to better approximations for the excluded volume effects. The theory developed by Tripathi and Chapman requires only the solving of a set of first-

order integral equations that does not depend on the chain length m . Such calculations can be performed using elementary numerical methods as commonly used in atomic DFTs.^{29-31,166-168}

Tripathi and Chapman have applied their theory to inhomogeneous solutions and blends of linear and branched chains. Branching is allowed in the theory by designating the backbone chain to have additional association sites to which the branch segments can form bonds (Figure 4.1). In addition, Tripathi and Chapman have also demonstrated successful application of the theory to lipids in solution and lipid bilayers. Dominik et al.¹⁶⁵ extended the theory to real systems, calculating the surface tension of n -alkanes and polymer melts. In this study, Dominik et al. showed how the bulk phase behavior and interfacial properties could be described using one set of parameters, thereby demonstrating how both systems can be studied within the single framework of *i*SAFT.

In the derivation of *i*SAFT, Tripathi and Chapman assumed that the theory satisfied stoichiometry (overall stoichiometry is satisfied if the average segment density of all segments on a molecule in the system are equal). However, it was later realized that this original form of *i*SAFT does not constrain all the segments in the system to satisfy stoichiometry, not even for the simple case of homonuclear chains (chains where all segments are identical). The approximation that each association site on a given molecule reaches its complete bonding limit at the same rate, i.e., $\chi_B^j(\mathbf{r}_2) \approx \chi_A^i(\mathbf{r}_1)$, does not constrain stoichiometry (while both $\chi_A^i(\mathbf{r}_1)$ and $\chi_B^j(\mathbf{r}_2)$ do approach zero in the complete bonding limit, they do not approach this limit at the same rate). This limitation becomes more pronounced when the theory is applied to heteronuclear chains. In the original *i*SAFT, each segment along a chain only retains information about its

neighboring segment. As a result, homonuclear systems still yield accurate results in comparisons with simulation data, despite not satisfying stoichiometry. However, for heteronuclear chains, it becomes essential to possess such information. It becomes important, for example, for segments in a molecular system to know if other segments are tethered to a surface, or in a diblock copolymer, for segments on one block to know information about the segments on its neighboring block. Recently, a modified version of *iSAFT* was introduced by Jain et al.³² that enforces stoichiometry and extends the theory to complex heteronuclear systems. The theory performs well for a wide range of systems, including copolymers in confinement¹⁹² and near selective surfaces,³² tethered polymers,¹⁹³ branched polymers,¹⁹⁴ polymer colloid mixtures,¹⁹⁵ and associating polyatomic systems¹⁹⁶ (the last two examples being work in this thesis). In the following chapters, the modified version of *iSAFT* is presented along with the developments of this research.

CHAPTER 5

Hydration structure and interfacial properties of water near a hydrophobic solute from a fundamental measure density functional theory

5.1 Introduction

Water is a unique solvent, not only because of its thermodynamic anomalies and complex hydrogen-bonding structure, but because it is also one of the few liquids found in nature that possesses the attractive force imbalances that drive hydrophobic behavior. The hydrophobic interactions in aqueous solutions play a significant role in many facets of chemistry and biology, most notably in self-assembly processes such as the formation of membranes and micelles in surfactant solutions, and the folding of proteins into stable, functional complexes.^{197,198} As mentioned, hydrophobic phenomena typically involve complicated amphiphilic macromolecules that are part hydrophobic and part hydrophilic. In order to study hydrophobic effects exclusively, researchers have focused on model hydrophobic hard sphere solutes, neglecting all other interaction effects. Using this approach, a better understanding of the molecular mechanisms behind hydrophobic hydration has been achieved, and valuable insight has been gained in the interactions that stabilize membranes, micelles, and proteins.

When a non-polar solute (e.g. a hydrocarbon) is immersed in water, the local structure of the liquid around the solute is altered. Hydrophobic hydration describes these

structural changes that bulk water undergo when a non-polar molecule is dissolved in it. Over three decades ago (1973), Stillinger¹⁹⁹ presented an improved scaled particle theory (SPT), from the classic SPT of Reiss et al.^{200,201} and Pierotti,²⁰² that introduced new ideas on the application of SPT to hydrophobic hydration of a hard sphere solute in water. Stillinger theorized that the density of water molecules at the surface of a hard solute was not a monotonic function of the radius of the solute particle, and hence suggested that the hydration mechanisms at a molecular scale differ from those at a macroscopic scale. He further predicted that near a large solute, water behaves much like that of a free vapor-liquid interface. Results from theory and simulation have since confirmed a crossover in the hydration of water between small and large length scales for hard sphere solutes.²⁰³⁻²⁰⁸ For small solute particles, the density of the water molecules at the surface is greater than the bulk density of water; for larger solute particles, a drying transition occurs, as predicted by Stillinger,¹⁹⁹ and in the limit of an infinitely large particle, a vapor-liquid-like interface is formed (for water at ambient conditions).

Such behavior is dictated by a crossover in entropic and energetic dominance, and therefore a theory capable of describing the hydrophobicity on both scales is of great interest to describing more complex phenomena. While Monte Carlo simulations have played a significant role in the progress and understanding of the structure of water around a hydrophobic solute, their application to describing hydrophobic interactions of large macromolecules can be computationally expensive. Lum, Chandler, and Weeks (LCW)²⁰⁸ were the first to propose a unified theory capable of describing the hydrophobic effects on both length scales for water. Their theory involves a two-step process, where the density profile is comprised of a slowly varying part and a rapidly

varying part. The advantage of their theory is that it is not as computationally expensive as simulation.

Density functional theory (DFT) is a tool with a statistical mechanics foundation that can be used to study inhomogeneous fluids, such as the case considered here. Like the theory of LCW, it offers a much less computationally demanding method when compared to simulation. This is advantageous because it imposes no limitations for later studies involving macromolecular fluids. When constructing a density functional theory, the physics and molecular interactions between solute and solvent molecules are used to express the free energy of the system as a functional of the density $\rho(\mathbf{r})$. Once this functional is obtained, it can be used to calculate the equilibrium molecular structure and thermodynamic functions such as phase behavior, interfacial properties, and surface forces. Unlike the LCW theory, density functional theory does not involve a two-step process, but instead everything is calculated from the same free energy functional. This provides for a more practical method and simplifies calculations. Sun²⁰⁹ constructed a DFT based not on a water-water intermolecular potential, but rather experimental observed liquid structure and thermodynamic data. Sun demonstrated that such a density functional theory could capture the qualitative behavior predicted by simulation.^{210,211} Reddy and Yethiraj²¹² compared results from a density functional theory²¹³ for a Yukawa fluid with results from simulation, and they too demonstrated the structural anomalies of their solvent around a solute particle of varying size. In addition, they also compared the results for a Yukawa fluid from their DFT to those predicted by the theory of LCW, and demonstrated that their DFT was in more quantitative agreement with simulation than the LCW theory.

In this chapter, we investigate the interfacial properties and structure of water around a solute particle as a function of the size of the solute. We extend a density functional theory originally proposed by Segura et al.²⁹ over 10 years ago, which was used for describing associating (hydrogen-bonding) atomic fluids near a hydrophobic hard wall. In the work of Segura et al., the Tarazona^{152,153} weighted density method for hard spheres was employed and the well-established association free energy based on Wertheim's first order thermodynamic perturbation theory (TPT1)⁴⁻⁷ was used to account for intermolecular hydrogen-bonding interactions. The Segura et al. approximation has been applied by numerous groups using different forms of weighting functions to study structure, phase behavior, and interfacial properties of associating fluids (both in confined environments and at vapor-liquid and solid-liquid interfaces). This includes work by Segura et al.,²⁹⁻³¹ Patrykiewicz et al.¹⁷⁷ and Pizio et al.¹⁷⁸ (applied a modified Meister-Kroll^{157,188-190} weighting), Yu and Wu¹⁷¹ (applied Rosenfeld¹⁵⁵ weighting), and Tripathi and Chapman¹⁶⁶⁻¹⁶⁸ (also applied Tarazona weighting). Results from the above theories were compared with molecular simulations²⁹ and found to be in excellent agreement. In this work, we use Rosenfeld's formalism¹⁵⁵ for hard spheres, and improve the water model suggested by Segura et al. to include long-range attractions. In addition, the theoretical model is modified from the planar wall case to the spherically symmetric case studied here.

Since this DFT accounts for the hydrogen bonding interactions, we expect results similar to real water and available simulation data. The theory provides an added advantage (over previous density functional theories used to study this case) as the influence of a solute particle on the hydrogen-bonding structure of water can be evaluated

as a result of varying solute size. Further, the theory can be used to study the temperature effects on the properties and structure of the system. This is important as hydrophobicity is temperature dependent and can therefore affect the function and stability of aqueous solutions and biological structures. For example, protein folding is one of the most extensively characterized self-assembly processes in aqueous solutions, a behavior that is highly temperature dependent and dictates whether the protein exists in a globular state or an unfolded state. All molecular parameters incorporated into the model have values that agree well with simulation data and experimental spectroscopic data for water.

Of course, the model used here for water is not complete, as multipolar interactions and solute-water van der Waals attractions are not included. Still it will be shown that the model used provides a good approximation to the real fluid behavior, capturing the distinguishing fluid structure and interfacial properties as a function of the size of the solute. Including attractions between the solute particle and the water molecules can have a notable effect. Simulation results from Hummer and Garde²¹⁴ and Ashbaugh et al.^{203,204,215} suggest the dewetting behavior for large solutes becomes less pronounced when the attractive solute-water interactions are included. For smaller solutes, there is little difference in the wetting behavior of water when solute-water attractions are present or absent. Huang and Chandler²⁰⁶ predicted similar results using a theory based on the approach of Lum et al.,²⁰⁸ demonstrating how the drying interface is translated for larger solutes. Solute-water attractions therefore affect the position of an interface, but are too weak to affect the existence of the interface formed for very large solute particles.

5.2 Theory

5.2.1 Model

In this work, we consider a hard sphere solute particle in a pure associating water solvent. Most models used in simulation treat water as a rigid molecule and make use of point charges placed strategically on the molecules to mimic the effects of hydrogen-bonding. Examples include the ST2 water model developed by Stillinger and Rahman,^{216,217} the SPC model by Berendsen et al.,^{218,219} and the TIP model by Jorgensen.²²⁰⁻²²² While such models are useful for molecular simulations, point charge models possess long-range Coulomb forces that are difficult to model within theory.²²³

In the work here, the water molecule is represented as a hard spherical repulsive core with diameter σ_w and four square-well bonding sites placed in tetrahedral symmetry, a model originally proposed by Bol.²²⁴ This model has proven to be a good alternative to the above mentioned point charge models, and has been used successfully in simulation studies by Kolafa and Nezbeda,²²⁵ and Ghonasgi and Chapman,²²⁶ and in theoretical studies^{29,226} in conjunction with Wertheim's Theory.⁴⁻⁷ The association sites mimic the directional interactions characterized by hydrogen bonds, which play a dominating role in determining the physical properties of aqueous systems. Using the notation of Yarrison and Chapman⁸¹ ($N_{\text{sites}}[N_{\text{proton acceptors}}, N_{\text{proton donors}}]$), the four site model (4[2,2]) accounts for the two electron lone pairs (e^-) and the two hydrogen sites (H^+) of the water molecule, as shown in Figure 5.1. The two electron lone pairs (e^-) are designated as type *A*, whereas the two hydrogen sites (H^+) are designated as type *B*. Using the (4[2,2]) model, each water molecule is capable of forming up to four hydrogen bonds.

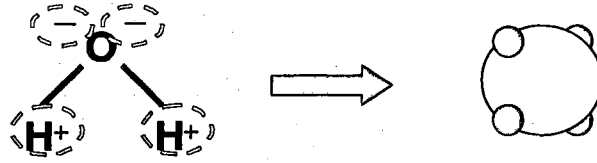


Figure 5.1: Water represented using the four site model (4[2,2]) accounts for the two electron lone pairs (e^-) and the two hydrogen sites (H^+) of the water molecule.

The intermolecular potential between any two molecules consists of a reference fluid contribution u^{ref} and a directional contribution u^{assoc}

$$u(\mathbf{r}_{12}, \boldsymbol{\omega}_1, \boldsymbol{\omega}_2) = u^{ref}(\mathbf{r}_{12}) + \sum_A \sum_B u_{AB}^{assoc}(\mathbf{r}_{12}, \boldsymbol{\omega}_1, \boldsymbol{\omega}_2) \quad (5.1)$$

where r_{12} is the distance between molecules 1 and 2, $\boldsymbol{\omega}_1$ and $\boldsymbol{\omega}_2$ are the orientations of the two molecules, and the two summations are over all hydrogen-bonding sites on the molecules. The reference fluid potential u^{ref} can be described as the sum of repulsive and attractive contributions

$$u^{ref}(r_{12}) = u^{hs}(r_{12}) + u^{an}(r_{12}) \quad (5.2)$$

where the hard sphere repulsion is given by

$$u^{hs}(r_{12}) = \begin{cases} \infty, & r_{12} < \sigma_w \\ 0, & r_{12} \geq \sigma_w \end{cases} \quad (5.3)$$

The attractive contribution uses a cut-and-shifted Lennard-Jones potential, with a Weeks, Chandler, and Andersen separation^{147,227,228} at $r_{min} = 2^{1/6} \sigma_w$

$$u^{an}(r_{12}) = \begin{cases} -\epsilon^{LJ} - u^{LJ}(r_{cut}), & \sigma_w < r_{12} \leq r_{min} \\ u^{LJ}(r_{12}) - u^{LJ}(r_{cut}), & r_{min} < r_{12} < r_{cut} \\ 0, & r_{12} \geq r_{cut} \end{cases} \quad (5.4)$$

where,

$$u^{LJ}(r_{12}) = 4\epsilon^{LJ} \left[\left(\frac{\sigma_w}{r_{12}} \right)^{12} - \left(\frac{\sigma_w}{r_{12}} \right)^6 \right] \quad (5.5)$$

where ϵ^{LJ} is the molecular interaction energy and r_{cut} is the position of the potential cut-off for the LJ potential, taken to be $r_{cut} = 3.0\sigma_w$. The association potential between an electron donor (e^-) site on molecule 1 and a hydrogen (H^+) site on molecule 2 is given as²⁹

$$u_{AB}^{assoc}(\mathbf{r}_{12}, \omega_1, \omega_2) = \begin{cases} -\epsilon^{HB}, & r_{12} < r_c; \theta_{A1} < \theta_c; \theta_{B2} < \theta_c \\ 0, & \text{otherwise} \end{cases} \quad (5.6)$$

where θ_{A1} is the angle between the vector from the center of molecule 1 to site A and the vector \mathbf{r}_{12} , and θ_{B2} is the angle between the vector from the center of molecule 2 to site B and the vector \mathbf{r}_{12} , as illustrated in Figure 5.2. As in the work from Segura et al.,²⁹ only bonding between an electron donor site and a hydrogen site are allowed, with a hydrogen-bonding energy of $\epsilon^{AB} = \epsilon^{BA} = \epsilon^{HB}$. Bonding of like sites have a bonding energy of zero ($\epsilon^{AA} = \epsilon^{BB} = 0$). The radial limits of square-well association were set to $r_c = 1.05\sigma_w$ and the angular limit to $\theta_c = 27^\circ$.

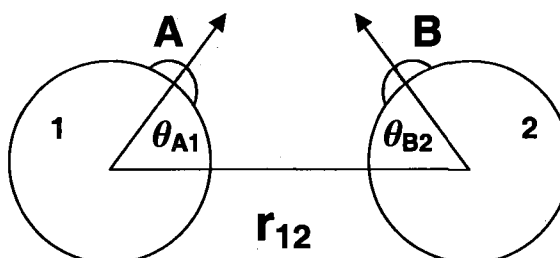


Figure 5.2: The association interaction potential model. From the theory, if molecule 1 is oriented within the constraints given in eq. (5.6) with respect to molecule 2, then a bond will form between the two molecules, given that their bonding sites are compatible.

In addition to the pair potential on the molecules, the hard solute particle introduces an external field $V^{ext}(\mathbf{r})$ into the system, given by

$$V^{ext}(r) = \begin{cases} \infty, & r < R \\ 0, & r \geq R \end{cases} \quad (5.7)$$

In eq. (5.7), r is the center-to-center distance of a given water molecule with radius r_w from the solute particle with radius r_s . R is the distance of closest approach between the solute and water molecule, $R = r_s + r_w$, as illustrated in Figure 5.3.

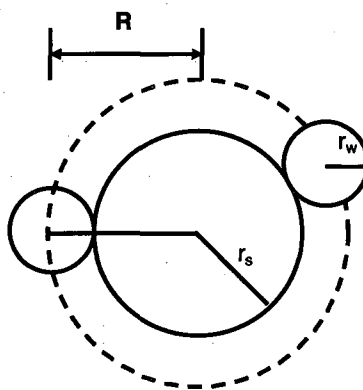


Figure 5.3: Geometry of a water molecule, with radius r_w , in contact with a hard solute, with radius r_s . R is the distance of closest approach between the solute and water molecule.

5.2.2 Density functional theory

The underlying motive behind density functional theory is to develop an expression for the grand potential $\Omega[\rho(\mathbf{r})]$ as a functional of the equilibrium density profile $\rho(\mathbf{r})$ of the fluid. From this, the desired thermodynamic and structural properties of the system can be determined. The grand potential is related to the Helmholtz free energy functional $A[\rho(\mathbf{r})]$ through the Legendre transform¹³

$$\Omega[\rho(\mathbf{r})] = A[\rho(\mathbf{r})] - \int d\mathbf{r}' (\mu - V^{ext}(\mathbf{r}')) \rho(\mathbf{r}') \quad (5.8)$$

where $\rho(\mathbf{r})$ denotes the equilibrium density at position \mathbf{r} , μ represents the chemical potential of the bulk fluid, and $V^{ext}(\mathbf{r})$ is the external field imposed on the system. The density profile is obtained by minimizing the grand potential of the system

$$\left. \frac{\delta \Omega[\rho(\mathbf{r})]}{\delta \rho(\mathbf{r})} \right|_{\text{equilibrium}} = 0 \quad (5.9)$$

The total Helmholtz free energy functional can be decomposed into an ideal and excess contribution,

$$A[\rho(\mathbf{r})] = A^{id}[\rho(\mathbf{r})] + A^{ex,hs}[\rho(\mathbf{r})] + A^{ex,att}[\rho(\mathbf{r})] + A^{ex,assoc}[\rho(\mathbf{r})] \quad (5.10)$$

where the excess contribution consists of changes in the free energy due to excluded volume (*hs*), long-range attraction (*att*), and association (*assoc*) over the ideal gas state.

The ideal functional is known exactly from statistical mechanics

$$\beta A^{id}[\rho(\mathbf{r})] = \int d\mathbf{r} \rho(\mathbf{r}) [\ln \rho(\mathbf{r}) - 1] \quad (5.11)$$

where the temperature-dependent term (the de Broglie wavelength λ) has been dropped since it is not density dependent and hence does not affect the structure of the fluid.

When a solute particle is placed in a solvent, the excluded volume can create density gradients and induce strong density oscillations in the system. Therefore, to approximate $A^{ex,hs}$, a weighted density formalism is an appropriate choice since it is capable of describing such systems. Various accurate models are available,^{13,152-155,157} and in this work, $A^{ex,hs}$ is represented using Rosenfeld's formalism.¹⁵⁵ Rosenfeld's fundamental measure theory (FMT) excess free energy for hard spheres was postulated to have the form

$$\beta A^{ex,hs}[\rho(\mathbf{r})] = \int d\mathbf{r} \Phi^{ex,hs}[n_i(\mathbf{r})] \quad (5.12)$$

where $\Phi^{ex,hs}[n_i(\mathbf{r})]$ is the excess Helmholtz free energy density due to the hard core interactions. $\Phi^{ex,hs}[n_i(\mathbf{r})]$ is assumed to be a function of only the system averaged fundamental geometric measures, $n_i(\mathbf{r})$, of the particles, given by (for a pure fluid)

$$n_i(\mathbf{r}) = \int \rho(\mathbf{r}') \omega^{(i)}(\mathbf{r} - \mathbf{r}') d\mathbf{r}' \quad (5.13)$$

where $i=0,1,2,3,V1,V2$, representative of the scalar and vector weighted densities. The weight functions $\omega^{(i)}$ characterize the geometry of the water molecules. The three independent functions are¹⁵⁵

$$\omega^{(2)} = \delta(r_w - r); \quad \omega^{(3)} = \Theta(r_w - r); \quad \omega^{(v2)} = \frac{\mathbf{r}}{r} \delta(r_w - r). \quad (5.14)$$

The remaining functions are proportional to the above geometric functions¹⁵⁵

$$\omega^{(0)} = \frac{\omega^{(2)}}{4\pi r_w^2}; \quad \omega^{(1)} = \frac{\omega^{(2)}}{4\pi r_w}; \quad \omega^{(v1)} = \frac{\omega^{(v2)}}{4\pi r_w}. \quad (5.15)$$

In eq. (5.14), $\delta(r)$ is the Dirac delta function, and $\Theta(r)$ is the Heaviside step function. For this study, inhomogeneities occur only in the r direction and the density profile of pure water around a hard solute particle has a spherical symmetry. Because of this symmetry, the weighted densities are given by²²⁹⁻²³¹

$$n_0(r) = \frac{n_1(r)}{r_w} = \frac{n_2(r)}{4\pi r_w^2}$$

$$n_2(r) = \frac{2\pi r_w}{r} \int_{-r_w}^{+r_w} dr' r' \rho(r')$$

$$n_3(r) = \frac{\pi}{r} \int_{-r_w}^{+r_w} dr' r' [r_w^2 - (r - r')^2] \rho(r')$$

$$\mathbf{n}_{v1}(\mathbf{r}) = \frac{\mathbf{n}_{v2}(\mathbf{r})}{4\pi r_w}$$

$$\mathbf{n}_{v2}(\mathbf{r}) = \frac{\mathbf{r}}{r} \frac{\pi}{r^2} \int_{-r_w}^{+r_w} dr' r' [r^2 - r'^2 + r_w^2] \rho(r') \quad (5.16)$$

In the FMT formalism, $\Phi^{ex,hs}[n_i(\mathbf{r})]$ has the form

$$\Phi^{ex,hs}[n_i(\mathbf{r})] = -n_0 \ln(1 - n_3) + \frac{n_1 n_2 - \mathbf{n}_{v1} \cdot \mathbf{n}_{v2}}{1 - n_3} + \frac{n_2^3 - 3n_2 \mathbf{n}_{v2} \cdot \mathbf{n}_{v2}}{24\pi(1 - n_3)^2} \quad (5.17)$$

The density distribution, in the limit of a homogeneous fluid, becomes the bulk density $\rho(\mathbf{r}) = \rho_b$. The vector-weighted densities vanish in the limit of a uniform fluid, whereas the scalar quantities of the bulk fluid take the form

$$\begin{aligned} n_0^b &= \rho_b \\ n_1^b &= r_w \rho_b \\ n_2^b &= 4\pi r_w^2 \rho_b \\ n_3^b &= \frac{4}{3} \pi r_w^3 \rho_b \end{aligned} \quad (5.18)$$

Segura et al.²⁹ previously introduced and successfully demonstrated two approaches to include intermolecular association. The first applies Wertheim's associating fluid functional as a perturbation to a reference fluid functional, while the second approach expresses the functional in a weighted fashion, using the bulk equation of state. In this work, we adopt the second method of Segura et al. so that the association contribution to the Helmholtz free energy is expressed in the following weighted form

$$\beta A^{ex,assoc}[\rho(\mathbf{r})] = \int d\mathbf{r} \Phi^{ex,assoc}[n_i(\mathbf{r})] \quad (5.19)$$

where $\Phi^{ex,assoc}[n_i(\mathbf{r})]$ is the Helmholtz free energy density due to association for the inhomogeneous fluid. This free energy density uses the bulk relations derived by Ghonasgi and Chapman,²²⁶ expressed in the weighted density form¹⁷¹

$$\Phi^{ex,assoc}[n_i(\mathbf{r})] = 4n_0\zeta \left[\ln \overline{\chi}_A(\mathbf{r}) - \frac{\overline{\chi}_A(\mathbf{r})}{2} + \frac{1}{2} \right] \quad (5.20)$$

where the vector-weighted densities are accounted for in the term $\zeta = 1 - \mathbf{n}_{v2} \cdot \mathbf{n}_{v2} / n_2^2$.

The weighted fraction of molecules at position \mathbf{r} not bonded at site A is represented by

$\overline{\chi}_A$ and is given as^{29,226}

$$\overline{\chi}_A(\mathbf{r}) = \frac{1}{1 + 2n_0\zeta \overline{\chi}_A(\mathbf{r}) \Delta^{AB}(\mathbf{r})} \quad (5.21)$$

where $\Delta^{AB}(\mathbf{r}) = 4\pi\kappa y^{hs}(\sigma_w, n_i) f_{AB}$. The geometric factor²⁹

$\kappa = 0.25(1 - \cos(\theta_c))^2 \sigma_w^2 (r_c - \sigma_w)$ accounts for the volume available for bonding

between molecules 1 and 2, $f_{AB} = \exp(\epsilon^{HB} / k_B T) - 1$ is the Mayer f -function defined in

terms of the hydrogen-bonding energy (ϵ^{HB}), and y^{hs} is an approximation of the

inhomogeneous hard sphere pair correlation function^{72,171}

$$y^{hs}(\sigma_w, n_i) = \frac{1}{1 - n_3} + \frac{\sigma_w}{2} \frac{n_2 \zeta}{2(1 - n_3)^2} + \left(\frac{\sigma_w}{2} \right)^2 \frac{n_2^2 \zeta}{18(1 - n_3)^3}. \quad (5.22)$$

The final contribution, the free energy due to the long-range attraction, is included within the mean field approximation¹⁴⁷

$$A^{ex,att}[\rho] = \frac{1}{2} \int_{|\mathbf{r}_2 - \mathbf{r}_1| > \sigma_w} d\mathbf{r}_1 d\mathbf{r}_2 u^{att}(|\mathbf{r}_2 - \mathbf{r}_1|) \times \rho(\mathbf{r}_1) \rho(\mathbf{r}_2). \quad (5.23)$$

Once the equilibrium density profile is obtained iteratively by solving eq. (5.9), the surface tension can be calculated and the hydrogen-bonding network can be evaluated.

The surface tension of the fluid is calculated from

$$\gamma = \frac{\Omega - \Omega_{bulk}}{A} \quad (5.24)$$

where Ω_{bulk} is the bulk grand potential and A is the interfacial area. The bulk grand potential is defined $\Omega_{bulk} = -pV$, where p is the pressure of the fluid and V is the solvent accessible volume. In this work, A is defined as the solvent accessible surface area, $A=4\pi R^2$, where $R = r_s + r_w$. To ensure consistency in the theory for planar symmetry, one can use the well-known sum rule for a flat wall, i.e. $\rho^+ = \beta p$, where ρ^+ is the density at contact. For a spherical wall, the sum rule is given as²³²

$$\beta \left(\frac{\delta \Omega}{\delta R} \right) = 4\pi R^2 \rho(R) \quad (5.25)$$

Combing eq. (5.24) with eq. (5.25), the sum rule can be expressed in relation to the surface tension

$$\rho(R) = \beta p + \frac{2\beta\gamma}{R} + \beta \left(\frac{\partial \gamma}{\partial R} \right)_{\mu, T} \quad (5.26)$$

where at large R , eq. (5.26) reduces to the sum rule for a flat wall.

To evaluate the hydrogen-bonding network, the fraction of molecules χ_A must be determined. We use the formalism of Wertheim's theory to obtain an iterative equation for the fraction of molecules not bonded at site A , following a similar procedure as the planar case previously done by Segura et al.^{29,186}

$$\chi_A^{i+1}(r) = \frac{1}{1 + \frac{1}{r\sigma_w} \int_{-\sigma_w}^{r+\sigma_w} r' \chi_A^i(r') \rho(r') \Delta^{AB}(r') dr'} \quad (5.27)$$

where Δ^{AB} is defined as before. In this approach, the orientation dependence of the fraction of molecules not bonded at site A is neglected. Further, Wertheim's first order perturbation theory^{4,7} neglects steric hindrances and assumes that all four association sites are available for bonding, regardless of the distance from the surface of the solute. Under these assumptions, Ghonasgi and Chapman²²⁶ derived the following equations for the fraction of molecules bonded at n sites at distance r from a hard surface:

$$\begin{aligned} \chi_0(r) &= \chi_A^4(r) \\ \chi_1(r) &= 4\chi_A^3(r)[1 - \chi_A(r)] \\ \chi_2(r) &= 6\chi_A^2(r)[1 - \chi_A(r)]^2 \\ \chi_3(r) &= 4\chi_A(r)[1 - \chi_A(r)]^3 \\ \chi_4(r) &= [1 - \chi_A(r)]^4. \end{aligned} \quad (5.28)$$

When using these expressions with theory, these fractions as a function of distance from a hard wall were found to be in very good agreement with molecular simulation.¹⁸⁶ Using these expressions, we can study how the hydrogen-bonding network changes, as a function of the distance from the surface of the solute, as the size of the solute particle is varied.

5.3 Results and discussion

For this model, four parameters are defined: the association geometric factor κ , the hydrogen-bonding energy ϵ^{HB} , the dispersion energy ϵ^{LJ} , and the diameter of the water

molecule σ_w . All parameter values selected were chosen to represent physical quantities that agree with values used previously in molecular simulation and obtained by experimental spectroscopic data for water. The same geometric factor used previously by Segura et al.²⁹ is used in this work. When determining the energy parameters, it is assumed that for ambient water around a large hard sphere solute particle, the surface tension closely resembles that of the vapor-liquid interfacial tension of water from experiment ($\gamma^\infty \approx 72 \text{ mN/m}$).²³³ In addition, the association energy is chosen so that the average number of hydrogen bonds per molecule in the bulk, $\langle N_{HB} \rangle$, agrees well with simulation and experiment ($\langle N_{HB} \rangle \approx 3.5$).^{222,234,235} Past reports of the hydrogen-bonding energy for water range from 3 to 8 kcal/mol.^{222,234,236-240} In this work, the hydrogen-bonding energy is taken to be 4.97 kcal/mol, which is equivalent to $\epsilon^{HB} / k_b = 2500 \text{ (K)}$. The dispersion energy chosen was $\epsilon^{LJ} / k_b = 253.5 \text{ (K)}$, also within the range of previous theoretical studies on water. The diameter of the water molecule, σ_w , was taken to be 2.8 Å. Table 5.1 provides a summary of the parameter values used for water in this work. All results presented and discussed below were obtained using this single set of parameters.

Table 5.1: Molecular parameters for water.

$\sigma_w \text{ (Å)}$	κ/σ_w^3	$\epsilon^{HB}/k_b \text{ (K)}$	$\epsilon^{LJ}/k_b \text{ (K)}$
2.80	1.4849E-04	2500	253.5

At ambient conditions, water is naturally near to liquid-vapor coexistence. Before elucidating the distinguishing fluid behavior at this natural state, the effect of varying solute sizes are studied at single-phase state points away from coexistence. Figure 5.4 demonstrates the density profiles of water around a solute particle of varying size at a low-density condition and at a liquid-like condition, both away from their respective saturated liquid densities. In Figure 5.4 (a), depletion effects play the dominant role in determining the structure of the fluid. Here the attractions between the solvent molecules draw the molecules away from the surface of the solute particle towards the bulk, where the molecules can experience greater nearest neighbor interactions. In contrast, Figure 5.4 (b) illustrates liquid-like ordering in the structure of the fluid at the surface, where packing effects dominate and favor density enhancement (excluded volume considerations force the solvent molecules to pack at the surface of the solute).

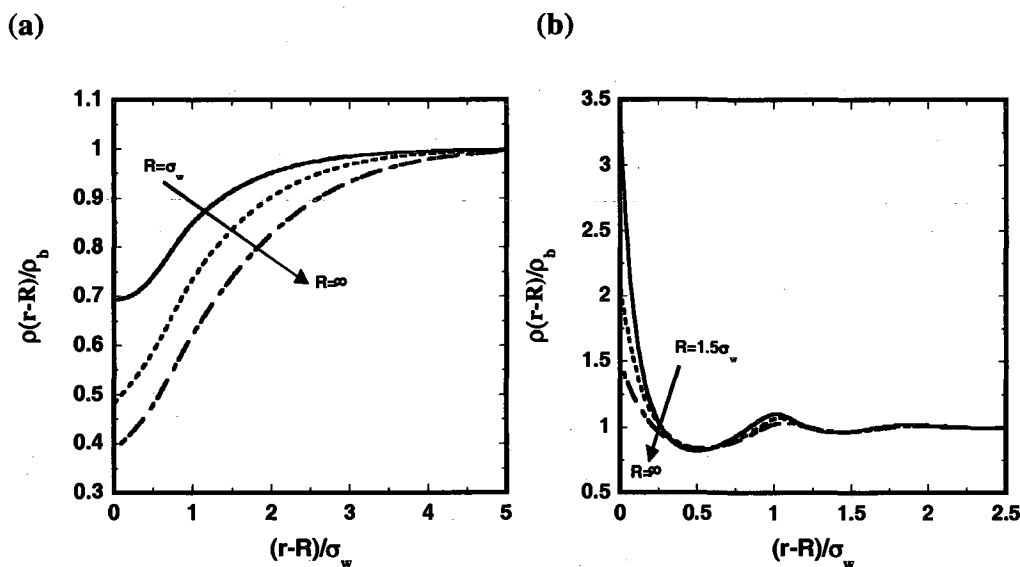


Figure 5.4: Density profiles for water around a hard sphere solute at conditions away from coexistence: (a) Low density condition at $T=400\text{K}$ ($\epsilon^{HB}/k_bT=6.250$, $\epsilon^{LJ}/k_bT=0.634$) and $\rho_b\sigma^3=0.20$ and (b) liquid-like condition $T=298\text{K}$ ($\epsilon^{HB}/k_bT=8.385$, $\epsilon^{LJ}/k_bT=0.850$) and $\rho_b\sigma^3=0.90$. The sizes of the solute particles in (a) are $R=\sigma$, 2.5σ , and ∞ (corresponding to planar wall), and in (b) $R=1.5\sigma$, 5.0σ , and ∞ , respectively.

Away from coexistence, the structure of a fluid at a surface is primarily dictated by the fluid density in the bulk – depletion (dewetting) at low densities and enhancement (wetting) at high densities. However, at coexistence conditions, either depletion or density enhancement at the surface can occur, depending on the size of the solute particle. This indicates a crossover in the free energy of the system from the changing entropic and enthalpic contributions. From the theory, the coexisting liquid and vapor densities for a given temperature, T , are found by satisfying the following criteria on the chemical potential (μ) and pressure in both the vapor (g) and liquid (l) phases:

$$\begin{cases} \mu_g = \mu_l \\ p_g = p_l \end{cases} \quad (5.29)$$

Figure 5.5 illustrates how the hydration mechanisms differ on a molecular scale from those on a macroscopic scale at coexistence conditions. From the figure, the solid curves show the density distribution of molecules around a solute particle for different solute radii. The dashed curve shows the density of molecules in contact with solute particles of different radii. For an infinitely small solute particle ($R/\sigma_w=0$), the structure of the solvent around the solute will resemble that of its bulk counterpart, and the density at the surface will therefore agree with the bulk value. This is because the solute is too small to alter the structure of the fluid around it. As the size of the solute particle increases, the fluid can reorganize around the solute and wet the surface (increasing solute size encourages more efficient packing of the water molecules around the solute), giving rise to a liquid-like structure with oscillations in the density profile. However, as illustrated by the figure, this behavior is not a monotonic function of the solute size R , and a crossover in the hydration structure of water around a solute particle induces a drying

transition as the solute size is increased. This behavior was first envisioned by Stillinger over 30 years ago,¹⁹⁹ but has just recently been confirmed by molecular simulation.^{203,205,241} At this crossover, packing effects no longer dominate the structure of the fluid. Instead, the hydration network is forced to break more hydrogen bonds as the molecules cannot reorganize themselves efficiently around the surface of the particle. Further, energetic effects begin to play a more prominent role, pulling these water molecules away from the surface where they can more effectively pack themselves. This is evident in Figure 5.5 for larger R , where the density at contact decreases and the oscillations dampen, and depletion sets in. As predicted by Stillinger¹⁹⁹, for solutes approaching the size of a planar interface ($R=\infty$), the behavior of the density of molecules at the surface resembles that at a free vapor-liquid interface. In the macroscopic limit ($R\rightarrow\infty$), the contact density continues to decrease until it reaches a value very close to the coexisting vapor density ($\rho_g\sigma_w^3=4.49 \times 10^{-4}$).

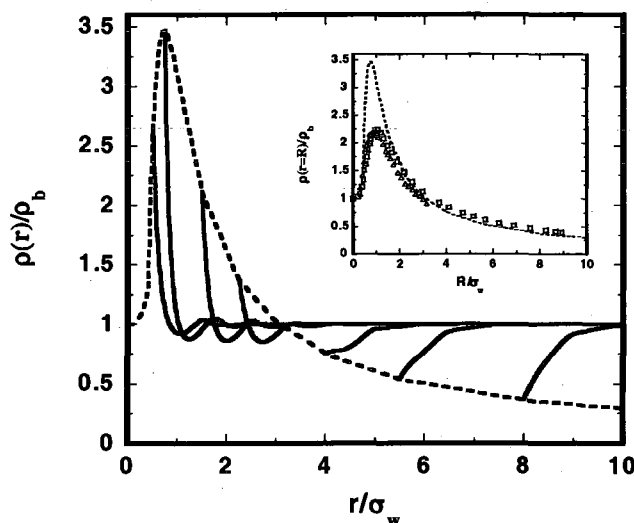


Figure 5.5: Density distribution of water around hard solutes of various sizes at coexistence conditions: $T=298 \text{ K}$ ($\epsilon^{HB}/k_bT=8.385$, $\epsilon^L/k_bT=0.850$) and $\rho_b\sigma^3=0.830$. The inset compares contact densities from this work (dashed line) with simulation and other theory (symbols). The diamonds represent data from simulations performed by Floris²⁰⁵ and squares represent predictions from revised SPT by Ashbaugh and Pratt.²⁰⁴

The inset of Figure 5.5 demonstrates how this density functional theory compares in predicting this crossover behavior with other theory and simulation. The symbols represent the contact densities at various R calculated from the revised SPT by Ashbaugh and Pratt,²⁰⁴ and simulation data from Floris.²⁰⁵ As illustrated in the inset, the density functional theory captures the correct crossover qualitatively. The quantitative difference may be attributed to the mean-field approximation used in the density functional theory to account for the attractive interactions between the water molecules. Previous studies^{242,243} for non-associating fluids have demonstrated that the mean-field approximation can be quantitatively inaccurate in comparison to simulation data. Possible techniques to improve the long-range attraction term include adopting non-mean-field prescriptions that describe the attractive interactions using the first order mean spherical approximation developed by Tang and Wu,²⁴² or using a weighted density approximation developed by Muller et al.²¹³ and demonstrated by Reddy and Yethiraj.²¹² These approaches will require additional development of the theory and will be the focus of future work. However, despite using the mean-field approximation in the work here, the DFT is still able to capture the distinguishing crossover behavior in the correct region. This is an important measure of the theory as it illustrates that this DFT is capable of correctly describing the behavior of the fluid on both the microscopic and macroscopic length scales.

Figure 5.6 shows how the surface tension varies with the size of the solute in comparison with results obtained by revised SPT by Ashbaugh and Pratt.²⁰⁴ The surface tension was calculated using eq. (5.24). Note that the calculations for surface tension are dependent on the location of the dividing surface. Here, the dividing surface is assumed

to be located at $r=R$, the radius where the density profile first becomes nonzero. The results from Figure 5.6 are at the coexistence conditions at 298 K. As shown in the figure, the results from this work are in good agreement with the results obtained by Ashbaugh and Pratt, demonstrating the correct surface tension behavior over a range of solute sizes. For smaller solute sizes, the surface tension is a rapidly varying function of R , growing linearly with the size of the solute. For larger R , the correct asymptotic behavior is predicted. The surface tension for macroscopic solutes (~ 70 mN/m) compares well with the vapor-liquid interfacial tension of water obtained from experiment²³³ (72 mN/m) and the SPC/E²⁴⁴ model for water (66 mN/m).

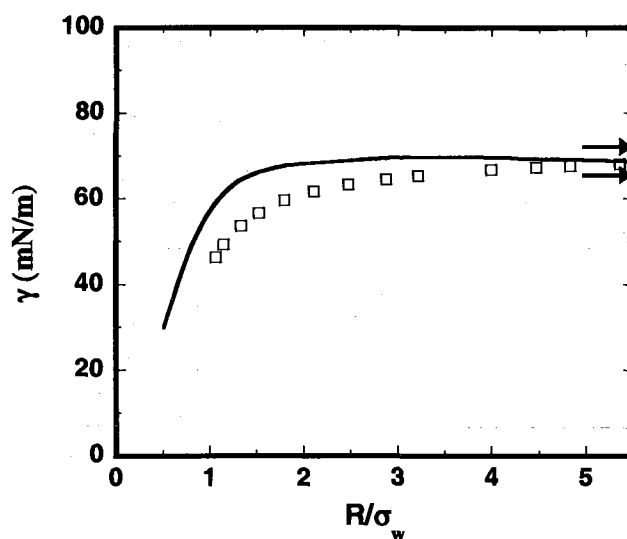


Figure 5.6: Surface tension of water near a solute of size R . The arrows at 72 mN/m and 66 mN/m represent the vapor-liquid interfacial tension of water obtained from experiment²³³ and SPC/E simulation.²⁴⁴ The solid line represents this work and the squares represent predictions from revised SPT by Ashbaugh and Pratt.²⁰⁴

As previously discussed, the structure of water around a solute particle changes as the particle size is increased, therefore suggesting the breaking of hydrogen bonds at the surface for large R . The density functional theory developed and used in this chapter can

monitor these changes in the hydration structure as the size of the solute particle changes. First, Figure 5.7 (a) illustrates how the fraction of molecules in contact with the solute particle that form n hydrogen bonds changes as a function of the size of the solute at 298 K. Note at this temperature how the majority of molecules experience a high degree of hydrogen bonding, with most molecules having 3 and 4 hydrogen bonds. At the surface, the fraction of molecules with 0, 1, and 2 bonds (X_0 , X_1 , and X_2) increases monotonically (for the sizes considered) with increasing solute size R , whereas the fraction of molecules bonded 4 times (X_4) decreases monotonically with increasing R . As one might expect, the fraction of molecules bonded 3 times (X_3) initially benefits from the hydrogen bonds broken from the molecules with 4 hydrogen bonds, but for very large R , lower degrees of surface curvature force these molecules to also give up hydrogen bonds.

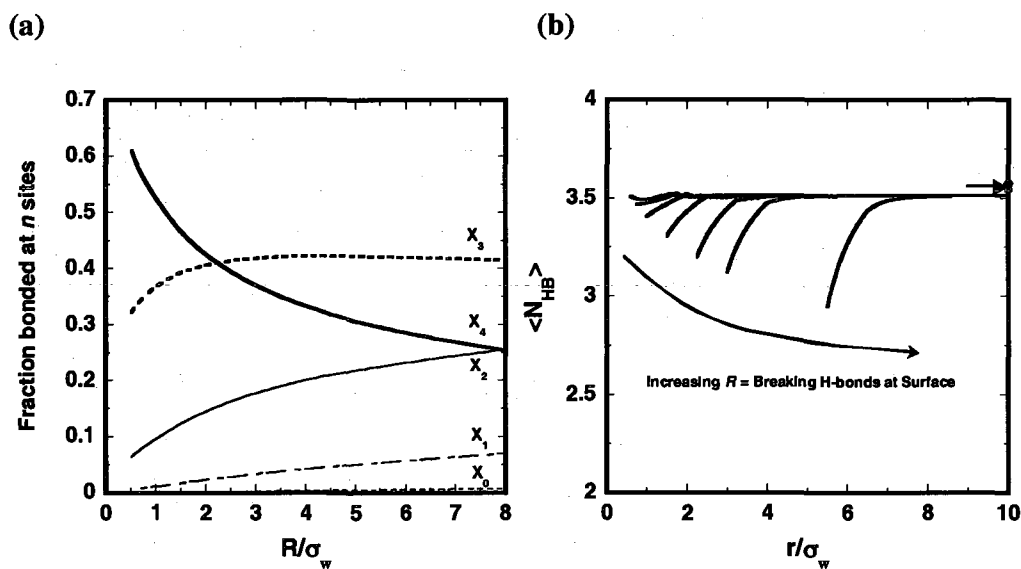


Figure 5.7: (a) Fraction of molecules in the monomer state (X_0) through the fraction of molecules with the maximum allowable bonds (X_4) for different size solutes at $T=298$ K. (b) Average number of hydrogen bonds per molecule $\langle N_{HB} \rangle$ at $T=298$ K for different size solutes as a function of the position in the fluid. The arrow and symbols refer to $\langle N_{HB} \rangle$ obtained from experiments by Luck²³⁴ and Soper et al.,²³⁵ and from TIP4P simulations for water by Jorgensen and Madura.²²²

Similarly, the disruption of the hydrogen-bond network (from increasing R) that leads to an increase in the number of molecules with fewer hydrogen bonds is also quantified in Figure 5.7 (b). For a very small solute particle ($R=0.1\sigma_w$) the hydrogen-bonding pattern, and thus the average number of hydrogen bonds, $\langle N_{HB} \rangle$, near the surface is very similar to that in the bulk. However, consistent with Figure 5.7 (a), near larger solutes hydrogen bonds are lost. This is due to the solute extending a surface with a lower degree of curvature for larger R , thus making it difficult for the molecules adjacent to the surface to maintain their hydrogen-bonding network. As a result, hydrogen bonds are broken at the surface of larger solutes. These results are in qualitative agreement with molecular simulations done by Predota et al.²⁴⁵ In addition, the results presented here indicate the average number of bonds in the bulk obtained at 298 K to be $\langle N_{HB} \rangle = 3.51$. This result is in very good agreement with the experimental values $\langle N_{HB} \rangle \approx 3.55$ obtained from IR data by Luck,²³⁴ and $\langle N_{HB} \rangle \approx 3.57$ from neutron diffraction studies performed by Soper et al.²³⁵ Jorgensen and Madura²²² also report the average number of bonds for water at ambient conditions to be $\langle N_{HB} \rangle \approx 3.59$ from their TIP4P simulation model for water.

While being able to correctly describe hydration structure and identifying a length scale associated with maximum hydrophobicity is important, it is also essential to have a model that can quantify the effects of temperature on the hydrophobicity of the system. Since hydrogen bonding is a function of temperature and is incorporated into this model, this DFT can capture temperature effects on the behavior of the system. This is important as hydrophobic interactions are temperature dependent and can therefore affect the function and stability of aqueous solutions and biological structures. Figure 5.8

demonstrates how temperature affects the contact densities, and additionally, how these temperature signatures are affected according to changing solute size. From the figure, the curves are very similar to each other qualitatively. Temperature effects are observed as the contact densities decrease with increasing temperature, and also the length associated with the maximum of each curve decreases with increasing temperature. Some theories, such as the original SPT, fail in describing such temperature dependencies. Ashbaugh and Pratt²⁰⁴ recently presented a revised version of SPT that corrects for this problem and gives results qualitatively consistent with the results presented here.

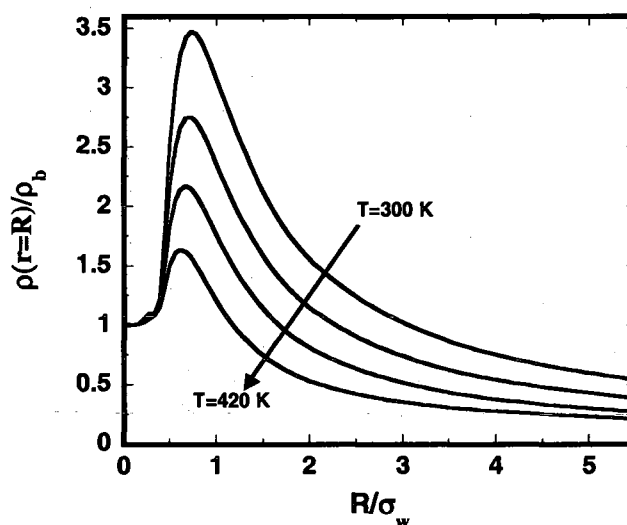


Figure 5.8: Contact density curves at $T=300\text{ K}$, 340 K , 380 K and 420 K , respectively, for water around solutes of different size. Contact densities are along the liquid saturation curve for each respective temperature.

Figure 5.9 illustrates the effect of increasing the temperature on the hydrogen-bonding network. As one might expect, as the temperature of the system is raised, more hydrogen bonds are broken and more molecules with fewer bonds are present in the fluid.

This is evident when comparing Figure 5.9 (a), which is at its saturated liquid density at $T=380$ K, to Figure 5.7 (a), which is at its saturated liquid density at $T=298$ K. Note the increased fraction of molecules present at the surface with 0, 1, and 2 bonds from before. As expected, Figure 5.9 (b) is qualitatively similar to Figure 5.7 (b), again demonstrating a lower average bonding per molecule for larger solute particles. However, the average number of hydrogen bonds per molecule in the bulk decreases from $\langle N_{HB} \rangle = 3.51$ to $\langle N_{HB} \rangle = 2.64$ as a result of the increased temperature.

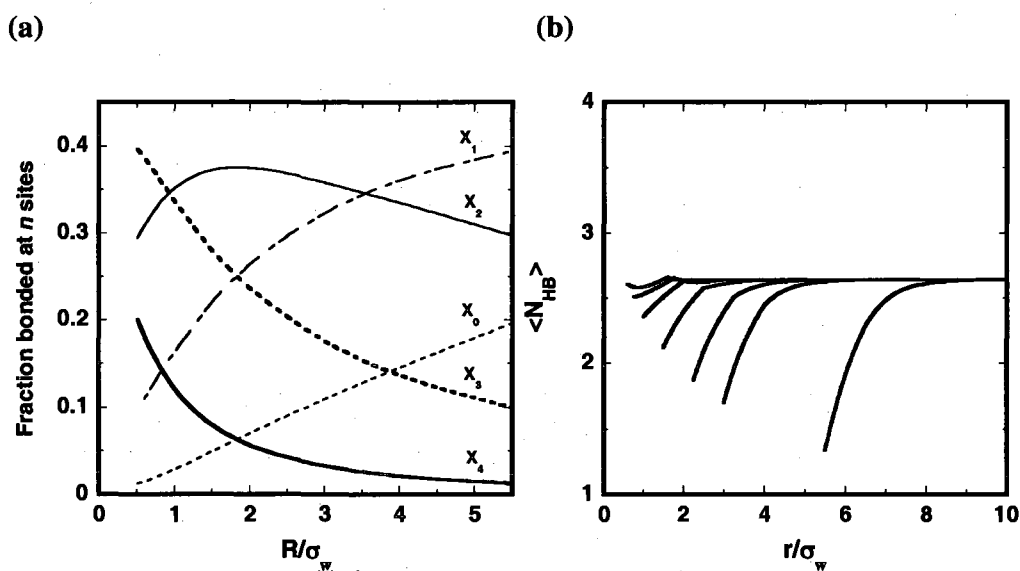


Figure 5.9: (a) Fraction of molecules in the monomer state (X_0) through the fraction of molecules with the maximum allowable bonds (X_4) for different size solutes at $T=380$ K. (b) Average number of hydrogen bonds per molecule $\langle N_{HB} \rangle$ at $T=380$ K for different size solutes as a function of the position in the fluid.

5.4 Conclusions

In this work, we have presented a density functional theory that captures the anomalous behaviors associated with the structure of water around a hydrophobic solute. The density functional theory is based on Rosenfeld's formalism for hard spheres and further accounts for hydrogen-bonding interactions by applying the same weighting

functions to Wertheim's bulk first-order perturbation theory. Attractive intermolecular interactions are treated through a mean-field approximation.

Away from coexistence conditions, the fluid displays depletion from the solute at lower densities. At high densities, packing effects dominate and an ordered, liquid-like structure is displayed. Under conditions where the liquid density coexists with its vapor (water at ambient conditions), a crossover occurs in the structure of the solvent at the surface as predicted by Stillinger.¹⁹⁹ For small solutes, an ordered, liquid-like structure is observed; however, for larger macroscopic solutes, more hydrogen bonds are broken at the surface and molecules are pushed away from the surface toward the bulk, leading to a drying transition. The DFT can successfully describe the surface tension with varying solute size, capturing the rapidly varying behavior for small solutes and asymptotic behavior for large solutes in quantitative agreement with the vapor-liquid interfacial tension of water. The incorporation of hydrogen-bonding interactions into the theory has several advantages. First, the theory can characterize the hydrogen-bonding network and the changes it experiences when placed near different size solutes. Further, since hydrogen bonding and hydrophobic interactions are temperature dependent, the theory can capture the effects of temperature on the hydrogen-bonding structure of the fluid and further the hydrophobicity of the system.

The density functional theory presented in this chapter for this fundamental case remains to be demonstrated in elucidating the role of hydrophobic effects in more complex cases. Recently, Tripathi and Chapman^{33,34} developed a polyatomic density functional theory, interfacial statistical associating fluid theory (*i*-SAFT), which retains the form of the atomic DFT presented in this work. The theory *i*-SAFT, in its short

existence, has proven to provide an accurate modeling framework for studying polymeric fluids at considerably moderate computational expense.^{32-34,165,192-196} Many of the same ideas manifested in this work can be transferred to study the role of hydrophobic effects in macromolecular fluids, where molecular size and shape, hydrogen-bonding forces, and intramolecular interactions affect the strength of hydrophobic interactions. Examples of such intramolecular processes include the formation of micelles in surfactant solutions and protein folding.

CHAPTER **6****Microstructure and depletion forces in polymer-colloid mixtures from an *i*SAFT DFT**

6.1 Introduction

Colloidal particles dispersed in dilute or concentrated polymer solution represent an important area of research today, as these systems are encountered and play an integral role in many everyday processes and products. Nanocolloid-polymer systems have attracted interests from a wide array of disciplines, ranging from biological and medical applications (drug delivery and medical diagnostics) to the design of materials with specific optical, electronic and mechanical properties (polymer-particle nanocomposites and self-healing materials).²⁴⁶⁻²⁵⁰ Despite the multidisciplinary interests that surround these systems, many challenges still remain for both experimentalists and theoreticians to understand the interplay of forces and microstructure with the multiple length scales and broad parameter space involved. The interaction between colloidal particles in polymer solution or melt, as well as the surrounding fluid structure, is dictated by a number of molecular parameters, including the particle/polymer size ratio, polymer chain length and concentration, and the nature of the polymer-particle interaction.

An important starting point to understanding such phenomena is to consider the simplest and most fundamental model of a colloidal suspension. The fundamental model

consists of a nonadsorbing polymer solution, characterized solely by hard-core repulsive interactions between all species (between colloidal particles and polymer molecules; solvent molecules are typically much smaller in size and are generally not considered explicitly). Although purely entropic in nature, the behavior of such a system is very rich and complex, dependent on the particle/polymer segment size ratio, polymer chain length, and the concentration of the polymer solution. At low polymer concentrations, molecules are depleted in the vicinity of an impenetrable colloidal particle. The range of this depletion layer exhibits two different length scales, decreasing with increasing polymer concentration. In the dilute regime, the depletion layer thickness is roughly on the order of the polymer radius of gyration R_g ; in the semidilute regime, the depletion layer thickness converges to a value of one polymer segment (one bond length). As the polymer concentration reaches the melt regime, polymer molecules will accumulate at the surface of the colloidal particles due to packing effects. Quantifying such depletion and packing effects have provided valuable insight into understanding the effective interactions between colloidal particles in polymer-particle mixtures. As two particles in polymer solution approach each other at dilute and semidilute concentrations, the chain molecules are expelled from the region between the two particles. When this occurs, an imbalance in the pressure exerted by the polymers on the outer walls of the interacting particles induces an effective attraction between the particles in solution. Such attraction is responsible for destabilization and flocculation of a colloidal suspension. However, at higher concentrations where packing effects play a significant role, a high value of osmotic pressure hinders the expulsion of chains from the region between the interacting

particles. In such cases, a repulsive barrier can form and potentially lead to restabilization of the colloidal dispersion.

Asakura and Oosawa^{15,16} recognized the importance of understanding such polymer-mediated forces by developing the first theory for athermal polymer-colloid suspensions. The Asakura-Oosawa (AO) theory^{15,16} is a geometry-based model that makes several simplifications, yet still addresses the entropy induced depletion attraction between two hard spheres dissolved in a polymer solution. First the polymer chains are treated as hard spheres in their interactions with the large colloids, therefore ignoring the internal structure of the chain. In addition, all polymer-polymer interactions and correlations are neglected; therefore the polymer chains are represented as ideal gas particles. Despite its simplicity, the AO theory captures the depletion force between two colloids in fair agreement with simulation and experiments in dilute solutions. The downfall of the theory is that the polymer-mediated potential of mean force (PMF) predicted increases monotonically with increasing polymer concentration and is therefore always attractive and fails to reproduce a repulsive barrier between colloidal particles at high polymer concentrations.

A number of investigations have been performed trying to resolve the shortcomings of the AO theory using theoretical approaches such as scaling theory,²⁵¹⁻²⁵⁵ mean-field approximations,²⁵⁶⁻²⁵⁹ self-consistent field theory (SCFT),^{260,261} integral equation theory (IET),^{23-25,262,263} and simulation techniques.²⁶⁴⁻²⁶⁹ Despite the enormous amount of work done in this area, even the more sophisticated approaches such as SCFT and IET still suffer from limitations. SCFT has been applied to compute depletion forces in dilute and semidilute polymer solutions, yet is not applicable to studying denser polymer fluids

where local density fluctuations and liquid-like ordering become important. Polymer Reference Interaction Site Model (PRISM) IET can provide accurate descriptions of fluids at a microscopic level. However it has been shown to be very sensitive to the particular closures employed, and to give unreliable results (both quantitatively and qualitatively) at moderate to high polymer densities and for cases when the colloid size is much larger than the radius of gyration of the polymer.^{23-26,180} Furthermore, considerations of future problems that entail complex intermolecular interactions pose significant challenges and difficulties for even the more sophisticated theoretical approaches such as SCFT and IET. Here SCFT does not retain the segment level details needed to describe such interactions, and standard closure approximations employed in IET cannot properly capture such non-hard-core phenomena.^{27,262} While simulations can follow more involved intermolecular interactions, they can often become computationally expensive, especially for polymer-particle mixtures where a wide range of particle size ratios and length scales are involved in the problem. As a result, applications are often limited to either the nanoparticle limit (where the polymer radius of gyration R_g is much larger than the particle radius R_c) or to the colloid limit (where the colloid is much larger than the polymer radius and can be represented by a planar wall). In addition to the above limitations, conflicting results have arisen between the different theoretical techniques. For example, in the nanoparticle regime, results from de Gennes²⁵² and Tuiner et al.^{270,271} predict that the colloid-colloid second virial coefficient remains positive under dilute polymer conditions (ideal chains), in disagreement to field theoretic²⁵⁶ and PRISM IET^{25,262} predictions. Thus, describing even this fundamental model presents a major challenge to all theories and much is left to be understood.

Recently density functional theory^{180,272-274} has emerged as a powerful tool to investigate the microstructure and interaction in polymer-particle mixtures, and can provide valuable insight to the understanding of polymer-colloid solutions. Density functional theory (DFT) is a tool with a statistical mechanics foundation that can adopt complex segment level interaction force descriptions, while retaining the microscopic details of a macroscopic system at a computational expense significantly lower than simulation methods. Density functional theory has been applied to calculate the hard chain distribution near flat hard walls^{34,275} and spherical hard particles²⁷⁶ in good agreement with simulation data. Calculating the colloidal forces between two planar walls is straightforward within a DFT framework; however, calculating the force between spheres is a more challenging problem due to the curvature effects and multidimensional density distribution of the polymers around the colloidal particles. Within density functional theory, there are several prescriptions that can be used to calculate the polymer-mediated forces between interacting particles. Patel and Egorov¹⁸⁰ used a two-dimensional density functional theory to calculate the interaction between two dilute colloidal particles in an athermal polymer solution. This brute force approach is very accurate in comparison to simulation studies, but comes at high computational cost. Other methods attempt to circumvent the numerical challenges of the multidimensional calculations via the Kirkwood superposition approximation^{277,278} or the Derjaguin approximation.²⁷⁹ The superposition approximation was found to be very accurate when calculating colloidal interactions in a hard-sphere solvent;²⁸⁰⁻²⁸² however, the accuracy of the method breaks down rapidly as the polymer chain length is increased.^{180,272} The Derjaguin approximation relates the forces between two colloid particles to that between

two planar surfaces but has been proven unreliable for the calculation of depletion forces between two particles in both hard-sphere and polymeric fluids.^{274,283-285} Recently, a method of investigating the depletion forces between colloidal particles via an insertion-route has proven valuable and accurate. The approach, developed by Roth et al.,²⁸⁵ is based on the potential distribution theorem²³² and links the depletion force between two colloidal particles to the density profile of solvent around a single isolated particle. The insertion-route approach avoids the numerical challenges and limitations of the aforementioned techniques. The method has been applied successfully within density functional theory to calculate the depletion potential in athermal binary hard-sphere mixtures,²⁸⁵ and recently to polymer-colloid mixtures.²⁷²⁻²⁷⁴

All the aforementioned DFT work^{180,272-274} on polymer-colloid systems are formulated on the basis of Wertheim's thermodynamic perturbation theory (TPT1).⁴⁻⁷ Each express the inhomogeneous free energy due to excluded-volume effects and chain connectivity by using the free energy of a homogeneous (bulk) fluid evaluated at a weighted density. In such DFTs, the weighted free energy due to chain connectivity only accounts for indirect intramolecular interactions due to volume exclusion. Therefore the intramolecular interactions due to the direct bonding potential are accounted for in the ideal free energy functional, which is based on the multi-point molecular density $\rho_M(\mathbf{R})$, where $\mathbf{R}(\equiv \{\mathbf{r}_i\}, i = 1, m)$ denotes the positions of all the segments on a polymer chain of m segments, as given by Woodward.^{185,286} The many body nature of the molecular density and the bonding constraints result in m^{th} order implicit integral equations for the density profile, which can make computations demanding for long chains. Recently, another version of DFT based on TPT1, labeled interfacial (or inhomogeneous) statistical

associating theory (*i*SAFT), was developed by Tripathi and Chapman^{33,34} using a segment-based formalism. This version of DFT offers accuracy comparable to the molecular based theories, but at a computational expense of an atomic DFT. The objective of this work is to demonstrate the applicability of *i*SAFT to describe the phenomena associated with polymer-particle mixtures through comparisons with model systems from simulations. *i*SAFT has already been successfully applied to study polymer melts, solutions, and blends confined in slit-like pores by Tripathi and Chapman,^{33,34} and it was also extended to real systems to calculate interfacial properties of *n*-alkanes and polymers by Dominik et al.¹⁶⁵ Recently, a modified version of *i*SAFT was introduced by Jain et al.³² that is better suited for complex heteronuclear systems and performs well for a wide variety of systems, including lipid and copolymer molecular systems^{32,192} and tethered polymers.¹⁹³ Although this work compares with simulations involving homonuclear polymers, we employ the *i*SAFT version by Jain et al.³² because of its potential to investigate a wider range of systems such as biomaterials, polyelectrolytes, surfactant-like molecules, and other molecules possessing heteronuclear architectures. Such will be the focus of future work.

In the next section, the *i*SAFT approach is presented and discussed. In section 6.3, we present a comprehensive study for nonadsorbing polymer-particle mixtures, discussing the structure of polymer segments near an isolated colloidal particle, the effective interactions between two particles in polymer solution (adopting the insertion-route developed by Roth et al.²⁸⁷), and the colloid-colloid osmotic second virial coefficient. *i*SAFT predictions are shown to be in excellent agreement with simulation data and to quantify the influence of polymer chain length, polymer solution density, and

the colloid/polymer segment size ratio on the behavior and stability of the colloidal dispersion. In addition, a preliminary investigation for an attractive polymer-particle system is presented and discussed. Here, the packing of polymer molecules at the surface of a particle, and hence the depletion forces between interacting particles, are no longer dictated by entropic effects exclusively, but also by enthalpic effects. Finally, concluding remarks and future work are discussed in section 6.4.

6.2 *i*SAFT model

In this work, we consider spherical colloidal particles in the one and two particle limit in a polymer solution composed of fully flexible polymer chains. Each chain consists of m tangentially bonded segments. The starting point of the density functional theory is the development of an expression for the grand free energy, Ω , as a functional of the equilibrium polymer density profile $\rho(\mathbf{r})$. From this, the desired thermodynamic and structural properties of the system can be determined. Working in the grand canonical ensemble, which has fixed volume (V), temperature (T), and chemical potential (μ) of the molecules, the grand free energy, Ω , of a polymer chain composed of m segments, can be related to the Helmholtz free energy functional $A[\rho(\mathbf{r})]$ through the Legendre transform,¹³

$$\Omega[\rho_i(\mathbf{r})] = A[\rho_i(\mathbf{r})] - \sum_{i=1}^m \int d\mathbf{r}' (\mu_i - V_i^{ext}(\mathbf{r}')) \rho_i(\mathbf{r}') \quad (6.1)$$

where $\rho_i(\mathbf{r})$ denotes the density of segment i on the polymer chain at position \mathbf{r} , μ_i is the chemical potential of segment i , and $V_i^{ext}(\mathbf{r})$ is the external field acting on segment i . The

equilibrium density profile of the segments is obtained by minimizing the grand potential of the system with respect to the density of segments

$$\frac{\delta\Omega[\rho_i(\mathbf{r})]}{\delta\rho_i(\mathbf{r})} = 0 \quad \forall i = 1, m \quad (6.2)$$

The total Helmholtz free energy functional can be decomposed into an ideal and excess contribution,

$$A[\rho_i(\mathbf{r})] = A^{id}[\rho_i(\mathbf{r})] + A^{ex,hs}[\rho_i(\mathbf{r})] + A^{ex,chain}[\rho_i(\mathbf{r})] + A^{ex,att}[\rho_i(\mathbf{r})] \quad (6.3)$$

where the excess contribution consists of changes in the free energy due to excluded volume (*hs*), chain connectivity (*chain*), and long-range attraction (*att*), over the ideal gas state of the atomic mixture.

6.2.1 Free energy functionals

The ideal gas functional is known exactly from statistical mechanics

$$\beta A^{id}[\rho_i(\mathbf{r})] = \int d\mathbf{r} \sum_{i=1}^m \rho_i(\mathbf{r}) [\ln \rho_i(\mathbf{r}) - 1] \quad (6.4)$$

where the temperature-dependent term (the de Broglie wavelength λ) has been dropped since it is not density dependent and hence does not affect the structure or thermodynamics of the fluid. The inverse temperature is represented by $\beta = 1/k_b T$, where k_b is the Boltzmann's constant. The free energy due to excluded volume/short range repulsion, $A^{ex,hs}$, is calculated using Rosenfeld's fundamental measure theory (FMT),^{155,156} postulated to have the form

$$\beta A^{ex,hs}[\rho_i(\mathbf{r})] = \int d\mathbf{r} \Phi^{ex,hs}[n_\alpha(\mathbf{r})] \quad (6.5)$$

where $\Phi^{ex,hs}[n_\alpha(\mathbf{r})]$ is the excess Helmholtz free energy density due to the hard core interactions. $\Phi^{ex,hs}[n_\alpha(\mathbf{r})]$ is assumed to be a function of only the system averaged fundamental geometric measures, $n_\alpha(\mathbf{r})$, of the particles, given by

$$n_\alpha(\mathbf{r}) = \sum_{i=1}^m n_{\alpha,i}(\mathbf{r}) = \sum_{i=1}^m \int \rho_i(\mathbf{r}') \omega_i^{(\alpha)}(\mathbf{r} - \mathbf{r}') d\mathbf{r}' \quad (6.6)$$

where $\alpha=0, 1, 2, 3, V_1, V_2$, representative of the scalar and vector-weighted densities.

The weight functions $\omega_i^{(\alpha)}$ characterize the geometry of the segments. The three independent functions are¹⁵⁵

$$\omega_i^{(2)} = \delta(R_i - r); \quad \omega_i^{(3)} = \Theta(R_i - r); \quad \omega_i^{(V_2)} = \frac{\mathbf{r}}{r} \delta(R_i - r). \quad (6.7)$$

whereas the remaining functions are proportional to the above geometric functions¹⁵⁵

$$\omega_i^{(0)} = \frac{\omega_i^{(2)}}{4\pi R_i^2}; \quad \omega_i^{(1)} = \frac{\omega_i^{(2)}}{4\pi R_i}; \quad \omega_i^{(V_1)} = \frac{\omega_i^{(V_2)}}{4\pi R_i}. \quad (6.8)$$

In eq. (6.7), $\delta(r)$ is the Dirac delta function, $\Theta(r)$ is the Heaviside step function and $R_i(=\sigma_i/2)$ is the radius of segment i on the chain. In the FMT formalism, $\Phi^{ex,hs}[n_\alpha(\mathbf{r})]$ has the form

$$\Phi^{ex,hs}[n_\alpha(\mathbf{r})] = -n_0 \ln(1 - n_3) + \frac{n_1 n_2 - \mathbf{n}_{V_1} \cdot \mathbf{n}_{V_2}}{1 - n_3} + \frac{n_2^3 - 3n_2 \mathbf{n}_{V_2} \cdot \mathbf{n}_{V_2}}{24\pi(1 - n_3)^2}. \quad (6.9)$$

The free energy due to the long-range attraction can be included within the mean field approximation¹⁴⁷

$$A^{ex,att}[\rho_i(\mathbf{r})] = \frac{1}{2} \sum_{i=1}^m \sum_{j=1}^m \int_{|\mathbf{r}_2 - \mathbf{r}_1| > \sigma_{ij}} d\mathbf{r}_1 d\mathbf{r}_2 u_{ij}^{att}(|\mathbf{r}_2 - \mathbf{r}_1|) \rho_i(\mathbf{r}_1) \rho_j(\mathbf{r}_2). \quad (6.10)$$

Previous studies^{179,288} have demonstrated that using the mean field approximation for polymeric fluids to treat for attractive interactions performs very well in comparison with simulation data. Attractive interactions are neglected for the majority of this work, but are included in a preliminary study for attractive polymer-particle mixtures in section 6.3.4.

The free energy chain functional, $A^{ex,chain}$, of m segments is derived from Wertheim's thermodynamic perturbation theory (TPT1)⁴⁻⁷ as the polyatomic system is formed from a mixture of associating atomic spheres in the limit of complete association. The association free energy functional was originally proposed by Chapman¹² on the basis of TPT1

$$\beta A^{ex,assoc}[\rho_i] = \int d\mathbf{r}_1 \sum_{i=1}^m \rho_i(\mathbf{r}_1) \sum_{A \in \Gamma^{(i)}} \left(\ln X_A^i(\mathbf{r}_1) - \frac{X_A^i(\mathbf{r}_1)}{2} + \frac{1}{2} \right). \quad (6.11)$$

The summations, from left to right, are over all the segments and over all the association sites on segment i , respectively, where $\Gamma^{(i)}$ is the set of all the associating sites on segment i . χ_A^i is the fraction of segments of type i that are not bonded at site A , given by^{12,29}

$$\chi_A^i(\mathbf{r}_1) = \frac{1}{1 + \int d\mathbf{r}_2 \chi_B^{i'}(\mathbf{r}_2) \Delta^{ii'}(\mathbf{r}_1, \mathbf{r}_2) \rho_{i'}(\mathbf{r}_2)}, \quad (6.12)$$

where i' denotes the neighboring segment that will bond to segment i , and

$\Delta^{ii'}(\mathbf{r}_1, \mathbf{r}_2) = KF^{ii'}(\mathbf{r}_1, \mathbf{r}_2)y^{ii'}(\mathbf{r}_1, \mathbf{r}_2)$. Here K is a geometric constant that accounts for the volume available for bonding between segments, and

$F^{ii'}(\mathbf{r}_1, \mathbf{r}_2) = [\exp(\beta\epsilon_0 - \beta v_{bond}^{ii'}(\mathbf{r}_1, \mathbf{r}_2)) - 1]$ represents the association Mayer f -function. For tangentially bonded spheres, the bonding potential is given as

$\exp[-\beta v_{bond}^{ii}(\mathbf{r}_1, \mathbf{r}_2)] = \frac{\delta(|\mathbf{r}_1 - \mathbf{r}_2| - \sigma^{ii})}{4\pi(\sigma^{ii})^2}$. The cavity correlation function $y^{ii}(\mathbf{r}_1, \mathbf{r}_2)$ is

approximated by

$$y^{ii}(\mathbf{r}_1, \mathbf{r}_2) = (y^{ii,bulk} \{\bar{\rho}_j(\mathbf{r}_1)\} \cdot y^{ii,bulk} \{\bar{\rho}_j(\mathbf{r}_2)\})^{1/2} \quad (6.13)$$

where $y^{ii,bulk}$ represents the bulk cavity correlation function⁷² evaluated at contact and

$\bar{\rho}_j(\mathbf{r}_1)$ represents the weighted density of segment j at position \mathbf{r}_1 . In this work, the

simple weighting is used

$$\bar{\rho}_j(\mathbf{r}_1) = \frac{3}{4\pi\sigma_j^3} \int_{|\mathbf{r}_1 - \mathbf{r}_2| < \sigma_j} d\mathbf{r}_2 \rho_j(\mathbf{r}_2) \quad (6.14)$$

where σ_j represents the diameter of segment j on the chain.

Originally, the chain functional in *i*SAFT was derived by taking eq. (6.11), and forcing the complete bonding limit ($\chi_A^i(\mathbf{r}) \rightarrow 0$ as the bonding energy $\epsilon_0 \rightarrow \infty$) while using the approximation that each site undergoes its complete bonding limit at the same rate, i.e. $\chi_B^i(\mathbf{r}_2) \approx \chi_A^i(\mathbf{r}_1)$.^{33,34} This assumes that all segments are identical and, thus, the approximation is most accurate for homonuclear chains. Recently, a modified version of *i*SAFT was introduced by Jain et al.³² This version of *i*SAFT solves self-consistently for the $\chi_A^i(\mathbf{r})$ and the segment densities to minimize the free energy. Thus, the model is accurate for heteronuclear molecules. The infinite bonding energy is an additive contribution to the chemical potential that is identical in the bulk and interface. Therefore, the $K \exp(\beta\epsilon_0)$ in the expressions for $\Delta(\mathbf{r}_1, \mathbf{r}_2)$ can be neglected. All the functional derivatives are essential in solving the Euler-Lagrange equations (from eq. (6.2)), which give the density profile. These expressions are presented below.

6.2.2 Free energy functional derivatives

Recalling eq. (6.2), to solve for the density profile, we obtain the following Euler-Lagrange equation

$$\frac{\delta\beta A^{id}[\rho_i]}{\delta\rho_j(\mathbf{r})} + \frac{\delta\beta A^{ex,hs}[\rho_i]}{\delta\rho_j(\mathbf{r})} + \frac{\delta\beta A^{ex,chain}[\rho_i]}{\delta\rho_j(\mathbf{r})} + \frac{\delta\beta A^{ex,att}[\rho_i]}{\delta\rho_j(\mathbf{r})} = \beta(\mu_j - V_j^{ext}(\mathbf{r})) \quad (6.15)$$

The functional derivatives are given as

$$\frac{\delta\beta A^{id}}{\delta\rho_j(\mathbf{r})} = \ln \rho_j(\mathbf{r}) \quad (6.16)$$

$$\frac{\delta\beta A^{ex,hs}}{\delta\rho_j(\mathbf{r})} = \int d\mathbf{r}_1 \frac{\delta\Phi^{ex,hs}[n_\alpha(\mathbf{r}_1)]}{\delta\rho_j(\mathbf{r})} \quad (6.17)$$

$$\frac{\delta\beta A^{ex,att}}{\delta\rho_j(\mathbf{r})} = \sum_{i=1}^m \int_{|\mathbf{r}-\mathbf{r}_1|>\sigma_{ij}} d\mathbf{r}_1 \beta u_{ij}^{att}(|\mathbf{r}-\mathbf{r}_1|) \rho_i(\mathbf{r}_1) \quad (6.18)$$

To arrive at the chain functional derivative, we follow Jain et al.'s³² approach by manipulating the inhomogeneous association chemical potential (association functional derivative) with the law of mass action (eq. (6.12)) and further applying the limit of complete association ($\varepsilon_0 \rightarrow \infty$), thereby giving³²

$$\frac{\delta\beta A^{ex,chain}[\rho_i]}{\delta\rho_j(\mathbf{r})} = \sum_{A \in \Gamma^{(j)}} \ln \chi_A^j(\mathbf{r}) - \frac{1}{2} \sum_{k=1}^m \sum_{k'}^{\{k'\}} \int \rho_k(\mathbf{r}_1) \frac{\delta \ln y^{kk',bulk}(\mathbf{r}_1)}{\delta\rho_j(\mathbf{r})} d\mathbf{r}_1 \quad (6.19)$$

where $\{k'\}$ is the set of all segments bonded to segment k . Here stoichiometry is enforced via the term χ_A^j . For the work considered here, each chain is comprised of m segments, with each end segment having one bonding site (A), and each middle segment

having two bonding sites (A and B), respectively. For each segment j , the fractions χ_A^j and χ_B^j are given as³²

$$\chi_A^j(\mathbf{r}_j) = \frac{1}{\exp(\beta(\mu_{j+1} + \mu_{j+2} + \dots + \mu_m)) \int \dots \int d\mathbf{r}_{j+1} d\mathbf{r}_{j+2} \dots d\mathbf{r}_m \exp[D_{j+1}(\mathbf{r}_{j+1}) - \beta V_{j+1}^{ext}(\mathbf{r}_{j+1}) + D_{j+2}(\mathbf{r}_{j+2}) - \beta V_{j+2}^{ext}(\mathbf{r}_{j+2}) + \dots + D_m(\mathbf{r}_m) - \beta V_m^{ext}(\mathbf{r}_m)] \Delta^{(j,j+1)}(\mathbf{r}_j, \mathbf{r}_{j+1}) \dots \Delta^{(m-1,m)}(\mathbf{r}_{m-1}, \mathbf{r}_m)} \quad (6.20)$$

and

$$\chi_B^j(\mathbf{r}_j) = \frac{1}{\exp(\beta(\mu_1 + \mu_2 + \dots + \mu_{j-1})) \int \dots \int d\mathbf{r}_1 d\mathbf{r}_2 \dots d\mathbf{r}_{j-1} \exp[D_1(\mathbf{r}_1) - \beta V_1^{ext}(\mathbf{r}_1) + D_2(\mathbf{r}_2) - \beta V_2^{ext}(\mathbf{r}_2) + \dots + D_{j-1}(\mathbf{r}_{j-1}) - \beta V_{j-1}^{ext}(\mathbf{r}_{j-1})] \Delta^{(1,2)}(\mathbf{r}_1, \mathbf{r}_2) \Delta^{(2,3)}(\mathbf{r}_2, \mathbf{r}_3) \dots \Delta^{(j-1,j)}(\mathbf{r}_{j-1}, \mathbf{r}_j)} \quad (6.21)$$

where $D_j(\mathbf{r})$ is given by

$$D_j(\mathbf{r}) = \frac{1}{2} \sum_{k=1}^m \sum_{k'}^{\{k\}} \int \rho_k(\mathbf{r}_1) \frac{\delta \ln y^{kk',bulk}(\mathbf{r}_1)}{\delta \rho_j(\mathbf{r})} d\mathbf{r}_1 - \frac{\delta \beta A^{ex,hs}}{\delta \rho_j(\mathbf{r})} - \frac{\delta \beta A^{ex,att}}{\delta \rho_j(\mathbf{r})} \quad (6.22)$$

6.2.3 Equilibrium density profile and grand free energy

To obtain the equilibrium density profile, the functional derivatives of the free energies are substituted into the Euler-Lagrange (eq. (6.15)) to give

$$\ln \rho_j(\mathbf{r}) + \frac{\delta \beta A^{ex,hs}}{\delta \rho_j(\mathbf{r})} + \frac{\delta \beta A^{ex,att}}{\delta \rho_j(\mathbf{r})} + \sum_{A \in \Gamma^j} \ln \chi_A^j(\mathbf{r}) - \frac{1}{2} \sum_{k=1}^m \sum_{k'}^{\{k\}} \int \rho_k(\mathbf{r}_1) \frac{\delta \ln y^{kk',bulk}(\mathbf{r}_1)}{\delta \rho_j(\mathbf{r})} d\mathbf{r}_1 = \beta(\mu_j - V_j^{ext}(\mathbf{r})) \quad (6.23)$$

This equation can be written to give the density profile

$$\rho_j(\mathbf{r}_j) = \exp(\beta\mu_M) \exp[D_j(\mathbf{r}_j) - \beta V_j^{ext}(\mathbf{r}_j)] I_{1,j}(\mathbf{r}_j) I_{2,j}(\mathbf{r}_j) \quad (6.24)$$

where $\mu_M \left(= \sum_{j=1}^m \mu_j \right)$ is the bulk chemical potential of the chain, and $I_{1,j}$ and $I_{2,j}$

represent the following multiple integrals, solved in a recursive fashion

$$\begin{aligned} I_{1,1}(\mathbf{r}_1) &= 1 \\ I_{1,j}(\mathbf{r}_j) &= \int I_{1,j-1}(\mathbf{r}_{j-1}) \exp[D_{j-1}(\mathbf{r}_{j-1}) - \beta V_{j-1}^{ext}(\mathbf{r}_{j-1})] \Delta^{(j-1,j)}(\mathbf{r}_{j-1}, \mathbf{r}_j) d\mathbf{r}_{j-1} \end{aligned} \quad (6.25)$$

and

$$\begin{aligned} I_{2,j}(\mathbf{r}_j) &= \int I_{2,j+1}(\mathbf{r}_{j+1}) \exp[D_{j+1}(\mathbf{r}_{j+1}) - \beta V_{j+1}^{ext}(\mathbf{r}_{j+1})] \Delta^{(j,j+1)}(\mathbf{r}_j, \mathbf{r}_{j+1}) d\mathbf{r}_{j+1} \\ I_{2,m}(\mathbf{r}_m) &= 1 \end{aligned} \quad (6.26)$$

Finally, the equilibrium grand free energy in this form is given by

$$\beta\Omega[\rho_j(\mathbf{r})] = A^{ex,hs}[\rho_j(\mathbf{r})] + A^{ex,att}[\rho_j(\mathbf{r})] + \sum_{j=1}^m \int d\mathbf{r}_j \rho_j(\mathbf{r}_j) \left[D_j(\mathbf{r}_j) + \frac{n(\Gamma^{(j)})}{2} - 1 \right] \quad (6.27)$$

where $n(\Gamma^{(j)})$ represents the total number of associating sites on a given segment j .

6.3 Results and discussion

In this work, we consider a polymer-particle mixture, where we first investigate the distribution of polymer segments near an isolated colloidal particle of diameter σ_c , in a good solvent. While the theory can easily handle heteronuclear chains, to compare with simulations, the polymers are represented as homonuclear chains comprised of m segments, where all segments have a diameter σ_s . First, we examine systems governed by excluded-volume interactions, where entropic effects determine the structure of the

fluid. Results for the polymer-mediated mean force between two dilute colloids and the colloid-colloid osmotic second virial coefficient are also presented. In this comprehensive study, the theoretical predictions are shown to be in excellent agreement with simulation data, and the effects of varying polymer chain lengths, polymer solution densities, and colloid/polymer-segment size ratios on the behavior of the system are quantified and discussed. Finally, some preliminary calculations are presented for an attractive polymer-particle system, where all non-bonded interactions are described by Lennard-Jones (LJ) potentials. In such a system, the fluid structure and behavior are no longer dictated by entropic effects exclusively, but also by enthalpic effects.

6.3.1 Local structure

First, we examine the structure of polymers in the vicinity of a single isolated nanoparticle, where polymer segment-segment and polymer-particle attractions are neglected. Recently, Doxastakis et al.²⁶⁶ investigated this case via Monte Carlo (MC) simulations, treating the polymer molecules as bead-spring chains and all nonbonded interactions with repulsive Lennard-Jones (LJ) interactions, truncated and shifted at the position of the potential minimum $r_{\min} = 2^{1/6} \sigma_s$. Doxastakis et al.²⁶⁶ performed their simulations at a temperature ($T^* = k_b T / \epsilon = 1.50579$) so that the effective diameter (d_s) was equivalent to the hard-sphere diameter (σ_s). To compare with these simulations, in *i*SAFT the polymer is represented as a hard-sphere chain (for the segment-segment interactions, the repulsive part of the LJ potential can be approximated by a hard-sphere potential with an effective diameter). Similar to the simulations, polymer-particle interactions are treated with repulsive LJ interactions, truncated and shifted at the minimum of the potential

$$V_{ext}(r) = \begin{cases} u_{cs}^{LJ}(r) + \epsilon_{cs}, & r - R_{cs} < r_{\min} \\ 0, & r - R_{cs} \geq r_{\min} \end{cases} \quad (6.28)$$

where, R_{cs} is the offset distance from the particle center to the center of the LJ interaction site inside the particle and r is the center-to-center distance between a given polymer segment and the particle. Here $R_{cs} = (\sigma_c - \sigma_s)/2$ and therefore $R_{cs} = 1.95\sigma_s$ for a particle of size $\sigma_c/\sigma_s = 4.9$, as in the simulations. The parameter ϵ_{cs} represents the energy strength between the colloidal particle and polymer segments, and the LJ potential u_{cs}^{LJ} is given by

$$u_{cs}^{LJ} = 4\epsilon_{cs} \left[\left(\frac{\sigma_s}{r - R_{cs}} \right)^{12} - \left(\frac{\sigma_s}{r - R_{cs}} \right)^6 \right] \quad (6.29)$$

Figure 6.1 shows the distribution of polymer chains near a particle of diameter $\sigma_c/\sigma_s = 4.9$, in comparison with simulations from Doxastakis et al.²⁶⁶ In the figure, chain lengths of $m=16$ and $m=120$ are studied at a range of concentrations, from the dilute regime ($\rho_b\sigma_s^3 = 0.025$) to the melt regime ($\rho_b\sigma_s^3 = 0.6$). In the dilute regime ($\rho_b\sigma_s^3 = 0.025$), the polymer is depleted from the surface of the particle due to a decrease of accessible chain conformations. When comparing results at this concentration for the chain lengths $m=16$ and $m=120$, it is evident that the range of depletion is dependent on chain length. Here the range of depletion increases with chain length, and as predicted by the AO theory,¹⁵ the thickness of the depletion layer is roughly on the order of the radius of gyration R_g . For chain lengths of $m=16$ and 120 , the radius of gyration at infinite dilution is estimated to be $R_g/\sigma_s = 2.35$ and 8.27 , respectively, using the correlation for hard-sphere chains given by MC simulations from Dautenhahn and Hall²⁸⁹

$$\ln(R_g / \sigma_s) = 0.6241 \ln(m) - 0.8753 \quad (6.30)$$

The thickness of the depletion layer decreases substantially as the concentration is increased ($\rho_b \sigma_s^3 = 0.2$) and becomes essentially independent of the length of chain.

Here the polymer concentration approaches (for $m=16$) and surpasses (for $m=120$) the overlap density of polymer segments ($\rho_{OL} = 3m / 4\pi R_g^3$; represents crossover from dilute to semidilute regime), and the thickness of the depletion layer becomes comparable to the polymer segment diameter.^{251,290} In the melt regime ($\rho_b \sigma_s^3 = 0.6$), the polymer accumulates at the surface of the particle due to excluded-volume (packing) effects. As illustrated by the oscillations and peaks present at integer bond lengths, at high concentrations the polymer segments form layers around the particle.

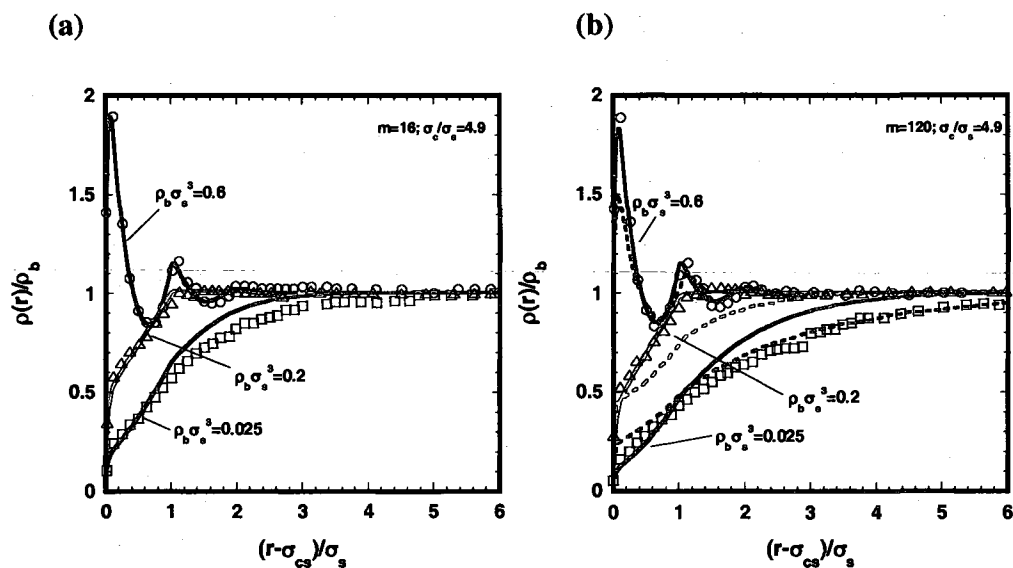


Figure 6.1: The density distribution of polymer segments near a LJ repulsive particle with diameter $\sigma_p/\sigma_s=4.9$ at concentrations $\rho_b \sigma_s^3=0.025, 0.2$, and 0.6 for the chain lengths (a) $m=16$ and (b) $m=120$. The symbols are simulation data²⁶⁶ and the solid lines are from *iSAFT*. In (b), the dashed lines represent results from *PRISM-PY-LJ*.²⁶⁶

From Figure 6.1, the predictions from *i*SAFT are in excellent agreement with the simulation data, especially at the intermediate and concentrated polymer densities. The slight shift in the peak densities between *i*SAFT and the simulations is due to using a slightly different chain model in *i*SAFT, where the bond length was designated as σ_s (a bond length of $1.12\sigma_s$ was used in the bead-spring model from simulations). For comparison, the predictions from *i*SAFT were compared to predictions from the well-established and widely used polymer integral-equation theory, specifically the polymer reference interaction site model (PRISM).^{161,291,292} Here we compare with PRISM calculations from Doxastakis et al.²⁶⁶ The PRISM calculations employ a Percus-Yevick (PY) closure²⁹³ with a short-range Lennard-Jones repulsive colloid and hard-sphere interactions between polymer segments. As seen from the figure, the predictions from *i*SAFT are superior to the PRISM calculations²⁶⁶ at high and intermediate densities. However, PRISM performs better in the dilute regime because *i*SAFT is based on first-order thermodynamic perturbation theory (TPT1) and therefore neglects long-range intrachain correlations beyond the nearest neighbor that are important at such a concentration. It should be noted, however, that such a case is not truly representative of a real, dilute polymer-colloid system as these results employ an implicit solvent.

As discussed in the theory, *i*SAFT can, in general, solve for the density distribution of each segment in the chain since the theory possesses the ability to track and retain information about each segment. Considering the previous system, it is interesting to examine the effect of preferential packing between end and middle segments on a chain near a surface. Figure 6.2 illustrates for a chain length of $m=16$, the preferential packing of end segments over middle segments as a function of distance from the surface of a

particle, for the dilute ($\rho_b \sigma_s^3 = 0.025$) and high density concentrations ($\rho_b \sigma_s^3 = 0.6$). As seen from the figure, chain ends always prefer to be near the surface of the particle compared to the middle segments due to the higher entropic penalty of the middle segments. At $\rho_b \sigma_s^3 = 0.025$, an end segment is more than twice as likely to be in contact with the particle in comparison to a middle segment. Of course, this effect becomes less pronounced as the density is increased (due to packing effects), as seen at $\rho_b \sigma_s^3 = 0.6$ in the figure, and in the inset. As observed in simulations,^{266,294} from the inset the preferential packing of end segments increases as the concentration of chain end segments decreases in the bulk (as the chain length of the polymer chain is increased).

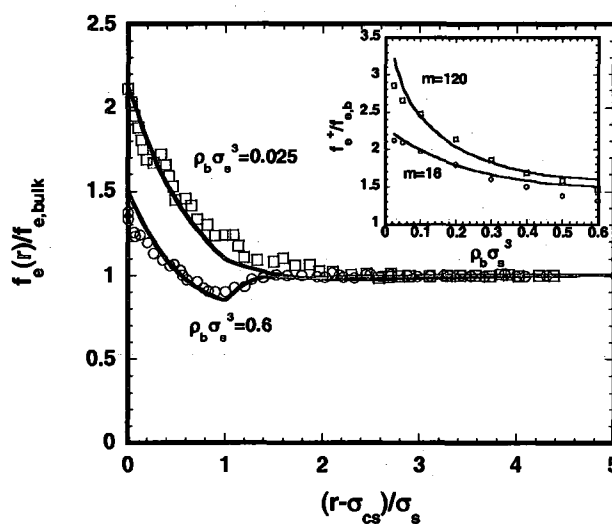


Figure 6.2: The fraction of end segment density to middle segment density ($f_e(r)$) normalized to the bulk value ($f_{e,bulk}$) as a function of distance from the surface of a LJ repulsive colloidal particle ($\sigma_e/\sigma_s=4.9$). Results are presented for the case of $m=16$ at densities $\rho_b \sigma_s^3=0.025$ and 0.6 . In the inset, the normalized contact fraction is plotted as a function of chain length ($m=16$ and $m=120$) and density. The symbols are simulation results²⁶⁶ and the solid lines are from *iSAFT*.

Although a simple case, this example illustrates the ability of *iSAFT* to distinguish and treat each segment differently in excellent agreement with simulation. This is a clear

advantage over existing theories, such as PRISM, where all segments on a chain are treated as equivalent. While such an effect may not be important in this case (as distinguishing end segments from middle segments will not affect the results presented in Figure 6.1), such a contribution can play a significant role in more complex heteronuclear systems, such as polymers with functional or hydrogen-bonding groups, polyelectrolytes, and branched polymers.

In Figure 6.3, we demonstrate the ability of the theory to handle long polymeric chains ($m=1000$) near hard-sphere particles ranging in size from the nanoparticle (protein) limit ($R_c \ll R_g$) to the colloid limit ($R_c \gg R_g$). Here, the external field introduced into the system by the hard-sphere particle is given by

$$V_{ext}(r) = \begin{cases} \infty, & r < \left(\frac{\sigma_c + \sigma_s}{2}\right) \\ 0, & r \geq \left(\frac{\sigma_c + \sigma_s}{2}\right) \end{cases} \quad (6.31)$$

where the potential is separated at the distance of closest approach between the particle and a given polymer segment. For simulations, such calculations become substantially expensive for long chains, and studies are usually limited to investigating either small particles (with a diameter close to the size of the polymer segments) or to large particles (where a colloid particle can be represented by a planar wall). *i*SAFT is not constrained by such limitations. Again, we investigate a range of concentrations, from the dilute regime ($\rho_b \sigma_s^3 = 0.001$) to the melt regime ($\rho_b \sigma_s^3 = 0.5$). Similar to Figure 6.1, depletion effects are captured at dilute and semidilute concentrations, and packing effects increase the accumulation of polymer at the surface as the concentration is increased. From

Figure 6.3, note that for cases where the depletion at the surface is present ($\rho_b \sigma_s^3 = 0.001$ and $\rho_b \sigma_s^3 = 0.1$), the range of depletion is not largely affected by varying the particle size. This is in agreement with Figure 6.1 and previous studies that demonstrate the range of depletion to be mainly dependent on the radius of gyration R_g and concentration.

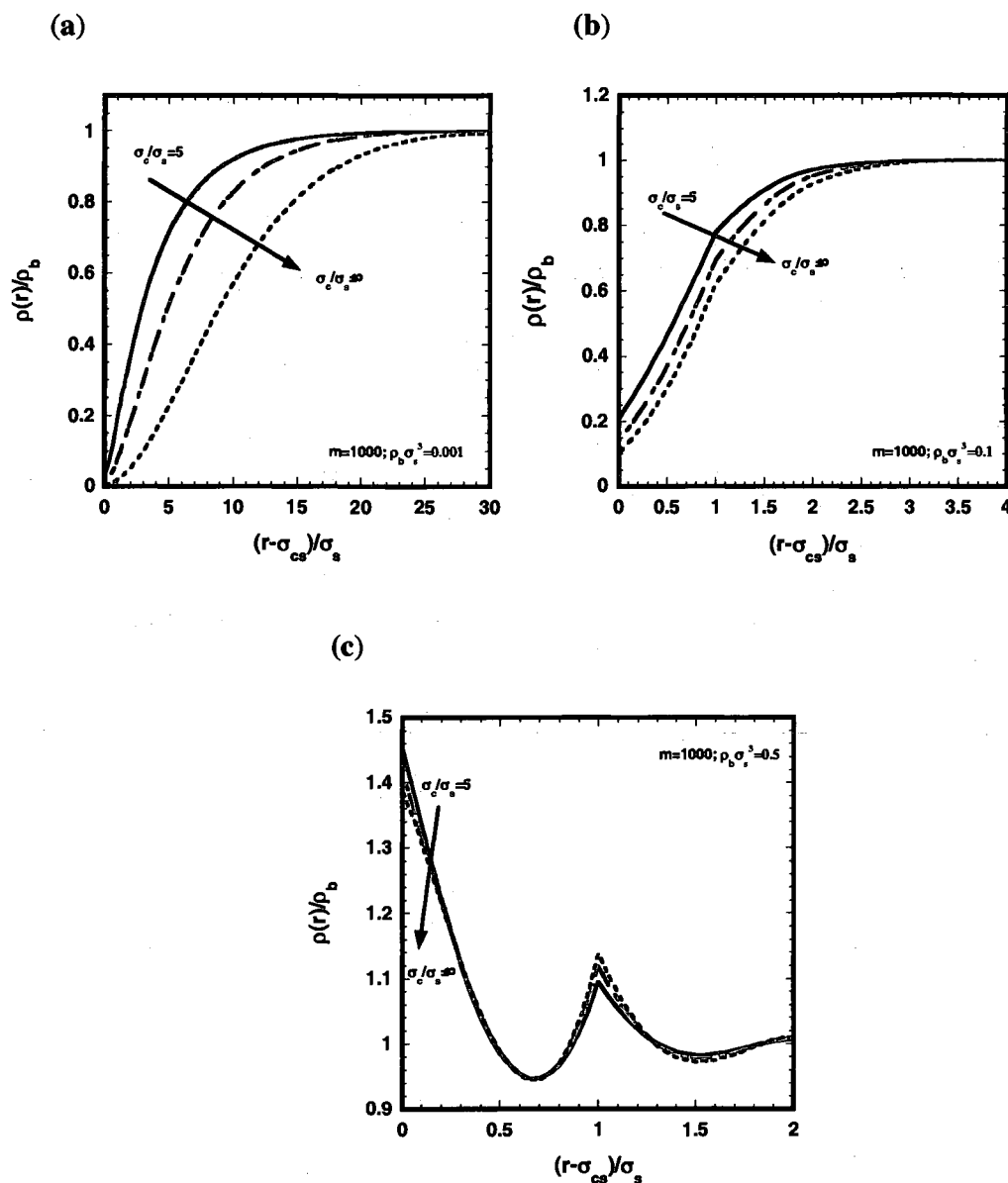


Figure 6.3: The density distribution of polymer segments near isolated hard particles of size $\sigma_s/\sigma_s=5, 15$, and ∞ are shown and represented by solid, dashed, and dotted lines, respectively. In all panels the chain length of $m=1000$ is used. The concentrations are (a) $\rho_b \sigma_s^3=0.001$, (b) $\rho_b \sigma_s^3=0.1$, and (c) $\rho_b \sigma_s^3=0.5$, respectively.

However, the particle size does have a substantial effect on the amount of depletion at the surface, increasing the surface deficit as the particle size increases. At high concentrations ($\rho_b \sigma_s^3 = 0.5$), the density profiles are nearly identical for all size ratios, except at contact and one polymer segment diameter away from the particle. For all concentrations, the contact density is higher for smaller particles than for larger colloids (for the size ratios considered). Such effects can be attributed to the polymer segments' ability to more efficiently pack at the surface of smaller particles. Here, as the particle increases in size from the nanoparticle limit to the colloid limit, surface curvature decreases and therefore hinders the polymer segments to efficiently pack at the surface. It is also noteworthy to mention that polymer chains near smaller particles are more likely to wrap around the particle, which may also contribute to the higher contact density obtained for smaller particles.

6.3.2 Polymer mediated forces

As discussed previously, there are several theoretical prescriptions used to calculate the polymer-mediated forces between interacting particles, some of which include brute force two-dimensional calculations,¹⁸⁰ the superposition approximation,¹⁸⁰ and the Derjaguin approximation.²⁹⁵ The following results apply the insertion-route developed by Roth et al.,²⁸⁷ which combines the potential distribution theorem²³² with a density functional theory for a mixture. This approach allows the potential distribution theorem to be combined with *i*SAFT and circumvents the numerical challenges of a multidimensional problem by linking the potential of mean force between two colloidal particles to the local distribution of polymer around a single particle. Roth et al.²⁸⁷ first applied this method to calculate the depletion potential of binary hard-sphere mixtures

(mixture of big and small hard-sphere particles); however, the techniques they developed are a general approach that is valid for an arbitrary number of components and interparticle potentials. The approach has been applied successfully to calculate depletion forces between nonspherical objects,²⁹⁶ as well as for the colloid/polymer systems^{295,297,298} considered here. Following this approach, a colloid particle can be fixed at the origin so that it acts as an external potential to the polymer solution. In response to the external field imposed on the system, the polymer molecules acquire an inhomogeneous density distribution near the particle, as illustrated and discussed in the previous section. The second step involves inserting the second colloidal particle at position \mathbf{r} in this inhomogeneous density field. The depletion potential, or potential of mean force, between the two particles can be written in terms of the one-body direct correlation function $c_c^{(1)}(\mathbf{r}) = -\beta \delta A^{ex} / \delta \rho_c(\mathbf{r})$,

$$\beta W(r) = c_c^{(1)}(r \rightarrow \infty) - c_c^{(1)}(r) \quad (6.32)$$

The above expression states that the reversible work required to bring two particles to a separation distance r is equal to the difference in the work required to insert one particle near a second particle (fixed at the origin) from that of the work required to insert the particle in the bulk fluid. It is noted that the direct correlation function used above in eq. (6.32) is dependent only on the equilibrium density profile before the second particle is inserted. The depletion force is then defined from the potential of mean force $W(r)$,

$$F(r) = -\frac{\partial}{\partial r} W(r) \quad (6.33)$$

In Figure 6.4 and Figure 6.5, calculated depletion interactions via the insertion-approach (coupled with *i*SAFT) are compared with recent MC simulations by Striolo et

al.²⁶⁹ and Doxastakis et al.²⁶⁵ In these figures, the polymer-mediated depletion forces and depletion potentials between two interacting particles are calculated at different concentrations and chain lengths of the polymer. As one can tell from the figures, the insertion method captures both the particle attractive force at short separations and the mid-range repulsion (present at higher polymer concentrations), with good agreement with simulation. The quantitative differences at contact and near the repulsive barrier may be attributed to *i*SAFT being based on TPT1, as discussed previously, as well as the sensitivity of the insertion approach to the weight functions and free energy expressions employed.

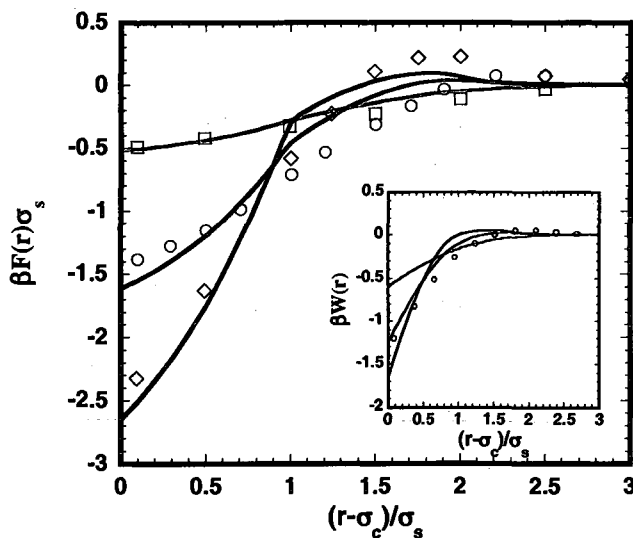


Figure 6.4: Depletion forces between two interacting particles of size ($\sigma_c/\sigma_s=5$) as a function of colloidal separation. Solid lines denote *i*SAFT results and symbols denote simulation data.²⁶⁹ Results are presented for $\rho_b\sigma_s^3=0.1$ and $m=30$ (\square), $\rho_b\sigma_s^3=0.225$ and $m=20$ (\circ), and $\rho_b\sigma_s^3=0.3$ and $m=10$ (\diamond). The inset shows the corresponding potential of mean force (PMF).

Figure 6.5 demonstrates the effect of polymer concentration on the depletion interactions between two colloids. In Figure 6.5 (a), the effect of density on the potential of mean force (PMF) is investigated for a size ratio $\sigma_c/\sigma_s=4.9$ and chain length $m=16$ and

is compared to simulation data from Doxastakis et al.²⁶⁵ As in the previous section, to compare with simulations, the polymer-particle interaction was modeled via a LJ repulsive interaction and the polymer as a hard chain (simulation employed LJ repulsion for all nonbonded interactions). Quantitative differences may be attributed in part to the different chain models used in *i*SAFT and the simulations, discussed in the previous section. Figure 6.5 (b) illustrates the effect of density on the polymer-mediated force

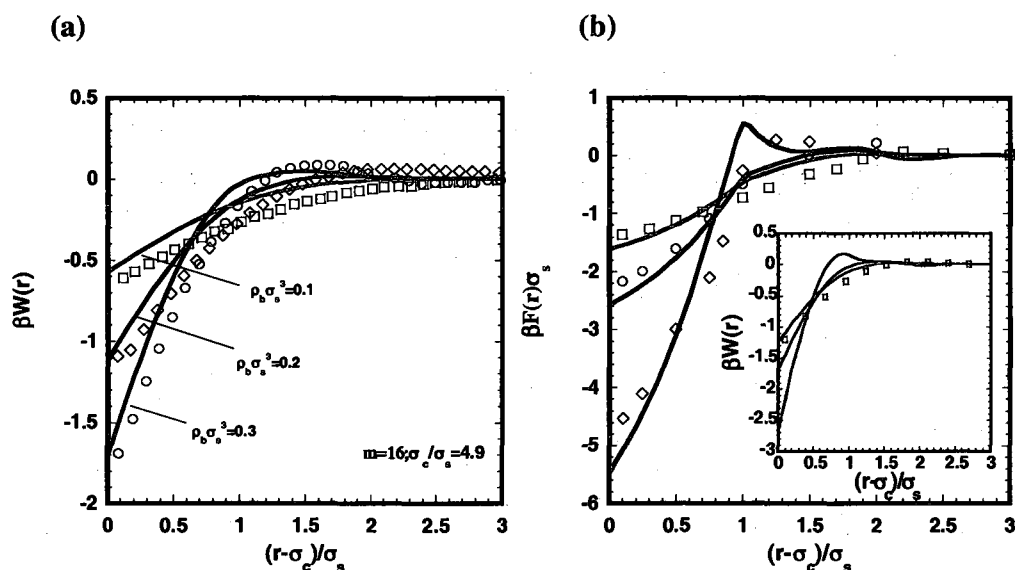


Figure 6.5: Effect of concentration on (a) the potential of mean force (PMF) between two interacting particles ($\sigma_c/\sigma_s=4.9$; $m=16$), and (b) the depletion force between two interacting particles ($\sigma_c/\sigma_s=5$; $m=20$). In (a), solid lines represent the *i*SAFT predictions and symbols denote MC simulations.²⁶⁵ The particle-polymer interaction is modeled via a LJ repulsive potential, consistent with the simulation data. The concentration is varied $\rho_b \sigma_s^3=0.1$ (\square), 0.2 (\diamond), and 0.3 (\circ). In (b), solid lines represent the *i*SAFT predictions and symbols denote MC simulations.²⁶⁹ All nonbonded interactions are of hard-sphere type, consistent with the simulation data. The concentration is varied: $\rho_b \sigma_s^3=0.225$ (\square), 0.3 (\circ), and 0.45 (\diamond). The inset shows the corresponding PMF.

between two colloidal particles of size $\sigma_c/\sigma_s=5$ and chain length $m=20$. The inset shows the corresponding PMF. Here all nonbonded interactions are modeled via a hard-sphere potential, consistent with simulations from Striolo et al.²⁶⁹ In Figure 6.5, the depletion potential and depletion force show similar behavior to one another. As the polymer

concentration increases, the attractive strength at contact increases. This entropic attraction occurs as the two particles approach each other and the polymer chains are expelled from the region between the two particles. As the concentration is increased, the osmotic pressure of the polymer solution exerted on the outer walls of the colloidal particles also increases, thus increasing the attractive force between particles at small separations. In addition, as the polymer concentration increases, the range of depletion attraction decreases, and a repulsive barrier forms at intermediate separations. The repulsive barrier forms at higher concentrations since higher osmotic pressures hinder the expulsion of the chains from the region between the particles into the bulk. Here the length scale for the colloidal interaction is determined by the polymer radius of gyration at low densities (maximum occurs $\sim \sigma_c + R_g$) and by the polymer segment diameter at high densities (maximum occurs $\sim \sigma_c + \sigma_s$) as a result of packing effects.

Comparing Figures 6.4 and 6.5 (b), as the chain length increases (at fixed concentration and colloid/segment size ratio), colloid-colloid repulsion decreases and is shifted to large separations due to excluded volume effects of the polymer chains. The effect of chain length on the colloid-colloid interaction is more evident in Figure 6.6 (a) at fixed concentration ($\rho_b \sigma_s^3 = 0.3$) and colloid/segment size ratio ($\sigma_c/\sigma_s = 5.0$). Because of entropic penalty, longer polymer chains are excluded from the region between the interacting particles, and therefore do not exhibit a mid-range repulsive barrier when the polymers are sufficiently large. Thus, as the length of the polymer is increased, the range of the depletion attraction becomes longer. This is reflected in both the depletion force and depletion potential. In addition, it is observed from the figure that the strength of the attractive force at contact decreases with increasing chain length m . This is expected

since smaller molecules reflect better packing efficiencies, and therefore smaller chains will exert a larger osmotic pressure on the colloidal particles compared to longer chains. Interestingly, the inset shows that this trend is inverted for the PMF, with the attractive strength of the PMF at contact increasing with increasing m .

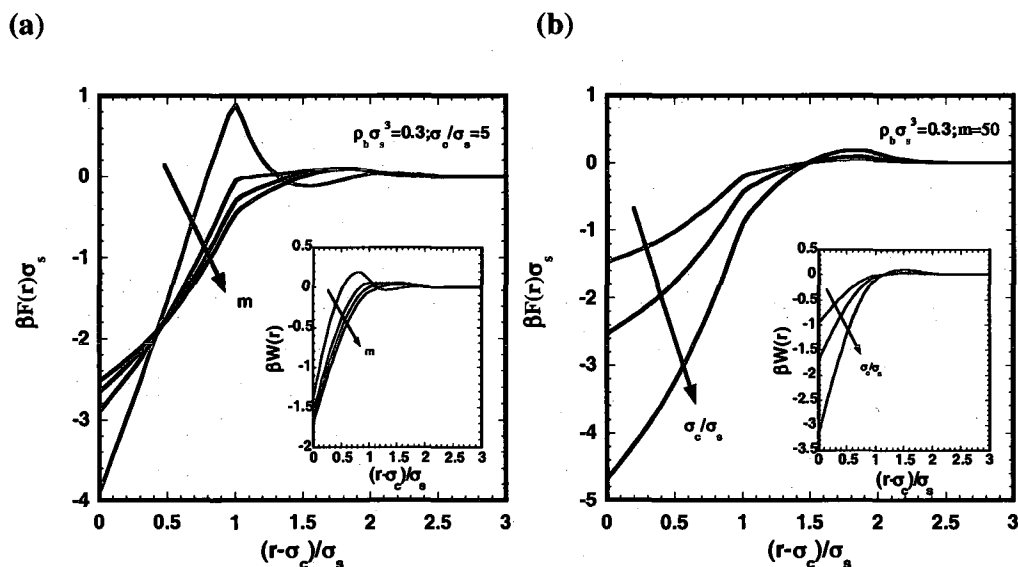


Figure 6.6: Effect of (a) chain length and (b) colloid/segment size ratio (σ_c/σ_s) on the depletion forces between two interacting particles. In (a), interacting particles are of size ($\sigma_c/\sigma_s=5$). The bulk segment density is $\rho_b \sigma_s^3=0.3$ and the chain length of the polymer chain is varied: $m=1, 4, 10$, and 100 , respectively, from bottom to top at contact. In (b), the bulk segment density is $\rho_b \sigma_s^3=0.3$ and the chain length of the polymer chain is $m=50$. The size ratio is varied: $\sigma_c/\sigma_s=2.5, 5$, and 10 , respectively. The corresponding PMFs are shown in each inset.

Finally, Figure 6.6 (b) illustrates the effect of the colloid/segment size ratio (σ_c/σ_s) on the colloidal interactions in polymer solution. Results are presented at a constant chain length ($m=50$) and polymer concentration ($\rho_b \sigma_s^3 = 0.3$) for different size ratios $\sigma_c/\sigma_s = 2.5, 5.0, 10.0$, respectively. As seen from the figure, both the attractive force at contact and the repulsive barrier at mid-range separations increase with increasing the size of the colloid. The attractive force at short separations increases for larger colloid particles because larger colloids exclude a larger volume, therefore increasing the influence of the

osmotic pressure exerted by the polymer solution on the outer walls of the colloidal particles. Also, the probability of finding polymer segments in the region between interacting colloids decreases with increasing colloid size, thus leading to a larger attractive force. The increasing height of the repulsive barrier with increasing size ratio reflects the greater tendency of the polymer to pack around the larger spheres. Similar behavior is reflected in the inset for the PMF.

6.3.3 Second virial coefficient

In the previous section, it was illustrated that the polymer mediated colloid-colloid force description can consist of attractive and repulsive regions. Such forces can compete against one another to determine the stability of the colloidal dispersion. The colloid-colloid osmotic second virial coefficient captures the net effect between such competition. Using the *i*SAFT results for $W(R)$, we compute the second virial coefficient (B_2) through the relation

$$B_2 = \frac{2}{3} \pi \sigma_c^3 + 2\pi \int_{\sigma_c}^{\infty} r^2 [1 - \exp(-\beta W(r))] dr \quad (6.34)$$

where the first term is the hard-sphere contribution and the second term is the polymer mediated contribution, respectively. Positive values of B_2 indicate a stable colloid dispersion (effective colloid-colloid repulsion), while negative values signify destabilization of the colloidal dispersion (effective colloid-colloid attraction). It should be noted that an accurate prediction for $W(r)$ is essential in the calculation of B_2 , as indicated by the integration of the quadratic term in eq. (6.34).

Figure 6.7 shows the density dependence of B_2 . Results from *i*SAFT are compared to simulation and PRISM-PY data by Doxastakis et al.²⁶⁵ ($m=16, 120$; $\sigma_c/\sigma_s=4.9$). In

addition, PRISM-PY results from Patel et al.¹⁸⁰ ($m=20$; $\sigma_c/\sigma_s=5$) and simulation data from Striolo et al.²⁶⁹ ($m=20$; $\sigma_c/\sigma_s=5$) have been included to demonstrate and compare with results at higher densities. The *i*SAFT results show a monotonic decrease of the virial coefficient over the density range studied. This indicates a stronger attractive effect for increasing densities, thereby indicating that the short-range attraction (shown to increase with density in Figure 6.5) controls the overall destabilization of the suspension.

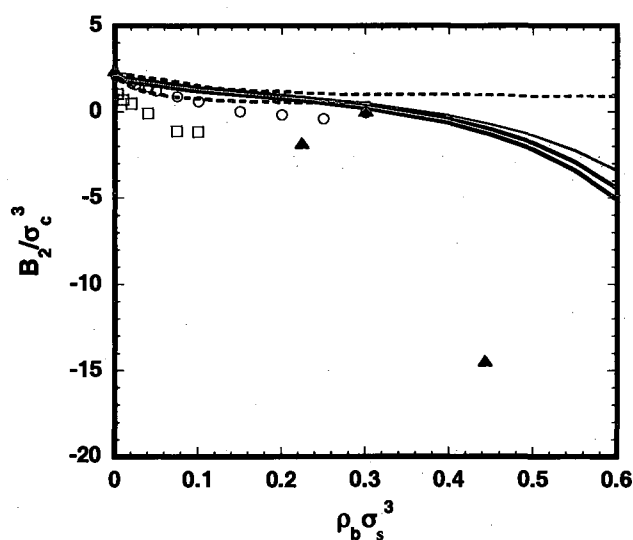


Figure 6.7: Second-virial coefficient as a function of bulk density ($\rho_b \sigma_s^3$) for different chain lengths. *i*SAFT predictions are represented by the solid lines; the thin red solid line represents the case $\sigma_c/\sigma_s=5$, $m=20$ while the thick solid lines represent cases $\sigma_c/\sigma_s=4.9$, $m=16$ (red) and $m=120$ (blue), respectively. Symbols represent simulation data from Doxastakis et al.,²⁶⁵ $\sigma_c/\sigma_s=4.9$, $m=16$ (\circ) and $m=120$ (\square), and from Striolo et al.,²⁶⁹ $\sigma_c/\sigma_s=5$, $m=20$ (\blacktriangle). PRISM-PY predictions (dashed lines) for $\sigma_c/\sigma_s=5$, $m=20$ (red, Patel et al.¹⁸⁰) and $\sigma_c/\sigma_s=4.9$, $m=120$ (blue, Doxastakis et al.²⁶⁵) are included for comparison.

It should be emphasized, however, that although thermodynamic considerations (B_2) favor aggregation, the growing repulsive maximum with bulk density (see Figure 6.5) provides a kinetic barrier that could potentially prevent aggregation. Comparisons with the simulation data indicate the *i*SAFT results to be in semiquantitative agreement. It should be noted that both sets of simulation data exhibit non-monotonic dependence of B_2

for the smaller chains considered (data for $m=120$ not available at higher densities). Still, both *i*SAFT and simulations from Striolo et al.²⁶⁹ indicate a net attraction at higher densities, although *i*SAFT does seem to underestimate this attraction (this is due to over predicting the repulsive maximum of the PMF by *i*SAFT at higher densities). In contrast, results from PRISM-PY^{180,265} yield second virial coefficients that are positive for all densities and become density independent at higher densities. This is consistent with previous studies demonstrating PRISM-PY to be unreliable at higher densities (for all chain lengths and size ratios) as B_2 approaches the same finite limiting value ($B_2^{HS}/4$).²³⁻²⁵ Such behavior has been attributed to the poor performance of PRISM-PY in calculating the potential of mean force (fails quantitatively and qualitatively at moderate to high polymer concentrations).^{26,180} The performance of PRISM IET has been shown to yield substantial improvements at moderate to high densities by employing a hyper-netted chain (HNC) closure instead of the PY closure.^{23,24,26}

While *i*SAFT indicates a decrease in the second virial coefficient as the chain length is increased (from $m=16$ to $m=120$), the magnitude of this effect is not captured quantitatively at very low densities (for $m=120$) in comparison to the simulation data.²⁶⁵ As discussed in previous sections, this may be attributed to *i*SAFT being based on TPT1, resulting in the dilute and semidilute regimes of long chains not being described as accurately. Still B_2 decreases with increasing chain length, consistent with the simulation and PRISM-PY results. Therefore colloids in solution of longer chains display a greater propensity towards aggregation. This effect is again emphasized in Figure 6.8 (a). Here B_2 falls very rapidly for small m , but then appears to approach saturation for longer chains. This is consistent with Figure 6.6 (a), which demonstrated a diminishing effect of

chain length on the effective force and an increasing attractive strength of the PMF at contact with increasing chain length. Figure 6.8 illustrates the size ratio (σ_c/σ_s) dependence of the colloid-colloid second virial coefficient (B_2) as a function of (a) chain length and (b) bulk polymer density. From the figure one sees that larger colloidal particles encourage attraction and a greater tendency towards aggregation, especially at higher concentrations, in accordance with the behavior in Figure 6.6 (b).

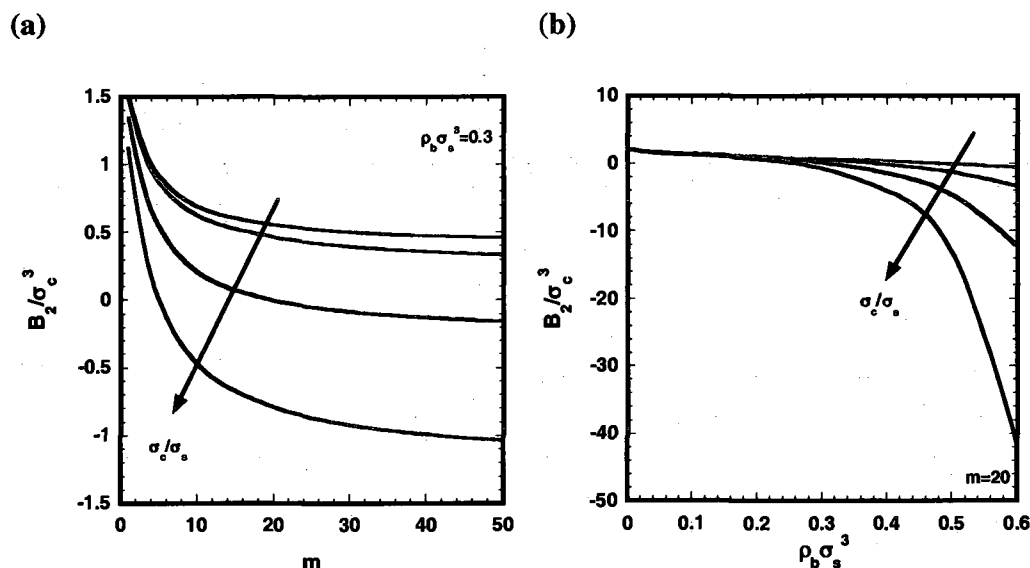


Figure 6.8: Second-virial coefficient for varying size ratios ($\sigma_c/\sigma_s=2.5, 5, 7.5, 10$) as a function of (a) chain length and (b) bulk polymer density. In (a) the bulk density is constant at $\rho_b \sigma_s^3=0.3$, while in (b) the chain length is constant at $m=20$.

6.3.4 A preliminary study: Effect of attractive interactions

While the fundamental model provides valuable insight to nonadsorbing colloidal suspensions, real polymer-colloid mixtures observed experimentally can involve complicated (non-hard-core) interactions such as van der Waals attractions, Coulomb forces, and/or specific polymer-particle attractive interactions. In such cases, the system is no longer dictated by entropic effects exclusively, but also by enthalpic effects that can

influence the packing of polymer molecules at the surface of a particle. Fewer studies have attempted to quantify the effects of including polymer-particle attractions. Hooper et al.²⁶ employed PRISM IET to investigate the effects of such attractions, capturing the correct behavior in qualitative agreement with simulation studies.^{299,300} Recently Patel and Egorov¹⁷⁹ extended their density functional theory from the hard-core polymer-particle system¹⁸⁰ to the attractive polymer-particle system, investigating the case where all non-bonded interactions were described by Lennard-Jones (LJ) potentials.

In this section, we test the ability of the *i*SAFT DFT to accurately describe attractive polymer-particle mixtures. In this preliminary study, the structure of polymer molecules near the surface of an attractive particle is compared with available simulation data²⁹⁹ to study how the temperature and the nature of the interactions between the particle and polymer matrix influence the behavior of the system. In this study all non-bonded interactions are modeled using a truncated and shifted Lennard-Jones interaction potential, similar to the simulation study by Bedrov et al.²⁹⁹ The polymer-particle interactions can be represented by

$$V_{ext}(r) = \begin{cases} \infty, & r < R_{cs} \\ u_{cs}^{LJ}(r) - u_{cs}^{LJ}(r_{cs}^{cut}), & R_{cs} < r < r_{cs}^{cut} \\ 0, & r \geq r_{cs}^{cut} \end{cases} \quad (6.35)$$

where R_{cs} is defined as before, $R_{cs} = (\sigma_c - \sigma_s)/2$, r is the center-to-center distance between a given polymer segment and the particle, and r_{cs}^{cut} is the cutoff distance of the LJ potential, set to $r_{cs}^{cut} = 4.5\sigma_s$ (consistent with the simulations from Bedrov et al.²⁹⁹). The LJ potential $u_{cs}^{LJ}(r)$ is given by eq. (6.29). Similarly, the interactions between polymer segments are described

$$u_{ss}^{att}(r_{12}) = \begin{cases} -\epsilon_{ss} - u_{ss}^{LJ}(r_{ss}^{cut}), & \sigma_s < r_{12} \leq r_{min} \\ u_{ss}^{LJ}(r_{12}) - u_{ss}^{LJ}(r_{ss}^{cut}), & r_{min} < r_{12} < r_{ss}^{cut} \\ 0, & r_{12} \geq r_{ss}^{cut} \end{cases} \quad (6.36)$$

where,

$$u_{ss}^{LJ}(r_{12}) = 4\epsilon_{ss} \left[\left(\frac{\sigma_s}{r_{12}} \right)^{12} - \left(\frac{\sigma_s}{r_{12}} \right)^6 \right] \quad (6.37)$$

and ϵ_{ss} is the molecular interaction energy between polymer segments, r_{ss}^{cut} is the position of the potential cutoff for the LJ potential taken to be $r_{ss}^{cut} = 2.5\sigma_s$ (consistent with the simulations²⁹⁹), and the minimum of the potential is located at $r_{min} = 2^{1/6}\sigma_s$. In the previous work of Patel and Egorov,¹⁷⁹ several methods of treating attractive interactions^{213,301,302} were tested to study the structure and nanoparticle interactions in polymer-particle mixtures. Interesting results from their work indicated the simple mean-field approximation provided the most accurate results, in quantitative agreement with molecular dynamics (MD) simulations.^{299,300} Here we also employ the mean field prescription to describe segment-segment attractive interactions using eqs. (6.10) and (6.18). The temperature-dependent diameter (d_s) is used to calculate the weighted densities used in the hard-sphere and chain contributions to the free energy. The temperature-dependent diameter of the polymer segments (d_s) can be approximated using³⁰³

$$d_s = \frac{1 + 0.2977(T^*)}{1 + 0.33163(T^*) + 0.00104771(T^*)^2} \sigma_s \quad (6.38)$$

where $T^* = k_b T / \epsilon_{ss}$.

In Figure 6.9, the *i*SAFT predictions are compared with simulation data from Bedrov et al.²⁹⁹ In this case, the density and temperature of the polymer melt are chosen to be $\rho_b \sigma_s^3 = 0.7$ and $T^* = 1.33$, while the chain length is set to $m=20$. The effective particle size given was $\sigma_c / \sigma_s = 5$. Results are presented for two particle-polymer attraction strengths: $\epsilon_{cs} / \epsilon_{ss} = 1$ and $\epsilon_{cs} / \epsilon_{ss} = 2$. As seen in the figure, the *i*SAFT predictions are in excellent agreement with the simulation results. As expected, increasing the particle-segment interaction energy results in a larger accumulation of polymer segment density near the surface of the particle. Based on the results in the previous sections (for the athermal system), such accumulation of chains at the surface of strongly attractive particles would lead to a more repulsive depletion potential (PMF) between two interacting particles, thus increasing the stability of the nanoparticle dispersion.

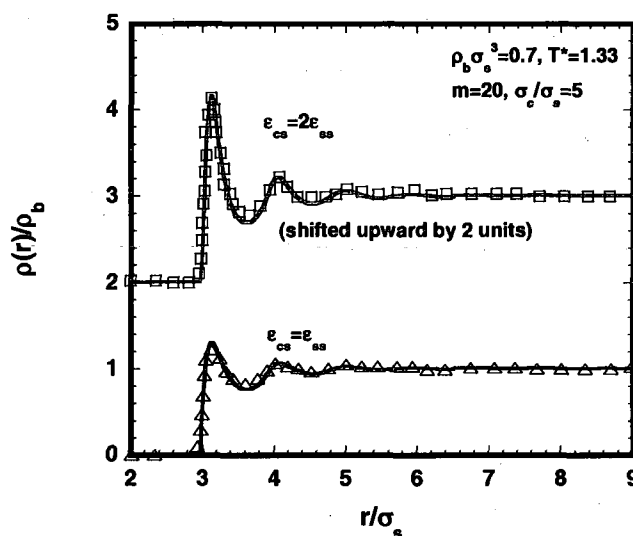


Figure 6.9: The density distribution of polymer segments near an attractive particle with diameter $\sigma_c / \sigma_s = 5$, at a concentration $\rho_b \sigma_s^3 = 0.7$, with polymer chain length $m=20$. The temperature was chosen to be $T^*=1.33$. All non-bonded interactions are modeled using a truncated and shifted LJ potential. The symbols represent MD simulation results,²⁹⁹ whereas the solid lines represent *i*SAFT predictions for $\epsilon_{cs} / \epsilon_{ss} = 1$ (blue, Δ) and $\epsilon_{cs} / \epsilon_{ss} = 2$ (red, \square).

Previous work¹⁷⁹ has indicated that increasing the temperature of the polymer solution promotes destabilization of the colloidal dispersion. Interestingly, results indicate the repulsive barrier formed at intermediate particle separations increases with temperature for a weakly attractive system, and decreases with increasing temperature for a strongly attractive system. The results presented in Figure 6.10 explain such behavior by considering the temperature effects on the polymer-segment density around a single isolated colloidal particle, first for a weakly attractive particle-polymer system (Figure 6.10 (a)), and then for a strongly attractive particle-polymer system (Figure 6.10 (b)). To

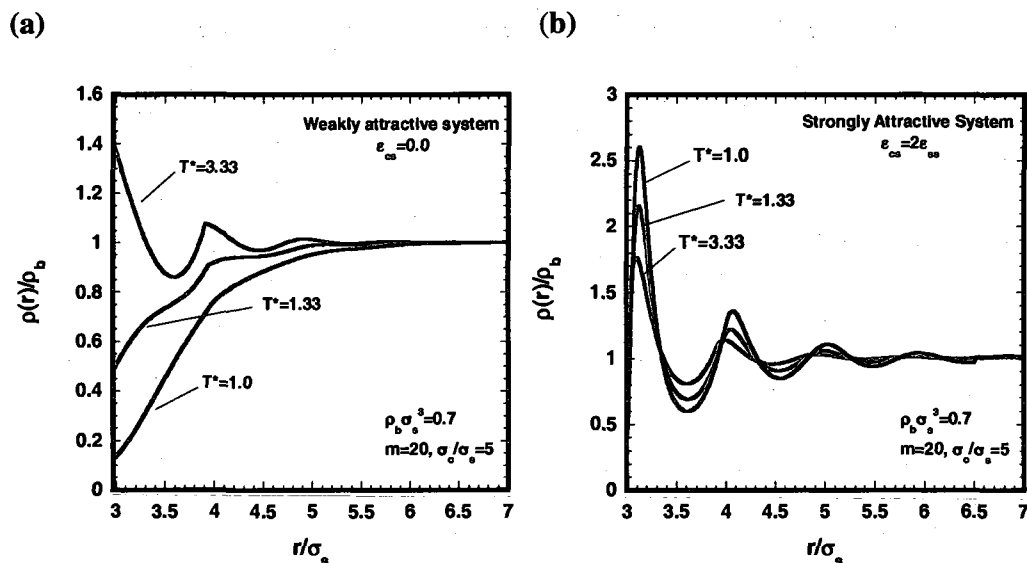


Figure 6.10: The density distribution of polymer segments near an attractive particle with diameter $\sigma_c/\sigma_s = 5$, at a concentration $\rho_b \sigma_s^3 = 0.7$, with polymer chain length $m = 20$. The temperature is varied ($T^* = 1.0$, $T^* = 1.33$, and $T^* = 3.33$) for (a) a weakly attractive polymer-colloid system, and (b) a strongly attractive polymer-colloid system.

study temperature effects exclusively, again the density was chosen as $\rho_b \sigma_s^3 = 0.7$, the chain length was set to $m = 20$, and the effective particle size was chosen as $\sigma_c / \sigma_s = 5$.

Different behavior is observed in each case. In Figure 6.10 (a), for the weaker interacting system with $\epsilon_{cs} = 0$, an increase in T^* increases the accumulation of polymer segments

near the surface of the colloid particle (thereby increasing steric stabilization). However, in Figure 6.10 (b), for the strongly attractive system with $\epsilon_{cs} / \epsilon_{ss} = 2$, an increase in T^* reduces the accumulation of polymer segments near the surface of the colloid (thereby reducing steric stabilization).

Although, one can qualitatively visualize how the stability of a colloid dispersion is affected with changing the nature of the polymer-particle interaction or with changing the temperature (as briefly discussed above), a more complete study could be conducted on the polymer-mediated forces involved in the above attractive systems. It would be interesting to see how accurate the insertion-route (employed for the athermal polymer-colloid system) would be in predicting the particle-particle interactions. The additional perturbation of the mean field attraction may make the approach less accurate. As mentioned previously in the chapter, the insertion approach is sensitive to the weight functions and free energy expressions employed. Therefore, it may be necessary to use a more sophisticated attraction term than the ones used in eqs. (6.10) and (6.18). Another alternative approach is to calculate the depletion forces of interacting particles by brute force.¹⁷⁹ Of course, this approach requires a two-dimensional DFT and comes at a high computational cost. Still, it would be of interest to understand completely the effects of including attractive interactions in the system, including quantifying the competition among contact aggregation, bridging effects, and steric stabilization.

6.4 Conclusions

In this work, we have demonstrated the ability of *i*SAFT density functional theory to successfully describe the structure and effective force interactions in polymer-colloid mixtures. A comprehensive comparison between theory and simulation was performed

for nonadsorbing mixtures, elucidating the roles of the broad parameter space involved in such systems: the particle/polymer segment size ratio, polymer chain length and polymer concentration.

For nonadsorbing polymer-colloid mixtures, the structure of polymers around a single isolated particle was investigated under a wide range of conditions. The theory's versatility was demonstrated under a tough test of conditions, from the nanoparticle limit to the colloid limit in different concentration regimes. Under dilute and semidilute concentrations, polymer segments are depleted from the surface of a particle. Here *i*SAFT correctly captures a depletion layer on two different length scales, one on the order of the segment diameter (semidilute regime), and the other on the order of the polymer radius of gyration (dilute regime). The range of depletion is relatively independent of the colloid size; however the total amount of depletion is dependent on the particle size as the surface deficit increases with increasing particle size. At higher concentrations, packing effects result in an accumulation of polymer segments near the colloidal surface. In this concentration regime, the effect of particle size and chain length on the density distribution of polymer segments diminishes significantly.

The theory captures the main characteristics of the polymer induced depletion interaction between colloidal particles, quantifying the effects of polymer density, polymer chain length, and particle/polymer-segment size ratio. Increasing the concentration of the polymer solution encourages the particle-particle attractive force at contact to increase, while decreasing the range of depletion attraction. Further, at high concentrations a repulsive barrier can form at intermediate separations. Increasing polymer chain length decreases the strength of the attractive force at contact, while

increasing the range of the depletion attraction. Both the attractive force at contact and the repulsive barrier at mid-range separations increase with increasing the size of the colloid.

The *i*SAFT results indicate the colloid-colloid second virial coefficient to decrease monotonically with increasing the polymer density, thereby indicating that net repulsion between colloids at low polymer densities gives way to net attraction at higher densities. The net attraction predicted at higher densities is in agreement with available simulation data.²⁶⁹ Further, the second virial coefficient decreases with increasing polymer chain length and/or increasing colloid size. Such effects indicate a higher tendency towards colloidal aggregation for larger colloids in solutions of longer chains.

Finally, a preliminary study was conducted for an attractive polymer-colloid system, demonstrating excellent agreement between the *i*SAFT predictions and available simulation data. In such a system, the fluid structure and behavior are no longer dictated by entropic effects exclusively, but also by enthalpic effects. Calculations were performed to quantify how the structure of polymer near a colloidal particle is affected by the temperature and the nature of the polymer-colloid interaction. Results suggest that increasing the particle-polymer attraction strength stabilizes the dispersion, as indicated by the aggregation of polymer segments to the surface of the particle. Previous work¹⁷⁹ has demonstrated that increasing the temperature of the polymer solution promotes destabilization. Still, it is interesting to note that the repulsive barrier formed at intermediate particle separations increases with temperature for a weakly attractive system, and decreases with increasing temperature for a strongly attractive system. The preliminary results presented in this chapter explain such behavior by considering the

temperature effects on the polymer structure around an isolated colloidal particle. An increase in temperature increases the accumulation of polymer segments near the surface of a colloid particle in a weak attractive polymer-colloid system (thereby increasing steric stabilization), whereas the opposite behavior is observed for the stronger interacting system. A more complete study could be conducted for the attractive polymer-colloid system to investigate the polymer mediated forces involved as well as the colloid-colloid second virial coefficient, to quantify the competition among contact aggregation, bridging effects, and steric stabilization.

CHAPTER **7****An *i*SAFT density functional theory for associating polyatomic molecules****7.1 Introduction**

Unfavorable interactions between unlike species play an important role in the phase behavior and microstructure of polymer systems, often leading to self-assembly of novel nano-structures or to undesirable macrophase separation in polymer blends. In recent years, macromolecules containing functional groups capable of forming reversible noncovalent bonds (via hydrogen bonding or ionic interactions) have attracted much attention from both experimentalists and theoreticians. The introduction of hydrogen-bonding or ionic interactions found in such associating macromolecules are important to the field of self-organizing soft materials, providing self-assembling mechanisms for a polymer blend that can potentially lead to the production of new, highly functional polymeric materials. Because of the reversible nature of such components, temperature can be used to control molecular connectivity, and hence the phase behavior (polymer-polymer miscibility, macrophase separation, and the self-assembly into mesostructures) and the unique material properties (physical properties and processability) of the system. Current and potential applications where such technology can be utilized include biosensors, separation devices, controlled drug delivery,³⁰⁴ thermal manipulation of the

viscosity,³⁰⁵ and the development of “smart materials” with novel chemical, electrical, mechanical, and optical (light emitting) properties,³⁰⁶⁻³¹⁴ where the functionality of the material can be switched on and off via temperature controlled phase transitions.

Experimental studies have provided many insights into associating polymers (e.g., surfactants, oligomers, copolymers, and biomolecules). Given the right conditions, or the right balance between the association forces and repulsive forces between polymer segments, experiments have observed some interesting phase behaviors and material properties. For example, the design of supramacromolecules varying in size and architecture (linear, comb, star, etc.) derived from hydrogen bonding has become an area of great interest in macromolecular science, due to the interesting morphologies and physical properties present in such systems.³⁰⁶⁻³¹⁷ Xiang et al.³¹⁷ investigated AB and CD copolymers blended in good solvent and demonstrated how micellar aggregates can form in solution when B and D are able to interact via hydrogen bonding interactions. Ruokolainen and coworkers³¹² demonstrated how hydrogen bonding interactions can control functional properties and lead to hierarchical structural formation in block copolymer/low molecular weight associating polymer blends (microphase separated lamellar morphology, re-entrant closed loop macrophase separation, and high temperature macrophase separation). Pan et al.³¹⁶ investigated hydrogen bonding AB/CD diblock copolymer blends and observed three phase structures, and Asari et al.³⁰⁶⁻³⁰⁸ demonstrated how block copolymers (blends of diblock/diblock and diblock/triblock copolymers) can self-assemble into several complex Archimedean tiling patterns in the bulk via hydrogen bonding interactions. In addition, many applications of these materials involve interactions with solid surfaces or colloidal particles and in confined geometries

(adhesion, lubrication and friction, nanocomposites, blood flow and drug delivery, etc.). For this reason, a number of experiments have also investigated associating polymer solutions or melts in confined geometries and near surfaces, measuring the polymer mediated forces involved.³¹⁸⁻³²¹ The aforementioned experimental studies are just a few examples of how associating/hydrogen bonding polymers can form complex molecular architectures, interesting phase transitions, and unique self-assembled patterns and microstructures. Unfortunately, although valuable, results from such studies are often confined to the specific system studied, leaving many unanswered questions.

Theoretical models will, without a doubt, play an important role in understanding and aiding the experimental design of more complex systems due to their ability to cover a wide parameter space that characterizes the polymer architectures and molecular weights, chemical incompatibilities, and bonding strengths between associating species in multicomponent polymer mixtures. One of the early theories for reversible bonding was developed by Tanaka and coworkers,^{322,323} who used the random phase approximation (RPA) to study the microphase and macrophase separation transitions in systems of supramolecular diblock and comblike polymers. A shortcoming of the theory is its inability to examine the mesophase structure and stability since the free energy of the ordered microstructure is not considered (limited to investigating the stability of homogeneous phases). Later, ten Brinke and coworkers^{324,325} were able to examine the mesophase structure and stability for graft and diblock copolymer systems using a higher order RPA, although the model is very laborious and restricted to the weak segregation limit. More recently, Feng et al.³²⁶ and Lee et al.³²⁷ have recast the field-theoretic description of supramolecular polymers to handle all segregation strengths, applying the

numerical self-consistent field theory (SCFT) within this framework to investigate the self-assembly of associating supramolecular polymers. Unfortunately, mean field theories and SCFT are not accurate in describing cases of macromolecules near solid surfaces or in confined nanoslits,^{21,22} where local density fluctuations and liquid-like ordering play a significant role. Molecular simulations have played an important role in the investigation of associating polymers for problems related both in the bulk³²⁸⁻³³³ and in confined geometries.³³⁴⁻³³⁶ However, due to the overwhelming amount of information that is retained in these computations, simulations can become computationally expensive, especially when considering supramacromolecules composed of long polymeric chains. Despite the success of all the aforementioned theoretical work, it is desirable to have a theory that is computationally efficient and capable of investigating associating polymer systems at any segregation strength and fluid density, as well as capable of providing structural and thermodynamic information not only for bulk microstructures, but also for fluids near surfaces or in confined environments, which are important to many applications, as mentioned previously.

Recently, density functional theory (DFT) has emerged as a powerful theoretical tool to investigate inhomogeneous polymer systems.²⁷ Density functional theory is a tool with a statistical mechanics foundation that includes more physics than mean field theories and SCFT, retaining statistical segment length-level information rather than a coarse-grained representation of the polymers, at an expense significantly lower than simulation methods. As mentioned, mean-field theories and SCFT neglect fluid fluctuations that become especially important near surfaces and in confined environments.^{21,22} Density functional theory, on the other hand, is formulated in the grand canonical ensemble where

the fluctuations in the number of polymer chains in the system maintain a constant chemical potential. Therefore, the system is compressible and phase transitions can include fluctuations in the density of the system, which is key especially near surfaces and in confined environments, where packing effects become important.

Chapman¹² was the first to suggest that Wertheim's first order thermodynamic perturbation theory (TPT1)⁴⁻⁷ free energy could be used naturally within a DFT formalism for inhomogeneous associating fluids. The first DFT for associating fluids within this framework was developed by Segura et al.,²⁹ who described associating atomic spheres near a hydrophobic hard wall. Segura et al.²⁹ introduced and successfully demonstrated two approaches to include intermolecular association between atomic species. The first applies an association free energy functional based on Wertheim's TPT1 as a perturbation to a reference fluid functional, while the second approach approximates the association free energy functional using the bulk equation of state at an effective density. The second (and more simple) approach has been applied with great success by numerous groups using various local or weighted density formalisms to study structure, phase behavior, and interfacial properties of associating atomic fluids (both in confined environments and at vapor-liquid and solid-liquid interfaces).^{29-31,168,177,178} The developments in density functional theory have led to the advancement of our ability to understand and investigate complex polymer systems. More recently the second approach of Segura et al. has been extended to associating polyatomic fluids, specifically to study the structure of associating molecules at liquid-vapor interfaces,^{95,337-339} in slit-like pores,³³⁷ and at solid surfaces.³⁴⁰ In these studies, simple association schemes were adopted based on the appropriate bulk free energy expressions for a polymer segment

with one association site. Such an approach, using the bulk free energy due to association, is dependent on the accuracy of the weighting functions used and may not produce the correct free energy in the limit of strong association.

In this chapter, we introduce an extension to the interfacial statistical associating fluid theory (*i*SAFT)³² for associating polymer systems. The *i*SAFT density functional theory is an extension to TPT1, where the contribution to the free energy due to chain formation is derived from the inhomogeneous free energy for association for a mixture of associating spheres, taken at the complete bonding limit. The theory has already been successfully applied to study a wide range of complex polymer systems. Tripathi and Chapman^{33,34} applied *i*SAFT to study polymer melts, solutions, and blends confined in slit-like pores and Dominik et al.¹⁶⁵ applied the theory to real systems, calculating interfacial properties of n-alkanes and homopolymers. Recently, an extension of *i*SAFT was introduced by Jain et al.³² that corrects approximations in the original theory and extends the theory to complex heteronuclear systems. For heteronuclear systems, *i*SAFT has been applied successfully to investigate block copolymers in confinement¹⁹² and near selective surfaces,³² tethered polymers,¹⁹³ and polymer-colloid mixtures.¹⁹⁵ The work in this chapter for associating polymers is based on Segura et al.'s work for associating spheres, where the first approach of Segura et al. (using the inhomogeneous form of the association functional) is extended to polyatomic molecules. This approach is consistent with the *i*SAFT approach for chains, reducing exactly to the *i*SAFT chain functional in the infinite bonding limit. The resulting free energy expressions that are derived are capable of modeling complex associating systems, where the full range of association can

be investigated for any association scheme (for molecules having any number of association sites on any segment along a polymer chain).

In the next section, the *i*SAFT approach is presented and discussed, along with the new theoretical developments for associating chains. In section 7.3, we demonstrate the applicability of the theory to associating polymers through various examples. The ability of the theory to handle associating polymers near surfaces and in the bulk will be demonstrated over a wide range of conditions. Further, the importance of such a theory will be elucidated through the complex behaviors observed for even the simple associating molecules chosen in this study, including the thermal reversible nature of forming larger supramolecules and molecules with complex architectures, and the resulting effect on the structure and phase behavior of the fluid (2 phase macroseparation and microphase separated lamellar morphologies, and reentrant order-disorder transitions, as observed by experiments). Finally, concluding remarks are discussed in section 7.4.

7.2 Theory

7.2.1 Model

The objective of this work is to study the full range of association for a fluid mixture composed of associating, fully flexible polymer chains. Each chain consists of m tangentially bonded spherical segments, where any number of association sites can be placed on any segment along the chain. For simplicity, in this work all the segments have the same diameter σ , although the theory is capable of defining each segment to be different. Here we consider linear chains, but the theory can also be applied to associating branched chains (for the theoretical formulation for branched chains, the reader is referred to the work by Jain and Chapman¹⁹⁴). The polymer segments can

interact through pairwise repulsive, attractive, and association contributions, given by the following pair potential

$$u(\mathbf{r}_{12}, \boldsymbol{\omega}_1, \boldsymbol{\omega}_2) = u^{ref}(\mathbf{r}_{12}) + \sum_A \sum_B u_{AB}^{assoc}(\mathbf{r}_{12}, \boldsymbol{\omega}_1, \boldsymbol{\omega}_2) \quad (7.1)$$

where u^{ref} represents the reference fluid contribution, u^{assoc} is the directional contribution, r_{12} is the distance between segment 1 and segment 2, ω_1 and ω_2 are the orientations of the two segments, and the summations are over all association sites in the system. The reference fluid potential u^{ref} can be described as the sum of repulsive and attractive contributions

$$u^{ref}(r_{12}) = u^{hs}(r_{12}) + u^{att}(r_{12}) \quad (7.2)$$

where the repulsive contribution between two segments on a chain is described using a hard sphere potential, given by

$$u^{hs}(r_{12}) = \begin{cases} \infty, & r_{12} < \sigma \\ 0, & r_{12} \geq \sigma \end{cases} \quad (7.3)$$

The attractive contribution uses a cut-and-shifted Lennard Jones (LJ) potential, with a Weeks, Chandler, and Andersen separation^{227,228} at $r_{min}=2^{1/6}\sigma$.

$$u^{att}(r_{12}) = \begin{cases} -\epsilon^{LJ} - u^{LJ}(r_{cut}), & \sigma < r_{12} \leq r_{min} \\ u^{LJ}(r_{12}) - u^{LJ}(r_{cut}), & r_{min} < r_{12} < r_{cut} \\ 0, & r_{12} \geq r_{cut} \end{cases} \quad (7.4)$$

where,

$$u^{LJ}(r_{12}) = 4\epsilon^{LJ} \left[\left(\frac{\sigma}{r_{12}} \right)^{12} - \left(\frac{\sigma}{r_{12}} \right)^6 \right] \quad (7.5)$$

where ε^{LJ} is the molecular interaction energy and r_{cut} is the position of the potential cutoff for the LJ potential, taken to be $r_{cut}=3.5\sigma$. Any segment along a chain can have multiple association sites capable of interacting with other sites on other polymer segments. The association contribution (important to the *i*SAFT chain functional and the full range association functional) is modeled via off centered sites that interact through a square-well potential of short range r_c . The interaction between site *A* on one segment and site *B* on another segment are modeled using the following association potential,

$$u_{AB}^{assoc}(\mathbf{r}_{12}, \omega_1, \omega_2) = \begin{cases} -\varepsilon_{AB}^{assoc}, & r_{12} < r_c; \theta_{A1} < \theta_c; \theta_{B2} < \theta_c \\ 0, & \text{otherwise} \end{cases} \quad (7.6)$$

where θ_{A1} is the angle between the vector from the center of segment 1 to site *A* and the vector \mathbf{r}_{12} , and θ_{B2} is the angle between the vector from center of segment 2 to site *B* and the vector \mathbf{r}_{12} , as illustrated previously in Figure 5.2. Of course, only bonding between compatible sites is permitted (two incompatible sites *A* and *B* have a bonding energy of zero, $\varepsilon_{AB}^{assoc} = 0$). The radial limits of square-well association were set to $r_c=1.05\sigma$ and the angular limit to $\theta_c=27^\circ$.

In addition to the pair potential between segments, an additional external field may be imposed on the system. In this work, results are presented for both bulk fluids and fluids near a hard surface. The external field introduced into the system by the hard wall is given by

$$V^{ext}(z) = \begin{cases} \infty, & z < \frac{\sigma}{2} \\ 0, & \text{otherwise} \end{cases} \quad (7.7)$$

where z is the distance normal to the surface.

7.2.2 *iSAFT density functional theory*

The density functional theory is formulated in the grand canonical ensemble, which has a fixed volume (V), temperature (T), and chemical potential (μ). The starting point of the density functional theory is the development of an expression for the grand free energy, Ω , as a functional of the equilibrium polymer density profile $\rho(r)$. From this, the desired thermodynamic and structural properties of the system can be determined. In this work, we consider associating fluid mixtures composed of polymeric components (C_1, C_2, \dots, C_n). The grand free energy can be related to the Helmholtz free energy functional $A[\rho(r)]$ through the Legendre transform,¹³

$$\Omega[\rho_i^{(C_1)}(\mathbf{r}), \rho_i^{(C_2)}(\mathbf{r}), \dots] = A[\rho_i^{(C_1)}(\mathbf{r}), \rho_i^{(C_2)}(\mathbf{r}), \dots] - \sum_{l=C_1, C_2, \dots} \sum_{i=1}^{m_l} \int d\mathbf{r}' \rho_i^{(l)}(\mathbf{r}') (\mu_{i,l} - V_{ext}^{i,l}(\mathbf{r}')) \quad (7.8)$$

where $\rho_i^{(l)}(\mathbf{r})$ is the density of the i th segment on chain l at position \mathbf{r} , $\mu_{i,l}$ is the chemical potential of that segment, and $V_{ext}^{i,l}$ is the external field acting on that segment. The first summation is over all chains l in the mixture (C_1, C_2, \dots, C_n), and the second summation is over all segments on chain l . Since *iSAFT* is a segment-based DFT that treats each segment differently, we can simplify this notation by combining these two sums to an equivalent sum over all segments (N) in the system, where $N = m_{C_1} + m_{C_2} + \dots + m_{C_n}$. At equilibrium, the following condition is satisfied

$$\frac{\delta \Omega}{\delta \rho_i(\mathbf{r})} = 0 \quad \forall i = 1, N \quad (7.9)$$

Solving this set of Euler-Lagrange equations gives the equilibrium density profile of the segments. The total Helmholtz free energy functional can be decomposed into an ideal and excess contribution,

$$A[\rho_i(\mathbf{r})] = A^{id}[\rho_i(\mathbf{r})] + A^{ex,hs}[\rho_i(\mathbf{r})] + A^{ex,chain}[\rho_i(\mathbf{r})] + A^{ex,att}[\rho_i(\mathbf{r})] + A^{ex,assoc}[\rho_i(\mathbf{r})] \quad (7.10)$$

where the excess contribution consists of changes in the free energy due to excluded volume (*hs*), chain connectivity (*chain*), long-range attraction (*att*), and association (*assoc*), over the ideal gas (*id*) state of the atomic mixture.

7.2.2.1 Free energy functionals

The ideal free energy functional is known exactly from statistical mechanics

$$\beta A^{id}[\rho_i(\mathbf{r})] = \int d\mathbf{r}_1 \sum_{i=1}^N \rho_i(\mathbf{r}_1) [\ln \rho_i(\mathbf{r}_1) - 1] \quad (7.11)$$

where the temperature-dependent term (the de Broglie wavelength λ) has been dropped since it is not density dependent and hence does not affect the structure or thermodynamics of the fluid. The inverse temperature is represented by $\beta = 1/k_b T$, where k_b is the Boltzmann's constant. The free energy due to excluded volume/short range repulsion, $A^{ex,hs}$, is calculated using Rosenfeld's fundamental measure theory (FMT),^{155,156} postulated to have the form

$$\beta A^{ex,hs}[\rho_i(\mathbf{r})] = \int d\mathbf{r} \Phi^{ex,hs}[n_\alpha(\mathbf{r})] \quad (7.12)$$

where $\Phi^{ex,hs}[n_\alpha(\mathbf{r})]$ is the excess Helmholtz free energy density due to the hard core interactions. $\Phi^{ex,hs}[n_\alpha(\mathbf{r})]$ is assumed to be a function of only the system averaged fundamental geometric measures, $n_\alpha(\mathbf{r})$, of the particles, given by

$$n_\alpha(\mathbf{r}) = \sum_{l=C1,C2,\dots} \sum_{i=1}^{m_l} n_{\alpha,i}(\mathbf{r}) = \sum_{i=1}^N \int \rho_i(\mathbf{r}_1) w_i^{(\alpha)}(\mathbf{r} - \mathbf{r}_1) d\mathbf{r}_1 \quad (7.13)$$

where $\alpha = 0, 1, 2, 3, V1, V2$, representative of the six scalar and vector weight functions used in Rosenfeld's formalism.^{155,156} In the FMT formalism, $\Phi^{ex,hs}[n_\alpha(\mathbf{r})]$ has the form

$$\Phi^{ex,hs}[n_\alpha(\mathbf{r})] = -n_0 \ln(1 - n_3) + \frac{n_1 n_2 - \mathbf{n}_{v1} \cdot \mathbf{n}_{v2}}{1 - n_3} + \frac{n_2^3 - 3n_2 \mathbf{n}_{v2} \cdot \mathbf{n}_{v2}}{24\pi(1 - n_3)^2} \quad (7.14)$$

The free energy due to long-range attraction can be included within the mean field approximation¹⁴⁷

$$A^{ex,att}[\rho_i(\mathbf{r})] = \frac{1}{2} \sum_{i=1}^N \sum_{j=1}^N \int_{|\mathbf{r}_2 - \mathbf{r}_1| > \sigma_{ij}} d\mathbf{r}_1 d\mathbf{r}_2 u_{ij}^{att}(|\mathbf{r}_2 - \mathbf{r}_1|) \rho_i(\mathbf{r}_1) \rho_j(\mathbf{r}_2) \quad (7.15)$$

The association functional was originally developed by Chapman^{12,29} by extending TPT1.

Below the association functional is given for an associating polyatomic mixture

$$\beta A^{ex,assoc}[\rho_i(\mathbf{r})] = \int d\mathbf{r}_1 \sum_{i=1}^N \rho_i(\mathbf{r}_1) \sum_{A \in \Gamma^{(i)}} \left(\ln \chi_A^i(\mathbf{r}_1) - \frac{\chi_A^i(\mathbf{r}_1)}{2} + \frac{1}{2} \right) \quad (7.16)$$

The first summation is over all segments (on all chains in the mixture) and the second summation is over all the associating sites on segment i of chain l . $\chi_A^i(\mathbf{r}_1)$ represents the fraction of segments of type i which are not bonded at their site A . This fraction unbonded is given by

$$\chi_A^i(\mathbf{r}_1) = \frac{1}{1 + \int d\mathbf{r}_2 \sum_{k=1}^N \rho_k(\mathbf{r}_2) \sum_{B \in \Gamma^{(k)}} \chi_B^k(\mathbf{r}_2) \Delta_{AB}^{ik}(\mathbf{r}_1, \mathbf{r}_2)} \quad (7.17)$$

The degree of association is controlled by the term

$$\Delta_{AB}^{ik}(\mathbf{r}_1, \mathbf{r}_2) = \kappa \left[\exp(\beta \varepsilon_{Ai, Bk}^{assoc}) - 1 \right] y^{ik}(\mathbf{r}_1, \mathbf{r}_2) \quad (7.18)$$

Here κ represents a geometric constant (accounts for the entropic cost associated with the orientations and bond volume of the associating segments), $\varepsilon_{Ai, Bk}^{assoc}$ is the associating energy between compatible sites A and B on segments i and k , and $y^{ik}(\mathbf{r}_1, \mathbf{r}_2)$ is the cavity correlation function for the inhomogeneous hard sphere reference fluid. The cavity correlation function can be approximated using its bulk value⁷² evaluated at contact using a weighted density^{33,34}

$$y^{ik}(\mathbf{r}_1, \mathbf{r}_2) \approx \left[y^{ik}(\sigma, \bar{\rho}_j(\mathbf{r}_1)) \times y^{ik}(\sigma, \bar{\rho}_j(\mathbf{r}_2)) \right]^{1/2} \quad (7.19)$$

where $\bar{\rho}_j(\mathbf{r}_1)$ represents the weighted density of segment j at position \mathbf{r}_1 . In this work, the simple weighting is used

$$\bar{\rho}_j(\mathbf{r}_1) = \frac{3}{4\pi\sigma^3} \int_{|\mathbf{r}_1 - \mathbf{r}_2| < \sigma} d\mathbf{r}_2 \rho_j(\mathbf{r}_2) \quad (7.20)$$

It has already been demonstrated how the association free energy functional based on Wertheim's first order thermodynamic perturbation theory can be used in the limit of complete association to form a polyatomic fluid (tangentially bonded chains) from a mixture of associating spheres.^{32,193,195} In this chapter we demonstrate how, starting from the same form of the inhomogeneous association free energy functional, the full range of

association can be investigated. When deriving the chain contribution to the free energy, $\epsilon^{assoc} \rightarrow \infty$ and an additional bonding potential $v_{bond}^{ik}(\mathbf{r}_1, \mathbf{r}_2)$ for tangentially bonded segments is included in the above expression.^{32-34,165,193,195}

7.2.2.2 Free energy functional derivatives

All the functional derivatives are essential in solving the Euler-Lagrange equations (from eq. (7.9)), which give the density profile. The functional derivative of the free energies are given

$$\frac{\delta \beta A^{id}}{\delta \rho_j(\mathbf{r})} = \ln \rho_j(\mathbf{r}) \quad (7.21)$$

$$\frac{\delta \beta A^{ex,hs}}{\delta \rho_j(\mathbf{r})} = \int d\mathbf{r}_1 \frac{\delta \Phi^{ex,hs}[n_i(\mathbf{r}_1)]}{\delta \rho_j(\mathbf{r})} \quad (7.22)$$

$$\frac{\delta \beta A^{ex,att}}{\delta \rho_j(\mathbf{r})} = \sum_{i=1}^N \int_{|\mathbf{r}-\mathbf{r}_i| > \sigma_{ij}} d\mathbf{r}_1 \beta u_{ij}^{att}(|\mathbf{r}-\mathbf{r}_1|) \rho_i(\mathbf{r}_1) \quad (7.23)$$

$$\frac{\delta \beta A^{ex,chain}}{\delta \rho_j(\mathbf{r})} = \sum_{A \in \Gamma^{(j)}} \ln \chi_A^j(\mathbf{r}) - \frac{1}{2} \sum_{k=1}^N \sum_{k'}^{\{k'\}} \int \rho(\mathbf{r}_1) \frac{\delta \ln y^{kk'}(\bar{\rho}_j(\mathbf{r}_1))}{\delta \rho_j(\mathbf{r})} d\mathbf{r}_1 \quad (7.24)$$

In the above chain functional derivative, all association sites considered in this expression are representative of the sites responsible for the molecular connectivity of the chains in the mixture, which are formed by applying the limit of complete association ($\{k'\}$ is the set of all segments bonded to segment k on chain l). Details regarding the above functional derivatives are given in earlier works.^{32,193,195} Below, the functional derivative for the full range of association is given. Details of this derivation can be found in the Appendix.

$$\frac{\delta \beta A^{ex,assoc}}{\delta \rho_j(\mathbf{r})} = \sum_{A \in \Gamma^{(j)}} (\ln \chi_A^j(\mathbf{r})) - \frac{1}{2} \sum_{i=1}^N \sum_{k=1}^N \int d\mathbf{r}_1 \rho_i(\mathbf{r}_1) \sum_{A \in \Gamma^{(i)}} (1 - \chi_A^i(\mathbf{r}_1)) \left[\frac{\delta \ln y^{ik}(\bar{\rho}_j(\mathbf{r}_1))}{\delta \rho_j(\mathbf{r})} \right] \quad (7.25)$$

The above expression is the final form for associating chains. The term $\frac{\delta \ln y^{ik}(\bar{\rho}_j(\mathbf{r}_1))}{\delta \rho_j(\mathbf{r})}$ only contributes for segments k with association sites that are eligible to bond to sites located on segment i . Substituting the functional derivatives of the free energies in the Euler-Lagrange (eq. (7.9)) allows for the solution of the equilibrium density profile of the polymer segments. For complete details of the density profile expressions, the reader is referred to previous work^{32,193,195} and chapter 6 (section 6.2.3).

7.3 Results and discussion

The primary focus of this section is to establish the capability of the theory to handle a wide range of associating polymer systems. In this section, results are presented for associating mixtures near surfaces and in the bulk, over a wide range of conditions in comparison with available simulation and experimental data. The associating schemes and mixtures investigated in this work are illustrated in Figure 7.1. First the theory is validated near a hard wall, illustrating the effect of varying the association strength on the behavior of the fluid (neglecting dispersion interactions). Next, an associating mixture is considered at high association strengths, showing how different association schemes can result in complex molecular architectures or supramolecules (see Figure 7.1 (b)). These results are compared and agree very well with available simulation results for a star polymer confined between two hard surfaces from Yethiraj and Hall.³⁴¹ Finally, the

theory is demonstrated for a challenging problem of interest, a bulk associating mixture of two homopolymers with end functional segments capable of reversibly bonding to form supramolecular diblock copolymers. For this system, we systematically explore the phase diagram, demonstrating how competing effects (chain length, chemical incompatibilities, and bonding energies) can result in unique polymer morphologies (microphase lamellar separation, two phase macrophase separation) and complex phase behavior (regions of reentrant order-disorder transitions in the phase diagram, as observed in experiments). These examples elucidate the ability of the theory to correctly model and capture the complex fluid behavior for associating polymer systems. Such a theory is important to the understanding and development in many problems and applications (discussed in the Introduction) where temperature can be used to control the reversible bonding, phase behavior, and material properties of the system.

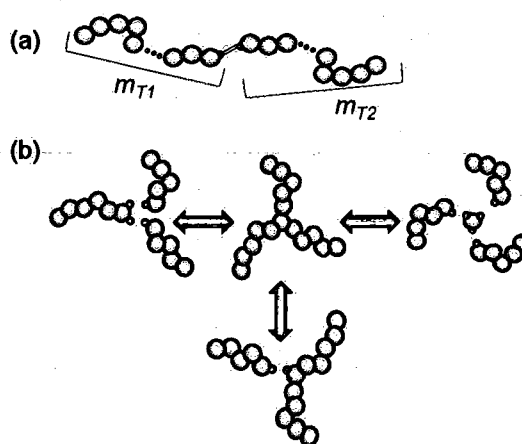


Figure 7.1: Illustration of associating schemes used in this work: (a) end associating functional groups (terminal associating segment with one site) and (b) schemes capable of forming a star polymer architecture (3 arms, $N=16$) at high association strengths.

7.3.1 Associating polymers near a wall

First, we apply the proposed theory to a simple model of associating molecules and investigate the structure of the fluid near a hard surface. As discussed previously in section 7.1, there are two approaches to include association.²⁹ The inhomogeneous approach (the proposed approach, outlined in section 7.2) and the weighted approach (included below) are compared in Figure 7.2. The second approach approximates the association free energy functional using the bulk equation of state evaluated a weighted density

$$\beta A^{ex,assoc}[\rho_i(\mathbf{r})] = \int d\mathbf{r}_1 \sum_{i=1}^N \rho_i(\mathbf{r}_1) \sum_{A \in \Gamma^{(i)}} \left(\ln \bar{\chi}_A^i(\mathbf{r}_1) - \frac{\bar{\chi}_A^i(\mathbf{r}_1)}{2} + \frac{1}{2} \right) \quad (7.26)$$

where the fraction of segments of type i which are not bonded at their site A is given by

$$\bar{\chi}_A^i(\mathbf{r}_1) = \frac{1}{1 + \sum_{k=1}^N \bar{\rho}_k(\mathbf{r}_2) \sum_{B \in \Gamma^{(k)}} \bar{\chi}_B^k(\mathbf{r}_2) \Delta_{AB}^{ik}(\mathbf{r}_1, \mathbf{r}_2)} \quad (7.27)$$

and $\Delta_{AB}^{ik}(\mathbf{r}_1, \mathbf{r}_2)$ is defined as before in eq. (7.18). The accuracy of the weighted approach is dependent on the weight functions used. For comparison, the same weighted density used in the calculation of the cavity correlation function in eqs. (7.19) and (7.20) is used in the second approach. The functional derivative can be found in previous work.³¹

Figure 7.2 captures the effect of varying the association strength on the structure of a pure associating fluid near a hard wall. Depletion from the surface is captured at low concentrations, while packing effects increase the accumulation of segments at the surface at higher densities (dispersion interactions are neglected here, $\epsilon^{LJ}=0$). In Figure 7.2 (a), the simple case of a dimerizing hard sphere fluid is presented at $\rho_b \sigma^3 = 0.1999$ and

$\epsilon^{assoc}/k_bT=14$ (right vertical axis), and at $\rho_b\sigma^3=0.4868$ and $\epsilon^{assoc}/k_bT=11$ (left vertical axis), in comparison with simulation data.³⁰ From these results, it is clear that at lower densities and high association energies, the weighted approach is unable to capture the correct structure of the fluid even qualitatively (these results are consistent with the results found previously by Segura et al.³⁰ using the Tarazona^{152,153} weight functions). In contrast, the inhomogeneous form provides a more accurate expression for the free energy of association and is able to capture the correct structure of the fluid at these conditions. At higher densities, the weighted approach is much improved, however the inhomogeneous approach is still superior and in better quantitative agreement with the simulations. In Figure 7.2 (b), the model assumes a pure homopolymer ($m=4$) where a

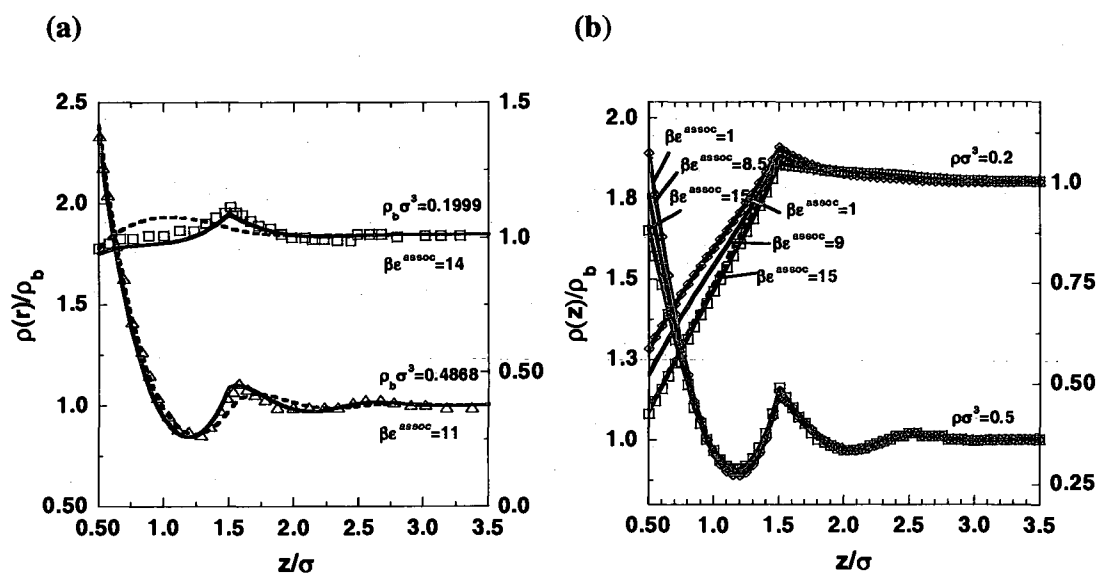


Figure 7.2: Effect of varying bonding strength (ϵ^{assoc}) on the structure of an associating fluid (associating scheme from Figure 7.1 (a)) near a smooth hard surface. Here dispersion interactions are neglected, $\epsilon^{LJ}=0$. Lines represent theoretical results using the inhomogeneous association free energy functional (solid lines) and the weighted bulk form association free energy functional (dashed lines, provided for comparison at highest association energies). In (a), a dimerizing hard sphere fluid is presented at $\rho_b\sigma^3=0.1999$ and $\beta\epsilon^{assoc}=14$ (right vertical axis), and at $\rho_b\sigma^3=0.4868$ and $\beta\epsilon^{assoc}=11$ (left vertical axis). Symbols represent simulation data.³⁰ In (b), the structure of an associating polymer fluid ($m=4$) is presented at $\rho_b\sigma^3=0.2$ (right vertical axis) and $\rho_b\sigma^3=0.5$ (left vertical axis). Here, symbols represent results for a nonassociating 4mer (\diamond) and 8mer (\square).

a single association site is located on one of the terminal segments of the chain and is able to bond with other chains in the fluid (see the association scheme presented in Figure 7.1 (a)). In Figure 7.2 (b), the symbols represent *i*SAFT results for a nonassociating 4mer (\diamond) and 8mer (\square), while the lines represent *i*SAFT results for the associating 4mers. The weighted approach is included for comparison at the highest association strengths (dashed lines). In Figure 7.2 (b), the results indicate that both approaches capture the correct behavior at high and low densities for associating chains, though there are some minor quantitative differences (hard to distinguish in figure). Such results suggest that the weighted approach may be sensitive to the concentration of associating segments in the system. In this example, as the chain length increases, the effect of association decreases and the concentration of bonding segments in the fluid decreases, scaling as $1/m$. In comparing parts (a) and (b) of Figure 7.2, both approaches are accurate for lower concentrations of associating segments (Figure 7.2 (b)), but give inaccurate structure under certain conditions (high association strengths at lower densities) for systems with a higher concentration of associating segments (Figure 7.2 (a)). All remaining results presented are therefore based on the inhomogeneous form of the association functional, because of its versatility and ability to handle any association scheme, especially for more complex heteronuclear systems that may involve many associating segments. From Figure 7.2 (b), as expected, the behavior of an associating linear chain (with one associating site on a terminal segment) varies between that of a nonassociating chain of the same length (in this case a 4mer) and that for a nonassociating chain twice as large (8mer). When the association energy is low ($\epsilon^{assoc}/k_bT=1$), the profiles are similar to the nonassociating 4mer. As the association energy increases, the concentration of 8mers in

the mixture also increases and approaches the behavior of a pure nonassociating 8mer. Higher association energies result in higher concentrations of longer chains, which lead to lower contact densities at the surface due to conformational entropic effects.

Of course, more involved association schemes, where the polymer molecule may involve multiple associating segments and/or multiple sites, can lead to more complex polymer architectures (at high association strengths). Figure 7.3 demonstrates such an example, again considering only association interactions. Here we consider a polymer mixture using any of the schemes presented in Figure 7.1 (b). High bonding strengths (results in Figure 7.3 use $\epsilon^{assoc}/k_b T \geq 30$) create a large population of star polymers (3 arms, $N=16$) in the melt, so that we are able to compare the structure of the fluid confined between two hard surfaces (separated at distance $H=16\sigma$) with available simulation data by Yethiraj and Hall.³⁴¹ The agreement between the theory and the simulation results are

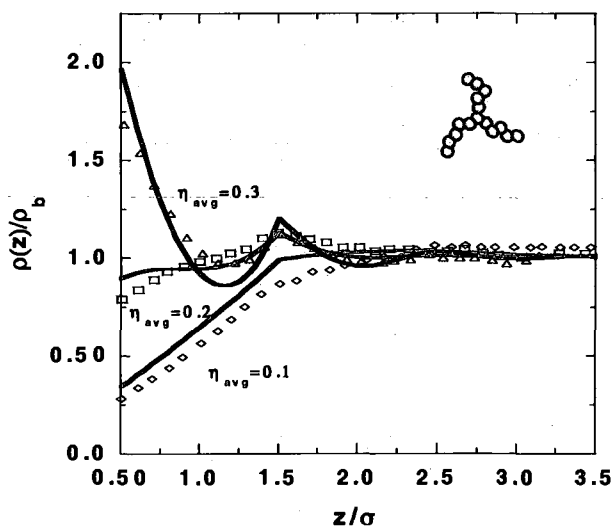


Figure 7.3: The density distribution of a star polymer (3 arms, $N=16$) between two hard walls separated at a distance $H=16\sigma$ (profile only given near one wall) at $\eta_{avg}=0.3, 0.2,$ and 0.1 . A high population of star polymers is formed in the melt at high bonding strengths (e.g., $\beta\epsilon^{assoc}=30$) using any of the association schemes given in Figure 7.1 (b). Symbols represent simulation data from Yethiraj and Hall³⁴¹ and lines represent results from *iSAFT*. The density profiles are normalized to the bulk value.

good, capturing the competition between packing and entropic effects at different average packing fractions (η_{avg}) of the fluid in the confined space. Symbols represent simulation data, while solid lines represent *i*SAFT results. In the figure, the density profiles are normalized to their bulk value (ρ_b). Because the profiles are symmetric about the middle of the confinement, only the profiles near one of the surfaces are shown. In our model, the concentration of star polymer formed in the melt, and thus the fluid structure at the surface, can be controlled by the temperature (or varying reversible bonding energy). Differences in the contact density can be attributed to inaccuracies in the bulk equation of state (which over predicts the pressure). Even more complex association schemes can be applied to multicomponent mixtures to form star and comb polymers with arms of arbitrary lengths.

In this section, the ability of the *i*SAFT DFT to capture compressibility effects and the local structure of associating macromolecules near surfaces and in confined environments was demonstrated. Future studies using *i*SAFT could provide interesting insights into some of today's more challenging problems involving associating polymers near surfaces and in confined environments, including lubrication and friction, adhesion, nanocomposites, blood flow and drug delivery.

7.3.2 Self-assembly of associating polymers into inhomogeneous phases

In this section, we consider a binary mixture of two homopolymers of equal concentrations and chain lengths. Homopolymer C_1 is assigned one association site (site A) on a terminal bead (see association scheme Figure 7.1 (a)) that is allowed to reversibly bond to a similar site (site B) on the other component in the mixture (C_2). All systems considered in this section have a melt-like, total segment density of $\rho_b\sigma^3=0.85$. In this

model, the dispersion energy defines the chemical incompatibilities of the two components in the mixture, where $\varepsilon^{C1,C1} = \varepsilon^{C2,C2} = \varepsilon^{LJ}$ and $\varepsilon^{C1,C2} = 0$. This parameter can be correlated with the traditional Flory Huggins interaction parameter χ .^{192,342} This particular system is of high interest because of the broad range of phase behaviors possible when unlike polymer species are linked by reversible bonds into supramolecular polymers, in this case supramolecular diblock copolymers. It is well known from experiments^{312,343} that reentrant behavior occurs for low molecular weight associating polymers upon raising or lowering the temperature. Here we systematically explore the phase diagram by varying the chain length ($N = m_{C1} + m_{C2}$), the dispersion energy (ε^{LJ}), and the association bonding energy (ε_{AB}^{assoc}), covering all segregation regimes.

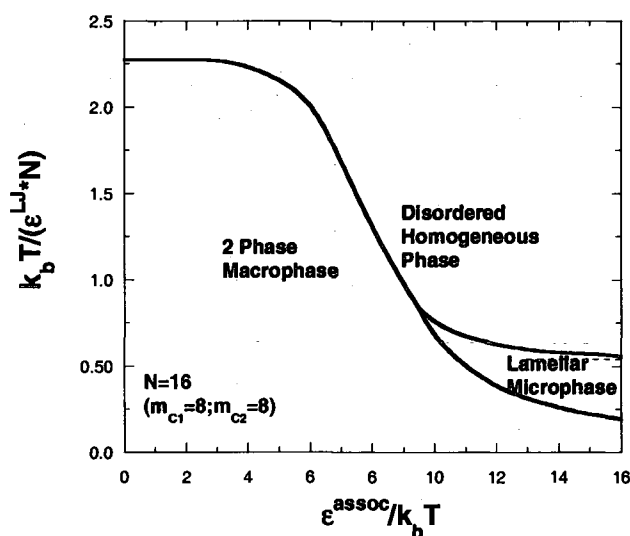


Figure 7.4: Phase diagram for an associating polymer mixture. The binary mixture is at a total segment density of $\rho_b \sigma^3 = 0.85$ and is symmetric ($m_{C1} = 8$ and $m_{C2} = 8$, equal concentrations, association scheme from Figure 7.1 (a)). Three distinct phases are present in the phase diagram: a homogeneous disordered phase, a 2 phase macrophase, and a lamellar microphase.

Figure 7.4 demonstrates how competing effects between the association bonding energy and the dispersion energy can lead to three distinct phases: a homogeneous

disordered phase (where C_1 and C_2 are miscible), a macrophase separation (liquid-liquid immiscibility), and a microphase lamellar separation. From the figure, low dispersion energies (low degree of incompatibility between the two components) and low association energies lead to a homogeneous disordered phase (DIS). Upon increasing ϵ^{LJ} at low association energies, a phase transition from the disordered state to a macrophase separation (2 phase) occurs. This occurs due to the increased incompatibility between the two components in the mixture and the low concentration of copolymer present in the system. Note that increasing ϵ^{LJ} at fixed ϵ^{assoc} does not correspond to decreasing the temperature, since ϵ^{assoc} is also temperature dependent (addressed below). An example of macrophase separation is illustrated in Figure 7.5 (a), characterized by the C_1 and C_2 rich phases. However, as the association strength is increased, the concentration of diblock

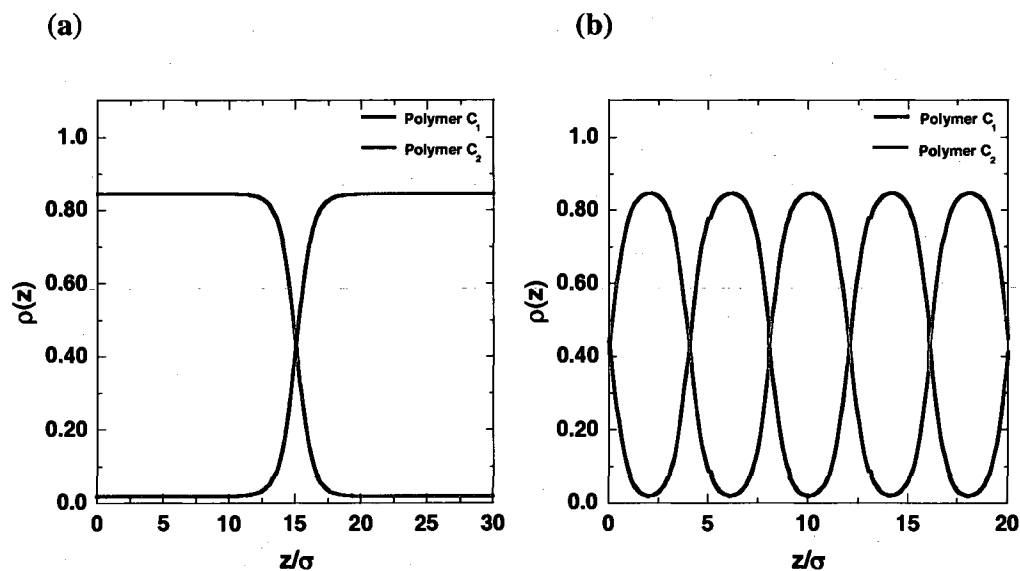


Figure 7.5: (a) Example of a typical density profile for a liquid-liquid macrophase separation. (b) Example of a typical density profile for a lamellar microphase separation. A lamellar phase can form at higher association strengths where a higher concentration of copolymer exists in the mixture. The lamellar period for this example structure is $L=8\sigma$. The equilibrium lamellar period (L_e) for the microphase is determined via the grand free energy (See Figure 7.6; changing the bonding energy or the dispersion energy affects the equilibrium spacing of the lamellar structure).

copolymer increases, thus increasing the probability of microphase separation (see Figure 7.4). Figure 7.5 (b) illustrates a typical microphase structure, where the increased concentration of diblock copolymers ($N=16$) may self-assemble into a lamellar phase.

When both the dispersion energy and the association energy are high, macrophase or microphase separation can occur. The phase boundary between these two phases can be determined by comparing the free energies to establish the more stable phase (the more thermodynamically favorable phase). In comparing the free energies between the macrophase and microphase, first the equilibrium lamellar period (L_e) for the microphase must be determined (as changing the bonding energy or the dispersion energy affects the equilibrium spacing of the lamellar structure). This is done by calculating the grand free energy (Ω) of the system. Figure 7.6 plots the grand free energy per volume for different association and dispersion strengths, as a function of the width of the computational domain. Similar results and trends are predicted under other sets of conditions. From the

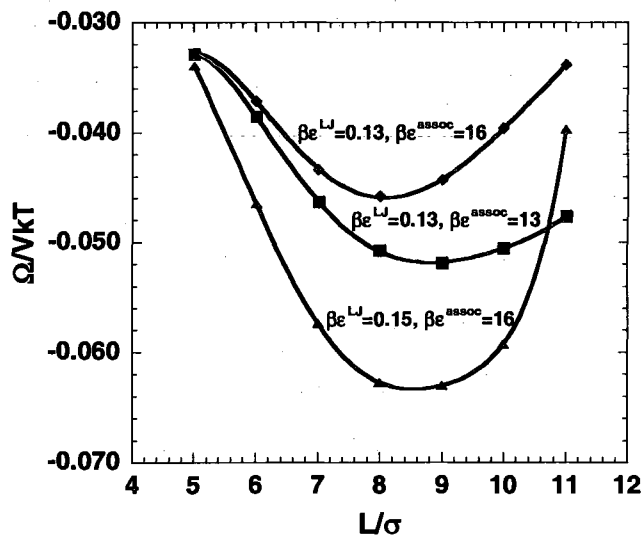


Figure 7.6: Grand free energy per volume as a function of the computational domain at given association and dispersion energies ($m_{C1}=8, m_{C2}=8, N=16$). The equilibrium spacing is determined as the width at which a minimum in the free energy occurs. Similar results and trends are predicted under other sets of conditions and chain lengths.

figure, the equilibrium spacing is determined as the width at which a minimum in the free energy occurs. For the lamellar phases, at a given association energy, the equilibrium lamellar period increases and the equilibrium free energy decreases as the dispersion energy becomes larger (the increasing incompatibility between the two components promotes a decreasing number of interfaces to minimize the number of contacts between C_1 and C_2). At fixed dispersion energy, decreasing the association energy results in a larger L_e (and decreases the equilibrium free energy). Both trends encourage macrophase separation, as the lamellar phase transitions into a liquid-liquid phase as reflected in the phase diagram in Figure 7.4.

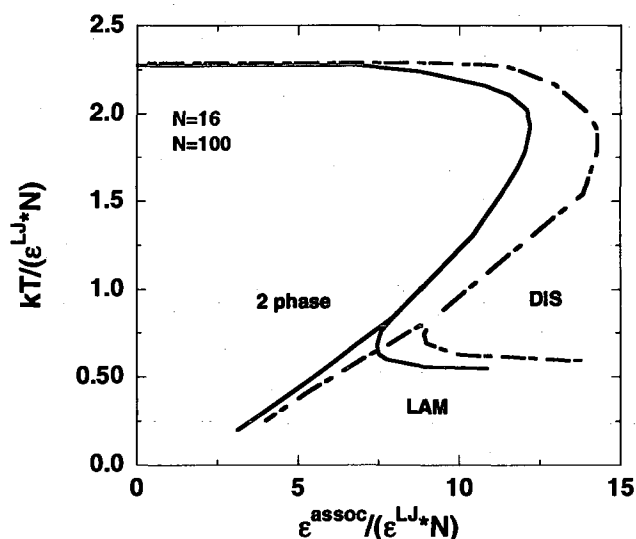


Figure 7.7: Phase diagram for associating polymer mixtures ($N=16$ and $N=100$) highlighting the effect of chain length and temperature on the phase behavior. Three distinct phases are present in the phase diagram: a homogeneous disordered phase (DIS), a macrophase (2 phase), and a lamellar microphase (LAM). Reentrant behavior is observed (DIS-2 phase-DIS and LAM-DIS-LAM) upon raising/lowering the temperature.

While Figure 7.4 highlights important features of the phase diagram, it does not show a clear dependence on temperature (as both coordinates are temperature dependent).

Figure 7.7 provides the phase diagram after scaling the thermal energy (k_bT) and the

bonding energy (ϵ^{assoc}) by the total dispersion interaction energy of the diblock chain ($\epsilon^{LJ} * N$). This provides a dimensionless temperature versus dimensionless bonding energy to demonstrate the effect of changing the temperature at a fixed ratio of ($\epsilon^{assoc} / \epsilon^{LJ} * N$).

When looking at this phase diagram, one notices regions where reentrant behavior occurs.

First, for $N=16$, it is obvious that reentrant behavior occurs upon raising/lowering the temperature over a large band of higher energy ratios ($\epsilon^{assoc} / \epsilon^{LJ} * N \approx 7.90-12.25$),

predicting a sequence of transitions from disordered to macrophase to disordered phases.

Here, such reentrant behavior is due to hydrogen-bonding interactions (similar behavior drives closed loop LL immiscibility, which is unique to unlike, associating mixtures). At low temperatures, the unlike pairs permit association and complete mixing (association between unlike species in the mixture result in the low temperature miscibility of the system, as indicated by the low temperature DIS). As the temperature is increased, many of these association bonds are broken, leading to immiscibility (2 phase separation).

Increasing the temperature further leads to increased kinetic motion in the fluid, which results in increased miscibility and complete mixing (high temperature DIS). A more narrow band ($\epsilon^{assoc} / \epsilon^{LJ} * N \approx 7.45-7.9$) displays transitions from lamellar to disordered to lamellar phases upon raising and lowering the temperature. Similar bands of reentrant behavior are also predicted in Figure 7.7 for longer diblock chains ($N=100$).

Homogeneous reentrant behavior has been observed experimentally.^{312,343} To our knowledge, no experiments have demonstrated reentrant behavior of an inhomogeneous phase in a supramolecular polymer system, although recent theoretical results (SCFT) by Feng et al.³²⁶ do predict inhomogeneous reentrant behavior involving a lamellar phase, consistent with the results presented here. It will therefore be interesting to see if such

reentrant inhomogeneous behavior can be observed in future experiments, based on these results. Finally, Figure 7.7 also highlights the effect of increasing the chain length in the associating mixture. As the chain length increases, the concentration of bonding segments in the mixture decreases (scales as $1/N$). As a result, for increasing N , a higher bonding energy is required to increase the concentration of copolymer in the mixture (needed to encourage microphase separation and a homogeneous disordered phase) and thus the two phase region becomes larger.

The *i*SAFT results presented in this section highlight the capabilities of the theory to correctly capture hydrogen bonding/association interactions in polyatomic systems. Even the fundamental case of associating homopolymers considered in this section challenges the theory to capture the presence and absence of mesophases and liquid-liquid phase behavior, as well as intriguing reappearing phases in the phase diagram. More detailed extensions of this study can be conducted, specifically to study and understand more complex, self-assembling associating polymer systems in the bulk. Such work includes multicomponent (ternary and higher) polymer blends, asymmetric cases (unequal concentrations and/or unequal chain lengths of the polymers), and multiple bonding sites on multiple polymer segments of varying size (leading to other supramolecular architectures beyond the diblock copolymer considered in this work). As the architecture becomes more complicated, the self-assembly of more complex, hierarchical morphologies can arise (for example, the self-assembly of Archimedean tiling patterns^{306-308,310}). Future studies of *i*SAFT to such challenging problems could aid in the development and production of high performance soft materials and separation applications.

7.4 Conclusions

The *i*SAFT density functional theory has been extended to associating polyatomic molecular systems, using the inhomogeneous form of the association functional. The approach provides a very accurate method for modeling a wide range of complex associating polyatomic systems, capable of investigating the full range of association for any bonding scheme. In this work, the ability of the theory to model associating polymers near surfaces and in the bulk over a wide range of conditions was demonstrated. Even for the fundamental associating polymers chosen in this work, the results highlight a wide range of complex behaviors, demonstrating how reversible bonding governs the structure of a fluid near a surface (in good agreement with available simulation data), the molecular connectivity (formation of supramolecules and complex architectures), and the phase behavior of the system (including reentrant order-disorder phase transitions). The introduction of hydrogen bonding interactions thus leads to a new class of self-assembling, highly functional materials. It is evident that *i*SAFT could significantly aid in the understanding and experimental design of more complex, associating polymer systems, with applications to the fields of biomolecules, separations, high performance soft materials, polymer mediated adhesion and lubrication, and polymer-inorganic nanocomposites.

CHAPTER 8

An *i*SAFT density functional theory for the intermolecular and intramolecular correlation functions of polymeric fluids

8.1 Introduction

There is considerable interest in developing theories capable of accurately predicting the microscopic liquid structure of polymeric fluids. Knowledge of the local structure provides information about how molecules pack against one another, as well as how thermodynamic properties of polymers are affected by bond angles (intramolecular stiffness and flexibility), chain branching, and local chemistry. Integral equation theory (IET) has long been used as the conventional method for predicting the correlation functions of chain fluids. Curro and Schweizer^{19,20} developed the polymer reference interaction site model (PRISM) theory for linear chain molecules by extending the RISM theory of Chandler et al.^{344,345} The intermolecular correlation functions are calculated for a given set of intramolecular correlation functions after the Ornstein-Zernike (OZ) equation is formulated (and coupled with a closure relation). The PRISM theory has been successfully applied to describe the microscopic structure of a broad range of polymeric systems, including polymer melts,³⁴⁶ polyelectrolytes,³⁴⁷⁻³⁴⁹ polymer blends,^{350,351} and liquid crystals.³⁵² Unfortunately, the PRISM approach does suffer from shortcomings. As mentioned, knowledge of the intramolecular correlation functions is

required to solve the intermolecular correlation functions (except for rigid molecules that have only one configuration and the inter- and intramolecular correlation functions are therefore not functionals of each other). Because the intramolecular correlations functions are typically unknown, self-consistency between inter- and intramolecular correlation functions are achieved via a single chain molecular simulation. As previously discussed in chapter 6, the PRISM IET has been shown to be very sensitive to the particular closures employed. For example, using standard closure approximations, PRISM IET predicts short-range structural correlations for rigid and semiflexible polymers, in the rod limit, that are qualitatively inaccurate.^{353,354} In addition, various closures to the PRISM equation often give different results, thereby making the development of closure approximations, especially for new situations, very difficult. Finally, the theory is very inaccurate at low densities.³⁵⁵ Since all routes to the thermodynamic properties of polymers require reliable structural properties from low to high densities, the integral equation approach is not best suited for phase diagram calculations.

Alternative theories based on Wertheim's theory for associating fluids⁴⁻⁷ have been developed as new liquid state theories for polymers. Kierlik and Rosenberg^{162,163} developed a density functional theory (DFT) for polymeric fluids based on Wertheim's thermodynamic perturbation theory (TPT), where a fluid of chains is formed from a system of associating monomers. The approach gives reasonable intermolecular correlation functions for short chains at high densities. However, the theory is not suited for long chains at semi-dilute and dilute conditions. In the theory, Kierlik and Rosenberg neglect intramolecular excluded volume effects (intramolecular structure factor is that of

an ideal freely jointed chain). As a result, the theory is unable to predict the nonideal behavior of intramolecular correlation functions of polymeric fluids. Alternatively, integral equation approaches based on Wertheim's theory have also been applied by numerous groups.³⁵⁶⁻³⁵⁸ These approaches fail to predict the nonideal behavior of intramolecular correlation functions even qualitatively, failing to correctly capture the packing effects on the intramolecular structure.

More recently, the Percus test-particle method has been used to investigate the correlation functions in polymeric fluids. From this idea,²⁶⁹ the structure of a fluid can be represented by the local inhomogeneous density profile around an arbitrary fixed particle. Yethiraj et al.³⁵⁹ applied this method and extended this idea to polymers. Using a density functional theory, Yethiraj et al. demonstrated how the intermolecular correlation functions could be calculated from the density profile of the fluid in the external field of a single polymer molecule fixed at the origin. The theory is very accurate in comparison with simulation data for hard-sphere chains. The drawback of the theory is that it is very computationally intensive and requires a two-molecule simulation as input.³⁵⁹ Unlike a monotomic fluid, the application of Percus' method to a fixed polymer molecule involves a complex external field that depends on the positions of all segments on the fixed molecule.

Alternatively, Yu and Wu³⁶⁰ also apply the Percus test-particle method using density functional theory, but circumvent the computational expense and the required molecular simulation input. Instead of fixing an entire polymer chain at the origin, Yu and Wu fix one segment at the origin. The inter- and intramolecular correlation functions are then calculated directly from the density distributions of segments around the fixed segment,

from the tethered chains (as part of the molecule containing the fixed segment) and from the free polymer chains.

In this chapter, Percus' test-particle method is applied to the *i*SAFT density functional theory using the extended approach from Yu and Wu.³⁶⁰ In the next section, the theory and model for this work are discussed. Results are presented in section 8.3 and compared with available simulation data for hard-sphere chains. Concluding remarks are then presented in section 8.4.

8.2 *i*SAFT model

8.2.1 Inter- and intramolecular correlation functions

In this work, we consider a polymeric fluid consisting of tangentially connected hard-sphere chains. Using the extended test-particle method proposed by Yu and Wu,³⁶⁰ we allow one segment from an arbitrary selected chain to be fixed at the origin. The system considered is equivalent to a mixture of 3 polymeric components (F , T_1 and T_2) in a

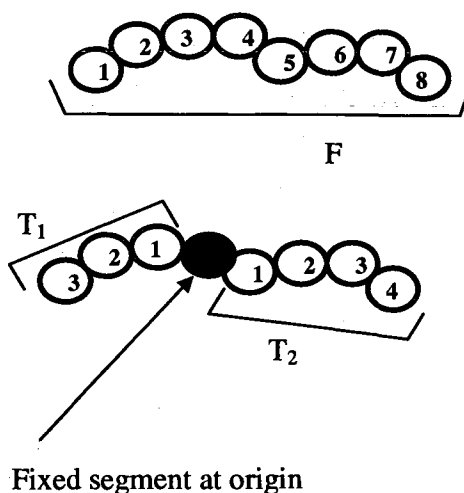


Figure 8.1: Schematic of the test particle model used in this work. Here a middle segment from a hard-sphere chain of 8 segments is fixed at the origin. The inter- and intramolecular segment-segment correlation functions are calculated from the density distributions of the tethered segments (T_1 and T_2) and of the free molecules (F) around the fixed segment at the origin.

spherically symmetric external field due to the fixed segment, as depicted in Figure 8.1. From the figure, the free molecules are represented by F composed of m_F segments, while the tethered fragments are represented by T_1 and T_2 composed of m_{T1} and m_{T2} segments, respectively. As demonstrated in previous chapters, the starting point of the density functional theory is the development of an expression for the grand free energy, Ω , as a functional of the equilibrium density profile in an external field. In the above model, the external field is a single, fixed polymer segment at the origin. The grand free energy can be related to the Helmholtz free energy $A[\rho(\mathbf{r})]$ through the Legendre transform,¹³

$$\begin{aligned} \Omega[\rho_i^{(F)}(\mathbf{r}), \rho_i^{(T1)}(\mathbf{r}), \rho_i^{(T2)}(\mathbf{r})] = & A[\rho_i^{(F)}(\mathbf{r}), \rho_i^{(T1)}(\mathbf{r}), \rho_i^{(T2)}(\mathbf{r})] \\ & - \sum_{l=F, T1, T2} \sum_{i=1}^{m_l} \int d\mathbf{r}' \rho_i^{(l)}(\mathbf{r}') (\mu_i^{(l)} - V_{ext}^{i,l}(\mathbf{r}')) \end{aligned} \quad (8.1)$$

where $\rho_i^{(l)}(r)$ is the density of the i th segment on chain l at position \mathbf{r} , $\mu_i^{(l)}$ is the chemical potential of that segment, and $V_{ext}^{i,l}$ is the external field acting on that segment. The first summation is over all chains l in the mixture (F, T_1, T_2), and the second summation is over all segments on chain l . The external field of the fixed segment exerted on a segment directly bonded to the fixed segment (segments '1' of T_1 and T_2 in Figure 8.1) is the segment-segment interaction plus the bonding energy (v_{bond}).

$$V_{ext}^{1,l}(r) = \begin{cases} v_{bond} & r = \sigma \\ \infty & r < \sigma \end{cases} \quad (8.2)$$

where $l=T_1, T_2$. The external field of the fixed segment on all other segments in the system is equal to the segment-segment interaction energy.

$$V_{ext}^{i,l}(r) = \begin{cases} \infty & r < \sigma \\ 0 & r \geq \sigma \end{cases} \quad (8.3)$$

By minimizing the grand free energy with respect to the density profiles, the density distribution of the free polymer segments and the tethered polymer segments can be determined.

$$\frac{\delta\Omega}{\delta\rho_i^{(F)}(\mathbf{r})} = \frac{\delta\Omega}{\delta\rho_i^{(T_1)}(\mathbf{r})} = \frac{\delta\Omega}{\delta\rho_i^{(T_2)}(\mathbf{r})} = 0 \quad (8.4)$$

The segment distribution of the free molecules (F) around the fixed segment is related to the intermolecular site-site correlation function

$$g_{ij}(r) = \frac{\rho_{i,j}^{(F)}(r)}{\rho_b^{(F)}} \quad (8.5)$$

where $\rho_{i,j}^{(F)}(r)$ is the density profile of segment i on molecule F around the fixed segment j . The distribution of segments from fragments T_1 and T_2 are related to the intramolecular correlation function

$$\omega_{ij}(r) = \rho_{i,j}^{(T)}(r). \quad (8.6)$$

where $\rho_{i,j}^{(T)}(r)$ is the density of segment i on the tethered chain (T_1 or T_2) from the fixed segment j . There is only one tethered polymer chain (one T_1 and/or one T_2), therefore the following normalization condition is satisfied

$$\int \rho_i^{(T)}(r) dr = 1 \quad (8.7)$$

From the site-site correlation functions, we calculate the average intermolecular correlation

$$g(\mathbf{r}) = \frac{1}{m_F} \sum_{i=1}^{m_F} \sum_{j=1}^{m_F} g_{ij}(\mathbf{r}) \quad (8.8)$$

and the average intramolecular correlation function is given as

$$\omega(\mathbf{r}) = \frac{1}{m_F} \sum_{i=1}^{m_F} \sum_{j=1}^{m_F} \omega_{ij}(\mathbf{r}) . \quad (8.9)$$

8.2.2 Free energies

The total Helmholtz free energy functional can be decomposed into an ideal and excess contribution,

$$A[\rho_i^{(F)}(\mathbf{r}), \rho_i^{(T1)}(\mathbf{r}), \rho_i^{(T2)}(\mathbf{r})] = A^{id}[\rho_i^{(F)}(\mathbf{r}), \rho_i^{(T1)}(\mathbf{r}), \rho_i^{(T2)}(\mathbf{r})] + A^{ex,hs}[\rho_i^{(F)}(\mathbf{r}), \rho_i^{(T1)}(\mathbf{r}), \rho_i^{(T2)}(\mathbf{r})] + A^{ex,chain}[\rho_i^{(F)}(\mathbf{r}), \rho_i^{(T1)}(\mathbf{r}), \rho_i^{(T2)}(\mathbf{r})] + A^{ex,att}[\rho_i^{(F)}(\mathbf{r}), \rho_i^{(T1)}(\mathbf{r}), \rho_i^{(T2)}(\mathbf{r})] \quad (8.10)$$

where the excess contribution consists of changes in the free energy due to excluded volume (*hs*), chain connectivity (*chain*), and long-range attraction (*att*), over the ideal gas state of the atomic mixture. In this work, long-range attractions are neglected. For brevity, the above expressions are not included here, but can be found in previous chapters (chapters 6 and 7).

8.2.3 Free energy derivatives

Recalling eq. (8.4), to solve the density profiles of all segments in the mixture, we obtain the following Euler-Lagrange equation,

$$\frac{\delta \beta A^{id}}{\delta \rho_j^l(\mathbf{r})} + \frac{\delta \beta A^{ex,hs}}{\delta \rho_j^l(\mathbf{r})} + \frac{\delta \beta A^{ex,chain}}{\delta \rho_j^l(\mathbf{r})} + \frac{\delta \beta A^{ex,att}}{\delta \rho_j^l(\mathbf{r})} = \beta(\mu_j^{(l)} - V_{ext}^{j,l}(\mathbf{r})) \quad (8.11)$$

Again, for brevity, the above expressions are not included in the text here. For complete details, the reader is referred back to previous chapters (chapters 6 and 7).

8.2.4 Equilibrium density profiles

Details regarding the expressions and procedure for solving the equilibrium density profiles are given in chapter 6 (section 6.2.3). For completeness, these expressions are reviewed again, with special emphasis on the new theory for the tethered chains. To obtain the equilibrium density profile, the functional derivatives of the free energies are substituted into the Euler-Lagrange equation (eq. (8.11)) to give

$$\ln \rho_j^{(l)}(\mathbf{r}) + \frac{\delta \beta A^{ex,hs}}{\delta \rho_j^{(l)}(\mathbf{r})} + \frac{\delta \beta A^{ex,att}}{\delta \rho_j^{(l)}(\mathbf{r})} + \sum_{A \in \Gamma^j} \ln \chi_A^{j,l}(\mathbf{r}) - \frac{1}{2} \sum_{q=F,T1,T2} \sum_{k=1}^{m_q} \sum_{k'}^{\{k'\}} \int \rho_k^{(q)}(\mathbf{r}_1) \frac{\delta \ln y^{kk',bulk}(\mathbf{r}_1)}{\delta \rho_j^{(l)}(\mathbf{r})} d\mathbf{r}_1 = \beta(\mu_j^{(l)} - V_{ext}^{j,l}(\mathbf{r})) \quad (8.12)$$

where $\{k'\}$ is the set of all segments bonded to segment k . This equation can be written to give the density profile

$$\rho_j^{(l)}(\mathbf{r}_j) = \exp(\beta \mu_{M_l}) \exp[D_j^{(l)}(\mathbf{r}_j) - \beta V_{ext}^{j,l}(\mathbf{r}_j)] I_{1,j}^{(l)}(\mathbf{r}_j) I_{2,j}^{(l)}(\mathbf{r}_j) \quad (8.13)$$

where $\mu_{M_l} \left(= \sum_{j=1}^{m_l} \mu_j^{(l)} \right)$ is the bulk chemical potential of chain l and $I_{1,j}^{(l)}(\mathbf{r}_j)$ and $I_{2,j}^{(l)}(\mathbf{r}_j)$

represent the multiple integrals. Recall from chapter 6 (section 6.2.2), $D_j^{(l)}(\mathbf{r})$ is given by

$$D_j^{(l)}(\mathbf{r}) = \frac{1}{2} \sum_{q=F,T1,T2} \sum_{k=1}^{m_q} \sum_{k'}^{\{k'\}} \int \rho_k^{(q)}(\mathbf{r}_1) \frac{\delta \ln y^{kk',bulk}(\mathbf{r}_1)}{\delta \rho_j^{(l)}(\mathbf{r})} d\mathbf{r}_1 - \frac{\delta \beta A^{ex,hs}}{\delta \rho_j^{(l)}(\mathbf{r})} - \frac{\delta \beta A^{ex,att}}{\delta \rho_j^{(l)}(\mathbf{r})} \quad (8.14)$$

In this problem, since all inhomogeneities are spherically symmetric, the density distribution of both free (F) and tethered (T_1 and T_2) polymer segments vary only in the radial direction. Therefore, the total density profile can be expressed as

$$\rho_j^{(l)}(\mathbf{r}_j) = \rho_j^{(l)}(r_j) \quad (8.15)$$

and eq. (8.13) thus simplifies to

$$\rho_j^{(l)}(r_j) = \exp(\beta\mu_{M_l}) \exp[D_j^{(l)}(r_j) - \beta V_{ext}^{j,l}(r_j)] I_{1,j}^{(l)}(r_j) I_{2,j}^{(l)}(r_j) \quad (8.16)$$

where $l=F, T_1$ and T_2 . In this work, only homonuclear chains are considered, therefore all segments on all chains have a hard-sphere diameter of σ . The multiple integrals, $I_{1,j}^{(l)}(r_j)$ and $I_{2,j}^{(l)}(r_j)$, are solved in a recursive fashion and are given below for each polymer chain. The following multiple integrals are given for the free polymer chains ($l=F$):

$$I_{1,1}^{(F)}(r) = 1$$

$$I_{1,j}^{(F)}(r) = \int I_{1,j-1}^{(F)}(r') \exp[D_{j-1}^{(F)}(r') - \beta V_{ext}^{j-1,F}(r')] \Delta_{j-1,j}^{(F)}(r', r) \left(\frac{r' \theta(\sigma - |r' - r|)}{r} \right) dr' \quad (8.17)$$

$$I_{2,j}^{(F)}(r) = \int I_{2,j+1}^{(F)}(r') \exp[D_{j+1}^{(F)}(r') - \beta V_{ext}^{j+1,F}(r')] \Delta_{j,j+1}^{(F)}(r, r') \left(\frac{r' \theta(\sigma - |r' - r|)}{r} \right) dr' \quad (8.18)$$

$$I_{2,m_F}^{(F)}(r) = 1$$

where $\Delta_{ij}^{(l)}(\mathbf{r}_1, \mathbf{r}_2)$ is defined as in chapter 6, $\Delta_{ij}^{(l)}(\mathbf{r}_1, \mathbf{r}_2) = K F_{ij}^{(l)}(\mathbf{r}_1, \mathbf{r}_2) y_{ij}^{(l)}(\mathbf{r}_1, \mathbf{r}_2)$. Here K is a geometric constant that accounts for the volume available for bonding between segments, and $F_{ij}^{(l)}(\mathbf{r}_1, \mathbf{r}_2) = [\exp(\beta\epsilon_0 - \beta v_{bond}^{ij}(\mathbf{r}_1, \mathbf{r}_2)) - 1]$ represents the association Mayer f -function. For tangentially bonded spheres, the bonding potential is given as

$\exp[-\beta v_{bond}^{ij}(\mathbf{r}_1, \mathbf{r}_2)] = \frac{\delta(|\mathbf{r}_1 - \mathbf{r}_2| - \sigma)}{4\pi(\sigma)^2}$. The cavity correlation function $y_{ij}^{(l)}(\mathbf{r}_1, \mathbf{r}_2)$ is

defined as in earlier chapters.

When considering the tethered chains ($l=T_1, T_2$), the following recurrence relations are given:

$$\begin{aligned}
 I_{1,1}^{(l)}(\sigma) &= 1 \\
 I_{1,2}^{(l)}(r) &= \exp[D_1^{(l)}(\sigma) - \beta V_{ext}^{1,l}(\sigma)] \Delta_{1,2}^{(l)}(\sigma, r) \left(\frac{\sigma \theta(\sigma - |r - \sigma|)}{r} \right) \\
 I_{1,j}^{(l)}(r) &= \int I_{1,j-1}^{(l)}(r') \exp[D_{j-1}^{(l)}(r') - \beta V_{ext}^{j-1,l}(r')] \Delta_{j-1,j}^{(l)}(r', r) \left(\frac{r' \theta(\sigma - |r' - r|)}{r} \right) dr'
 \end{aligned} \tag{8.19}$$

$$\begin{aligned}
 I_{2,m_l}^{(l)}(r) &= 1 \\
 I_{2,j}^{(l)}(r) &= \int I_{2,j+1}^{(l)}(r') \exp[D_{j+1}^{(l)}(r') - \beta V_{ext}^{j+1,l}(r')] \Delta_{j,j+1}^{(l)}(r, r') \left(\frac{r' \theta(\sigma - |r' - r|)}{r} \right) dr' \\
 I_{2,1}^{(l)}(\sigma) &= \int I_{2,2}^{(l)}(r') \exp[D_2^{(l)}(r') - \beta V_{ext}^{2,l}(r')] \Delta_{1,2}^{(l)}(\sigma, r') \left(\frac{r' \theta(\sigma - |r' - \sigma|)}{\sigma} \right) dr'
 \end{aligned} \tag{8.20}$$

The chemical potential (μ_{MF}) needed in eq. (8.16) for solving the density profiles of the free molecules (F) is obtained directly from Wertheim's TPT1 bulk equation of state for hard-sphere chains. The chemical potentials of the tethered fragments (T_1 and T_2) can be determined using the normalization conditions

$$\begin{aligned}
 \int 4\pi r^2 \rho_j^{(T_1)}(r) dr &= 1 \\
 \int 4\pi r^2 \rho_j^{(T_2)}(r) dr &= 1
 \end{aligned} \tag{8.21}$$

where $j=1, 2, 3, \dots, m_l$, for $l=T_1$ or T_2 . Therefore μ_{MT_1} and μ_{MT_2} can be solved by combining eq. (8.16) with eq. (8.21), using any of the segments $j=1, 2, 3, \dots, m_l$. (This

also serves as a good check as using the expressions for any of the segments on a given chain should yield the same chemical potential for the chain). For the first tethered segment (segment '1' of $l=T_1$ or T_2)

$$\int 4\pi r^2 \left\{ \exp(\beta\mu_{M_1}) \exp(D_1^{(l)}(r)) \exp(-\beta V_{ext}^{1,l}(r)) I_{1,1}^{(l)}(r_j) I_{2,1}^{(l)}(r_j) \right\} dr = 1 \quad (8.22)$$

which yields

$$\exp(\beta\mu_{M_1}) = \frac{1}{\exp(D_1^{(l)}(\sigma)) I_{1,1}^{(l)}(\sigma) I_{2,1}^{(l)}(\sigma)} \quad (8.23)$$

Using other segments yield equivalent results for μ_{M_l} . Combining eq. (8.23) with eq. (8.16) thus gives

$$\rho_1^{(\tau 1)}(r) = \rho_1^{(\tau 2)}(r) = \frac{\delta(r - \sigma)}{4\pi\sigma^2} \quad (8.24)$$

which matches the known condition for the tethered segment. Solving for the other segments ($j=2, 3, \dots, m_l$) gives

$$\rho_j^{(l)}(r_j) = \frac{1}{\exp(D_1^{(l)}(\sigma)) I_{1,1}^{(l)}(\sigma) I_{2,1}^{(l)}(\sigma)} \exp[D_j^{(l)}(r_j) - \beta V_{ext}^{j,l}(r_j)] I_{1,j}^{(l)}(r_j) I_{2,j}^{(l)}(r_j) \quad (8.25)$$

The density profiles of the free polymer and of the tethered fragments around a fixed segment of a polymer chain are used to calculate the inter- and intramolecular correlation functions. The segments of a polymer chain are fixed one by one. Due to symmetry, $m_F/2$ calculations are required if m_F is even, and $(m_F + 1)/2$ calculations are required if m_F is odd. Calculations can be simplified for very long polymers by assuming that all middle segments have similar site-site correlation functions, and therefore only correlations related to end and middle segments need be calculated.

8.3 Results and discussion

The radial distribution functions for fully flexible hard-sphere chains of length $m=4$ and $m=8$ were calculated and compared with available simulation data. In this model, the tangent hard-sphere freely jointed chain molecules are represented as a string of hard spheres with fixed bond lengths equal to the hard-sphere diameter. There are no additional torsional or bending potentials. In the calculations, the overall packing fraction η is defined as $\eta = \pi\rho_b\sigma^3/6$, where ρ_b is the number density of polymer segments. Figures 8.2 and 8.3 compare *i*SAFT predictions for the site-site and average intermolecular correlation functions for hard-sphere 4mers and 8mers with simulation data from Yethiraj et al.³⁶¹ The theory is in good agreement with the simulation results at both high and low densities. The depletion of intermolecular segments at low density is due to the chain connectivity, while packing effects lead to the opposite effect at higher densities. The cusp at $r=2\sigma$ is related to the fixed bond length. The theory does tend to overestimate the values of the distribution functions at contact, more specifically for the end-middle and middle-middle segment radial distribution functions. From the figures, one can also see that the correlation hole between the middle segments is more pronounced than that involving the end segments (end-middle and end-end segments), in agreement with simulation. It is expected that the middle segments are more sensitive to multi-body correlations because of the close connectivity with neighboring segments. Improvement might be possible by introducing the multi-body correlation functions in the chain-connectivity contribution to the free energy.

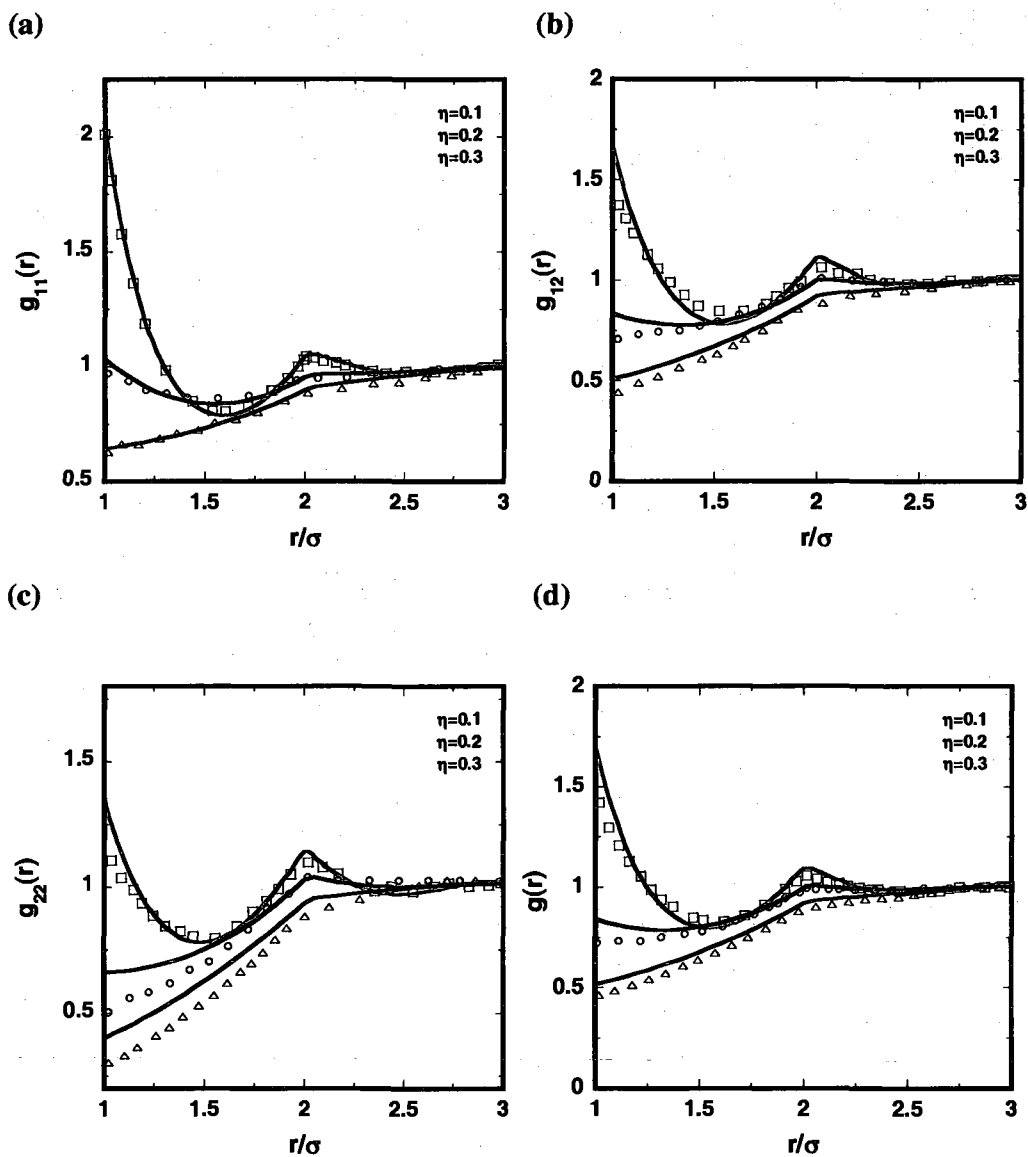


Figure 8.2: In (a-c), the intermolecular site-site distribution functions of freely jointed hard-sphere 4mers are given at the overall packing fractions of $\eta=0.1, 0.2,$ and 0.34 : (a) $g_{11}(r)$, $g_{12}(r)$, and (c) $g_{22}(r)$. The corresponding average pair correlation function $g(r)$ is given in (d). Symbols represent simulation data from Yethiraj et al.³⁶¹

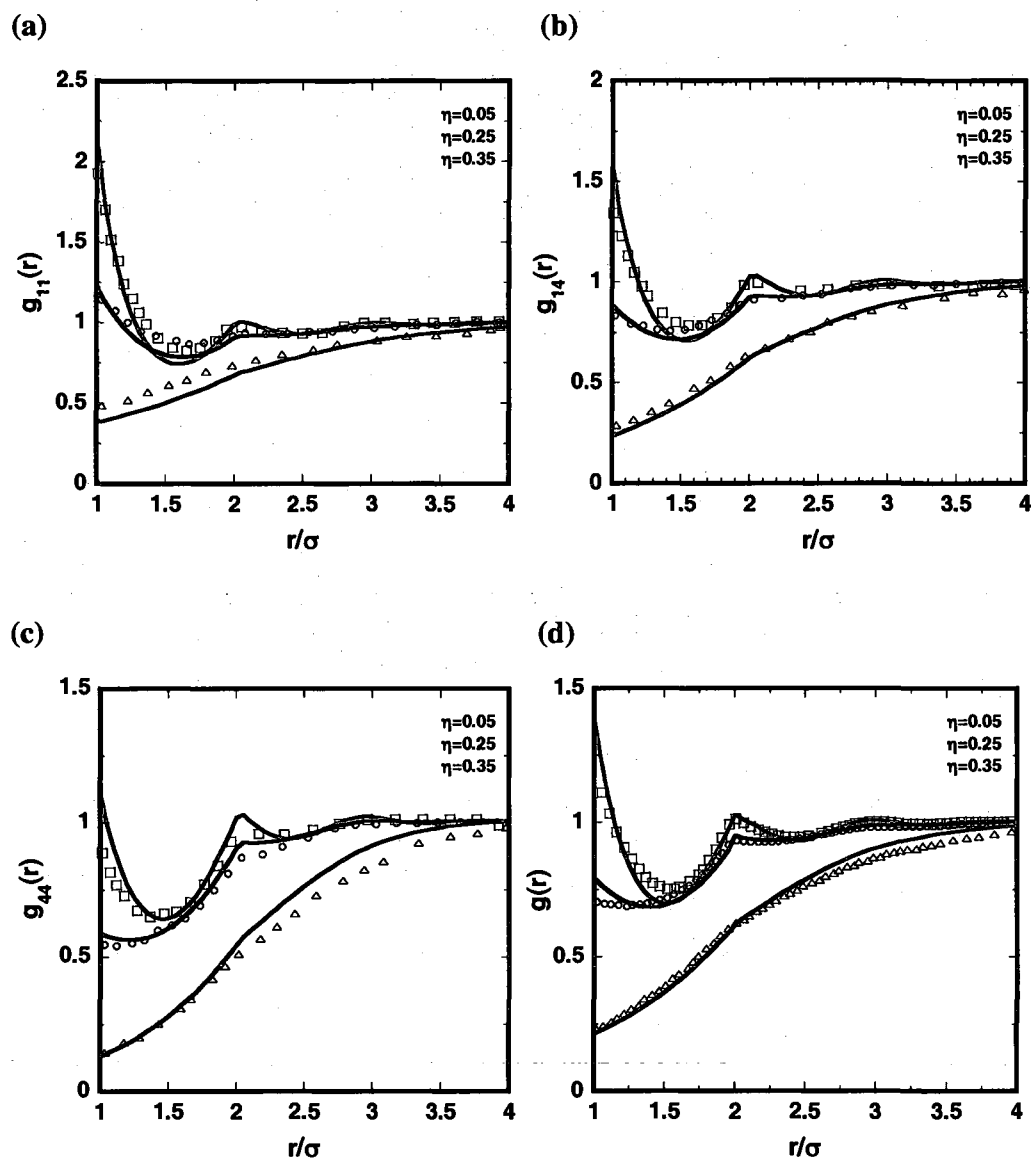


Figure 8.3: In (a-c), the intermolecular site-site distribution functions of freely jointed hard-sphere 8mers are given at the overall packing fractions of $\eta=0.05$, 0.25, and 0.35: (a) $g_{11}(r)$, $g_{14}(r)$, and (c) $g_{44}(r)$. The corresponding average pair correlation function $g(r)$ is given in (d). Symbols represent simulation data from Yethiraj et al.³⁶¹

Figures 8.4 and 8.5 compare the average inter- and intramolecular correlation functions predicted by *iSAFT* with simulation data by Chang and Sandler³⁵⁸ for 4mers and 8mers. Figure 8.4 (a) and Figure 8.5 (a) present accurate predictions of the average

pair distribution functions $g(r)$ by the theory. The theory does slightly overestimate the value of $g(r)$ at contact at higher densities. For the systems considered in this work, the *i*SAFT density functional theory provides slightly more accurate intermolecular correlation functions than Wertheim's multi-density integral equation theory,^{356-358,362} especially at low densities as the chain length is increased. The theory also provides improvements in the intermolecular correlation functions in comparison to the density functional theory by Yu and Wu,³⁶⁰ especially for longer chains at higher densities.

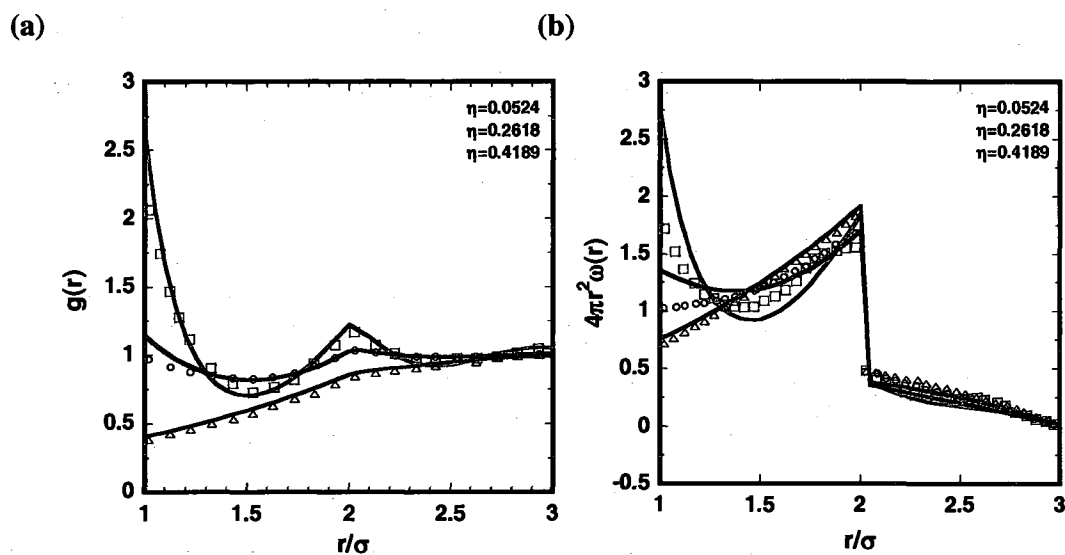


Figure 8.4: The average correlation functions of freely-jointed 4mers at $\eta=0.0524$, 0.2618, and 0.4189. The average intermolecular correlation function is presented in (a), and the average nonbonded intramolecular correlation function is presented in (b). Symbols represent simulation data from Chang and Sandler.³⁵⁸

Figure 8.4 (b) and Figure 8.5 (b) present the corresponding average nonbonded intramolecular radial distribution functions $4\pi r^2 \omega(r)$. Unlike the alternative approaches in the literature (mentioned in the Introduction, integral equation approaches³⁵⁶⁻³⁵⁸ and the DFT by Kierlik and Rosenberg^{162,163}), the *i*SAFT density

functional theory is able to correctly capture the nonideal behavior of intramolecular correlation functions, specifically the packing effects on the intramolecular structure.

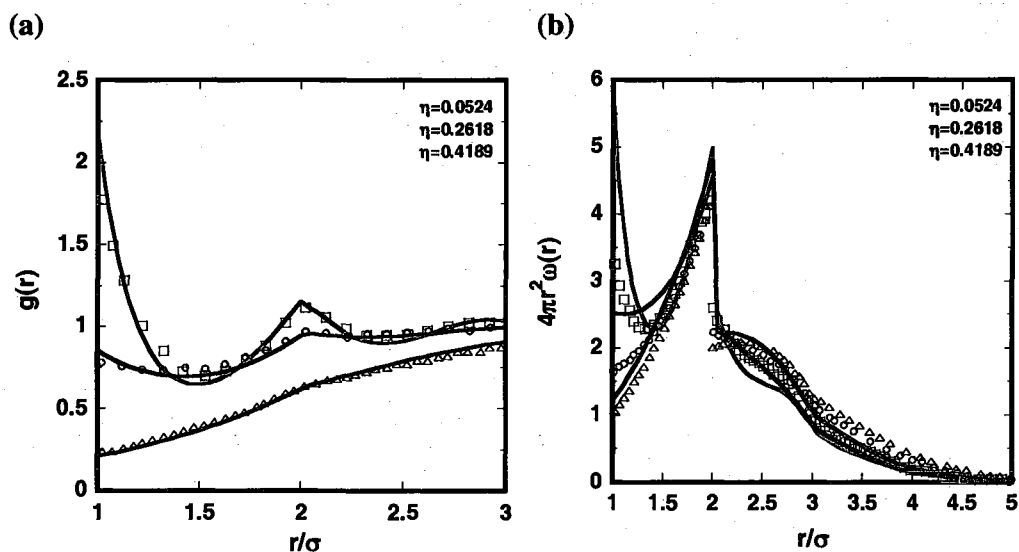


Figure 8.5: The average correlation functions of freely-jointed 8mers at $\eta=0.0524$, 0.2618, and 0.4189. The average intermolecular correlation function is presented in (a), and the average nonbonded intramolecular correlation function is presented in (b). Symbols represent simulation data from Chang and Sandler.³⁵⁸

From part (b) of the figures, a discontinuity occurs at $r=2\sigma$ due to the direct interaction of nearest neighbors along the polymer chain. At low densities, the intramolecular correlation function increases in a monotonic fashion for separations $r < 2\sigma$. At higher densities, a minimum occurs at approximately $r=1.5\sigma$. For $r > 2\sigma$, the theory predicts the essential features of nonmonotonic decay of the intramolecular correlation functions. Unfortunately, the agreement between the theory and the simulation results is only semi-quantitative, especially at the contact values. The discrepancy between the theory and the simulation results is most likely due to the use of two-body correlation functions in the free energy expressions for chain connectivity. When a segment is fixed at the origin, the intramolecular structure is sensitive to multi-body correlations among the segments

belonging to the same molecule. The DFT by Yu and Wu³⁶⁰ also predicts intramolecular structure that is semi-quantitative with simulation. The *i*SAFT density functional theory overestimates the intramolecular structure at contact, whereas the DFT by Yu and Wu underestimates the structure at contact. This suggests that the intramolecular structure may be sensitive to the weighting functions used in the chain free energy contributions.

8.4 Conclusions

A density functional theory based on Wertheim's theory is presented for the correlation functions of polymeric liquids. The theory uses an extension of Percus' test particle method, where the external field is a fixed polymer segment at the origin. The *i*SAFT DFT is able to predict both the inter- and intramolecular correlation functions. In comparison with alternative approaches found in the literature, the structural and thermodynamic properties can be solved in a self-consistent manner, and the theory requires no simulation data as input. In addition, the theory is able to capture the nonideal behavior of intramolecular correlation functions. Improvements to the theory include the use of multi-body correlations among the segments, and more sophisticated weighted functions in the chain contribution.

CHAPTER 9

Concluding remarks

This thesis work has been devoted to the development of molecular modeling with emphasis and application in molecular thermodynamics. The statistical associating fluid theory (SAFT) and inhomogeneous SAFT (*i*SAFT) were extended to study the phase behavior and microstructure of various complex systems. The key advances and findings from this work are discussed below:

- The perturbed-chain SAFT (PC-SAFT) equation of state was extended to include a crossover correction. In the critical region, the improved crossover equation of state provides the correct nonclassical critical exponents. Away from the critical region, the crossover equation reduces to the original PC-SAFT equation, therefore maintaining the accuracy of PC-SAFT in this region. No modifications to the original PC-SAFT molecular parameters were necessary. Excellent agreement with vapor-liquid equilibrium experimental data for the *n*-alkane family was obtained inside and outside the critical region, and all critical constants T_c , P_c , and ρ_c were calculated within their respective experimental errors. Future applications of this development include applying the theory to simple fluid mixtures^{50,54,56,94} and within a density functional construct.^{52,95,96}

- PC-SAFT was used as a predictive tool for natural gas mixtures, to aid in the understanding of the complex phase behavior involved, and in the design and operation of more efficient removal processes. The theory was tested against available VLE data for binary mixtures of constituents typically found in sour gas treating services (hydrocarbons/H₂S, hydrocarbons/sulfides, H₂S/sulfides, solvent/sulfides). The theory performed very well over a wide range of conditions, capturing the wide variety of phase behavior in comparison with available experimental data. Multicomponent mixtures were discussed, with a comparison (of mercaptan solubility) between aqueous amine solutions and physical solvents. Results suggest an increased solubility in organic (nonamine, physical) solvents, compared to water and aqueous amine solutions. A more detailed investigation could be carried out on the performance of commercial physical solvents in the future.
- Using a density functional theory (DFT) based on Rosenfeld's formalism for hard spheres, the influence of model solutes of different sizes on the structure and interfacial properties of water was investigated. In the theory, water was modeled as a spherical hard core with four highly anisotropic square-well association or hydrogen-bonding sites. The hydrogen-bonding interactions were accounted for using the association free energy based on Wertheim's first order thermodynamic perturbation theory. Long-range attractions were accounted for using a mean-field approximation. From the DFT, the distinguishing fluid structure and interfacial properties as a function of solute size were captured, demonstrating the ability of the theory to successfully describe hydrophobic phenomena on both microscopic and macroscopic length scales. In addition, details of structural changes in the hydrogen-

bonding network of water due to increasing solute size were quantified and discussed. The temperature effects were also investigated, which are known to play an important role in determining the hydrophobicity of the system.

- Using *i*SAFT, the structure and effective forces in nonadsorbing polymer-colloid mixtures were investigated. The theory was tested under a wide range of conditions and performed very well in comparison to simulation data. A comprehensive study was conducted characterizing the role of polymer concentration, particle/polymer-segment size ratio, and polymer chain length on the structure, polymer induced depletion forces, and the colloid-colloid osmotic second virial coefficient. The theory correctly captures a depletion layer on two different length scales, one on the order of the segment diameter (semidilute regime), and the other on the order of the polymer radius of gyration (dilute regime). The particle/polymer-segment size ratio was demonstrated to play a significant role on the polymer structure near the particle surface at low polymer concentrations, but this effect diminishes at higher polymer concentrations. Results for the polymer-mediated mean force between colloidal particles shows that increasing the concentration of the polymer solution encourages particle-particle attraction, while decreasing the range of depletion attraction. At intermediate to high concentrations, depletion attraction can be coupled to a mid-range repulsion, especially for colloids in solutions of short chains. Colloid-colloid second virial coefficient calculations indicate that net repulsion between colloids at low polymer densities gives way to net attraction at higher densities, in agreement with available simulation data. Furthermore, results indicate a higher tendency towards colloidal aggregation for larger colloids in solutions of longer chains.

- The *i*SAFT DFT was extended to associating polyatomic molecular systems, using the inhomogeneous form of the association functional. Such a development provides a very accurate method for modeling complex associating polyatomic systems, capable of investigating the full range of association for any bonding scheme. Theoretical results demonstrate the ability of the theory to model problems near surfaces and in the bulk over a wide range of conditions. The examples elucidate the importance of this theoretical development, highlighting how reversible bonding governs the structure of a fluid near a surface and in confined environments, the molecular connectivity (formation of supramolecules, star polymers, etc.) and the phase behavior of the system (including reentrant order-disorder phase transitions).
- The *i*SAFT DFT was extended to predict the inter- and intramolecular correlation functions of polymeric fluids using Percus' test particle method. Results from the theory for the inter- and intramolecular distribution functions, as well as the site-site correlation functions, are in good agreement with available simulations for flexible, hard chain fluids. Unlike the integral equation approaches and alternative density functional theories, no molecular simulation is required as input. The method is general and applicable to other polymeric fluids with more involved intermolecular interactions. Knowledge of the inter- and intramolecular structure can be used to enhance our understanding of the effect of local chemistry, bond flexibility, and chain branching on the thermodynamic properties of polymers.

While the last few years have seen much growth and advancement to the *i*SAFT density functional theory, the theory is still young, possessing opportunity for further development and broader application. In addition, several problems involving

inhomogeneous fluids in 2/3 dimensions await (see applications discussed in chapter 5-7), thus requiring the use of more efficient numerical methods and algorithms.³⁶³ A brief description of potential future research utilizing these molecular tools, namely *iSAFT*, is included below.

Broad application of polyatomic association

The work in this dissertation extended *iSAFT* to include hydrogen-bonding interactions on polyatomic molecules, where the full range of molecular association as a function of temperature can be considered. Chapter 7 demonstrated how hydrogen bonding can play a key role in determining molecular connectivity and the minimization of the grand free energy of the system (the driving force behind the self-assembly and stabilization of mesostructures). Broader application of the theory can be used to investigate more complex molecular systems, with more involved association schemes (the theory was derived to account for any association scheme, with any number of association sites on any polymer segment). This extension of the theory is important to many industrial and biological processes, most notably in self-assembly processes such as the formation of membranes and micelles in surfactant solutions, and the folding of proteins into stable, functional complexes. Chapter 7 also listed additional applications involving complex associating polymers that can self-assemble into hierarchical morphologies (e.g., the self-assembly of Archimedean tiling patterns^{306-308,310}). The application of *iSAFT* to such challenging problems could aid in the development and production of high performance soft materials, separation devices, and other smart materials.

Improving long-range dispersion interactions

Results in this work account for long-range dispersion interactions via a mean-field Lennard-Jones treatment. Although effective, it is still desirable to develop a more sophisticated long-range attraction term. As mentioned briefly in chapter 5, possible techniques to improve the long-range attraction term include adopting non-mean-field prescriptions that describe the attractive interactions using the first order mean spherical approximation developed by Tang and Wu,²⁴² or using a weighted density approximation developed by Muller et al.²¹³ and demonstrated by Reddy and Yethiraj.²¹² A density functional theory with a more sophisticated dispersion term that reduces to the dispersion term incorporated in an equation of state (e.g., PC-SAFT) is of high interest. As previously discussed, *i*SAFT shares a common basis with SAFT. Such self-consistency is significant because while bulk properties of solutions are experimentally accessible, fewer experimental results for interfacial properties are readily available. Dominik et al.¹⁶⁵ have already demonstrated how *i*SAFT can be used to simultaneously model the bulk phase behavior and the interfacial properties of *n*-alkanes and polymer melts. In this work, Dominik et al. used a mapping procedure to determine the appropriate DFT attractive energies from the PC-SAFT attractive energies. Ideally, no parameter mapping of the dispersion energies would be necessary, and parameters used in the bulk equation of state could be transferred directly to the *i*SAFT model.

Intramolecular flexibility and stiffness

Research in this dissertation is presented for fully flexible chains. While sufficient for capturing the essential physics of polyatomic systems, the ability to account for chain flexibility or stiffness is important in determining the structure and properties of many

systems, including polymer solutions and melts,³⁶⁴⁻³⁶⁶ as well as some lipid/surfactant molecules. Previous work developed the effect of an intramolecular bonding potential on the bulk properties of polyatomic molecules.³⁶⁷ The theory accurately predicted the difference in bulk properties between linear, bent, and cyclic molecules. The theory for intramolecular bonding can be redeveloped in the form of density functional theory to account for the effects of chain flexibility or stiffness, and tested versus molecular simulation for semiflexible chains.³⁶⁴⁻³⁶⁶ In addition to the hard sphere models, the DFT can be used to model particles/molecules varying in size and shape (e.g., rods, discs, etc.) using alternative formalisms of the fundamental measure theory.³⁶⁸⁻³⁷¹

Dynamic density functional theory

The development of a time-dependent form of the density functional theory presented in this thesis would extend the ability of the theory to predict non-equilibrium, dynamic behavior and transport properties.³⁷²⁻³⁷⁶ Applications include supercooled liquids, and time-dependent copolymer and surfactant mesostructures.

APPENDIX **A**

Derivation of $\frac{\delta\beta A^{ex,assoc}}{\delta\rho_j(\mathbf{r})}$ (For Chapter 7)

Here we include the details of the polyatomic full range association functional derivative. We begin by first writing the associating contribution to the free energy. This is arrived at by working within the framework an extension^{12,29} of Wertheim's theory of association.⁴⁻⁷ As Segura et al.^{12,29,186} previously introduced and successfully demonstrated (for spherical molecules), there are two approaches to include intermolecular association. The first applies Wertheim's associating fluid functional as a perturbation to a reference fluid functional,

$$\beta A^{ex,assoc}[\rho_i^{(C1)}(\mathbf{r}), \rho_i^{(C2)}(\mathbf{r}), \dots] = \sum_{l=C1, C2} \int d\mathbf{r}_1 \sum_{i=1}^{m_l} \rho_i^{(l)}(\mathbf{r}_1) \sum_{A \in \Gamma^{(l)}} \left(\ln \chi_A^{i,l}(\mathbf{r}_1) - \frac{\chi_A^{i,l}(\mathbf{r}_1)}{2} + \frac{1}{2} \right) \quad (\text{A.1})$$

The first summation is over all chains l in the mixture (C_1, C_2, \dots), the second summation over all segments on chain l , and the final summation is over all the associating sites on segment i of chain l . $\chi_A^{i,l}(\mathbf{r}_1)$ represents the fraction of segments of type i on chain l which are not bonded at their site A . We simplify this notation by combining the first two sums to an equivalent sum over all segments (N) in the system.

$$\beta A^{ex,assoc}[\rho_i(\mathbf{r})] = \int d\mathbf{r}_1 \sum_{i=1}^N \rho_i(\mathbf{r}_1) \sum_{A \in \Gamma^{(i)}} \left(\ln \chi_A^i(\mathbf{r}_1) - \frac{\chi_A^i(\mathbf{r}_1)}{2} + \frac{1}{2} \right) \quad (\text{A.2})$$

The fraction of unbounded segments i at site A is given by

$$\chi_A^i(\mathbf{r}_1) = \frac{1}{1 + \int d\mathbf{r}_2 \sum_{k=1}^N \rho_k(\mathbf{r}_2) \sum_{B \in \Gamma^{(k)}} \chi_B^k(\mathbf{r}_2) \Delta_{AB}^{ik}(\mathbf{r}_1, \mathbf{r}_2)} \quad (\text{A.3})$$

To solve the Euler-Lagrange equation for the density profile, the functional derivative is needed. This is given as

$$\frac{\delta \beta A^{ex,assoc}}{\delta \rho_j(\mathbf{r})} = \sum_{A \in \Gamma^{(j)}} \left(\ln \chi_A^j(\mathbf{r}) - \frac{\chi_A^j(\mathbf{r})}{2} + \frac{1}{2} \right) + \sum_{i=1}^N \int d\mathbf{r}_1 \rho_i(\mathbf{r}_1) \sum_{A \in \Gamma^{(i)}} \left(\frac{1}{\chi_A^i(\mathbf{r}_1)} - \frac{1}{2} \right) \left(\frac{\delta \chi_A^i(\mathbf{r}_1)}{\delta \rho_j(\mathbf{r})} \right) \quad (\text{A.4})$$

We can manipulate the functional to remove the functional derivative $\left(\frac{\delta \chi_A^i(\mathbf{r}_1)}{\delta \rho_j(\mathbf{r})} \right)$.

Such an algebraic manipulation was demonstrated for bulk systems by Michelson and Hendricks.³⁷⁷ A similar approach was used to derive the chain free energy functional.³²

The derivation begins by rearranging the definition of the fraction of unbounded segments (eq. (A.3)) to give

$$\frac{1}{\chi_A^i(\mathbf{r}_1)} = 1 + \int d\mathbf{r}_2 \sum_{k=1}^N \rho_k(\mathbf{r}_2) \sum_{B \in \Gamma^{(k)}} \chi_B^k(\mathbf{r}_2) \Delta_{AB}^{ik}(\mathbf{r}_1, \mathbf{r}_2) \quad (\text{A.5})$$

Differentiating this with respect to $\rho_j(\mathbf{r})$ gives

$$\begin{aligned}
-\left(\frac{1}{\chi_A^i(\mathbf{r}_1)}\right)^2 \left(\frac{\delta\chi_A^i(\mathbf{r}_1)}{\delta\rho_j(\mathbf{r})}\right) &= \left(\sum_{B \in \Gamma^{(j)}} \chi_B^j(\mathbf{r}) \Delta_{AB}^j(\mathbf{r}_1, \mathbf{r})\right) + \int d\mathbf{r}_2 \sum_{k=1}^N \rho_k(\mathbf{r}_2) \sum_{B \in \Gamma^{(k)}} \left(\frac{\delta\chi_B^k(\mathbf{r}_2)}{\delta\rho_j(\mathbf{r})}\right) \Delta_{AB}^{ik}(\mathbf{r}_1, \mathbf{r}_2) \\
&\quad + \int d\mathbf{r}_2 \sum_{k=1}^N \rho_k(\mathbf{r}_2) \sum_{B \in \Gamma^{(k)}} \left(\frac{\delta\Delta_{AB}^{ik}(\mathbf{r}_1, \mathbf{r}_2)}{\delta\rho_j(\mathbf{r})}\right) \chi_B^k(\mathbf{r}_2)
\end{aligned} \tag{A.6}$$

Multiplying both sides by $\left(-\int d\mathbf{r}_1 \sum_{i=1}^N \rho_i(\mathbf{r}_1) \sum_{A \in \Gamma^{(i)}} \chi_A^i(\mathbf{r}_1)\right)$

$$\begin{aligned}
\int d\mathbf{r}_1 \sum_{i=1}^N \rho_i(\mathbf{r}_1) \sum_{A \in \Gamma^{(i)}} \left(\frac{1}{\chi_A^i(\mathbf{r}_1)}\right) \left(\frac{\delta\chi_A^i(\mathbf{r}_1)}{\delta\rho_j(\mathbf{r})}\right) &= -\int d\mathbf{r}_1 \sum_{i=1}^N \rho_i(\mathbf{r}_1) \sum_{A \in \Gamma^{(i)}} \chi_A^i(\mathbf{r}_1) \left(\sum_{B \in \Gamma^{(j)}} \chi_B^j(\mathbf{r}) \Delta_{AB}^j(\mathbf{r}_1, \mathbf{r})\right) \\
&\quad - \iint d\mathbf{r}_1 d\mathbf{r}_2 \sum_{i=1}^N \sum_{k=1}^N \rho_i(\mathbf{r}_1) \rho_k(\mathbf{r}_2) \sum_{A \in \Gamma^{(i)}} \sum_{B \in \Gamma^{(k)}} \chi_A^i(\mathbf{r}_1) \left(\frac{\delta\chi_B^k(\mathbf{r}_2)}{\delta\rho_j(\mathbf{r})}\right) \Delta_{AB}^{ik}(\mathbf{r}_1, \mathbf{r}_2) \\
&\quad - \iint d\mathbf{r}_1 d\mathbf{r}_2 \sum_{i=1}^N \sum_{k=1}^N \rho_i(\mathbf{r}_1) \rho_k(\mathbf{r}_2) \sum_{A \in \Gamma^{(i)}} \sum_{B \in \Gamma^{(k)}} \chi_A^i(\mathbf{r}_1) \chi_B^k(\mathbf{r}_2) \left(\frac{\delta\Delta_{AB}^{ik}(\mathbf{r}_1, \mathbf{r}_2)}{\delta\rho_j(\mathbf{r})}\right)
\end{aligned} \tag{A.7}$$

Rearranging,

$$\begin{aligned}
\int d\mathbf{r}_1 \sum_{i=1}^N \rho_i(\mathbf{r}_1) \sum_{A \in \Gamma^{(i)}} \left(\frac{1}{\chi_A^i(\mathbf{r}_1)}\right) \left(\frac{\delta\chi_A^i(\mathbf{r}_1)}{\delta\rho_j(\mathbf{r})}\right) &= -\int d\mathbf{r}_1 \sum_{i=1}^N \rho_i(\mathbf{r}_1) \sum_{A \in \Gamma^{(i)}} \chi_A^i(\mathbf{r}_1) \left(\sum_{B \in \Gamma^{(j)}} \chi_B^j(\mathbf{r}) \Delta_{AB}^j(\mathbf{r}_1, \mathbf{r})\right) \\
&\quad - \int d\mathbf{r}_2 \sum_{k=1}^N \rho_k(\mathbf{r}_2) \sum_{B \in \Gamma^{(k)}} \left(\frac{\delta\chi_B^k(\mathbf{r}_2)}{\delta\rho_j(\mathbf{r})}\right) \int d\mathbf{r}_1 \sum_{i=1}^N \rho_i(\mathbf{r}_1) \sum_{A \in \Gamma^{(i)}} \chi_A^i(\mathbf{r}_1) \Delta_{AB}^{ik}(\mathbf{r}_1, \mathbf{r}_2) \\
&\quad - \iint d\mathbf{r}_1 d\mathbf{r}_2 \sum_{i=1}^N \sum_{k=1}^N \rho_i(\mathbf{r}_1) \rho_k(\mathbf{r}_2) \sum_{A \in \Gamma^{(i)}} \sum_{B \in \Gamma^{(k)}} \chi_A^i(\mathbf{r}_1) \chi_B^k(\mathbf{r}_2) \left(\frac{\delta\Delta_{AB}^{ik}(\mathbf{r}_1, \mathbf{r}_2)}{\delta\rho_j(\mathbf{r})}\right)
\end{aligned} \tag{A.8}$$

We know from equation (A.3) that

$$\left(\frac{1}{\chi_B^k(\mathbf{r}_2)} - 1\right) = \int d\mathbf{r}_1 \sum_{i=1}^N \rho_i(\mathbf{r}_1) \sum_{A \in \Gamma^{(i)}} \chi_A^i(\mathbf{r}_1) \Delta_{AB}^{ik}(\mathbf{r}_1, \mathbf{r}_2) \quad (\text{A.9})$$

Substitution of expression (A.9) into (A.8) gives us,

$$\begin{aligned} \int d\mathbf{r}_1 \sum_{i=1}^N \rho_i(\mathbf{r}_1) \sum_{A \in \Gamma^{(i)}} \left(\frac{1}{\chi_A^i(\mathbf{r}_1)}\right) \left(\frac{\delta \chi_A^i(\mathbf{r}_1)}{\delta \rho_j(\mathbf{r})}\right) &= - \int d\mathbf{r}_1 \sum_{i=1}^N \rho_i(\mathbf{r}_1) \sum_{A \in \Gamma^{(i)}} (\chi_A^i(\mathbf{r}_1)) \left(\sum_{B \in \Gamma^{(j)}} \chi_B^j(\mathbf{r}) \Delta_{AB}^{ij}(\mathbf{r}_1, \mathbf{r})\right) \\ &\quad - \int d\mathbf{r}_2 \sum_{k=1}^N \rho_k(\mathbf{r}_2) \sum_{B \in \Gamma^{(k)}} \left(\frac{\delta \chi_B^k(\mathbf{r}_2)}{\delta \rho_j(\mathbf{r})}\right) \left(\frac{1}{\chi_B^k(\mathbf{r}_2)} - 1\right) \\ &\quad - \iint d\mathbf{r}_1 d\mathbf{r}_2 \sum_{i=1}^N \sum_{k=1}^N \rho_i(\mathbf{r}_1) \rho_k(\mathbf{r}_2) \sum_{A \in \Gamma^{(i)}} \sum_{B \in \Gamma^{(k)}} \chi_A^i(\mathbf{r}_1) \chi_B^k(\mathbf{r}_2) \left(\frac{\delta \Delta_{AB}^{ik}(\mathbf{r}_1, \mathbf{r}_2)}{\delta \rho_j(\mathbf{r})}\right) \end{aligned} \quad (\text{A.10})$$

We can replace the dummy variables on the second term (RHS): B, k, \mathbf{r}_2 by A, i, \mathbf{r}_1

$$\begin{aligned} \int d\mathbf{r}_1 \sum_{i=1}^N \rho_i(\mathbf{r}_1) \sum_{A \in \Gamma^{(i)}} \left(\frac{1}{\chi_A^i(\mathbf{r}_1)}\right) \left(\frac{\delta \chi_A^i(\mathbf{r}_1)}{\delta \rho_j(\mathbf{r})}\right) &= - \int d\mathbf{r}_1 \sum_{i=1}^N \rho_i(\mathbf{r}_1) \sum_{A \in \Gamma^{(i)}} (\chi_A^i(\mathbf{r}_1)) \left(\sum_{B \in \Gamma^{(j)}} \chi_B^j(\mathbf{r}) \Delta_{AB}^{ij}(\mathbf{r}_1, \mathbf{r})\right) \\ &\quad - \int d\mathbf{r}_1 \sum_{i=1}^N \rho_i(\mathbf{r}_1) \sum_{A \in \Gamma^{(i)}} \left(\frac{\delta \chi_A^i(\mathbf{r}_1)}{\delta \rho_j(\mathbf{r})}\right) \left(\frac{1}{\chi_A^i(\mathbf{r}_1)} - 1\right) \\ &\quad - \iint d\mathbf{r}_1 d\mathbf{r}_2 \sum_{i=1}^N \sum_{k=1}^N \rho_i(\mathbf{r}_1) \rho_k(\mathbf{r}_2) \sum_{A \in \Gamma^{(i)}} \sum_{B \in \Gamma^{(k)}} \chi_A^i(\mathbf{r}_1) \chi_B^k(\mathbf{r}_2) \left(\frac{\delta \Delta_{AB}^{ik}(\mathbf{r}_1, \mathbf{r}_2)}{\delta \rho_j(\mathbf{r})}\right) \end{aligned} \quad (\text{A.11})$$

Collecting like terms and multiplying by (1/2) gives us

$$\begin{aligned} \int d\mathbf{r}_1 \sum_{i=1}^N \rho_i(\mathbf{r}_1) \sum_{A \in \Gamma^{(i)}} \left(\frac{1}{\chi_A^i(\mathbf{r}_1)} - \frac{1}{2}\right) \left(\frac{\delta \chi_A^i(\mathbf{r}_1)}{\delta \rho_j(\mathbf{r})}\right) &= -\frac{1}{2} \int d\mathbf{r}_1 \sum_{i=1}^N \rho_i(\mathbf{r}_1) \sum_{A \in \Gamma^{(i)}} (\chi_A^i(\mathbf{r}_1)) \left(\sum_{B \in \Gamma^{(j)}} \chi_B^j(\mathbf{r}) \Delta_{AB}^{ij}(\mathbf{r}_1, \mathbf{r})\right) \\ &\quad - \frac{1}{2} \iint d\mathbf{r}_1 d\mathbf{r}_2 \sum_{i=1}^N \sum_{k=1}^N \rho_i(\mathbf{r}_1) \rho_k(\mathbf{r}_2) \sum_{A \in \Gamma^{(i)}} \sum_{B \in \Gamma^{(k)}} \chi_A^i(\mathbf{r}_1) \chi_B^k(\mathbf{r}_2) \left(\frac{\delta \Delta_{AB}^{ik}(\mathbf{r}_1, \mathbf{r}_2)}{\delta \rho_j(\mathbf{r})}\right) \end{aligned} \quad (\text{A.12})$$

Substituting this into expression (A.4) in the functional derivative gives

$$\begin{aligned}
\frac{\delta\beta A^{ex,assoc}}{\delta\rho_j(\mathbf{r})} &= \sum_{A \in \Gamma^{(j)}} \left(\ln \chi_A^j(\mathbf{r}) - \frac{\chi_A^j(\mathbf{r})}{2} + \frac{1}{2} \right) \\
&\quad - \frac{1}{2} \int d\mathbf{r}_1 \sum_{i=1}^N \rho_i(\mathbf{r}_1) \sum_{A \in \Gamma^{(i)}} (\chi_A^i(\mathbf{r}_1)) \left(\sum_{B \in \Gamma^{(j)}} \chi_B^j(\mathbf{r}) \Delta_{AB}^{ij}(\mathbf{r}_1, \mathbf{r}) \right) \\
&\quad - \frac{1}{2} \iint d\mathbf{r}_1 d\mathbf{r}_2 \sum_{i=1}^N \sum_{k=1}^N \rho_i(\mathbf{r}_1) \rho_k(\mathbf{r}_2) \sum_{A \in \Gamma^{(i)}} \sum_{B \in \Gamma^{(k)}} \chi_A^i(\mathbf{r}_1) \chi_B^k(\mathbf{r}_2) \left(\frac{\delta \Delta_{AB}^{ik}(\mathbf{r}_1, \mathbf{r}_2)}{\delta \rho_j(\mathbf{r})} \right)
\end{aligned} \tag{A.13}$$

Again recognizing that $\left(\frac{1}{\chi_B^j(\mathbf{r})} - 1 \right) = \int d\mathbf{r}_1 \sum_{i=1}^N \rho_i(\mathbf{r}_1) \sum_{A \in \Gamma^{(i)}} \chi_A^i(\mathbf{r}_1) \Delta_{AB}^{ij}(\mathbf{r}_1, \mathbf{r})$. We can simplify

$$\begin{aligned}
\frac{\delta\beta A^{ex,assoc}}{\delta\rho_j(\mathbf{r})} &= \sum_{A \in \Gamma^{(j)}} \left(\ln \chi_A^j(\mathbf{r}) - \frac{\chi_A^j(\mathbf{r})}{2} + \frac{1}{2} \right) \\
&\quad + \sum_{B \in \Gamma^{(j)}} \left(\frac{\chi_B^j(\mathbf{r})}{2} - \frac{1}{2} \right) \\
&\quad - \frac{1}{2} \iint d\mathbf{r}_1 d\mathbf{r}_2 \sum_{i=1}^N \sum_{k=1}^N \rho_i(\mathbf{r}_1) \rho_k(\mathbf{r}_2) \sum_{A \in \Gamma^{(i)}} \sum_{B \in \Gamma^{(k)}} \chi_A^i(\mathbf{r}_1) \chi_B^k(\mathbf{r}_2) \left(\frac{\delta \Delta_{AB}^{ik}(\mathbf{r}_1, \mathbf{r}_2)}{\delta \rho_j(\mathbf{r})} \right)
\end{aligned} \tag{A.14}$$

which, after changing the indices in term 2 of the RHS (from B to A), terms cancel and the expression simplifies further to give

$$\frac{\delta\beta A^{ex,assoc}}{\delta\rho_j(\mathbf{r})} = \sum_{A \in \Gamma^{(j)}} (\ln \chi_A^j(\mathbf{r})) - \frac{1}{2} \iint d\mathbf{r}_1 d\mathbf{r}_2 \sum_{i=1}^N \sum_{k=1}^N \rho_i(\mathbf{r}_1) \rho_k(\mathbf{r}_2) \sum_{A \in \Gamma^{(i)}} \sum_{B \in \Gamma^{(k)}} \chi_A^i(\mathbf{r}_1) \chi_B^k(\mathbf{r}_2) \left(\frac{\delta \Delta_{AB}^{ik}(\mathbf{r}_1, \mathbf{r}_2)}{\delta \rho_j(\mathbf{r})} \right) \tag{A.15}$$

The degree of association is controlled by the term

$$\Delta_{AB}^{ik}(\mathbf{r}_1, \mathbf{r}_2) = \kappa \left[\exp(\beta \epsilon_{A_i, B_k}^{assoc}) - 1 \right] y^{ik}(\mathbf{r}_1, \mathbf{r}_2) \tag{A.16}$$

Here κ represents a geometric constant, $\varepsilon_{Ai,Bk}^{assoc}$ is the associating energy, and y^{ik} is the cavity correlation function for the inhomogeneous hard sphere reference fluid.

Calculating the derivative of expression (A.16) needed for expression (A.15)

$$\frac{\delta \Delta_{AB}^{ik}(\mathbf{r}_1, \mathbf{r}_2)}{\delta \rho_j(\mathbf{r})} = \Delta_{AB}^{ik}(\mathbf{r}_1, \mathbf{r}_2) \frac{\delta \ln y^{ik}(\mathbf{r}_1, \mathbf{r}_2)}{\delta \rho_j(\mathbf{r})} \quad (\text{A.17})$$

We approximate $y^{ik}(\mathbf{r}_1, \mathbf{r}_2)$ to be at contact, and further by its bulk counterpart evaluated at a weighted density $\bar{\rho}_j$, so that

$$\ln y^{ik}(\mathbf{r}_1, \mathbf{r}_2) = \frac{1}{2} \left[\ln y^{ik}(\sigma, \bar{\rho}_j(\mathbf{r}_1)) + \ln y^{ik}(\sigma, \bar{\rho}_j(\mathbf{r}_2)) \right] \quad (\text{A.18})$$

We are left with

$$\frac{\delta \Delta_{AB}^{ik}(\mathbf{r}_1, \mathbf{r}_2)}{\delta \rho_j(\mathbf{r})} = \frac{1}{2} \Delta_{AB}^{ik}(\mathbf{r}_1, \mathbf{r}_2) \left[\frac{\delta \ln y^{ik}(\bar{\rho}_j(\mathbf{r}_1))}{\delta \rho_j(\mathbf{r})} + \frac{\delta \ln y^{ik}(\bar{\rho}_j(\mathbf{r}_2))}{\delta \rho_j(\mathbf{r})} \right] \quad (\text{A.19})$$

Finally, we can substitute expression (A.19) into expression (A.15)

$$\begin{aligned} \frac{\delta \beta A^{ex,assoc}}{\delta \rho_j(\mathbf{r})} &= \sum_{A \in \Gamma^{(j)}} (\ln \chi_A^j(\mathbf{r})) \\ &- \frac{1}{4} \iint d\mathbf{r}_1 d\mathbf{r}_2 \sum_{i=1}^N \sum_{k=1}^N \rho_i(\mathbf{r}_1) \rho_k(\mathbf{r}_2) \sum_{A \in \Gamma^{(i)}} \sum_{B \in \Gamma^{(k)}} \chi_A^i(\mathbf{r}_1) \chi_B^k(\mathbf{r}_2) \left[\Delta_{AB}^{ik}(\mathbf{r}_1, \mathbf{r}_2) \frac{\delta \ln y^{ik}(\bar{\rho}_j(\mathbf{r}_1))}{\delta \rho_j(\mathbf{r})} \right] \\ &- \frac{1}{4} \iint d\mathbf{r}_1 d\mathbf{r}_2 \sum_{i=1}^N \sum_{k=1}^N \rho_i(\mathbf{r}_1) \rho_k(\mathbf{r}_2) \sum_{A \in \Gamma^{(i)}} \sum_{B \in \Gamma^{(k)}} \chi_A^i(\mathbf{r}_1) \chi_B^k(\mathbf{r}_2) \left[\Delta_{AB}^{ik}(\mathbf{r}_1, \mathbf{r}_2) \frac{\delta \ln y^{ik}(\bar{\rho}_j(\mathbf{r}_2))}{\delta \rho_j(\mathbf{r})} \right] \end{aligned} \quad (\text{A.20})$$

Further using $\left(\frac{1}{\chi_A^j(\mathbf{r}_1)} - 1\right) = \int d\mathbf{r}_2 \sum_{k=1}^N \rho_k(\mathbf{r}_2) \sum_{B \in \Gamma^{(k)}} \chi_B^k(\mathbf{r}_2) \Delta_{AB}^{ik}(\mathbf{r}_1, \mathbf{r}_2)$ in the second term and $\left(\frac{1}{\chi_B^k(\mathbf{r}_2)} - 1\right) = \int d\mathbf{r}_1 \sum_{i=1}^N \rho_i(\mathbf{r}_1) \sum_{A \in \Gamma^{(i)}} \chi_A^i(\mathbf{r}_1) \Delta_{AB}^{ik}(\mathbf{r}_1, \mathbf{r}_2)$ in the third term (RHS)

$$\begin{aligned} \frac{\delta \beta A^{ex,assoc}}{\delta \rho_j(\mathbf{r})} &= \sum_{A \in \Gamma^{(j)}} (\ln \chi_A^j(\mathbf{r})) - \frac{1}{4} \int d\mathbf{r}_1 \sum_{i=1}^N \sum_{k=1}^N \rho_i(\mathbf{r}_1) \sum_{A \in \Gamma^{(i)}} (1 - \chi_A^i(\mathbf{r}_1)) \left[\frac{\delta \ln y^{ik}(\bar{\rho}_j(\mathbf{r}_1))}{\delta \rho_j(\mathbf{r})} \right] \\ &\quad - \frac{1}{4} \int d\mathbf{r}_2 \sum_{k=1}^N \sum_{i=1}^N \rho_k(\mathbf{r}_2) \sum_{B \in \Gamma^{(k)}} (1 - \chi_B^k(\mathbf{r}_2)) \left[\frac{\delta \ln y^{ik}(\bar{\rho}_j(\mathbf{r}_2))}{\delta \rho_j(\mathbf{r})} \right] \end{aligned} \quad (\text{A.21})$$

which is equivalent to

$$\frac{\delta \beta A^{ex,assoc}}{\delta \rho_j(\mathbf{r})} = \sum_{A \in \Gamma^{(j)}} (\ln \chi_A^j(\mathbf{r})) - \frac{1}{2} \sum_{i=1}^N \sum_{k=1}^N \int d\mathbf{r}_1 \rho_i(\mathbf{r}_1) \sum_{A \in \Gamma^{(i)}} (1 - \chi_A^i(\mathbf{r}_1)) \left[\frac{\delta \ln y^{ik}(\bar{\rho}_j(\mathbf{r}_1))}{\delta \rho_j(\mathbf{r})} \right] \quad (\text{A.22})$$

The above expression is the final form for associating chains (eq. (7.25) in the text). The

term $\frac{\delta \ln y^{ik}(\bar{\rho}_j(\mathbf{r}_1))}{\delta \rho_j(\mathbf{r})}$ only contributes for segments k with association sites that are

eligible to bond to sites located on segment i .

APPENDIX **B**

Solving for $\chi_A^i(\mathbf{r}_1)$ (For Chapter 7)

From eq. (A.3)

$$\chi_A^i(\mathbf{r}_1) = \frac{1}{1 + \int d\mathbf{r}_2 \sum_{k=1}^N \rho_k(\mathbf{r}_2) \sum_{B \in \Gamma^{(k)}} \chi_B^k(\mathbf{r}_2) \Delta_{AB}^{ik}(\mathbf{r}_1, \mathbf{r}_2)} \quad (\text{A.3})$$

Assuming that $\chi_A^i(\mathbf{r}_1)$ is only dependent on the z direction and is not a strong function of orientation (this is true in the bulk, but such an assumption may break down near a surface). For the planar symmetry considered in this work, the density ρ is only dependent on z .

$$\chi_A^i(z_1) + \chi_A^i(z_1) \int d\mathbf{r}_2 \sum_{k=1}^N \rho_k(z_2) \sum_{B \in \Gamma^{(k)}} \chi_B^k(z_2) \Delta_{AB}^{ik}(\mathbf{r}_1, \mathbf{r}_2) = 1 \quad (\text{B.1})$$

Recall eq. (A.16), $\Delta_{AB}^{ik}(\mathbf{r}_1, \mathbf{r}_2) = \kappa [\exp(\beta \mathcal{E}_{Ai, Bk}^{assoc}) - 1] y^{ik}(\mathbf{r}_1, \mathbf{r}_2)$ where $\kappa = \frac{(1 - \cos \theta_c)^2}{4}$. We

assume that the cavity correlation function can be approximated at contact using its bulk counterpart evaluated at a weighted density^{33,34}

$$y^{ik}(r_{12}, \mathbf{r}_1, \mathbf{r}_2) = y^{ik}(\sigma, \bar{\rho}_j(z_1), \bar{\rho}_j(z_2)) = [y^{ik}(\sigma, \bar{\rho}_j(z_1)) \times y^{ik}(\sigma, \bar{\rho}_j(z_2))]^{1/2} \quad (\text{B.2})$$

This gives

$$\chi_A^i(z_i) + \chi_A^i(z_1) \int d\mathbf{r}_2 \sum_{k=1}^N \rho_k(z_2) \sum_{B \in \Gamma^{(k)}} \chi_B^k(z_2) \left\{ \kappa [\exp(\beta \varepsilon_{Ai, Bk}^{assoc}) - 1] y^{ik}(\sigma, \bar{\rho}_j(z_1), \bar{\rho}_j(z_2)) \right\} = 1 \quad (\text{B.3})$$

Given the position z_i of segment i , we can integrate over the range of positions for segment k that allow bonding. We perform the following change of variables

$$\int d\mathbf{r}_2 = \int_0^{2\pi} d\phi \int_1^1 d \cos \theta \int_{\sigma}^{r_c} r_{12}^2 dr_{12} \quad (\text{B.4})$$

Under our assumption, $r_{12}^2 y^{ik}(r_{12}, z_1, z_2) \approx \sigma^2 y^{ik}(\sigma, z_1, z_2)$ over the range of bonding.

Neglecting the change in z_2 as r_{12} goes from σ to r_c , we integrate $\int_{\sigma}^{r_c} dr_{12} = (r_c - \sigma)$ and

$\int_1^1 d \cos \theta = \int_{-1}^1 d(z_2 - z_1) = \int_{-1+z_1}^{1+z_1} dz_2$, which after substitution lead to

$$\chi_A^i(z_i) + 2\pi\kappa\sigma^2(r_c - \sigma) \chi_A^i(z_1) \int_{-1}^{1+z_1} \sum_{k=1}^N \rho_k(z_2) \times \sum_{B \in \Gamma^{(k)}} \chi_B^k(z_2) \left\{ [\exp(\beta \varepsilon_{Ai, Bk}^{assoc}) - 1] y^{ik}(\sigma, \bar{\rho}_j(z_1), \bar{\rho}_j(z_2)) \right\} dz_2 = 1 \quad (\text{B.5})$$

Rearranging, we are left with

$$\chi_A^i(z_i) = \frac{1}{1 + 2\pi\kappa\sigma^2(r_c - \sigma) \int_{-1}^{1+z_1} \sum_{k=1}^N \rho_k(z_2) \sum_{B \in \Gamma^{(k)}} \chi_B^k(z_2) \left\{ [\exp(\beta \varepsilon_{Ai, Bk}^{assoc}) - 1] y^{ik}(\sigma, \bar{\rho}_j(z_1), \bar{\rho}_j(z_2)) \right\} dz_2} \quad (\text{B.6})$$

The above equation is applicable to a polyatomic fluid in planar geometry, with any number of association sites (the expression is similar to the expression derived by Segura et al.¹⁸⁶ for a four site associating sphere). From this χ_A^i can be solved in an iterative fashion.

References

- (1) Redlich, O.; Kwong, J. N. S. *Chemical Reviews* **1949**, *44*, 233-244.
- (2) Peng, D. Y.; Robinson, D. B. *Ind. Eng. Chem. Fundam.* **1976**, *15*, 59.
- (3) Wei, Y. S.; Sadus, R. J. *AIChE Journal* **2000**, *46*, 169-196.
- (4) Wertheim, M. S. *J. Stat. Phys.* **1984**, *35*, 19.
- (5) Wertheim, M. S. *J. Stat. Phys.* **1984**, *35*, 35.
- (6) Wertheim, M. S. *J. Stat. Phys.* **1986**, *42*, 459.
- (7) Wertheim, M. S. *J. Stat. Phys.* **1986**, *42*, 477.
- (8) Chapman, W. G., K.E. Gubbins, G. Jackson *Mol. Phys.* **1988**, *65*, 1057.
- (9) Chapman, W. G., K. E. Gubbins, G. Jackson, M. Radosz *Ind. Eng. Chem. Res.* **1990**, *29*, 1709.
- (10) Chapman, W. G., K. E. Gubbins, G. Jackson *Mol. Phys.* **1988**, *65*, 1.
- (11) Chapman, W. G. *J. Chem. Phys.* **1990**, *93*, 4299.
- (12) Chapman, W. G., Ph.D. Thesis. Cornell University, 1988.
- (13) Evans, R. In *Fundamentals of Inhomogeneous Fluids*; Henderson, D., Ed.; Marcel-Dekker: New York, 1992, p 85-175.
- (14) Degennes, P. G. *Macromolecules* **1980**, *13*, 1069-1075.
- (15) Asakura, S.; Oosawa, F. *J. Polym. Sci.* **1958**, *33*, 183.
- (16) Asakura, S.; Oosawa, F. *J. Chem. Phys.* **1954**, *22*, 1255.
- (17) Edwards, S. F. *Proceedings of the Physical Society of London* **1965**, *85*, 613.
- (18) Degennes, P. G. *Reports on Progress in Physics* **1969**, *32*, 187.
- (19) Curro, J. G.; Schweizer, K. S. *Journal of Chemical Physics* **1987**, *87*, 1842-1846.
- (20) Schweizer, K. S.; Curro, J. G. *Physical Review Letters* **1987**, *58*, 246-249.

- (21) Geisinger, T.; Muller, M.; Binder, K. *Journal of Chemical Physics* **1999**, *111*, 5241-5250.
- (22) Geisinger, T.; Muller, M.; Binder, K. *Journal of Chemical Physics* **1999**, *111*, 5251-5258.
- (23) Chatterjee, A. P.; Schweizer, K. S. *Journal of Chemical Physics* **1998**, *109*, 10464-10476.
- (24) Chatterjee, A. P.; Schweizer, K. S. *Journal of Chemical Physics* **1998**, *109*, 10477-10488.
- (25) Fuchs, M.; Schweizer, K. S. *Physical Review E* **2001**, *64*, 021514.
- (26) Hooper, J. B.; Schweizer, K. S.; Desai, T. G.; Koshy, R.; Koblinski, P. *Journal of Chemical Physics* **2004**, *121*, 6986-6997.
- (27) Wu, J. *AIChE J.* **2006**, *52*, 1169-1193.
- (28) Wu, J. Z.; Li, Z. D. *Annual Review of Physical Chemistry* **2007**, *58*, 85-112.
- (29) Segura, C. J.; Chapman, W. G.; Shukla, K. P. *Molecular Physics* **1997**, *90*, 759-771.
- (30) Segura, C. J.; Vakarin, E. V.; Chapman, W. G.; Holovko, M. F. *Journal of Chemical Physics* **1998**, *108*, 4837-4848.
- (31) Segura, C. J.; Zhang, J.; Chapman, W. G. *Molecular Physics* **2001**, *99*, 1-12.
- (32) Jain, S.; Dominik, A.; Chapman, W. G. *Journal of Chemical Physics* **2007**, *127*, 244904.
- (33) Tripathi, S.; Chapman, W. G. *Physical Review Letters* **2005**, *94*, 087801.
- (34) Tripathi, S.; Chapman, W. G. *Journal of Chemical Physics* **2005**, *122*, 094506.
- (35) Sengers, J. M. H. L. *Supercritical Fluid Technology Reviews in Modern Theory and Applications*; CRC, 1991.
- (36) Sengers, J. V.; Sengers, J. M. H. L. *Annu. Rev. Phys. Chem* **1986**, *37*, 189.
- (37) Chen, Z. Y., P.C. Albright, J.V. Senger *Phys. Rev. A* **1990**, *41*, 3160.
- (38) Chen, Z. Y., A. Abbaci, S. Tang, J.V. Senger *Phys. Rev. A* **1990**, *42*, 3370.
- (39) Salvino, L. W., J.A. White *J. Chem. Phys.* **1992**, *96*, 4559.

- (40) White, J. A. *Fluid Phase Equilib.* **1992**, *75*, 53.
- (41) White, J. A., S. Zhang *J. Chem. Phys.* **1993**, *99*, 2012.
- (42) White, J. A., S. Zhang *J. Chem. Phys.* **1995**, *103*, 1922.
- (43) White, J. A. *J. Chem. Phys.* **1999**, *111*, 9352.
- (44) Kiselev, S. B. *Fluid Phase Equilib.* **1998**, *147*, 7.
- (45) Kiselev, S. B., J.F. Ely *Ind. Eng. Chem. Res.* **1999**, *38*, 4993.
- (46) Adidharma, H., M. Radosz *J. Chem. Phys.* **1998**, *37*, 4453.
- (47) McCabe, C., S. B. Kiselev *Ind. Eng. Chem. Res.* **2004**, *43*, 2839.
- (48) Wilson, K. G. *Phys. Rev. B* **1971**, *4*, 3174.
- (49) Wilson, K. G., M.E. Fisher *Phys. Rev. Lett.* **1972**, *28*, 240.
- (50) Lue, L.; Prausnitz, J. M. *AIChE J.* **1998**, *44*, 1455.
- (51) Lue., L., J.M. Prausnitz *J. Chem. Phys.* **1998**, *108*, 5529.
- (52) Tang, Y. *J. Chem. Phys.* **1998**, *109*, 5935.
- (53) Jiang, J., J.M. Prausnitz *J. Chem. Phys.* **1999**, *111*, 5964.
- (54) Jiang, J.; Prausnitz, J. M. *AIChE J.* **2000**, *46*, 2525.
- (55) Llovell, F., Josep C. Pamies, Lourdes F. Vega. *J. Chem. Phys.* **2004**, *121*, 10715.
- (56) Llovell, F.; Vega, L. F. *J. Phys. Chem. B.* **2006**, *110*, 1350.
- (57) Fu, D.; Li, X.-S.; Yan, S.; Liao, T. *Ind. Eng. Chem. Res.* **2006**, *45*, 8199-8206.
- (58) Gross, J., G. Sadowski *Ind. Eng. Chem. Res.* **2001**, *40*, 1244.
- (59) Banaszak, M., Y.C. Chiew, R. O'Lenick, M. Radosz *J. Chem. Phys.* **1994**, *100*, 3803.
- (60) Blas, F. J., L.F. Vega. *Mol. Phys.* **1997**, *92*, 135.
- (61) Ghonasgi, D., W.G. Chapman. *AIChE J.* **1994**, *40*, 878.

- (62) Ghonasgi, D.; Llano-Restrepo, M.; Chapman, W. G. *J. Chem. Phys.* **1993**, *98*, 5662.
- (63) Johnson, J. K., E.A. Müller, K.E. Gubbins. *J. Phys. Chem.* **1994**, *98*, 6413.
- (64) Muller, E. A.; Vega, L. F.; Gubbins, K. E. *Mol. Phys.* **1994**, *83*, 1209.
- (65) Huang, S. H., M Radosz. *Ind. Eng. Chem. Res.* **1990**, *29*, 2284.
- (66) Huang, S. H., M Radosz. *Ind. Eng. Chem. Res.* **1991**, *30*, 1994.
- (67) Chen, S. S., A. Kreglewski *Ber. Bunsen-Ges* **1977**, *81(10)*, 1048.
- (68) Gil-Villegas, A.; Galindo, A.; Whitehead, P. J.; Mills, S. J.; Jackson, G. *J. Chem. Phys.* **1997**, *106*, 4168.
- (69) Dominik, A.; Jain, S.; Chapman, W. G. *Ind. Eng. Chem. Res.* **2007**, *46*, 5766-5774.
- (70) Barker, J., D. Henderson *J. Chem. Phys.* **1967**, *47*, 2857.
- (71) Barker, J., D. Henderson *J. Chem. Phys.* **1967**, *47*, 4714.
- (72) Carnahan, N. F., K.E. Starling *J. Chem. Phys.* **1969**, *51*, 635.
- (73) Gross, J., G. Sadowski *Supercritical Fluids as Solvents and Reaction Media* **2004**, 295-322.
- (74) Gross, J., G. Sadowski *Ind. Eng. Chem. Res.* **2002**, *41*, 5510.
- (75) Dominik, A., W.G. Chapman *Ind. Eng. Chem. Res.* **2005**, *44(17)*, 6928.
- (76) Ghosh, A. J. B., P.K. Jog, W.G. Chapman *Macromolecules* **2005**, *38*, 1025.
- (77) Dominik, A., W. G. Chapman *Macromolecules* **2005**, *38(26)*, 10836.
- (78) Gross, J., G. Sadowski *Ind. Eng. Chem. Res.* **2002**, *41*, 1084.
- (79) Tumakaka, F., J. Gross, G. Sadowski *Fluid Phase Equilib.* **2002**, *194-197*, 541-551.
- (80) Gonzalez, D. L., D.P. Ting, G. J. Hirasaki, W.G. Chapman *Energy & Fuels* **2005**, *19(4)*, 1230.
- (81) Yarrison, M., W.G. Chapman *Fluid Phase Equilib.* **2004**, *226*, 195.

- (82) Lee, L. L. *Molecular Thermodynamics of Nonideal Fluids*; Butterworth: Boston, 1988.
- (83) Negele, J. W., H. Orland *Quantum Many-Particle Systems*; Addison-Wesley: Redwood City, CA, 1988.
- (84) Battle, G. *Recent Advances in Wavelet Analysis*; Academic: Boston, 1994.
- (85) <http://webbook.nist.gov/>.
- (86) Amoros, J. *Phys. Chem. Liq.* **2002**, *40*, 269.
- (87) Rosenthal, D. J.; Teja, A. S. *AIChE J.* **1989**, *35*, 1829.
- (88) Teja, A. S.; Lee, R. J.; Rosenthal, D. J.; Anselme, M. J. In *5th IUPAC Conference on Alkanes and Alkanols* Gradisca, 1989.
- (89) Nikitin, E. D.; Pavlov, P. A.; Bessonova, N. V. *J. Chem. Thermodyn.* **1994**, *26*, 177.
- (90) Nikitin, E. D.; Pavlov, P. A.; Popov, A. P. *Fluid Phase Equilib.* **1997**, *141*, 155.
- (91) Ambrose, D.; Tsonopoulos, C. *J. Chem. Eng. Data* **1995**, *40*, 531.
- (92) Rosenthal, D. J.; Teja, A. S. *AIChE Journal* **1989**, *35*, 1829-1834.
- (93) Nath, S. K.; Escobedo, F. A.; Pablo, J. J. d. *J. Chem. Phys.* **1998**, *108*, 9905.
- (94) Cai, J., J.M. Prausnitz *Fluid Phase Equilib.* **2004**, *219*, 205.
- (95) Fu, D.; Wu, J. *Ind. Eng. Chem. Res.* **2005**, *44*, 1120.
- (96) Fu, D.; Zhao, Y. *Chinese Journal of Chemistry* **2005**, *23*, 386.
- (97) Astarita, G.; Savage, D.; Bisio, A. *Gas Treating with Chemical Solvents*; John Wiley and Sons: New York, 1983.
- (98) Cullinane, J. T.; Northrop, P. S., Private Communication.
- (99) Valencia, J. A.; Denton, R. D.; Exxon Production Research Co. (Houston, TX) United States, 1985.
- (100) Kohl, A. L.; Riesenfeld, F. *Gas Purification*; Gulf Publishing Company: Houston, TX, 1985.

- (101) Huang, S. H.; Ng, H. J. *Gas Processors Association Research Report RR-155* **1998**.
- (102) Jou, F. Y.; Carroll, J. J.; Mather, A. E.; Otto, F. D. *Journal of Chemical and Engineering Data* **1993**, *38*, 75-77.
- (103) Jou, F. Y.; Mather, A. E.; Otto, F. D. *Industrial & Engineering Chemistry Process Design and Development* **1982**, *21*, 539-544.
- (104) Jou, F. Y.; Otto, F. D.; Mather, A. E. *Industrial & Engineering Chemistry Research* **1994**, *33*, 2002-2005.
- (105) Jou, F. Y.; Otto, F. D.; Mather, A. E. *Journal of Chemical and Engineering Data* **1996**, *41*, 1181-1183.
- (106) Sidi-Boumedine, R.; Horstmann, S.; Fischer, K.; Provost, E.; Furst, W.; Gmehling, J. *Fluid Phase Equilibria* **2004**, *218*, 85-94.
- (107) Awan, J. A.; Chareton, A.; Valtz, A.; Dieu, F.; Coquelet, C.; Richon, D. *Gas Processors Association Status Report, GPA Project 037*. **March 2008**.
- (108) Jou, F. Y.; Mather, A. E.; Ng, H. J.; Elsevier Science Bv: 1999, p 933-938.
- (109) Jou, F. Y.; Mather, A. E.; Schmidt, K. A. G.; Ng, H. J. *Journal of Chemical and Engineering Data* **1999**, *44*, 833-835.
- (110) Ng, H. J.; Jou, F. Y.; Mather, A. E. *Gas Processors Association Research Report RR-164* **1998**.
- (111) Abrams, D. S.; Prausnitz, J. M. *AIChE Journal* **1975**, *21*, 116-128.
- (112) Fredenslund, A.; Gmehling, J.; Rasmussen., P. *Vapor-Liquid Equilibria using UNIFAC*; Elsevier: Amsterdam, 1977.
- (113) Prausnitz, J. M.; Lichtenthaler, R. N.; Azevedo, E. G. d. *Molecular Thermodynamics of Fluid-Phase Equilibria*; 3rd ed.; Prentice Hall: Englewood Cliffs, NJ, 1999.
- (114) Renon, H.; Prausnit.Jm *AIChE Journal* **1968**, *14*, 135.
- (115) Soave, G. *Chemical Engineering Science* **1972**, *27*, 1197-&.
- (116) Hu, Y.; Liu, H. L.; Prausnitz, J. M. *Journal of Chemical Physics* **1996**, *104*, 396-404.

- (117) Economou, I. G. *Industrial & Engineering Chemistry Research* **2002**, *41*, 953-962.
- (118) Economou, I. G.; Donohue, M. D.; Elsevier Science Bv: 1996, p 518-529.
- (119) Muller, E. A.; Gubbins, K. E. *Industrial & Engineering Chemistry Research* **2001**, *40*, 2193-2211.
- (120) Boublik, T. *Journal of Chemical Physics* **1970**, *53*, 471.
- (121) Mansoori, G. A.; Carnahan, N. F.; Starling, K. E.; Leland, T. W. *Journal of Chemical Physics* **1971**, *54*, 1523.
- (122) Wolbach, J. P.; Sandler, S. I. *Industrial & Engineering Chemistry Research* **1998**, *37*, 2917-2928.
- (123) Li, X. S.; Wu, H. J.; Englezos, P. *Industrial & Engineering Chemistry Research* **2006**, *45*, 2131-2137.
- (124) Design Institute for Physical Properties, Sponsored by AIChE; 2008 Design Institute for Physical Property Data/AIChE.
- (125) Bymaster, A.; Emborsky, C.; Dominik, A.; Chapman, W. G. *Industrial & Engineering Chemistry Research* **2008**, *47*, 6264-6274.
- (126) Kohn, J. P.; Kurata, F. *AIChE Journal* **1958**, *4*, 211-217.
- (127) Kalra, H.; Robinson, D. B.; Krishnan, T. R. *Journal of Chemical and Engineering Data* **1977**, *22*, 85-88.
- (128) Carroll, J. J.; Mather, A. E. *Fluid Phase Equilibria* **1992**, *81*, 187-204.
- (129) Scott, R. L.; Royal Soc Chemistry: 1999, p 4225-4231.
- (130) Vankonynenburg, P. H.; Scott, R. L. *Philosophical Transactions of the Royal Society of London Series a-Mathematical Physical and Engineering Sciences* **1980**, *298*, 495-540.
- (131) Guilbot, P.; Fischer, K.; Valtz, A.; Theveneau, P.; Baba-Ahmed, A.; Richon, D. *Fluid Phase Equilibria* **2007**, *260*, 49-59.
- (132) Guilbot, P. F., K.; Valtz, A.; Theveneau, P.; Baba-Ahmed, A. and D. Richon. *Gas Processors Association RR-170 June* **2000** .
- (133) Privat, R.; Jaubert, J. N.; Mutelet, F. *The Journal of Chemical Thermodynamics* **2008**, *40*, 1331-1341.

- (134) Lee, J. I.; Mather, A. E.; Otto, F. D. *Journal of Chemical and Engineering Data* **1978**, *23*, 78-79.
- (135) Shuo, X.; Qing, S. J.; Zhen, Z. S.; Zhang, C. F.; Carroll, J. J. *Fluid Phase Equilibria* **1991**, *67*, 197-201.
- (136) Saul, A.; Wagner, W. *Journal of Physical and Chemical Reference Data* **1987**, *16*, 893-901.
- (137) Kilner, J.; McBain, S. E.; Roffey, M. G. *Journal of Chemical Thermodynamics* **1990**, *22*, 203-210.
- (138) Kuranov, G.; Rumpf, B.; Maurer, G.; Smirnova, N.; Elsevier Science Bv: 1997, p 147-162.
- (139) Bedell, S. A.; Miller, M. *Industrial & Engineering Chemistry Research* **2007**, *46*, 3729-3733.
- (140) Henni, A.; Tontiwachwuthikul, P.; Chakma, A. *Journal of Chemical and Engineering Data* **2006**, *51*, 64-67.
- (141) Nassar, V. L. B., J.A.; and L.G. Lyddon. *Bryan Research and Engineering, Inc. – Technical Papers*. **2006**.
- (142) Nassar, V. L. B., J.A.; and L.G. Lyddon. *Bryan Research and Engineering, Inc. – Technical Papers*. **2008**.
- (143) Bedell, S. A.; Pirtle, L. L.; Griffin, J. M. *Hydrocarbon Processing* **2007**, *86*, 49-50.
- (144) Hohenberg, P.; Kohn, W. *Phys. Rev.* **1964**, *136*, B864.
- (145) Kohn, W.; Sham, L. J. *Phys. Rev.* **1965**, *140*, A1133.
- (146) Ebner, C.; Saam, W. F.; Stroud, D. *Phys. Rev. A*. **1976**, *14*, 2264.
- (147) McQuarrie, D. A. *Statistical Mechanics*; University Science Books: Sausalito, CA, 2000.
- (148) Huang, K. *Statistical Mechanics*; John Wiley and Sons: New York, 1987.
- (149) McMullen, W. E.; Freed, K. F. *J. Chem. Phys.* **1990**, 1413-1426.
- (150) Evans, R. *Adv. Phys.* **1979**, *28*, 143.

- (151) Vanderlick, T. K.; Scriven, L. E.; Davis, H. T. *J. Chem. Phys.* **1989**, *90*, 2472.
- (152) Tarazona, P. *Phys. Rev. A* **1985**, *31*, 2672.
- (153) Tarazona, P. *Phys. Rev. A* **1985**, *32*, 3148.
- (154) Curtin, W. A.; Ashcroft, N. W. *Phys. Rev. Lett.* **1986**, *56*, 2775.
- (155) Rosenfeld, Y. *Phys. Rev. Lett.* **1989**, *63*, 980.
- (156) Rosenfeld, Y. *Phys. Rev. A* **1990**, *42*, 5978.
- (157) Meister, T. F.; Kroll, D. M. *Phys. Rev. A* **1985**, *31*, 4055.
- (158) Chandler, D.; McCoy, J. D.; Singer, S. J. *J. Chem. Phys.* **1986**, *85*, 5971.
- (159) Chandler, D.; McCoy, J. D.; Singer, S. J. *J. Chem. Phys.* **1986**, *85*, 5977.
- (160) McCoy, J. D.; Singer, S. J.; Chandler, D. *J. Chem. Phys.* **1987**, *87*, 4853.
- (161) Schweizer, K. S.; Curro, J. G. *Phys. Rev. Lett.* **1988**, *60*, 809.
- (162) Kierlik, E.; Rosinberg, M. L. *J. Chem. Phys.* **1992**, *97*, 9222.
- (163) Kierlik, E.; Rosinberg, M. L. *J. Chem. Phys.* **1993**, *99*, 3950.
- (164) Kierlik, E.; Rosinberg, M. L. *J. Chem. Phys.* **1994**, *100*, 1716.
- (165) Dominik, A.; Tripathi, S.; Chapman, W. G. *Industrial & Engineering Chemistry Research* **2006**, *45*, 6785-6792.
- (166) Tripathi, S.; Chapman, W. G. *J. Chem. Phys.* **2003**, *119*, 12611.
- (167) Tripathi, S.; Chapman, W. G. *Condensed Matter Physics* **2003**, *6*, 523.
- (168) Tripathi, S.; Chapman, W. G. *Journal of Chemical Physics* **2003**, *118*, 7993-8003.
- (169) Cao, D.; Wu, J. *Macromolecules* **2005**, *38*, 971.
- (170) Cao, D.; Wu, J. *J. Chem. Phys.* **2004**, *121*, 4210.
- (171) Yu, Y.-X.; Wu, J. *J. Chem. Phys.* **2002**, *116*, 7094.
- (172) Yu, Y.-X.; Wu, J. *J. Chem. Phys.* **2002**, *117*, 2368.

- (173) Bryk, P.; Bucior, K.; Sokolowski, S.; Zukocinski, G. *J. Phys. Chem. B.* **2005**, *109*, 2977.
- (174) Bryk, P.; Pizio, O.; Sokolowski, S. *J. Chem. Phys.* **2005**, *122*, 194904.
- (175) Bryk, P.; Sokolowski, S. *J. Chem. Phys.* **2004**, *121*, 11314.
- (176) Malijevsky, A.; Bryk, P.; Sokolowski, S. *Phys. Rev. E.* **2005**, *72*, 032801.
- (177) Patrykiewicz, A.; Sokolowski, S.; Henderson, D. *Molecular Physics* **1998**, *95*, 211.
- (178) Pizio, O.; Patrykiewicz, A.; Sokolowski, S. *J. Chem. Phys.* **2000**, *113*, 10761.
- (179) Patel, N.; Egorov, S. A. *Journal of Chemical Physics* **2005**, *123*, 144916.
- (180) Patel, N.; Egorov, S. A. *Journal of Chemical Physics* **2004**, *121*, 4987-4997.
- (181) Blas, F. J.; Rio, E. M. D.; Miguel, E. D.; Jackson, G. *Molecular Physics* **2001**, *99*, 1851.
- (182) Gloor, G.; Blas, F. J.; Rio, E. M. d.; Miguel, E. d.; Jackson, G. *Fluid Phase Equilib.* **2002**, *194-197*, 521.
- (183) Kierlik, E.; Rosinberg, M. L. *Phys. Rev.* **1990**, *42*, 3382.
- (184) Yethiraj, A.; Hall, C. K. *Macromolecules* **1990**, *23*, 1865.
- (185) Yethiraj, A.; Woodward, C. E. *J. Chem. Phys.* **1995**, *102*, 5499.
- (186) Segura, C. J.; Chapman, W. G. *Molecular Physics* **1995**, *86*, 415-442.
- (187) Tripathi, S., Ph.D. Thesis. Rice University, 2004.
- (188) Calleja, M.; Rickayzen, G. *Mol. Phys.* **1993**, *79*, 809.
- (189) Groot, R. D. *Mol. Phys.* **1987**, *60*, 45.
- (190) Marsh, P.; Rickayzen, G.; Calleja, M. *Mol. Phys.* **1995**, *84*, 799.
- (191) Woodward, C. E. *Journal of Chemical Physics* **1991**, *94*, 3183-3191.
- (192) Jain, S.; Chapman, W. G. *Molecular Physics* **2009**, *107*, 1-17.
- (193) Jain, S.; Jog, P.; Weinhold, J.; Srivastava, R.; Chapman, W. G. *Journal of Chemical Physics* **2008**, *128*.

- (194) Jain, S.; Chapman, W. G. *Molecular Physics* **2009**, *Submitted*.
- (195) Bymaster, A.; Jain, S.; Chapman, W. G. *Journal of Chemical Physics* **2008**, *128*, 13.
- (196) Bymaster, A.; Chapman, W. G. *In preparation*. **2009**.
- (197) Kauzmann, W. *Adv. Protein Chem.* **1959**, *14*, 1.
- (198) Tanford, C. *The Hydrophobic Effect: Formation of Micelles and Biological Membranes*; 2nd. ed.; Wiley: New York, 1980.
- (199) Stillinger, F. H. *J. Solution Chem.* **1973**, *2*, 141.
- (200) Reiss, H. *Adv. Chem. Phys.* **1965**, *9*, 1.
- (201) Reiss, H.; Frisch, H. L.; Lebowitz, J. L. *J. Chem. Phys.* **1959**, *31*, 369.
- (202) Pierroti, R. A. *J. Chem. Phys.* **1965**, *69*, 281.
- (203) Ashbaugh, H. S.; Paulaitis, M. E. *J. Am. Chem. Soc.* **2001**, *123*, 10721.
- (204) Ashbaugh, H. S.; Pratt, L. R. *Reviews of Modern Physics* **2006**, *78*, 159.
- (205) Floris, F. *J. Phys. Chem. B.* **2005**, *109*, 24061.
- (206) Huang, D.; Chandler, D. *J. Phys. Chem. B.* **2002**, *106*, 2047.
- (207) Huang, D.; Geissler, P. L.; Chandler, D. *J. Phys. Chem. B.* **2001**, *105*, 6704.
- (208) Lum, K.; Chandler, D.; Weeks, J. *J. Phys. Chem. B.* **1999**, *103*, 4570.
- (209) Sun, S. X. *Phys. Rev. E.* **2001**, *64*, 021512.
- (210) Floris, F. M.; Selmi, M.; Tani, A.; Tomasi, J. *J. Chem. Phys.* **1997**, *107*, 6353.
- (211) Hummer, G.; Garde, S.; Garcia, A. E.; Pohorille, A.; Pratt, L. R. *Proc. Natl. Acad. Sci. U.S.A.* **1996**, *93*, 8951.
- (212) Reddy, G.; Yethiraj, A. *J. Chem. Phys.* **2004**, *121*, 4203.
- (213) Muller, M.; MacDowell, L. G.; Yethiraj, A. *J. Chem. Phys.* **2003**, *118*, 2929.
- (214) Hummer, G.; Garde, S. *Phys. Rev. Lett.* **1998**, *80*, 4193.

- (215) Ashbaugh, H. S.; Pratt, L. R.; Paulaitis, M. E.; Clohery, J.; Beck, T. L. *J. Am. Chem. Soc.* **2005**, *127*, 2808.
- (216) Stillinger, F. H. *Adv. Chem. Phys.* **1975**, *31*, 1.
- (217) Stillinger, F. H.; Rahman, A. *J. Chem. Phys.* **1974**, *60*, 1545.
- (218) Berendsen, H. J. C.; Grigera, J. R.; Straatsma, T. P. *J. Phys. Chem.* **1987**, *91*, 6269.
- (219) Berendsen, H. J. C.; Postma, J. M. P.; van Gunsteren, W. F.; Hermans, J. In *Intermolecular Forces*; Pullman, B., Ed.; D. Reidel: Dordrecht, 1981, p 331.
- (220) Jorgensen, W. L. *J. A. Chem. Soc.* **1981**, *103*, 335.
- (221) Jorgensen, W. L. *J. Chem. Phys.* **1982**, *77*, 4156.
- (222) Jorgensen, W. L.; Madura, J. D. *Mol. Phys.* **1985**, *56*, 1381.
- (223) Muller, E. A.; Gubbins, K. E. *Ind. Eng. Chem. Res.* **1995**, *34*, 3662.
- (224) Bol, W. *Mol. Phys.* **1982**, *45*, 605.
- (225) Kolafa, J.; Nezbeda, I. *Mol. Phys.* **1991**, *61*, 161.
- (226) Ghonasgi, D.; Chapman, W. G. *Mol. Phys.* **1993**, *79*, 291.
- (227) Chandler, D.; Weeks, J. D. *Phys. Rev. Lett.* **1970**, *25*, 149.
- (228) Weeks, J. D.; Chandler, D.; Andersen, H. C. *J. Chem. Phys.* **1971**, *54*, 5237.
- (229) Groh, B.; Mulder, B. *Phys. Rev. E.* **2000**, *61*, 3811.
- (230) Warshavsky, V. B.; Song, X. *Phys. Rev. E.* **2004**, *69*, 061113.
- (231) Yu, Y.; Wu, J. *J. Chem. Phys.* **2002**, *117*, 10156.
- (232) Henderson, J. R. *Mol. Phys.* **1983**, *50*, 741.
- (233) Pallas, N. R.; Harrison, Y. *Colloids and Surfaces* **1990**, *43*, 169-194.
- (234) Luck, W. A. P. *Discussions of the Faraday Society* **1967**, 115.
- (235) Soper, A. K.; Bruni, F.; Ricci, M. A. *Journal of Chemical Physics* **1997**, *106*, 247-254.

- (236) Bondarenko, G. V.; Gorbaty, Y. E. *Molecular Physics* **1991**, *74*, 639-647.
- (237) Jackson, G.; Chapman, W. G.; Gubbins, K. E. *Molecular Physics* **1988**, *65*, 1-31.
- (238) Joesten, M. D.; Schaad, L. *Hydrogen Bonding*; Dekker: New York, 1974.
- (239) Suresh, S. J.; Naik, V. M. *Journal of Chemical Physics* **2000**, *113*, 9727-9732.
- (240) Zielkiewicz, J. *Journal of Chemical Physics* **2005**, *123*.
- (241) Huang, D.; Chandler, D. *Phys. Rev. E* **2000**, *61*, 1501.
- (242) Tang, Y.; Wu, J. *Phys. Rev. E* **2004**, *70*, 011201.
- (243) Tang, Z.; Scriven, L. E.; Davis, H. T. *J. Chem. Phys.* **1991**, *95*, 2659.
- (244) Alejandre, J.; Tildesley, D. J.; Chapela, G. A. *Journal of Chemical Physics* **1995**, *102*, 4574-4583.
- (245) Predota, M.; Nezbeda, I.; Cummings, P. T. *Mol. Phys.* **2002**, *100*, 2189.
- (246) Lee, J. Y.; Buxton, G. A.; Balazs, A. C. *J. Chem. Phys.* **2004**, *121*, 5531.
- (247) Sinani, V.; Kokysh, D. S.; Yun, B.-G.; Matts, R. L.; Pappas, T. C.; Motamedi, M.; Thomas, S. N.; Kotov, N. A. *Nano Lett.* **2003**, *3*, 1177.
- (248) Smith, K. A.; Tyagi, S.; Balazs, A. C. *Macromolecules* **2005**, *38*, 10138.
- (249) Spoerke, E.; Stupp, S. *J. Biomed. Mater. Res.* **2003**, *67A*, 960.
- (250) White, S.; So Hos, N. R.; Geubelle, P. H.; Moore, J. S.; Kessler, M. R.; Sriram, S. R.; Brown, E. N.; Viswanathan, S. *Nature* **2001**, *409*, 794.
- (251) deGennes, P. *Scaling Concepts in Polymer Physics*; Cornell University Press: Ithaca, 1979.
- (252) deGennes, P. G. *C.R. Acad. Sci., Paris B* **1979**, *288*, 359.
- (253) Joanny, J. R.; Leibler, L.; Gennes, P. G. D. *J. Poly. Sci., Polym. Phys. Ed.* **1979**, *17*, 1073.
- (254) Sear, R. P. *Eur. Phys. J. B.* **1999**, *1*, 313.
- (255) Sear, R. P. *J. Chem. Phys.* **2001**, *115*, 575.
- (256) Eisenriegler, E. *J. Chem. Phys.* **2000**, *113*, 5091.

- (257) Maassen, R.; Eisenriegler, E.; Bringer, A. *J. Chem. Phys.* **2001**, *115*, 5292.
- (258) Surve, M.; Pryamitsyn, V.; Ganesan, V. *J. Chem. Phys.* **2005**, *122*, 154901.
- (259) Tuinier, R.; Fleer, G. J. *Macromolecules* **2004**, *37*, 8764.
- (260) Scheutjens, J. M. H. M.; Fleer, G. J. *Adv. Colloid Interface Sci.* **1982**, *16*, 361.
- (261) Yang, S.; Yan, D.; Tan, H.; Shi, A. C. *Phys. Rev. E.* **2006**, *74*, 041808.
- (262) Fuchs, M.; Schweizer, K. S. *Journal of Physics-Condensed Matter* **2002**, *14*, R239-R269.
- (263) Yethiraj, A.; Hall, C. K.; Dickman, R. *Journal of Colloid and Interface Science* **1992**, *151*, 102-117.
- (264) Dickman, R.; Yethiraj, A. *J. Chem. Phys.* **1994**, *100*, 4683.
- (265) Doxastakis, M.; Chen, Y.-L.; de Pablo, J. J. *J. Chem. Phys.* **2005**, *123*, 034901.
- (266) Doxastakis, M.; Chen, Y.-L.; Guzman, O.; de Pablo, J. J. *J. Chem. Phys.* **2004**, *120*, 9335.
- (267) Louis, A. A.; Bolhuis, P. G.; Meijer, E. J. *J. Chem. Phys.* **2002**, *116*, 10547.
- (268) Louis, A. A.; Bolhuis, P. G.; Meijer, E. J.; Hansen, J. P. *J. Chem. Phys.* **2002**, *117*, 1893.
- (269) Striolo, A.; Colina, C. M.; Gubbins, K. E.; Elvassore, N.; Lue, L. *Molecular Simulation* **2004**, *30*, 437.
- (270) Tuinier, R.; Lekkerkerker, H. N. W.; Aarts, D. G. A. L. *Phys. Rev. E.* **2002**, *65*, 060801.
- (271) Tuinier, R.; Vliegthart, G. A.; Lekkerkerker, H. N. W. *J. Chem. Phys.* **2000**, *113*, 10768.
- (272) Chen, X.; Cai, J.; Liu, H.; Hu, Y. *Molecular Simulation* **2006**, *32*, 877-885.
- (273) Kim, S. C.; Leez, S. H. *Molecular Physics* **2006**, *104*, 1487-1495.
- (274) Li, Z. D.; Wu, J. Z. *Journal of Chemical Physics* **2007**, *126*, 1449041.
- (275) Woodward, C. E.; Yethiraj, A. *J. Chem. Phys.* **1994**, *100*, 3181.
- (276) Freasier, B. C.; Woodward, C. E. *Comput. Theor. Polym. Sci.* **1999**, *9*, 141.

- (277) Hansen, J. P.; McDonald, I. R. *Theory of Simple Liquids*; 3rd ed.; Academic Press: San Diego, CA, 2006.
- (278) Kirkwood, J. G. *J. Chem. Phys.* **1935**, *3*, 300.
- (279) Derjaguin, B. V. *Kolloid-Z.* **1934**, *69*, 155.
- (280) Attard, P. *J. Chem. Phys.* **1989**, *91*, 3083.
- (281) Biben, T.; Bladon, P.; Frenkel, D. *J. Phys.: Condens. Matter* **1996**, *8*, 10799.
- (282) Louis, A. A.; Allahyarov, E.; Lowen, H.; Roth, R. *Phys. Rev. E.* **2002**, *65*, 061407.
- (283) Gotzelmann, B.; Evans, R.; Dietrich, S. *Physical Review E* **1998**, *57*, 6785-6800.
- (284) Mao, Y.; Cates, M. E.; Lekkerkerker, H. N. W. *Physica A* **1995**, *222*, 10-24.
- (285) Roth, R.; Evans, R.; Dietrich, S. *Physical Review E* **2000**, *62*, 5360-5377.
- (286) Woodward, C. E. *J. Chem. Phys.* **1991**, *94*, 3183.
- (287) Roth, R.; Evans, R.; Dietrich, S. *Phys. Rev. E.* **2000**, *62*, 5360.
- (288) Li, Z. D.; Cao, D. P.; Wu, J. Z. *Journal of Chemical Physics* **2005**, *122*.
- (289) Dautenhahn, J.; Hall, C. K. *Macromolecules* **1994**, *27*, 5399.
- (290) Bolhuis, P. G.; Meijer, E. J.; Louis, A. A. *Phys. Rev. Lett.* **2003**, *90*, 068304.
- (291) Schweizer, K. S.; Curro, J. G. *Adv. Polym. Sci.* **1994**, *116*, 319.
- (292) Schweizer, K. S.; Curro, J. G. *Adv. Chem. Phys.* **1997**, *98*, 1.
- (293) Percus, J.; Yevick, G. *Phys. Rev.* **1958**, *110*, 1.
- (294) Picu, R. C.; Ozmusul, M. S. *J. Chem. Phys.* **2003**, *118*, 11239.
- (295) Li, Z.; Wu, J. *J. Chem. Phys.* **2007**, *126*, 1449041.
- (296) Konig, P. M.; Roth, R.; Dietrich, S. *Phys. Rev. E.* **2006**, *74*, 0414041.
- (297) Chen, X.; Cai, J., J.M. Prausnitz; Hu, Y. *Molecular Simulation* **2006**, *32*, 877.
- (298) Kim, S. C.; Lee, S. H. *Mol. Phys.* **2006**, *104*, 1487.

- (299) Bedrov, D.; Smith, G. D.; Smith, J. S. *Journal of Chemical Physics* **2003**, *119*, 10438-10447.
- (300) Smith, J. S.; Bedrov, D.; Smith, G. D. *Composites Science and Technology* **2003**, *63*, 1599-1605.
- (301) Patra, C. N.; Yethiraj, A. *J. Chem. Phys.* **2000**, *112*, 1579.
- (302) Patra, C. N.; Yethiraj, A. *J. Chem. Phys.* **2003**, *118*, 4702.
- (303) Cotterman, R. L.; Schwarz, B. J.; Prausnitz, J. M. *AIChE Journal* **1986**, *32*, 1787-1798.
- (304) Li, J.; Li, X.; Ni, X. P.; Wang, X.; Li, H. Z.; Leong, K. W. *Biomaterials* **2006**, *27*, 4132-4140.
- (305) Sijbesma, R. P.; Beijer, F. H.; Brunsveld, L.; Folmer, B. J. B.; Hirschberg, J.; Lange, R. F. M.; Lowe, J. K. L.; Meijer, E. W. *Science* **1997**, *278*, 1601-1604.
- (306) Asari, T.; Arai, S.; Takano, A.; Matsushita, Y. *Macromolecules* **2006**, *39*, 2232-2237.
- (307) Asari, T.; Matsuo, S.; Takano, A.; Matsushita, Y. *Macromolecules* **2005**, *38*, 8811-8815.
- (308) Asari, T.; Matsuo, S.; Takano, A.; Matsushita, Y. *Polymer Journal* **2006**, *38*, 258-263.
- (309) Beck, J. B.; Rowan, S. J. *Journal of the American Chemical Society* **2003**, *125*, 13922-13923.
- (310) Matsushita, Y. *Macromolecules* **2007**, *40*, 771-776.
- (311) Noro, A.; Matsushita, Y.; Lodge, T. P. *Macromolecules* **2008**, *41*, 5839-5844.
- (312) Ruokolainen, J.; Mäkinen, R.; Torkkeli, M.; Mäkelä, T.; Serimaa, R.; ten Brinke, G.; Ikkala, O. *Science* **1998**, *280*, 557-560.
- (313) Ruokolainen, J.; Saariaho, M.; Ikkala, O.; ten Brinke, G.; Thomas, E. L.; Torkkeli, M.; Serimaa, R. *Macromolecules* **1999**, *32*, 1152-1158.
- (314) Shen, J. G.; Hogen-Esch, T. *Journal of the American Chemical Society* **2008**, *130*, 10866.
- (315) Dai, J.; Goh, S. H.; Lee, S. Y.; Siow, K. S. *Polymer Journal* **1994**, *26*, 905-911.

- (316) Pan, J.; Chen, M. F.; Warner, W.; He, M. Q.; Dalton, L.; Hogen-Esch, T. E. *Macromolecules* **2000**, *33*, 7835-7841.
- (317) Xiang, M. L.; Jiang, M.; Zhang, Y. B.; Wu, C.; Feng, L. X. *Macromolecules* **1997**, *30*, 2313-2319.
- (318) Dai, L. M.; Toprakcioglu, C. *Macromolecules* **1992**, *25*, 6000-6006.
- (319) Kim, H. S.; Lau, W.; Kumacheva, E. *Macromolecules* **2000**, *33*, 4561-4567.
- (320) Kim, S. D.; Torkelson, J. M. *Macromolecules* **2002**, *35*, 5943-5952.
- (321) Ruths, M.; Granick, S. *Journal of Physical Chemistry B* **1999**, *103*, 8711-8721.
- (322) Tanaka, F.; Ishida, M. *Macromolecules* **1997**, *30*, 1836-1844.
- (323) Tanaka, F.; Ishida, M.; Matsuyama, A. *Macromolecules* **1991**, *24*, 5582-5589.
- (324) Angerman, H. J.; ten Brinke, G. *Macromolecules* **1999**, *32*, 6813-6820.
- (325) Dormidontova, E.; ten Brinke, G. *Macromolecules* **1998**, *31*, 2649-2660.
- (326) Feng, E. H.; Lee, W. B.; Fredrickson, G. H. *Macromolecules* **2007**, *40*, 693-702.
- (327) Lee, W. B.; Elliott, R.; Katsov, K.; Fredrickson, G. H. *Macromolecules* **2007**, *40*, 8445-8454.
- (328) Ayyagari, C.; Bedrov, D.; Smith, G. D. *Polymer* **2004**, *45*, 4549-4558.
- (329) Guo, L.; Luijten, E. *Journal of Polymer Science Part B-Polymer Physics* **2005**, *43*, 959-969.
- (330) Huh, J.; Ikkala, O.; ten Brinke, G. *Macromolecules* **1997**, *30*, 1828-1835.
- (331) Huh, J.; ten Brinke, G. *Journal of Chemical Physics* **1998**, *109*, 789-797.
- (332) Koga, T.; Tanaka, F. *European Physical Journal E* **2005**, *17*, 115-118.
- (333) Sung, B. J.; Yethiraj, A. *Journal of Chemical Physics* **2003**, *119*, 6916-6924.
- (334) Chen, C. C.; Dormidontova, E. E. *Macromolecules* **2006**, *39*, 9528-9538.
- (335) Malvaldi, M.; Allegra, G.; Ciardelli, F.; Raos, G. *Journal of Physical Chemistry B* **2005**, *109*, 18117-18126.

- (336) Malvaldi, M.; Bruzzone, S.; Raos, G.; Allegra, G. *Journal of Physical Chemistry B* **2007**, *111*, 4141-4149.
- (337) Bryk, P.; Sokolowski, S.; Pizio, O. *Journal of Chemical Physics* **2006**, *125*, 024909.
- (338) Gloor, G. J.; Jackson, G.; Blas, F. J.; del Rio, E. M.; de Miguel, E. *Journal of Physical Chemistry C* **2007**, *111*, 15513-15522.
- (339) Gloor, G. J.; Jackson, G.; Blas, F. J.; del Rio, E. M.; de Miguel, E. *Journal of Chemical Physics* **2004**, *121*, 12740-12759.
- (340) Bucior, K.; Fischer, J.; Patrykiewicz, A.; Tscheliessnig, R.; Sokolowski, S. *Journal of Chemical Physics* **2007**, *126*, 094704.
- (341) Yethiraj, A.; Hall, C. K. *Journal of Chemical Physics* **1991**, *94*, 3943-3948.
- (342) Frischknecht, A. L.; Curro, J. G.; Frink, L. J. D. *Journal of Chemical Physics* **2002**, *117*, 10398-10411.
- (343) Walker, J. S.; Vause, C. A. *Scientific American* **1987**, *256*, 98-&.
- (344) Chandler, D. *Journal of Chemical Physics* **1973**, *59*, 2742-2746.
- (345) Chandler, D.; Andersen, H. C. *Journal of Chemical Physics* **1972**, *57*, 1930.
- (346) Schweizer, K. S.; Curro, J. G. In *Advances in Chemical Physics*, Vol 98 1997; Vol. 98, p 1-142.
- (347) Shew, C. Y.; Yethiraj, A. *Journal of Chemical Physics* **1999**, *110*, 11599-11607.
- (348) Yethiraj, A. *Journal of Chemical Physics* **1999**, *111*, 1797-1800.
- (349) Yethiraj, A.; Shew, C. Y. *Physical Review Letters* **1996**, *77*, 3937-3940.
- (350) Schweizer, K. S.; Curro, J. G. *Journal of Chemical Physics* **1989**, *91*, 5059-5081.
- (351) Schweizer, K. S.; Yethiraj, A. *Journal of Chemical Physics* **1993**, *98*, 9053-9079.
- (352) Pickett, G. T.; Schweizer, K. S. *Journal of Chemical Physics* **1999**, *110*, 6597-6600.
- (353) Yethiraj, A. *Journal of Chemical Physics* **1994**, *101*, 9104-9112.
- (354) Yethiraj, A.; Dickman, R.; Szamel, G.; Kierlik, E.; Rosinberg, M. L. *Molecular Physics* **1994**, *82*, 937-955.

- (355) Yethiraj, A.; Hall, C. K. *Journal of Chemical Physics* **1992**, *96*, 797-807.
- (356) Kalyuzhnyi, Y. V.; Cummings, P. T. *Journal of Chemical Physics* **1995**, *103*, 3265-3267.
- (357) Chang, J.; Kim, H. *Journal of Chemical Physics* **1998**, *109*, 2579-2587.
- (358) Chang, J. E.; Sandler, S. I. *Journal of Chemical Physics* **1995**, *102*, 437-449.
- (359) Yethiraj, A.; Fynewever, H.; Shew, C. Y. *Journal of Chemical Physics* **2001**, *114*, 4323-4330.
- (360) Yu, Y. X.; Wu, J. Z. *Journal of Chemical Physics* **2003**, *118*, 3835-3842.
- (361) Yethiraj, A.; Hall, C. K.; Honnell, K. G. *Journal of Chemical Physics* **1990**, *93*, 4453-4461.
- (362) Wertheim, M. S. *Journal of Chemical Physics* **1987**, *87*, 7323-7331.
- (363) Frink, L. J. D.; Salinger, A. G.; Sears, M. P.; Weinhold, J. D.; Frischknecht, A. L. *Journal of Physics-Condensed Matter* **2002**, *14*, 12167-12187.
- (364) Fynewever, H.; Yethiraj, A. *J. Chem. Phys.* **1998**, *108*, 1636-1644.
- (365) Kumar, S. K.; Yethiraj, A.; Schweizer, K. S. *J. Chem. Phys.* **1995**, *103*, 10332-10346.
- (366) Yethiraj, A.; Fynewever, H. *Mol. Phys.* **1998**, *93*, 693-701.
- (367) Ghonasgi, D.; Perez, V.; Chapman, W. G. *J. Chem. Phys.* **1994**, *101*, 6880-6887.
- (368) Schmidt, M. *Physical Review E* **2001**, *63*, 4.
- (369) Esztermann, A.; Reich, H.; Schmidt, M. *Physical Review E* **2006**, *73*, 16.
- (370) Bryk, P.; Roth, R. *Physical Review E* **2005**, *71*, 8.
- (371) Hansen-Goos, H.; Mecke, K. *Physical Review Letters* **2009**, *102*, 4.
- (372) Frink, L. J. D.; Thompson, A.; Salinger, A. G. *Journal of Chemical Physics* **2000**, *112*, 7564-7571.
- (373) Matuszak, D.; Aranovich, G. L.; Donohue, M. D. *Journal of Non-Equilibrium Thermodynamics* **2006**, *31*, 355-384.

(374) Zvelindovsky, A. V.; Sevink, G. J. A.; van Vlimmeren, B. A. C.; Maurits, N. M.; Fraaije, J. *Physical Review E* **1998**, *57*, R4879-R4882.

(375) Morita, H.; Kawakatsu, T.; Doi, M.; Yamaguchi, D.; Takenaka, M.; Hashimoto, T. *Macromolecules* **2002**, *35*, 7473-7480.

(376) Chakrabarti, J.; Dzubiella, J.; Lowen, H. *Europhysics Letters* **2003**, *61*, 415-421.

(377) Michelsen, M. L.; Hendriks, E. M. *Fluid Phase Equilibria* **2001**, *180*, 165-174.